
Electronic Thesis and Dissertation Repository

1-29-2020 11:00 AM

Studying Resting State and Stimulus Induced BOLD Activity using the Generalized Ising Model and Independent Component Graph Analysis

Sivayini Kandeepan
The University of Western Ontario

Supervisor
Soddu, Andrea
The University of Western Ontario Co-Supervisor
Valluri, Sreeram
The University of Western Ontario

Graduate Program in Physics

A thesis submitted in partial fulfillment of the requirements for the degree in Doctor of Philosophy

© Sivayini Kandeepan 2020

Follow this and additional works at: <https://ir.lib.uwo.ca/etd>



Part of the [Statistical, Nonlinear, and Soft Matter Physics Commons](#)

Recommended Citation

Kandeepan, Sivayini, "Studying Resting State and Stimulus Induced BOLD Activity using the Generalized Ising Model and Independent Component Graph Analysis" (2020). *Electronic Thesis and Dissertation Repository*. 6801.

<https://ir.lib.uwo.ca/etd/6801>

This Dissertation/Thesis is brought to you for free and open access by Scholarship@Western. It has been accepted for inclusion in Electronic Thesis and Dissertation Repository by an authorized administrator of Scholarship@Western. For more information, please contact wlsadmin@uwo.ca.

Abstract

Although many technical advancements have been made, neuroscientists still struggle to explain the underlying behaviour of how brain regions communicate with each other to form large-scale functional networks. functional Magnetic Resonance Imaging (fMRI) has been commonly used to investigate changes between brain regions over time using the Blood Oxygen Level Dependent (BOLD) signal.

The goal of this thesis is to show the applicability of novel techniques and tools, such as the generalized Ising model (GIM) and the independent component graph analysis (GraphICA), to obtain information on the functional connectivity of populations with altered perception of consciousness. The GIM was used to model brain activity in healthy brains during various stages of consciousness, as induced by an anesthetic agent, propofol, in the auditory paradigm. GraphICA, a tool that combines ICA and graph theory was used to investigate the functional connectivity of resting state networks (RSNs) in patients with altered perception caused by tinnitus and in patients with altered states of consciousness caused by severe brain injury. For the tinnitus patients, we examined whether a correlation exists between tinnitus behavioural scores and functional brain connectivity of RSNs. Moreover, for the severely brain injured patients, a multimodal neuroimaging approach with hybrid FDG-PET/MRI was implemented to study the functional connectivity changes of the RSNs.

The GIM simulated with an external field was able to model the brain activity at different levels of consciousness under naturalistic stimulation, at a temperature in the super critical regime. Further, a strong correlation was observed between tinnitus distress and the connectivity pattern within and between the right executive control network and the other RSNs. This suggests that tinnitus distress is the consequence of a hyperactive attention condition. A variability was observed

in the appearance and temporal/spatial patterns of RSNs among the two resting state fMRI acquisitions acquired within the same scanning session of the severely brain injured patients. This suggests the need for new strategies to be developed in order to pick the best RSN from each acquisition. Overall, this work demonstrated that the GIM and GraphICA were promising tools to investigate brain activity of populations with altered perception of consciousness and in future can be extended to investigate different neurological populations.

Key words: Resting state fMRI, Generalized Ising model, Graph theory, Independent component analysis, Tinnitus, Disorders of consciousness, Anesthesia, Naturalistic external stimuli

Summary for Lay Audience

The human brain is one of the largest and most complex organs. It acts as the commanding center of the nervous system. It is made up of more than a hundred billion neurons that work together to successfully generate and transfer information. Despite recent advancements in neuroscience, researchers still struggle to explain how the brain functions in order to effectively complete specific tasks.

Our research is to map out the differences in functional connectivity in altered states of consciousness, arising either by the intake of an anesthetic agent or due to pathological conditions. In the first project, we successfully modelled the brain activity of healthy subjects while they were listening to an audio clip from a movie, in awake, mildly sedated, deeply sedated and recovered back, due to anesthesia. Further, synchronization among subjects' brain regions responsible for perception was found only when the individuals were listening to the movie. In future, this simple model will permit us to see whether a non-responsive patient has the same neural experience of a healthy individual.

In the second project, a study focussed on tinnitus (ringing in ears without any sound) patients, we found that distress resulted due to hyper-activity of brain regions in charge of executive functioning. This concludes that tinnitus distress is mainly caused by hyper attention towards internally generated auditory sensations, "auditory hallucinations". In our final project on patients with disorders of consciousness, we observed a variability between MRI scans acquired within a temporal gap of 30 min. This suggests a necessity to perform multiple scans in the same session to reduce misdiagnosis.

Co-Authorship Statement

This thesis is comprised of three manuscripts which were co-authored with various collaborators. The second (Chapter 3) and third (Chapter 4) papers have been published in “Journal of Neurology” and “Frontiers in Neuroscience”, respectively, and the first (Chapter 2) manuscript will be submitted soon. I am the principal author of projects in Chapters 2 and 3 and co-first author of the project in Chapter 4. For the project in Chapter 2 (generalized Ising model), I modified the generalized Ising model code developed by Dr. Thushar Das, previous member of the group, to incorporate external stimuli. I performed all the simulations using the modified generalized Ising model code, calculated the inter-subject correlations, plotted the brain maps, and wrote the chapter completely. The fMRI data for the project in Chapter 2 were acquired by Dr. Lorina Naci from Robarts Research Institute at the University of Western Ontario. Preprocessing of the fMRI data and extraction of the features of the audio clip were performed by Jorge Rudas, who will be a co-author.

Projects in Chapters 3 (Kandeepan et al., 2019) and 4 (Cavaliere and Kandeepan et al., 2018), involved the “GraphICA” tool, which was developed by Demetrius Rebeiro de Paula, from our lab. This tool preprocesses the fMRI data and extracts the resting state networks. For the project in Chapter 3 (tinnitus), I calculated the graph strengths of all the resting state networks and performed correlation analysis. Moreover, I developed codes to perform group statistical analysis such as the stepwise fit analysis, visualized all the results and composed 85% of the manuscript. The fMRI data of 135 tinnitus patients from the University Hospital of Antwerp used in this project were provided by Prof. Dirk de Ridder. Dr. Audrey Maudoux—co-first author of the paper—contributed in writing the introduction and discussion sections.

The project in Chapter 4 (disorders of consciousness) used fMRI and PET data of the patients with severe brain injury from the Neurorehabilitation Unit at Maugeri Clinical and Scientific Institutes, Telese Terme, Italy, and acquired at the SDN of Naples, Italy. I performed correlation analysis between fMRI and PET data obtained from GraphICA, at the network level, while behavioural assessments were performed by members of Dr. Anna Estraneo's group. I introduced a technique called the ratio of fitness to choose the component which best resembles the network from two different fMRI acquisitions. I developed a code to visualize regions belonging/not belonging to a network and composed about 50% of this chapter, while the remainder was composed by the other co-authors.

Acknowledgments

I would like to express my greatest gratitude to my supervisor Prof. Andrea Soddu for his continuous guidance and tireless explanation throughout the project. I am indebted to him for helping me in defining the problem, providing insights to the solution and ultimately guiding me to make my research a success. I also wish to thank my co-supervisor Prof. Sree Ram Valluri for his patience and support provided throughout the project.

I would also like to extend my gratitude to my advisory committee members, Prof. Alex Buchel and Prof. Blaine Chronik, for spending their time to evaluate my work and provide thoughtful discussions. I wish to thank the staff members of the Department of Physics and Astronomy, as well as the Brain and Mind Institute for being so kind to me and always available whenever assistance was needed.

My special thanks go to my group members Dr. Emily Nichols, Pubuditha Abeyasinghe, Nasim Mortazavi, Sina Khajehabdollahi, Demetrius Ribeiro de Paula, and Marwa Dawaga for their valuable suggestions. In particular, Pubu was there beside me to provide endless moral support and positive energy whenever I was feeling down. My heartfelt thanks are also extended to Jorge Rudas and all my colleagues who stood beside me during this journey. Further, I thank the collaborators around the world who provided more intuitions and suggestions to the work we carried out.

Moreover, I would like to extend my appreciation to my family members for their moral support, their love, and the encouragement they gave me to pursue my interest in this research, even being a thousand of miles apart. Finally, I am deeply thankful to my husband Kandeepan for his continuous support, his unlimited love, and his patience and understanding throughout my entire journey; and to my son, Akaran, without whom my life would not have been so joyful.

Table of Contents

Abstract	ii
Summary for Lay Audience	iv
Co-authorship Statement	v
Acknowledgements	vii
List of Figures	xiii
List of Tables	xviii
1 Introduction	1
1.1 Objectives	3
1.2 Overview of the Brain.....	4
1.2.1 Neuronal Communication.....	4
1.2.2 Parcellation of the Brain.....	6
1.3 Brain Connectivity.....	8
1.3.1 Structural Connectivity.....	8
1.3.2 Functional Connectivity.....	9
1.4 Magnetic Resonance Imaging (MRI).....	10
1.4.1 Basic Principles of MRI.....	10
1.4.2 Functional Magnetic Resonance Imaging (fMRI).....	12
1.4.3 Resting State Functional Resonance Imaging (rs-fMRI).....	14
1.4.4 Preprocessing of MRI Data.....	15
Motion Correction.....	15
Temporal Filtering.....	16
Spatial Smoothing.....	16
Spatial Normalization.....	17
1.5 Resting State Networks (RSNs).....	18
1.6 Modelling the Brain.....	19
1.6.1 Overview.....	19
1.6.2 Generalized Ising Model.....	22
1.6.3 Generalized Ising Model with External Stimuli.....	29
1.6.4 Comparison Between the Generalized Ising Model and the Generalized Kuramoto Model.....	30

1.7	Examining the Organization of the Brain Network using GraphICA....	32
1.7.1	Exploring the Functional Brain Network.....	32
1.7.2	ICA Applied to Resting-state fMRI.....	32
1.7.3	Graph Theory Applied to Resting-state fMRI.....	34
1.7.4	Applications of GraphICA on Different Populations.....	36
	Tinnitus.....	36
	Disorders of Consciousness.....	37
1.8	Chapter Preview.....	38
	Bibliography.....	40
2	Modelling an Auditory Stimulated Brain Under Altered States of Consciousness using the Generalized Ising Model.....	48
2.1	Introduction.....	48
2.2	Methodology.....	52
2.2.1	Task Protocol.....	52
2.2.2	Administration of Propofol.....	52
2.2.3	Sedation Assessment.....	54
2.2.4	fMRI Data Acquisition.....	54
2.2.5	Preprocessing of fMRI Data.....	55
2.2.6	fMRI Signal Extraction Based on a Parcellation.....	55
2.2.7	Extraction of Features from the Audio Clip.....	56
2.2.8	Inter-Subject Correlation (ISC).....	57
2.2.9	Generalized Linear Modelling (GLM).....	59
2.2.10	Generalized Ising Model (GIM) Simulation.....	59
2.2.11	Construction of Resting State Networks (RSNs).....	62
2.3	Results.....	63
2.4	Discussion.....	79
2.5	Conclusion.....	84
2.6	Future Work.....	84
	Bibliography.....	86
3	Tinnitus Distress: A Paradoxical Attention to the Sound?.....	90
3.1	Introduction.....	90

3.2	Methods.....	93
3.2.1	Participants.....	93
3.2.2	fMRI Data Acquisition and Preprocessing.....	94
3.2.3	Extraction and Identification of Resting State Networks.....	95
3.2.4	Applying Graph Theory.....	96
3.2.5	fMRI Second-Level Statistical Analysis.....	96
3.3	Results.....	99
3.3.1	Patients.....	99
3.3.2	Neural Correlates of Tinnitus Characteristics.....	99
3.4	Discussion.....	107
3.5	Conclusion.....	110
3.6	Future Work.....	110
	Bibliography.....	111
4	Multimodal Neuroimaging Approach to Variability of Functional Connectivity in Disorders of Consciousness: A PET/MRI Pilot Study.....	118
4.1	Introduction.....	118
4.2	Materials and Methods.....	120
4.2.1	Participants.....	120
4.3	Experimental Procedures.....	121
4.3.1	Clinical Assessment.....	121
4.3.2	Neurophysiological Evaluation.....	122
4.3.3	PET/MRI Acquisition Protocol.....	123
4.3.4	fMRI and FDG-PET Processing.....	125
4.3.5	Statistical Analysis.....	130
4.4	Results.....	130
4.4.1	Clinical Features.....	130
4.4.2	Neurophysiological Findings.....	133
4.4.3	Within-Session fMRI Variability.....	133
4.4.4	Mutual fMRI Findings.....	138
4.4.5	Functional-Metabolic Correlation.....	141
4.5	Discussion.....	141

	Limitations of the Study.....	144
4.6	Conclusions.....	146
4.7	Future Work.....	146
	Bibliography.....	147
5	Discussion and Future Work.....	155
5.1	Discussion.....	155
	5.1.1 The Generalized Ising Model.....	155
	5.1.2 Tinnitus.....	158
	5.1.3 Disorders of Consciousness (DOC).....	159
5.2	Future Work.....	161
	Bibliography.....	163
A	Appendices: Chapter 2.....	165
A.1	t-maps of the empirical and simulated data at T^* obtained from the β -values (coefficients) calculated using GLM between the subjects' time series and the 18 audio features (P1 – P18) are presented.	165
A.2	DMN of empirical and simulated data under all levels of consciousness. Simulated resting and simulated stimulated networks were constructed at T_{min} and T^* respectively.....	175
A.3	ECNL of empirical and simulated data under all levels of consciousness. Simulated resting and simulated stimulated networks were constructed at T_{min} and T^* respectively.....	177
A.4	ECNR of empirical and simulated data under all levels of consciousness. Simulated resting and simulated stimulated networks were constructed at T_{min} and T^* respectively	
A.5	P -stats obtained from the DMN network at different levels of consciousness.....	181
A.6	P -stats obtained from the ECNL network at different levels of consciousness.....	181

A.7	<i>P</i> -stats obtained from the ECNR network at different levels of consciousness.....	182
B	Appendices: Chapter 3.....	183
B.1	Patients' demographic characteristics	183
B.2	Masks of resting state networks.....	186
B.3	Correlation between behavioural scores (BS) and graph strengths (GS) for tinnitus patients.....	187
B.4	Representation of correlation between BS and GS for tinnitus patients.....	188
B.5	<i>T</i> -stats obtained from the correlation between BS and GS for tinnitus patients with different types of lateralization.....	189
B.6	Representation of the Correlation Between BS and GS for tinnitus patients with different types of lateralization.....	192
C	Appendices: Chapter 4.....	193
C.1	Coma Recovery Scale-Revised total and sub-scores in the EMCS, MCS and UWS patients.....	193
C.2	Classification criteria for visual analysis of EEG background Activity.....	194
C.3	Clinical sketches of patients	195
C.4	GS scalar maps of the nine RSNs of patients in EMCS, MCS, and UWS patients.....	199
C.5	Motion curves of EMCS, MCS and UWS patients.....	200
C.6	Scatter plots for the EMCS, MCS and patients in UWS showing the correlation between the FDG-PET and GS of the 1015 parcellated ROI.....	200
C.7	Distribution plots of GS for the best acquisition, concatenated data and FDG-PET for patients in EMCS, MCS and UWS.....	201
	Curriculum Vitae.....	202

List of Figures

1.1	Structure of a neuron.....	4
1.2	Action potential [17].....	6
1.3	Brain parcellation schemes, where each colour represents a brain region a) AAL2 (84 ROI) [21] b) Lausanne 2008 (1015 ROI) [22].....	8
1.4	Fibers reconstructed using DTI [26]. Fiber orientations along the x, y and z directions are represented by red, blue and green	9
1.5	Spin echo measurement depicting the 90° and 180° pulses along with the received spin echo signal.....	12
1.6	BOLD activity a) hemodynamic response function b) fMRI image with increased activity in the visual area [32]	14
1.7	Resting state networks [39]	19
1.8	Representation of a two-dimensional lattice arrangement. The nearest neighbours of the lattice site (in red) are represented in green	22
1.9	Representation of spins in the Ising model with the parcellated brain regions.....	25
1.10	Normalized structural connectivity matrix obtained from DTI for the 84 parcellated regions.....	26
1.11	Ordered parameters a) Magnetization vs. temperature for the generalized Ising model [7] and b) Synchrony vs. coupling strength for the generalized Kuramoto model [49]	31
1.12	Illustration of ICA decomposition into spatial and time courses.....	33
2.1	Thermodynamic properties of the synthetic data a) Magnetization b) Energy c) Susceptibility.....	64
2.2	Thermodynamic properties, a) Magnetization b) Energy c) Susceptibility calculated from the GIM during resting and under stimulation at four different levels of consciousness. The dashed lines represent the critical temperatures.....	65

2.3	Critical temperature variation during resting and under stimulation at four different levels of consciousness.....	66
2.4	Distance (calculated using the <i>ks</i> -test) between the normalized empirical and simulated ISC under stimulation, at four different levels of consciousness. The red line represents the minimized distance which minimizes between empirical and simulated ISC. Magenta, green dashed, and blue dashed lines represent the critical, sub, and super, critical temperatures, respectively, under stimulation. The black line represents the distance that minimizes the distance between the empirical and simulated correlation matrices.	67
2.5	Time series of subjects 1 and 3 for the ROI 29 (left superior temporal) in awake condition for the following data a) empirical task b) empirical resting c) simulated at T^* for task d) simulated at T^* for resting.....	68
2.6	ISC calculated from the stimulated empirical data at four different levels of consciousness.....	70
2.7	Normalized audio features extracted from the audio clip using pyAudio Analysis and the original audio clip.....	71
2.8	ISC calculated from the simulated task data at the critical (T_c), sub- ($T < T_c$), and super- ($T > T_c$) critical temperatures and at the temperature that minimized the distance between the ISC of the empirical and simulated data (T^*) in the awake condition.....	72
2.9	ISC calculated from the simulated task data at the critical (T_c), sub- ($T < T_c$), and super- ($T > T_c$) critical temperatures and at the temperature that minimized the distance between the ISC of the empirical and simulated data (T^*) during mild sedation.....	73
2.10	ISC calculated from the simulated task data at the critical (T_c), sub- ($T < T_c$), and super- ($T > T_c$) critical temperatures and at the temperature that minimized the distance between the ISC of the empirical and simulated data (T^*) during deep sedation.....	73

2.11	ISC calculated from the simulated task data at the critical (T_c), sub- ($T < T_c$), and super- ($T > T_c$) critical temperatures and at the temperature that minimized the distance between the ISC of the empirical and simulated data (T^*) during recovery.....	54
2.12	Correlation values calculated between the empirical ISC and simulated ISC at T^* obtained from the GIM simulations performed using J_{ij} and beta values, permuted J_{ij} values and permuted beta values for the awake, mild sedation, deep sedation and recovery.....	75
2.13	Auditory network of empirical and simulated data at four different levels of consciousness. Networks for the simulated resting and simulated task data were constructed at T_{\min} and T^* respectively.....	78
3.1	Mean Graph Strength (GS) plots of auditory (Aud), Default Mode Network (DMN), Executive Control Network Left (ECNL), Executive Control Network Right (ECNR) and salience (Sal) separated by different colours for each network for tinnitus patients. Only the GS values greater than 0.5 of the maximum GS value of that network are plotted.....	101
3.2	Axial slices of the mean GS (normalized to 1) of tinnitus patients implemented on the normalized structure.....	102
3.3	Representation of the correlation between GS and Behavioural Scores (BS) of tinnitus patients for a) ECNR and distress b) DMN and age.....	104
4.1	Flow chart of patient selection in each step of the study.....	131
4.2	Coma Recovery Scale-Revised total score and neurophysiological (EEG and evoked related potential) evaluations recorded in the 3 rd and 5 th day before PET/fMRI exam and in the 7 th and 9 th day after the PET/fMRI exam. The green arrow marks the day of neuroimaging acquisition. The blue diamond and line denote the patient in unresponsive wakefulness syndrome (UWS). The orange square and line denote the patient in minimally conscious state (MCS). The gray triangle and line denote the patient emerged from MCS (EMCS). CRS-R, Coma Recovery Scale-Revised; P,	

	presence of P300 on evoked related potential; A, absence of P300 on evoked related potential; +, presence of EEG reactivity to eye opening and closing; – , absence of EEG reactivity to eye opening and closing; MiA, mildly abnormal EEG background activity; MoA, moderately abnormal EEG background activity; DS, Diffuse slowing EEG background activity; LV, Low voltage EEG background activity.....	132
4.3	A visual representation of the regions highlighted by the thresholded GS (values greater than half of the maximum GS value for the network), separated by the regions within and outside the network for patients in EMCS, MCS and UWS for nine RSNs. Regions belonging to the network and having GS values greater than the thresholded GS are represented by green, regions which should be in the network but do not have GS values greater than the thresholded GS are represented by blue, regions outside the network but have GS values greater than the thresholded GS are represented by red color. NN represents non-neuronal networks. Here the size of the circle doesn't represent the value of the GS, all the regions with a GS value are plotted evenly.....	136
4.4	Three most representative axial slices of the GS implemented on the normalized structure of the DMN network are presented for the three patients for the best functional pattern and concatenated data.....	140
A.1	<i>t</i> -maps of the empirical and simulated data at T^* obtained from the β -values (coefficients) calculated using GLM between the subjects' time series and the 18 audio features (P1 – P18) are presented.....	165
A.2	DMN of empirical and simulated data under all levels of consciousness. Simulated resting and simulated stimulated networks were constructed at T_{\min} and T^* respectively.....	175
A.3	ECNL of empirical and simulated data under all levels of consciousness. Simulated resting and simulated stimulated network were constructed at T_{\min} and T^* respectively.....	177

A.4	ECNR of empirical and simulated data under all levels of consciousness. Simulated resting and simulated stimulated network were constructed at T_{\min} and T^* respectively.....	179
B.2	Masks of Resting State Networks	186
B.4	Representation of the correlation between BS and GS of tinnitus patients	188
B.6	Representation of the correlation between BS and GS for tinnitus patients with different types of lateralization	192
C.4	GS scalar maps of the nine RSNs of patients in EMCS, MCS, and UWS patients.....	198
C.5	Motion curves of EMCS, MCS and UWS patients. Motion curves illustrate translation (in mm) for x (blue), y (red), and z (orange) and rotation (in °) for pitch (blue), roll (red), and yaw (orange) parameters, and the time courses of each the nine RSNs (auditory, DMN, ECNL, ECNR, salience, sensorimotor, VL, VM, and VO) over 480 s	199
C.6	Motion curves of EMCS, MCS and UWS patients. Motion curves illustrate translation (in mm) for x (blue), y (red), and z (orange) and rotation (in °) for pitch (blue), roll (red), and yaw (orange) parameters, and the time courses of each the nine RSNs (auditory, DMN, ECNL, ECNR, salience, sensorimotor, VL, VM, and VO) over 480 s.....	200
C.7	Distribution plots of GS for the best acquisition, concatenated data and FDG-PET for patients in EMCS, MCS and UWS.....	201

List of Tables

2.1	<i>P</i> -stats calculated from the <i>t</i> -tests performed between different levels of consciousness for the auditory network.....	79
3.1	Correlation between the BS obtained from 135 patients.....	103
3.2	Correlation between the GS averaged over all 1015 regions with BS for tinnitus patients.....	104
3.3	Correlation between the distress and GS on the ECNR network for tinnitus patients.....	105
3.4	Correlation between the age and GS on the DMN network for tinnitus patients.....	106
4.1	ROF values calculated from regions belonging to the GS values, separated into the regions belonging to the network itself and outside the network.....	135
4.2	ROF and Correlation values between GS and FDG-PET) for the two acquisitions of tinnitus patients.....	138
A.5	<i>P</i> -stats obtained from the DMN network at different levels of consciousness.....	181
A.6	<i>P</i> -stats obtained from the ECNL network at different levels of consciousness.....	181
A.7	<i>P</i> -stats obtained from the ECNR network at different levels of consciousness.....	182
B.1	Patients' demographic characteristics.....	183
B.3	Correlation between Behavioural Scores (BS) and Graph Strength (GS) for tinnitus patients.....	187
B.5	<i>T</i> -stats obtained from the correlation between BS and GS for tinnitus patients with different types of lateralization	189
C.1	Coma Recovery Scale-Revised total and sub-scores of the EMCS, MCS and UWS patients	192
C.2	Classification criteria for visual analysis of EEG background activity.....	193

Chapter 1

Introduction

Interest in the complex functioning of the human brain has persisted for hundreds of years, but despite the multitude of scientific investigations of healthy and diseased brains, much work remains in order to fully and accurately explain human behavior and to develop novel diagnostic and therapeutic procedures. Single neurons, at the microscopic level, are the fundamental units of the brain's architecture, and are responsible for processing and transmitting electrical signals throughout the body in both chemical and electrical forms. However, an abundance of research has established that ensembles of interacting neurons at the mesoscopic level can perform the information processing essential for brain functions, such as action, perception, and cognition, in both healthy and diseased brains [1,2]. Interestingly, recent advances in structural and functional neuroimaging have provided new tools by which to measure and examine the structural and functional interactions between brain regions. Non-invasive measurements, such as functional magnetic resonance imaging (fMRI), are able to capture the indirect activity of neuronal ensembles at this mesoscopic level [3]. fMRI measures the level of oxygen in the blood, which can be used to represent the changes in the activity of neural ensembles. Despite the fact that electrophysiological techniques like M/EEG (Magneto/electro encephalogram) have high temporal resolution and directly measure neuronal activity, fMRI provides much higher spatial resolution [4]. Specifically, resting state fMRI investigation is not only able to provide insights into the fundamental functional organization of the human brain, its low cognitive demand is also a favorable aspect for clinical research and applications [5].

Neuroimaging techniques such as fMRI allow us to obtain information on the function of the brain and its possible reorganization in altered states of perception [6]. Understanding the brain's spatiotemporal organization can then be used to explore the neurobiological mechanisms of brain networks and their modifications in pathological and pharmacologically-induced conditions. This knowledge can be used to better understand how brain phenomena such as cognition or consciousness emerge and to improve innovative biomarkers for the diagnosis and prognosis of diseases related to cognition or consciousness.

In combination with these neuroimaging techniques, computational models are able to simulate the spontaneous activity of the brain [7, 8]. Simulating different levels of consciousness of the brain during rest or during task using computational models can provide more insights into functions of the brain. Specifically, computer simulations provide an opportunity to virtually perform experiments by altering input parameters such as, for example, the anatomical connectivity of the brain; and to test their output, which might not be clinically feasible.

Graph theory has provided another platform by which to characterize the structural and functional connectivity of the brain [9, 10]. The brain is an efficient network in exchanging information, consisting of a large number of regions with their own tasks and functions, continuously sharing information between structurally and functionally connected regions. A graph analytical approach helps us to understand the overall organization of brain networks and how information is integrated amongst various parts of the brain. The graph theoretical approach has revealed that the brain network has tightly interconnected clusters of regions called hubs and processes information efficiently [11, 12]. This is referred to as small-world behavior.

1.1 Objectives

My thesis describes two techniques—the generalized Ising model (GIM) and Independent Component Graph Analysis (GraphICA)—and explores how they can be applied more broadly, with the ultimate goal of obtaining information about functional connectivity in various neurological states. To achieve this, I applied these techniques and models in three different unique populations in which resting state fMRI and/or fMRI under naturalistic stimulation were acquired. Here, we discuss different techniques that can be used on data that do not necessarily represent healthy controls, but with altered perception of consciousness induced by either a pharmacological agent or due to pathology. My goal is to show the applicability of these novel techniques in populations with altered perception of consciousness and to extract interesting and useful information regarding their functional connectivity and to show that these analytical techniques have wide applications and that they can be applied to address different problems in neuroscience.

My first project involved developing the GIM model to fit fMRI data acquired while healthy controls were listening to an audio clip (naturalistic stimulation) at different levels of consciousness induced by the pharmacological agent propofol. My second and third projects involved the application of GraphICA to map out the changes in functional connectivity of resting state networks in altered perceptions of consciousness due to pathological conditions, namely tinnitus (perception of ringing in the ears in the absence of external sound) and disorders of consciousness (DOC) caused by severe brain injury. Before moving into the details of the projects, some of the fundamentals related to brain, neuroimaging, modelling and graph theory applied to study brain dynamics are described in the following sections.

1.2 Overview of the Brain

1.2.1 Neuronal Communication

The human brain is one of the largest and most complex organs in the human body. It is the command center for the human nervous system which consists of more than 100 billion neurons that communicate in trillions of connections called synapses [13]. Neuronal communication is an electrochemical event. A neuron, the basic unit of the nervous system, is an electrically excitable cell that consists of a cell body, dendrites and an axon (**Fig. 1.1**) [14]. Dendrites are fibers extending from the cell body that receive electrochemical stimulation from other neurons, whereas axons conduct electrical impulses away from the cell body and transmit information to different neurons, muscles and glands. These neurons serve as the interconnected information processors that allow the transfer of messages to and from different brain regions at speeds of up to 100 ms^{-1} [15]. They do not function alone as a single neuron, but instead work together to efficiently orchestrate all the complex tasks of the nervous system.

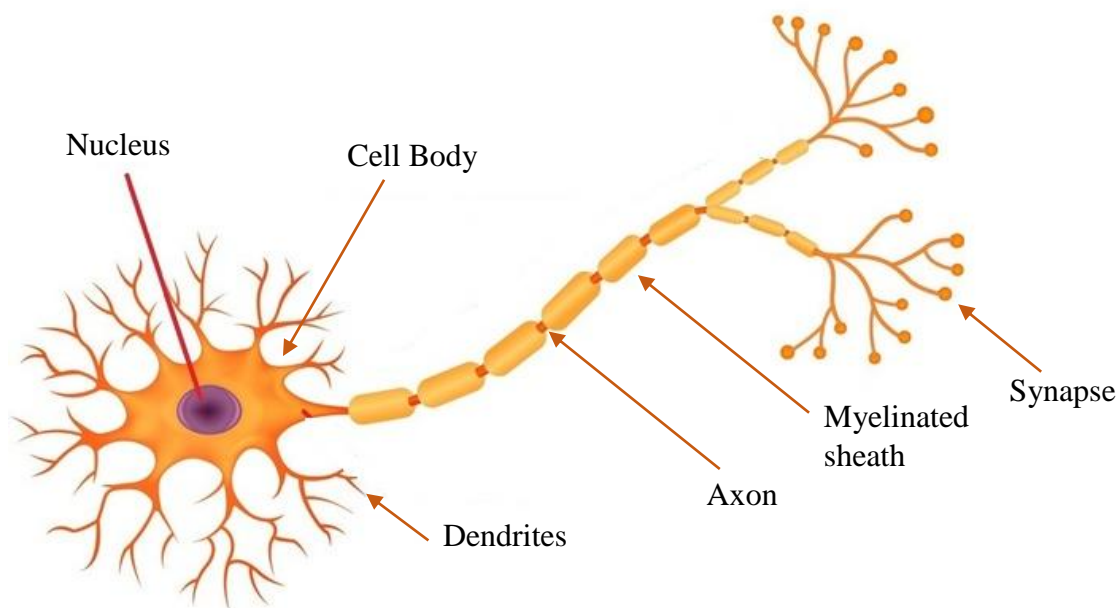


Fig. 1.1 Structure of a neuron [14]

Neurons communicate with each other via an electrical event called the “action potential”. When a neuron is at rest, the potential created across the inside and outside of the neuron cell membrane by the Na^+ and K^+ ions is called the resting potential, and is usually about -70 mV [16]. This means that the inside of the neuron is at a negative potential relative to the outside. The cell membrane consists of voltage-gated ion channels, which open or close to allow the ions to pass depending upon the voltage across the membrane. When a signal is received from other neurons, it changes the voltage across the membrane, allowing more positive ions to pass through the gates into the inside of the neuron. This causes the neurons to temporarily shift away from the resting potential and become more depolarized; that is, the potential inside the neuron becomes less negative. If the signals received from other neurons are sufficiently large enough to create a voltage inside the neuron above the threshold (-55 mV) [16], an explosion of electrical activity occurs, which is sometimes called a “spike”. This spiking event is referred to as the “action potential” (**Fig. 1.2**). This activity produces a current that travels down the axon and is transmitted onto the next neuron. While travelling along the axon, it depolarizes the adjacent areas of the membrane and—if sufficient—causes an action potential in these areas. This activity will continue, transmitting signals from one neuron to the next as a propagating wave. Speed of the wave depends upon the diameter of the axons as well as the myelinated sheath coating present in some axons. Larger axonal diameters have more room for the current flow, thereby increasing the conduction velocity. The myelinated sheath is a fatty layer that surrounds the axon. It acts as an insulating coating by reducing the ability of current to leak out of the axon and to enhance the conduction of electrical signals along the axon.

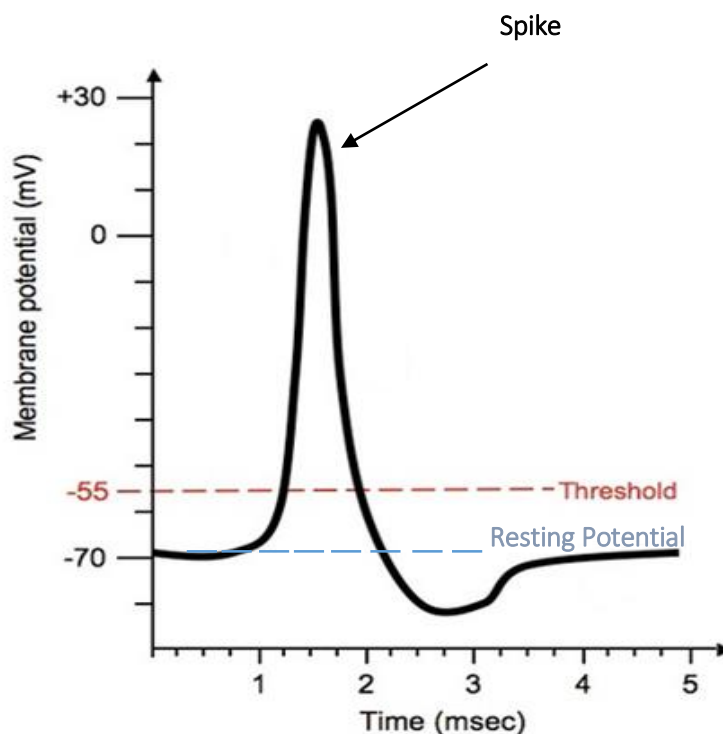


Fig. 1.2 Action potential (adapted from [17])

1.2.2 Parcellation of the Brain

Although neurons communicate with each other, neuroimaging is performed at the voxel level. A voxel (1mm^3 to 3mm^3) is an artificially created 3-dimensional building block used in neuroimaging that comprises millions of neurons. Recent studies suggest that voxel level imaging is sufficient to convey information of an ensemble of neurons, as the neurons do not function alone in performing tasks, but in a collective manner [18].

Interpreting the brain at the voxel level is still tedious, as it requires a large degree of computational power and is time consuming. An alternate approach is to further group the voxels or to parcellate the brain into structurally or functionally homogeneous regions, called Regions of Interest (ROI) [19]. These parcellation schemes are sometimes referred to as atlases and are derived by applying specific clustering algorithms to brain images. However, the parcellation does

not always fully represent the intrinsic organization of the brain, leading to loss of information. Results may also vary depending upon the resolution of the parcellation scheme [20]. Moreover, parcellation schemes can be mutually inconsistent, i.e. same parcellated ROI in two different schemes might represent different regions of the brain. Also they are data-driven, causing some of the atlases to not fit specific data.

An atlas can be created either by considering regions with similar anatomical tissue properties or with similar functional connectivities. Although there are many parcellation schemes available, in this thesis, two parcellation schemes were used which were created based upon the anatomical tissue properties: 1) AAL2 (Automated Anatomical Labelling) parcellation with 84 ROIs [21] and 2) Lausanne 2008 Atlas with 1015 ROI [22], both of which are available in FSL (software library containing image analysis and statistical tools for functional, structural and diffusion MRI brain imaging data). In Chapter 2, we chose a parcellation scheme with a lower number of ROIs (84) due to the high computational power needed for the simulations. **Fig. 1.3** displays the two parcellation schemes with the AAL2 showing two views (lateral and medial) for both left and right hemispheres of the brain.

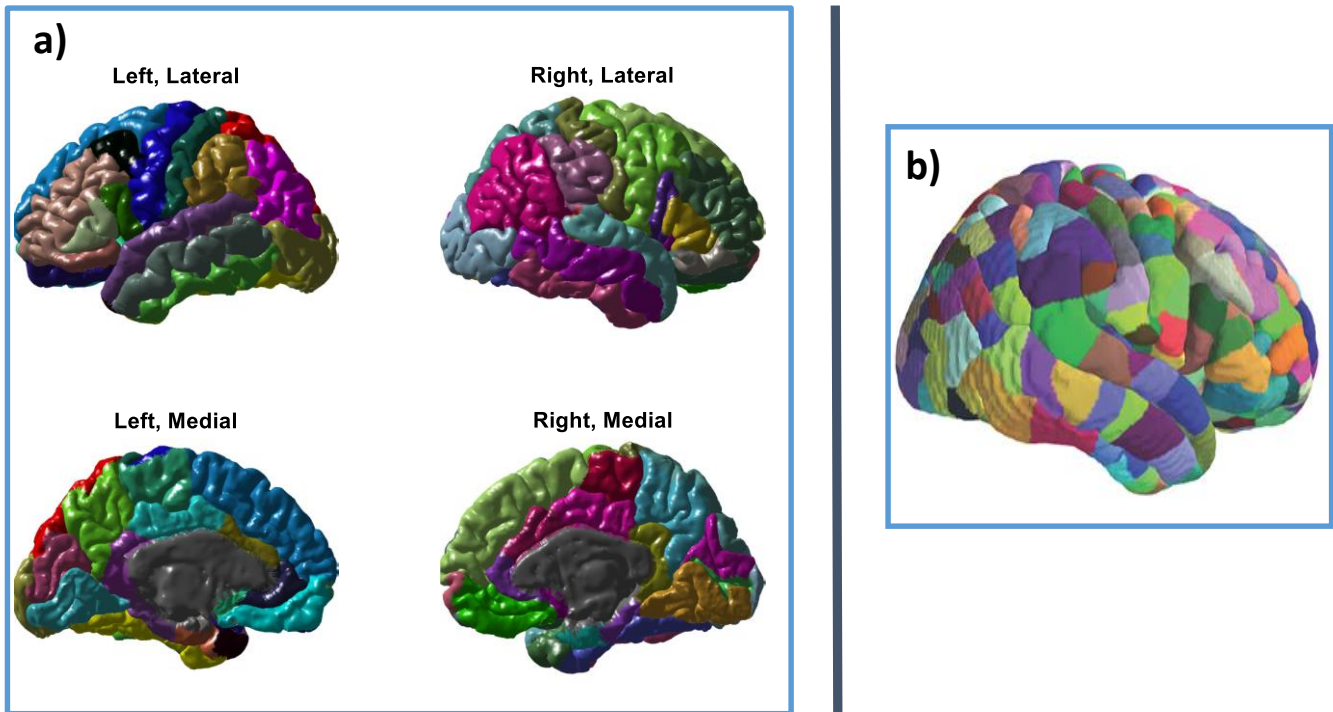


Fig. 1.3 Brain parcellation schemes, where each colour represents a brain region a) AAL2 (84 ROI) [21] b) Lausanne 2008 (1015 ROI) [22]

1.3 Brain Connectivity

1.3.1 Structural Connectivity

The brain consists of many specialized areas that are anatomically connected, and between which information is exchanged or communicated through the intricate axonal fibers architecture [23]. These attachments are called the structural (anatomical) connectivities, and connective fibers are inferred by a technique called Diffusion Tensor Imaging (DTI) [24]. DTI is a specific Magnetic Resonance Imaging (MRI) technique, which, by tracing water molecule diffusion and by post-processing tractography (3D modeling technique used to estimate the orientation and location of fiber tracts) analysis, permits the reconstruction of the fibers' bundles distribution in the brain as

shown in **Fig. 1.4** [25]. Deterministic and probabilistic tractography methods are two basic tractography methods employed to trace the white matter fiber bundles. In deterministic tractography, one orientation is assigned per voxel, while in probabilistic tractography, a distribution of orientations is assigned to each voxel, depending upon the directionality of the diffusion of water molecules. Integrating the directionalities of all the voxels, will provide the fiber tracts.

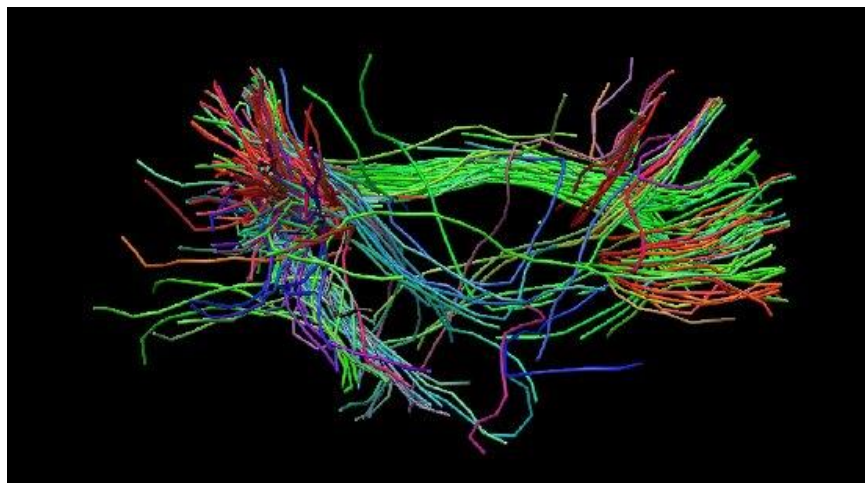


Fig. 1.4 Fibers reconstructed using DTI [26]. Fiber orientations along the x, y and z directions are represented by red, blue and green

1.3.2 Functional Connectivity

Understanding how the brain works requires knowledge of how brain regions communicate with one another to form large-scale functional networks. Functional connectivity is the quantification of the inter-regional correlations between fluctuations of MR signals obtained from different regions of the brain [27]. It is a measure of similarity in the neuronal activity between these brain regions and shows how strongly the regions synchronize together in time. Brain regions do not necessarily have to be structurally connected in order to have functional connectivity.

Measuring these connections at any scale is a great challenge. A variety of neuroimaging and electrophysiological recording methods, such as Electroencephalography (EEG), Magnetoencephalography (MEG), Positron Emission Tomography (PET) and functional Magnetic Resonance Imaging (fMRI), have been used to measure the changes in the functional connectivity of the brain [28, 29]. In particular, fMRI has been shown to be a promising imaging method due to its high spatial resolution than EEG, MEG and PET, and unlike PET, does not involve the injection of radioactive tracers [30].

1.4 Magnetic Resonance Imaging (MRI)

1.4.1 Basic Principles of MRI

MRI uses strong magnetic fields and radio frequency (RF) electromagnetic waves to generate detailed images of biological tissues in the body with spatial resolution approaching 1 mm^3 . The human body is predominantly composed of water molecules, which contain hydrogen nuclei (protons). Because of the magnetic moment of the nucleus, it orients in a magnetic field. During an MR acquisition, the patient is positioned in a strong static magnetic field ($\sim 1.5 - 7.0 \text{ T}$), which aligns the protons to a specific orientation (z-axis) [31]. Changing magnetic field gradients are applied to cause a variation in the magnetic field across the body which allows the spatial encoding of the magnetic resonance produced by the tissues. This alignment is perturbed by the introduction of RFs that rotate the protons from the Z axis to the X-Y plane. When the RF is turned off, the protons gradually return to their original position (z-axis), producing a RF signal detectable by the scanner. Depending on the density of protons in the tissue being examined, time taken by these protons to return to their equilibrium position will vary. This produces a spatial map of relaxation times and from which the shape, thickness, hardness of the organ can be inferred accordingly.

The two basic images used to characterize tissues in MRI are the T1 and T2 weighted images. Once the RF pulse is removed, the protons (spins) interact with adjacent protons and quickly start dephasing (i.e., lose their coherence) in the transverse plane while the longitudinal magnetization recovers slowly. T1 is the longitudinal relaxation time which determines the rate at which excited protons return to equilibrium in the z-axis (direction of the external field). T2 is the transverse relaxation time constant responsible for the decay of transverse magnetization (x-y plane) observed with spin echo (SE) or gradient spin-echo (GRE) sequences. T2* is the relaxation time obtained due to the combination of T2 and relaxation caused by magnetic field inhomogeneities.

In a SE sequence, the initial 90° pulse is followed by a 180° inversion pulse. After the initial 90° pulse, due to the slight variation of the local field, spins precess in different speeds in the transverse plane. This dephases the spins in the transverse plane, leading to an irreversible loss of magnetization. The 180° pulse inverts the magnetization vectors in the transverse plane like a pancake, making the slower precessing spins leading, while the faster precessing spins to be at the back. With continued phase evolution, faster precessing spins catch up with the slower ones, unwinding the net phase accumulation and producing the echo signal. Whereas, a GRE is produced by a single RF pulse followed with a gradient reversal pulse. Initially a gradient pulse is applied to phase disperse the precessing spins and to lose their magnetization. Then a gradient pulse with opposite sign or called as a gradient reversal pulse is applied to reverse the signal loss, creating an echo signal. In both sequences, echo time (TE) is the time interval between the RF pulse and the echo signal, and repetition time (TR) is the time between two consecutive excitation RF pulses. **Fig. 1.5** depicts a SE measurement showing the 90° and 180° pulses along with the received SE signal. Typically, a T1 weighted image is used to obtain the anatomical image, while a T2*

weighted image is used to obtain the functional images, which are 3D brain images scanned repetitively over a specific time interval. Tissues with longer relaxation times will appear brighter in the image.

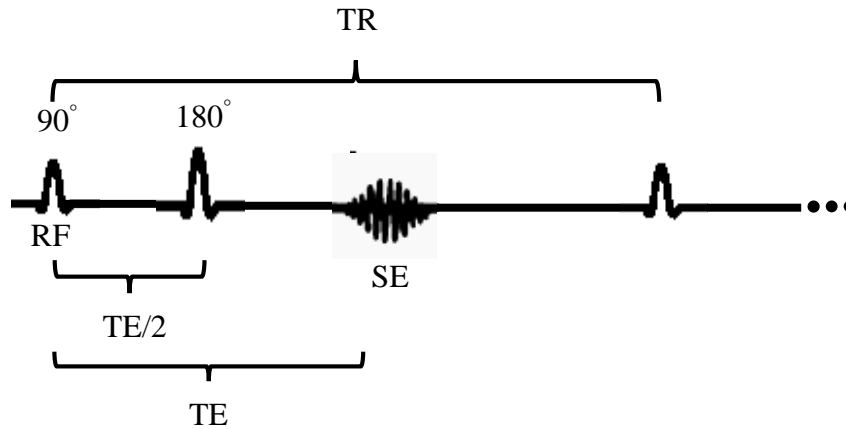


Fig. 1.5 Spin echo measurement depicting the 90° and 180° pulses along with the received spin echo signal

1.4.2 Functional Magnetic Resonance Imaging (fMRI)

Standard MRI scans are useful for detecting anomalies in tissue structure, whereas fMRI helps researchers learn about the function of a normal, diseased, or injured brain. fMRI has been commonly used to investigate changes in brain function over time using the Blood Oxygen Level Dependent (BOLD) signal, a proxy for degree of neural activity [32, 33]. The procedure is similar to MRI but uses changes in magnetization between oxygen-rich and oxygen-poor blood as its basic measure.

The brain requires oxygen to sustain its neural activity, and blood oxygen levels change rapidly following these activities. When neurons are activated due to a stimulus, blood releases oxygen to these active neurons at a greater rate than the inactive neurons through a process called the hemodynamic response (HDR). This process results in a change in terms of the relative levels

of oxyhemoglobin (when oxygen is bound with the hemoglobin, a protein found in the blood) and deoxyhemoglobin (hemoglobin without oxygen). Deoxygenated hemoglobin distorts the surrounding magnetic field by creating susceptibility gradients and dephasing the neighbouring protons to lose their magnetization faster via the $T2^*$ decay. Thus MR pulse sequences sensitive to $T2^*$ show a higher MR signal in places where the oxygenated hemoglobin is present and a lower signal when it is not. **Fig. 1.6a** illustrates the mechanism of a typical HDR. The initial dip, (lasting for 1 – 2 sec) is caused by the transient increase in the deoxyhemoglobin level due to oxygen consumption, followed by a dominant tall peak due to the increase in the ratio of oxy to de-oxy hemoglobin given by the neuronal activity, lasting for about 2 to 5 sec [34]. Finally, a post-stimulus undershoot is observed due to a combination of decreased regional cerebral blood flow and increased blood vessel volume. Monitoring which regions of the brain utilize oxygen for a given response or stimulation can ultimately localize brain activity on a second-by-second basis, and within millimeters of its origin. This will provide information of the variation of the BOLD signals of each region with time, delivering the BOLD time series. By calculating the correlation between these BOLD time series, functional connectivity can be obtained. **Fig. 1.6b** depicts an fMRI image, showing the increased BOLD activity in regions of the visual area due to an external visual stimulus [35].

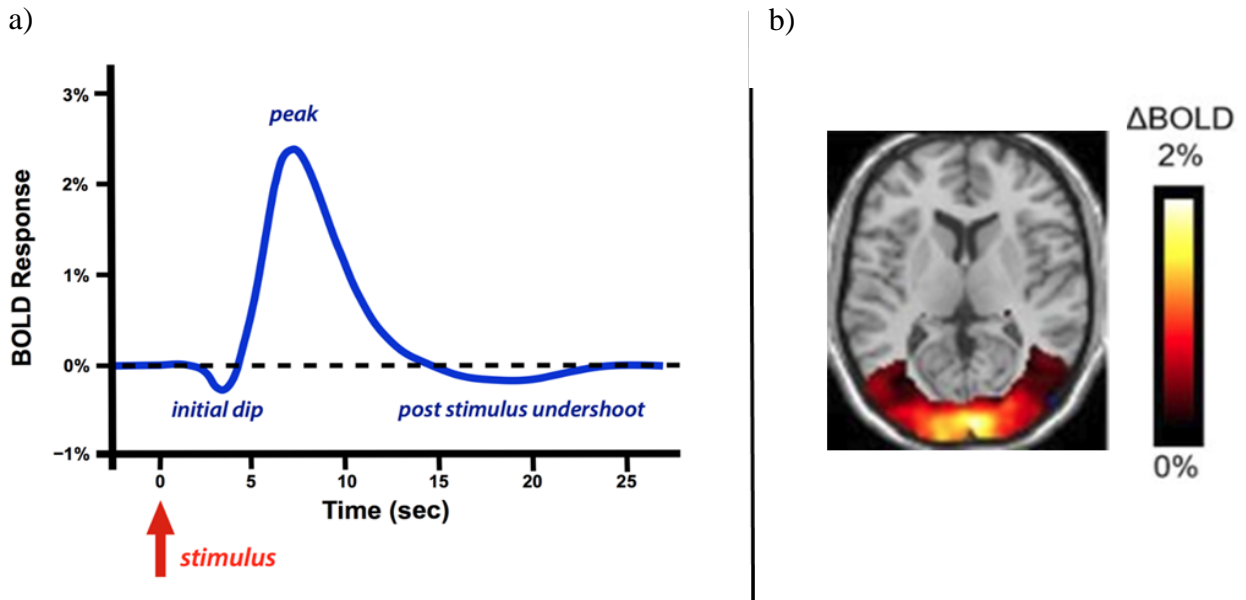


Fig. 1.6 BOLD activity a) hemodynamic response function [34] b) fMRI image with increased activity in the visual area [35]

1.4.3 Resting State Functional Magnetic Resonance Imaging (rs-fMRI)

Besides task-related fMRI, which demands the conscious cooperation of the subject, rs-fMRI has been widely used to study the spontaneous activity of the brain in both healthy subjects as well as patients with various neurological disorders [36]. Here the focus is on the intrinsic activity within the brain, in the absence of any sensory or cognitive stimulus. The low-frequency oscillations of the BOLD signal in the rs-fMRI signal have been shown to relate to complex spontaneous neural activity, previously neglected as background noise. This concept was first described by Biswal et al. in 1995 and has since been widely used [32]. Specifically, rs-fMRI is useful when the subjects are not able to follow commands or instructions as in active task-based fMRI. In addition, energy consumption in resting state represents one-fifth of the body's energy and is mostly used to support the activity of ongoing neuronal signals [37]. In contrast, the energy consumption in task-state is usually small (<5% compared to resting energy consumption) and,

therefore, provides a lower signal to noise ratio than the resting state condition [38]. During resting-state acquisition, the subjects are simply at rest, awake, and usually have their eyes closed, although this depends on the experiment.

1.4.4 Preprocessing of MRI Data

Preprocessing of raw MR data obtained from the scanner is performed in order to reduce noise and artifacts, so that the data is ready for statistical analysis. It includes various image and signal processing steps such as motion correction, temporal filtering, slice timing correction, spatial normalization, and spatial smoothing, which are discussed below in detail.

Motion Correction

Head movement in the scanner is one of the largest sources of noise in fMRI studies, especially in patients with specific disorders. A variety of strategies such as immobilization of the head using cushions or vacuumed pillows have been employed to manage this problem. Most of the time this movement cannot be avoided during scanning. But correction for head movement is crucial for analysis and therefore spatial transformation algorithms are employed to overcome this problem. Since many functional images are acquired within a limited time frame, as time increases, the head movement will vary the position of the brain in the subsequent images. That is, a voxel's time series might not reflect the same point in the brain. Head is considered as a rigid body with three directions of translation x , y , z and three axes of rotation around x , y , z . In order to overcome this issue, one functional image is chosen as the reference and all the other images are co-registered (overlapping on top of each other) and realigned to fit to this reference image using spatial transformation. In some cases, these six parameters are used as nuisance regressors and removed from the raw signal.

Temporal Filtering

Removal of noise or non-neuronal signals resulting from physiological confounds, such as heartbeat and breathing or scanner-related drifts, from the fMRI signal is known as temporal filtering. Fourier transformation is performed on the fMRI time series to transform it into the frequency domain, and then unwanted signal is removed using either low-pass or high-pass filters.

Slice-timing Correction

A full 3D brain image is obtained by scanning through 2D slices using a field gradient, in which the time taken for each slice is equivalent to the repetition time (TR) divided by the number of slices. Since all the volumes, which form a scan of the full brain, are not acquired at the same time, it causes a delay between each slice, which has a larger effect when a higher TR ($> 3s$) is used. Exact timing is crucial for BOLD signal statistics. Temporal adjustment within the slices are performed by phase shifting the time series using either nearest neighbour or linear interpolation techniques.

Spatial Smoothing

Smoothing is a process which increases the signal to noise ratio by averaging the data points with their neighbours (voxels) and sometimes removing high-frequency signals. Usually a Gaussian kernel is applied to smooth the data. The kernel defines the shape of the function that is used to take the average of the neighbouring points. A Gaussian kernel is a kernel with the shape of a Gaussian (normal distribution) curve and is defined in terms of FWHM (full width at half maximum). Typically, for smoothing, the FWHM is set to 4 - 6 mm for single subject studies and about 6 - 8 mm for multi-subject analyses [39]. After applying a kernel, each voxel obtains a weighted value in which the nearest neighbours have contributed a higher weight with the weights

decreasing with distance from that voxel. Although smoothing increases the signal to noise ratio, it reduces spatial resolution and the image looks more blurred.

Spatial Normalization

Human brains differ in size and shape. Spatial normalization refers to transforming or deforming the brain into a standard template (e.g., the Montreal Neurological Institute - MNI atlas) so that each voxel in the subject's brain scan will represent the same location in other subjects' scans, allowing for inter-subject brain studies. Both the anatomical and functional images should be normalized. Functional images are low in resolution compared to the anatomical image. Due to this, in most cases functional images are co-registered (aligned and overlaid) with its own anatomical image or to a standard template [40]. Then the anatomical images are transformed into the standard template using displacement, rotation, reflection, zooming and shearing transforms [41]. Finally, the parameters obtained from these transformations are applied to the functional images.

These are the basic preprocessing steps involved in the MR data. In the following chapters of my thesis, the exact steps employed varied slightly depending on the data used. Additionally, usually the first few scans are removed from the analysis due to saturation effect in MRI scanner. When the TR of the RF pulses is low, the excited protons due to the RF sometimes may not be able to return back to the original position in the longitudinal plane before the next RF is applied. Protons within these imaged volumes are said to be partially saturated as their signal will be less than the expected. Moreover, before these preprocessing steps were performed, visual inspection was done on the raw brain images using SPM (Statistical Parametric Mapping in MATLAB) and tissue segmentation (extracting the grey matter, white matter, cerebral spinal fluid from the anatomical image), was performed using GraphICA (a tool which will be discussed later on this

chapter) to assess the quality of the data. Grey matter mainly consists of neuronal cell bodies, white matter is the myelinated (fatty substance) axonal fibers which connect the cell bodies and cerebral spinal fluid is a colourless fluid that protects brain and spinal cord from trauma.

1.5 Resting State Networks (RSNs)

Even when the brain is at rest, it exhibits a baseline level of brainwave oscillation signifying its constant working. This spontaneous activity of the brain is an intrinsic physiological process in the absence of any sensory inputs or motor outputs [42]. This observation suggests that brain regions that often work together form a network depending on their functionality, such as vision hearing, etc. and these regions tend to oscillate together in time. These networks are called resting state networks (RSNs), as they happen to be strongly functionally correlated even during rest. Recent comprehensive studies of functional brain connectivity at rest have revealed a number of networks consistently found in healthy subjects that tend to have specific synchronous activities [43]. That is, the resting brain dynamics can be broken down into a relatively small set of RSNs that relate to specific functions and that have varied topologies. In the present research, I focus on nine overlapping networks (i.e., the regions of each network may overlap between networks): the Default Mode Network (DMN), auditory network (Aud), Executive Control Left and Right (ECNL and ECNR), salience (Sal), sensorimotor (Sen), Visual Lateral (VL), Visual Medial (VM) and Visual Occipital (VO). These nine networks are visualized in **Fig. 1.7** [44, 45].

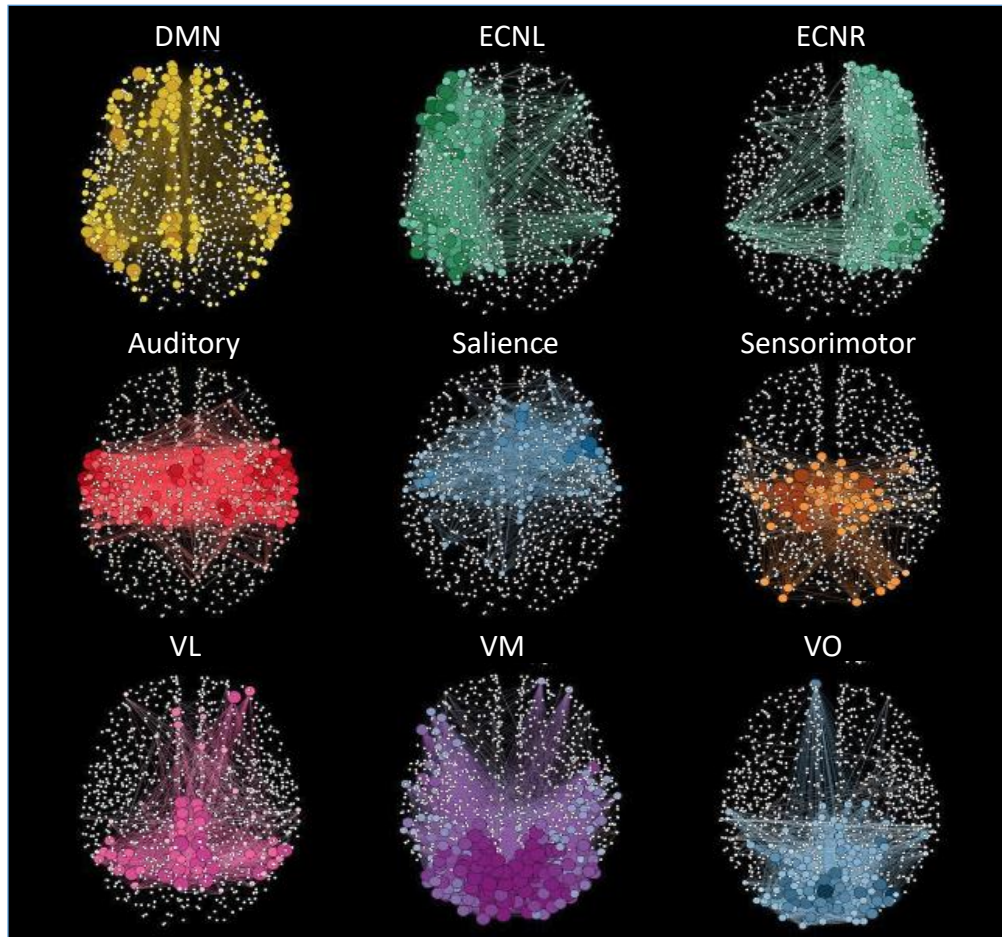


Fig. 1.7 Resting state networks [45]

1.6 Modelling the Brain

1.6.1 Overview

Even with the advancement of new technology, neuroscientists still struggle to understand the behaviour of the brain due to its vast complexity. A promising approach to better understand the brain is through computational models. Several models have been used to describe the neuronal dynamics of the brain, including the Kuramoto model [46, 47], neural mass model [48] and the Ising model [7, 27].

The Kuramoto model is a mathematical model used to examine the effects of synchronous behavior in a lattice of coupled oscillators. It has been used to study brain dynamics by a set of oscillators with their own natural frequencies, where each oscillator represents a brain region [46]. This model hypothesizes that the collective behavior of the states of the neurons can be captured by a single phase (θ), represented by a set of N coupled differential equations given in **Eq. 1.1** [47].

$$\frac{d\theta_i}{dt} = \omega_i + \frac{K}{N} \sum_{j=1}^N \sin(\theta_j - \theta_i), \quad i = 1, 2, \dots, N \quad (1.1)$$

where, $\frac{d\theta_i}{dt}$ represents the rate of change of phase of the i^{th} oscillator, ω_i is the natural frequency of the i^{th} oscillator and K is the global coupling strength which scales the strength of all connections. The natural frequency of the oscillator can be compared with the natural firing rate of a neuron and the coupling strength can be compared to the degree of excitation/inhibition that is undergone through the dendrites from neighbouring neurons to stimulate a neuron to fire [48]. This is a deterministic model consisting of a set of differential equations, i.e. there is no randomness in the model. But by adding a noise term, it can be made non-deterministic. Degree of synchronization of the neuronal population can be obtained using **Eq. 1.2**:

$$R(t)e^{i\phi(t)} = \frac{1}{N} \sum_{n=1}^N e^{i\theta_n(t)} \quad (1.2)$$

where $R(t)$ and $\phi(t)$ are the time-varying amplitude and phase, respectively. $R(t)$ can vary between 0 and 1 and higher values represent stronger synchronization. When the coupling constant is increased, the system shifts from a non-synchronised state to a synchronised state. This model assumes that the coupling is weak, the oscillators are identical, and the interactions depend sinusoidally on the phase difference between each pair of objects. Kuramoto demonstrated that an ensemble of nearly identical phase oscillators with weak couplings approximates the long-term behavior of any ensemble of interacting oscillatory systems, permitting a variety of insights into

the relationship between the phase response curve and the nature of synchronous activity at the neuronal level [46].

Recently, steps have been taken to generalize the model (**Eq. 1.3**) by using time-varying natural frequencies and coupling strengths to provide a more realistic picture of synchronization in the brain, and were able to explain the fluctuating beta oscillations in the human cortex [46, 49].

$$\dot{\theta}_i = \omega_i(t) + \frac{K}{N} \sum_{j=1}^N C_{ij} \sin(\theta_j - \theta_i) \quad (1.3)$$

where C_{ij} is the relative coupling strength between nodes i and j based on the empirical structural connectivity matrix, K is the global coupling strength which scales all connections' strength and $\omega_i(t)$ is the time varying frequency.

On the other hand, neural mass models are low dimensional models which have been actively used since the 1970s to model the coarse grained activity of large populations of neurons and synapses to specifically understand brain rhythms [50]. This model tracks the activity of an excitatory population of neurons coupled to an inhibitory population which quantify the mean firing rates and mean membrane potentials of large neural ensembles, so-called neural masses (NMs), using differential equations. These models describe brain functions on a mesoscopic scale that is highly relevant for brain functions, and have been used to understand EEG rhythms ranging from delta (1–4 Hz) through to gamma (30–70 Hz), brain resonance phenomena and resting state brain activity [51]. Lately, the theta–neuron (ϑ -neuron) model is now widely used in computational neuroscience to describe the synaptic coupling of neurons in which the neuronal firing rate couples with the synchrony of the neuron ensembles [52]. In the work of Byrne et al. [52], it is mentioned that the firing rate can be considered the real part of the complex synchronization parameter in the Kuramoto model.

The generalized Ising model, on the other hand, is a simple model which uses only temperature of the thermal bath as the fitting parameter and bridges structural and functional connectivity. This model is able to provide insights on the functioning of the brain using only the structural connectivity as input [7].

1.6.2 The Generalized Ising Model

The Ising Model, which was introduced by Ernest Ising in 1925, has recently received much attention for its statistical description of neural spike data [53, 54]. In 1944, Onsager published the analytic solution of the two-dimensional model in the absence of an external field [55]. The Ising model is a statistical model originally used to describe ferromagnetism with magnetic dipole moments of atomic spins, where each of the spin states can be specified either by +1 (up) or -1 (down) as shown in **Fig 1.8**.

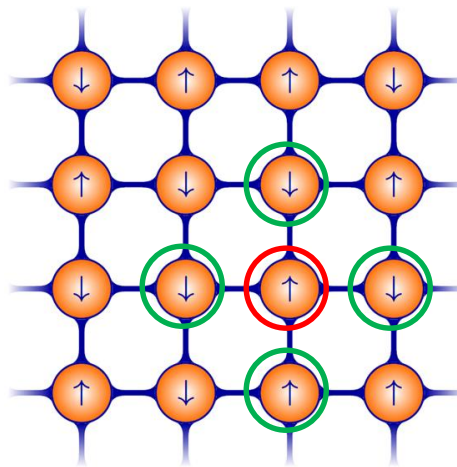


Fig. 1.8 Representation of a two-dimensional lattice arrangement. The nearest neighbours of the lattice site (in red) are represented in green.

The 2D classical Ising model considers that the spin states of each atom interact with only their neighbouring atoms with an equivalent coupling strength. As depicted in **Fig. 1.7**, if we

consider the atom highlighted by red, it will interact only with the four nearest neighbouring atoms which are represented in green. Therefore, the energy of this spin configuration at any state 'x' in the absence of an external magnetic field can be calculated using **Eq. 1.4** (54):

$$E = -J \sum_{i,j=nn(i)}^N s_i s_j \quad (1.4)$$

where J is the coupling constant between the i^{th} and the j^{th} site and is assumed to be $+1$, s_i and s_j are the spins of the i^{th} and the j^{th} site, N is the total number of spin sites and the summation is carried out only over the nearest neighbours (nn).

This spin configuration is kept in a thermal bath of temperature T , which is the only fitting parameter in the model. This temperature influences the effective interaction between the spins and produces different spin configurations at different temperatures. The probability of finding the system in the state x with energy $E(x)$ is given by **Eq. 1.5**:

$$P(x) = \frac{1}{Z} \exp\left(-\frac{E(x)}{k_B T}\right) \quad (1.5)$$

where k_B is the Boltzmann constant and Z is the partition function (**Eq. 1.6**) calculated using all the possible configurations (2^N) denoted by x .

$$Z = \sum_{\{x\}} \exp\left(-\frac{E(x)}{k_B T}\right) \quad (1.6)$$

At lower temperatures the interaction energy between the spins dominates over the thermal energy ($k_B T$) provided by the temperature T . It causes the spins of the system to align in the same direction and to be ordered. At higher temperatures, because thermal energy wins over the interaction energy, the spins align in random directions causing the system to be disordered. At a temperature between these two extreme temperatures a phase transition from an ordered to a

disordered state occurs [7]. This temperature is called the critical temperature (T_c). For a 2D classical Ising model with finite lattice size, T_c depends only on the lattice size. At this criticality, the correlation length, that is, how much a change in the spin will spread through the lattice, is maximized (since ordered clusters of spins are formed), depicting long range spatiotemporal correlations [7, 54]. Long range correlations refer to interactions observed between spins that are spatially distant from each other, even when the interaction was restricted only to nearest neighbors. These long range correlations exhibited at criticality can be compared to the interactions observed between brain regions.

The balance between segregation and integration of brain regions is essential for efficient information processing and rapid information transfer within and among the networks [56, 57]. Segregation refers to the communication within clusters of brain regions (i.e., networks) that function together in time to perform specific tasks. Integration is the communication between these clusters of regions in the brain. While the regions of networks perform tasks separately, they also interact with each other, transferring information amongst them and functioning completely as a whole brain. This is comparable to the order (i.e., spins are aligned in the same direction) and disorder (i.e., spins are randomly oriented) of the Ising model [7, 56] and synchrony versus asynchrony in the Kuramoto model [49]. Due to this similarity, it has been shown that the Ising model at criticality can describe the dynamics of the resting brain [7, 54]. This provided evidence for the emergence of self-organized criticality in the neural system, allowing efficient and maximum transfer of information among brain regions [56].

The Generalized Ising model (GIM) is a modification of the 2D classical Ising model, in which it is extended to interact with not only its nearby neighbours but to all other parts of the system, with different interacting strengths. In Chapter 2, which applies the Ising model to varying

states of consciousness, we have parcellated the brain into 84 ROI, in which each ROI can be represented by a spin ‘up’ (+1) or ‘down’ (-1) as shown in (**Fig. 1.9**). BOLD activity higher than a specified baseline can be represented by spins ‘up’ and BOLD activity lower than that baseline can be represented by spins ‘down’ (**Fig. 1.9**).

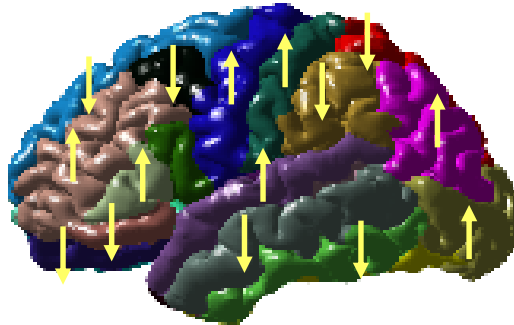


Fig. 1.9 Representation of spins in the Ising model with the parcellated brain regions

Moreover, there is a one-to-one relationship between the spins of the GIM and the brain regions, because each spin of the lattice site represents a particular parcellated region of the brain. In the classical Ising model, spins of the lattice do not correspond to a particular region of the brain, but in the generalization of the Ising model, each brain region corresponds to a particular spin in the lattice site. Accordingly, the structural connectivity matrix J_{ij} , which gives the coupling strength between two regions in the model, is built such that it corresponds to the number of fibers connected between these regions. Because we have parcellated the brain into 84 regions, J_{ij} is an 84 x 84 matrix and the couplings are normalized in such a way that the highest coupling has a value of one (**Fig. 1.10**). Considering this one-to-one relationship between the spin sites and the brain regions, this model can be used to simulate the BOLD activity either during resting state (spontaneous activity) or while engaged in a task.

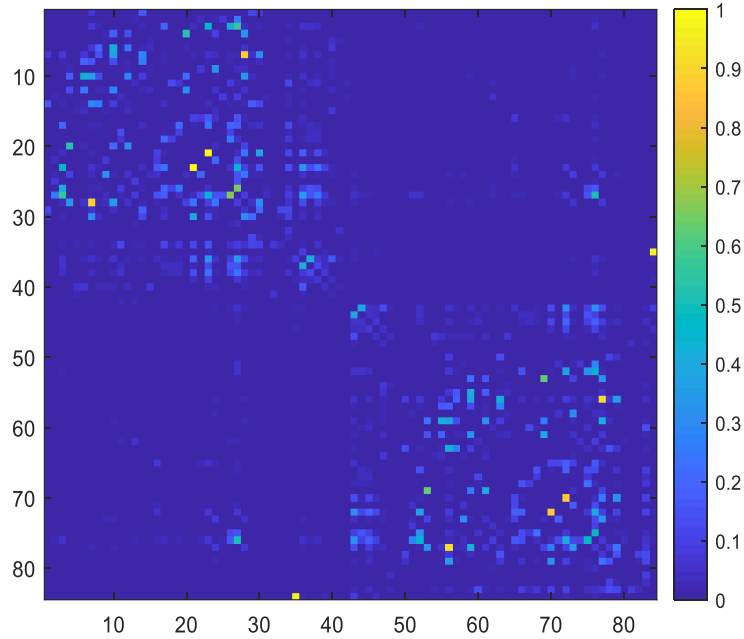


Fig. 1.10 Normalized structural connectivity matrix obtained from DTI for the 84 parcellated regions

The energy of the spin system in the absence of an external stimuli system (spontaneous activity of the brain) using the generalized Ising model is given by **Eq. 1.7**,

$$E = -\sum_{i,j;i \neq j}^N J_{ij} S_i S_j \quad (1.7)$$

where J_{ij} is the coupling constant between the i^{th} and j^{th} site, S_i and S_j are the spins of the i^{th} and j^{th} site and N is the total number of spin sites.

The Metropolis Monte Carlo algorithm is considered the most successful method to sample the canonical ensemble (Boltzmann distribution) which describes the Ising model. It can be used to establish the equilibrium energy configuration for a given temperature, starting from a random spin configuration [7, 56]. One-time point is considered after $N \times N \times 10$ (N is the number of spins)

number of flips have been performed to confirm that equilibrium has been reached [7, 54]. By repeating these steps to equal number of time points of fMRI data, each time confirming the equilibrium condition, the simulated time series can be obtained.

The Ising model itself is a statistical model which produces different equilibrium configurations of spins by minimizing the energy of the system and which does not include a time variable. Time is artificially introduced only when time series are being generated. Once the time series are generated, we can calculate the correlation matrix and test whether it matches with the empirical correlation matrix, using temperature as a fitting parameter. In the classical Ising model there is no one-to-one match between the spin sites and brain regions, and only the histograms of the correlations can be compared [54]. For the generalized version, we can compare one-to-one the simulated correlation matrices with the empirical correlation matrix [7]. Moreover, contrary to other studies in which the hemodynamic response function is used to convolve the generated time courses to match the BOLD signal [58], as reported in Fraimann et al. [54], we claim that our model can simulate the BOLD signal directly from the simulated time series.

Once the equilibrium condition is reached, thermodynamic properties such as energy (E), magnetization (M), magnetic susceptibility (χ), and specific heat (C) can be calculated from the average over all the possible configurations using **Eq. 1.7 – Eq. 1.10**. Magnetization is calculated by summing up the spins which consists of +1 (spin up) and -1 (spin down) and dividing by the total number of spin (**Eq. 1.8**) and has the highest value (i.e., close to one) at ordered state (i.e., at lower temperatures) and decreases in the disordered state (i.e., at higher temperatures).

$$M = \frac{1}{N} \left| \sum_{i=1}^N S_i \right| \quad (1.8)$$

Magnetic susceptibility and specific heat are the derivatives of magnetization and energy with respect to temperature. However, due to the statistical noise in the magnetization and energy, we use the variances of these parameters, which are standard results obtained from equilibrium statistical thermodynamics to calculate the susceptibility and specific heat, respectively [59] as shown in **Eqs. (1.9)** and **(1.10)**. The critical temperature can be obtained from the temperature at which the susceptibility maximizes.

$$\chi = \frac{1}{NT} [\langle M^2 \rangle - \langle M \rangle^2] \quad (1.9)$$

$$C = \frac{1}{NT^2} [\langle E^2 \rangle - \langle E \rangle^2] \quad (1.10)$$

Although there is no direct relationship with these thermodynamic properties and any parameters of the brain, we hypothesize that the spins of the Ising model can describe the BOLD signal of the parcellated regions. Moreover, some preliminary results [60] suggest that the temperature of the Ising model could relate inversely to the average global metabolic activity of the brain. At higher temperatures (lower metabolic activity), average frequency of the spin flip increases in the Ising model. In Guldenmund et al. [60], they reported that in healthy subjects anesthetized with propofol (lower metabolic activity), the mean frequency of the BOLD signal was shown to increase in the frontal regions, supporting our hypothesis. Further, we can represent the magnetization of the Ising model to be related to the state of synchronization of the patches of neuronal activity in the brain. When the magnetization is high it means that most of the regions (or groups of neurons) are active at the same time. Since the magnetic susceptibility represents the change in magnetization with temperature, it can be inferred as the change in synchronization of the patches of neuronal activity, when the metabolic activity of neurons is changed. Additionally, the energy of the Ising model can correspond to the energy consumption of groups of neurons.

But, in the Ising model, energy is high at higher temperatures, while in the brain, higher energy consumption is obtained when the brain is more metabolically active. Therefore, we expect that the energy of the Ising model and the energy consumption in the brain should probably be inversely related to each other.

1.6.3 Generalized Ising Model with External Stimuli

The brain is characterized by heterogeneous patterns of structural connections supporting cognition and a wide range of complex behaviours. Although several new non-invasive imaging techniques allow comprehensive mapping of these patterns, how the brain's structural wiring supports cognitive processes still remains a fundamental challenge. Specifically, how the brain responds to external inputs and the structural architectures responsible for these processes continue to be an important topic among neuroscientists.

Regardless of recent advances in brain research, there are fewer efforts made on mathematical modeling of the human brain's response to external stimuli [61, 62, 63]. The Ising model can not only simulate the spontaneous activity of the brain, but can also be extended to simulate the brain's activity upon receiving time varying naturalistic external stimuli. To simulate the brain in the presence of any external stimuli (in Chapter 2 of this thesis, an auditory stimulus from an audio clip of a movie), energy due to the coupling of the external stimuli with a spin site should be added to Eq. 1.5, leading to **Eq. 1.11**:

$$E = -\sum_{i,j,i \neq j}^N J_{ij} S_i S_j - H(t) \sum_i^N \mu_i S_i \quad (1.11)$$

where $H(t)$ represents the external stimulus applied to the system, which varies with time, and where μ_i provides a measure of how the external field is coupled to the spin S_i . In a real world scenario, μ_i depends on how the individuals engage with the external stimuli as well as the

conscious level of the subjects. This μ_i does not vary with time and depends on the features of the external field. The external field is used as a driving force to synchronize subjects' conscious experience, and more details of this process are provided in Chapter 2. The addition of these parameters allows us to model how neural activity propagate along structural connections due to external perturbation not only in the awake condition, but also in different stages of sedation such as mild sedation, deep sedation and recovery, after being induced by an anesthetic agent. The brain's activity not only can be revealed using mathematical models, but a graph theoretical approach can also be applied and is discussed in Section 1.7.

1.6.4 Comparison Between the Generalized Ising Model and the Generalized Kuramoto Model

As explained in sections 1.6.1 and 1.6.2, Kuramoto model is a deterministic model, but can be made non-deterministic by adding a noise term. On contrary, the Ising model is made to be a probabilistic model, by employing MMC algorithm to generate randomness, where a probability is assigned for a spin flip to be accepted. Moreover, the Ising model is a simple model which has only one fitting parameter, while the Kuramoto model has at least two parameters, the coupling constant and the initial frequencies of the coupled oscillators.

In the Ising model, criticality is obtained by tuning the temperature of the heat bath in which the spins are kept, to the value where the phase transition occurs between ordered and disordered states of equilibrium spin configurations. Similarly, by considering coupled oscillators to represent the behavior of neurons in the Kuramoto model, criticality is obtained by tuning the coupling constant between an optimum value of synchronization and non-synchronization. As the temperature of the Ising model is increased, the system moves from an ordered to a disordered state, while as the coupling constant of the Kuramoto model is increased, the system transitions

from a non-synchronized to a synchronized state. Ordered states represent a highly synchronized state. This shows that the temperature of the Ising model and the coupling constant of the Kuramoto model can be related to be inversely proportional to each other. This relationship is illustrated in **Fig. 1.11** which shows the variations in the magnetization (M) and the synchronization (R) which are the ordered parameters of the Ising and Kuramoto models, respectively [7, 49]. The magnetization plot was obtained from the work of Abeyasinghe et al. [7], in which the generalized Ising model without an external field was simulated at different temperatures using 84 spins and the magnetization was obtained at each temperature once the equilibrium was reached. The synchronization plot was retrieved from the work of Lee et al. [46], which was obtained from simulations of the generalized Kuramoto model with 66 oscillators at various global coupling strengths, when an external field was not present.

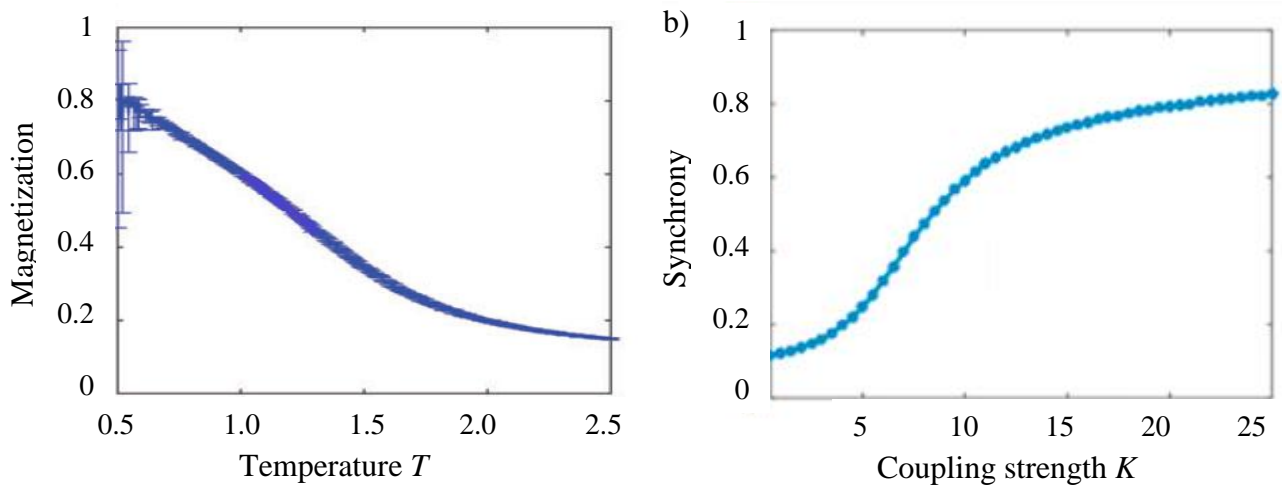


Fig. 1.11 Ordered parameters a) Magnetization vs. temperature for the generalized Ising model [7] and b) Synchrony vs. coupling strength for the generalized Kuramoto model [49]

1.7 Examining the Organization of the Brain Network using GraphICA

1.7.1 Exploring the Functional Brain Network

In the past, advancements in graph theory have provided many new approaches for topologically analyzing complex networks, some of which have already been applied to the characterization of anatomical and functional brain networks [64]. Not restricted only to characterize healthy brains, graph theory also holds great promise to quantify abnormality of structural and functional network properties in schizophrenia, Alzheimer's disease, lesions and other disorders [65].

GraphICA (BraiNet-Brain Imaging Solution Inc.-Sarnia, ON, Canada) is the tool used in this research to investigate the connections among regions of resting state functional brain networks in healthy and diseased subjects [45, 66, 67]. This tool combines Independent Component Analysis (ICA) with graph theory, and allows us to visualize and calculate the graph properties of each of the RSNs.

1.7.2 ICA Applied to Resting-State fMRI

There are several approaches that can be applied for the analysis of rs-fMRI such as seed-based analysis, which estimates the relationship between a predefined region called a “seed” and all the voxels around the brain, and Principal Component Analysis (PCA), which identifies the component that accounts for the most variability until the desired number of components have been extracted. But in reality, the amplitude of the BOLD signal is much smaller when compared to the noise in the signal, from sources such as breathing, head movement, and eye movements. Reducing the spatial dimensionality of the data by retaining the components with high variance can sometimes eliminate the signal from neuronal activity. ICA [68], a relatively new approach

that was initially introduced to fMRI data in 1998 by McKeown and colleagues [69], shows high consistency and robustness in isolating low-frequency resting-state patterns [70]. ICA involves higher order statistics such as kurtosis, a statistical measure that defines the degree of distortion from the symmetrical Gaussian distribution, to recover non-Gaussian distributed independent components from the signal. As input, it takes the 4D fMRI dataset (which captures change in intensity over time in all voxels) of the whole-brain BOLD signal and decomposes into several contributing spatial maps of resting-state signals or components (X) that are maximally independent in space and their associated time courses (A) [69].

Let Y be the 4D fMRI data with dimensions $T_p \times N_v$, where N_v and T_p are the total number of voxels and time points respectively. After ICA decomposition, Y can be written using **Eq. 1.12**:

$$Y = AX \tag{1.12}$$

where, A is the matrix of time courses with dimensions $T_p \times N$, X is the matrix of spatial maps (independent components) with dimensions $N \times N_v$ and N is the total number of independent components (ICs) or spatial maps as shown in **Fig. 1.12**. The output of ICA is the matrix A containing the IC time courses, and the matrix X containing z -values for each component, which represent how likely a single voxel's time course can be explained by that component.

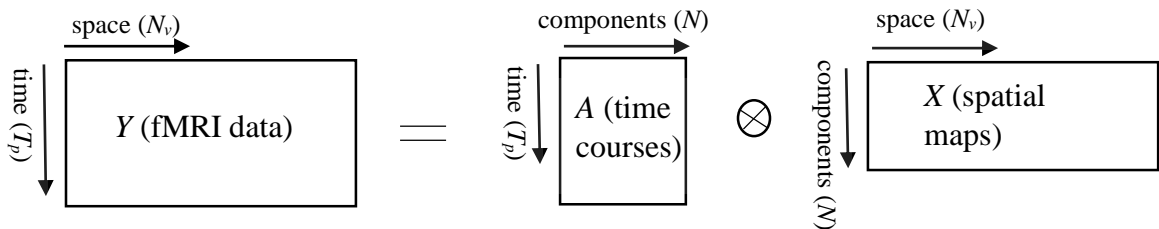


Fig. 1.12 Illustration of ICA decomposition into spatial and time courses

1.7.3 Graph Theory Applied to Resting-state fMRI

Graph theory is a mathematical tool that can be used to model relationships between objects with complex topologies. GraphICA is a tool that utilizes both ICA and graph theory in order to extract the resting state networks from the fMRI BOLD signals. In GraphICA, initially PCA is used to reduce the dimension of the data to a predefined number of components (N) equal to 30 and then independent components are identified using ICA [45]. Nine RSNs are extracted from the 30 components, by obtaining the components that maximize the goodness-of-fit to a binary pre-defined template while considering all the RSNs simultaneously [45]. The templates for each RSN were selected by an expert after visual inspection from a set of spatial maps resulting from a Group ICA decomposition performed on 12 independently assessed controls and were confirmed by another expert for accuracy of structural labeling [71]. Out of the selected RSNs, a binary classifier that is trained on the “fingerprints” (which provide both spatial and temporal characterizations) of healthy subjects is used to select only the neuronal components from the extracted networks. Even if the resting state networks are recognized from the spatial maps, sometimes the networks tend to be non-neuronal [72]. The “fingerprint” consists of degree of clustering, skewness, kurtosis, spatial entropy, one-lag autocorrelation, temporal entropy and power of five frequency bands: 0–008Hz, 0.008–0.02Hz, 0.02–0.05Hz, 0.05–0.1Hz, and 0.1–0.25Hz [71]. Signals arising from changes in local hemodynamics which result solely from alterations in neuronal activity represented by low-frequency (0.01–0.05Hz) are called neuronal signals. Non-neuronal signals are high frequency signals mainly arising from cardiac cycles, eye and head movements [73]. Next, graph theory is applied to the identified RSNs to determine the degree of functional connectivity amongst the regions of the networks.

Once the RSNs are extracted from GraphICA, each of these RSNs are parcellated into 1015 anatomical regions using the Lausanne 2008 Atlas [23]. Then each of the anatomically parcellated regions is considered as the node of a graph and the edges which connect the nodes typically carry weights describing the correlation, similarity, or degree of connectivity between nodes. Once ICA is applied to decompose the fMRI signal, as shown in **Eq. (1.12)**, the matrix X consists of the spatial maps of the ICs. Here X_{ab} represents the coefficient needed to be assigned to the a^{th} component's time course in order to describe the contribution of that component to the BOLD signal of the b^{th} voxel. Since these coefficient values are of arbitrary size and variance and cannot be interpreted directly, they are transformed (or normalized) into t -values using the following **Eq. (1.13)** [45]:

$$T = \frac{c^T X}{\sqrt{\text{Var}(\varepsilon) c^T (Y^T Y)^{-1} c}} \quad (1.13)$$

where, ε is an error term defined by $\varepsilon = Y - AX$, c is a vector indexing each IC and T is the matrix consisting of t -values for each region and IC. Then these t -values are used to build the weighted matrices (w_{ij}) for each of the IC (network). A scheme was introduced to calculate the edge weights using **Eq. 1.14** [45, 66, 67]:

$$w_{ij} = |t_i| + |t_j| - |t_i - t_j| \quad (1.14)$$

where w_{ij} represents the connectivity between regions i and j , according to the time course of the corresponding IC (scalar map), and t_i, t_j are the t -values which are obtained from the ICs for nodes ' i ' and ' j ' respectively. Here, the scheme is chosen such that regions with similar and high t -values will contribute largely to the regional fMRI time series. These matrices (dimension of 1015 x 1015) not only allow us to calculate the global graph properties, but also the graph strength (sum of

weighted connections of a node), degree (number of connections of a node), efficiency (how efficiently information flows across a node), small-worldness etc. of each network can be calculated locally for each region.

1.7.4 Applications of GraphICA on Different Populations

Tinnitus

Tinnitus, the perception of sound in the absence of external stimuli, is often a disturbing symptom for which the underlying functional neuroanatomy still remains poorly understood [67]. It is usually referred to as ringing or buzzing noise in one or both ears, without any auditory stimuli. About 15% of the population is affected by chronic tinnitus significantly affecting quality of life via issues such as sleep deprivation, memory problems, stress, depression, and anxiety and irritability [74]. The prevailing opinion is that peripheral lesions in the cochlea or the auditory nerve produce dysfunctional neural input to the central auditory pathway and induce changes in the auditory system [67]. These altered patterns of intrinsic neural activity can be caused by chronic health conditions, injuries, or conditions that affect the nerves in the ear or the hearing center of the brain that interprets nerve signals as sound. De Ridder et al. has proposed that because the brain is organized into networks specialized for specific tasks, tinnitus may be due to overlapping of dysfunctional networks [75]. Specifically, the auditory phantom caused by tinnitus creates a sensory deafferentation and then for the brain to be aware of the phantom, it should reach the perceptual network [75]. Therefore, this process involves the auditory, sensory and perceptual networks. In this approach, tinnitus can be considered as an emergent property of multiple overlapping dynamic brain networks [75]. GraphICA can be used to visualize the changes occurring within and between each of these brain networks, permitting us to see the regions affected by tinnitus.

Disorders of Consciousness (DOC)

One of the ultimate goals of neuroscience is to be able to explain the everyday experience of conscious life. Consciousness is a state of having awareness on internal and external existence. One should be aware, defined as having the ability to respond to an external stimulus, and wakeful, defined as the ability to open the eyes, in order to be conscious. DOC are states that inhibit consciousness caused by severe brain injuries. Patients with this condition can be categorized as in a vegetative state (the absence of responsiveness and awareness but in which wakefulness is present), a minimally consciousness state (limited but reproducible signs of awareness) or emergence from minimally consciousness state in which patients can communicate or make proper functional use of an object [66]. These patients face a significant lack of treatment options. Clinical expression of consciousness of these patients is often limited, inconsistent and easily exhausted, hampering assessment of cognitive functions. Classification of patients with DOC is pivotal for optimizing treatment, but challenging also due to the minimal amount of differences in brain activity amongst these patients. Behavioral assessments alone are not sufficient to provide accurate diagnostic information in individuals with disorders of consciousness [76]. Multimodal neuroimaging techniques, combining different types of neuroimaging modalities, which do not require active participation of the patients, integrated with clinical assessments, may provide an improved understanding of neural networks involved in consciousness [66]. In fact, neuroimaging techniques allow the collection of a large amount of information that is inaccessible using bedside clinical evaluation. Specifically, the combination of fludeoxyglucose (FDG-)PET with MRI has shown promising approach in order to diagnose the patient's condition accurately [66, 77]. FDG-

PET is a technique that is used to observe metabolic activity in the body using the introduction of a radioactive molecule (usually a glucose compound) into the body.

GraphICA permits us to extract the functionality of the RSNs of patients from the rs-fMRI and enables us to compare these results with metabolic activity, which can be simultaneously acquired from the PET data. Although the fMRI signal consists of time series, we will be extracting the RSNs (scalar maps which are time independent) using GraphICA and comparing the graph strengths obtained from the functional connectivity of these networks with the PET data. Functional connectivity gives an idea on how brain regions are functionally connected with each other. PET gives information about the metabolic activity of brain regions. Therefore, we will be comparing the results obtained from these techniques as described in detail in Chapter 4. This may reduce clinical misdiagnosis and form a pathway to improve the life styles of the individuals suffering from disorders of consciousness, reducing the burden of their families as well.

1.8 Chapter Preview

The thesis consists of three papers compiled into an integrated article thesis format along with an overall introduction which is already provided and discussion sections. The rest of the four chapters of the thesis are organized as follows. Chapter 2 is a project that combines both the methodology and application of the generalized Ising model. This model is used to model the brain activity in different brain conditions as induced by the anesthetic propofol, in addition to when an external stimulus was applied. This manuscript will be submitted for publication soon. The generalized Ising model code without external field was initially developed by Dr. Das in our group. I further developed it to incorporate the external field and subsequently applied it to fMRI data which were acquired when subjects were listening to an audio clip and in different conscious

states. Our goal was to test the applicability of the generalized Ising model to fit the empirical data obtained under complex naturalistic stimulation, such as listening to a movie.

Chapters 3 and 4 demonstrate the applicability of a previously developed method, GraphICA, that combines graph theory and ICA, to investigate functional connectivity of patient populations. GraphICA was developed by Ribeiro De Paula, a previous member in our group. In Chapter 3, GraphICA is applied to a data set of patients with tinnitus, in which the patients' brains are not much altered from the healthy brains, to assess the correlation of clinical behaviors with functional connectivity. I developed code for group statistical analysis. A version of the published paper (Journal of Neurology [57]) is presented in the thesis.

In Chapter 4, GraphICA is used to extract features or the networks from the fMRI data of patients with DOC, for whom the brains are severely damaged. I developed a strategy to look at these features and to select the best feature out of the two acquisitions collected within the same scanning session. This technique will be useful when comparing results obtained in a longitudinal study, by selecting the best feature for each acquisition. It will confirm whether the changes we see in the functional connectivity are caused by the patients' evolution or due to some artifacts. This chapter is a pilot study performed on three patients with DOC and is a combination of both methodology and application. A version of the published paper (Frontiers in Neurology [56]) is presented in the thesis. The overall goals of Chapters 3 and 4 was to determine whether GraphICA is a valid technique for interrogating information from patient populations, both with brains that resemble healthy brains and then to extend it to see if it also can be applied to populations with extensive structural brain damage. The final Chapter 5 consists of the general discussion of this study, followed by future directions.

Throughout these chapters we hope to investigate whether these novel techniques, specifically GIM and combining graph theory with ICA are useful methods that could be adopted to further answer questions in neuroscience.

Bibliography

- 1) Spiegler, A., Knösche, T. R., Schwab, K., Haueisen, J., & Atay, F. M. (2011). Modeling brain resonance phenomena using a neural mass model. *PLOS Computational Biology*, 7(12), e1002298.
- 2) Coombes, S. (2010). Large-scale neural dynamics: simple and complex. *NeuroImage*, 52(3), 731-739.
- 3) Huettel, S. A., Song, A. W., & McCarthy, G. (2009). Functional magnetic resonance imaging. *Yale Journal of Biology and Medicine*, 82(4), 233.
- 4) Glover, G. H. (2011). Overview of functional magnetic resonance imaging. *Neurosurgery Clinics*, 22(2), 133-139.
- 5) Greicius, M. (2008). Resting-state functional connectivity in neuropsychiatric disorders. *Current Opinion in Neurology*, 21(4), 424-430.
- 6) Van Den Heuvel, M. P., & Pol, H. E. H. (2010). Exploring the brain network: a review on resting-state fMRI functional connectivity. *European Neuropsychopharmacology*, 20(8), 519-534.
- 7) Abeyasinghe, P. M., de Paula, D. R., Khajehabdollahi, S., Valluri, S. R., Owen, A. M., & Soddu, A. (2018). Role of dimensionality in predicting the spontaneous behavior of the brain using the classical Ising model and the Ising model implemented on a structural connectome. *Brain Connectivity*, 8(7), 444-455.
- 8) Farisco, M., Kotaleski, J. H., & Evers, K. (2018). Large-scale brain simulation and disorders of consciousness. Mapping technical and conceptual issues. *Frontiers in Psychology*, 9, 585.
- 9) Sporns, O. (2018). Graph theory methods: applications in brain networks. *Dialogues in Clinical Neuroscience*, 20(2), 111.

- 10) Vecchio, F., Miraglia, F., & Rossini, P. M. (2017). Connectome: Graph theory application in functional brain network architecture. *Clinical Neurophysiology Practice*, 2, 206-213.
- 11) Stam, C. J., Jones, B. F., Nolte, G., Breakspear, M., & Scheltens, P. (2006). Small-world networks and functional connectivity in Alzheimer's disease. *Cerebral Cortex*, 17(1), 92-99.
- 12) Bassett, D. S., Meyer-Lindenberg, A., Achard, S., Duke, T., & Bullmore, E. (2006). Adaptive reconfiguration of fractal small-world human brain functional networks. *Proceedings of the National Academy of Sciences*, 103(51), 19518-19523.
- 13) Logothetis, N. K. (2008). What we can do and what we cannot do with fMRI. *Nature*, 453(7197), 869.
- 14) Lodish, H., Berk, A., Zipursky, S. L., Matsudaira, P., Baltimore, D., & Darnell, J. (2000). Overview of neuron structure and function. *Molecular Cell Biology*. 4.
- 15) Dicke, U., & Roth, G. (2016). Neuronal factors determining high intelligence. *Philosophical Transactions of the Royal Society B: Biological Sciences*, 371(1685), 20150180.
- 16) Wright, S. H. (2004). Generation of resting membrane potential. *Advances in Physiology Education*, 28(4), 139-142.
- 17) Oja, S. S., & Saransaari, P. (2010). Neurons, action potentials, and synapses. *Medical and Health Sciences*, 4, 250.
- 18) Sporns, O., Tononi, G., & Kötter, R. (2005). The human connectome: a structural description of the human brain. *PLOS Computational Biology*, 1(4), e42.
- 19) Thirion, B., Varoquaux, G., Dohmatob, E., & Poline, J. B. (2014). Which fMRI clustering gives good brain parcellations? *Frontiers in Neuroscience*, 8, 167.
- 20) Arslan, S., Ktena, S. I., Makropoulos, A., Robinson, E. C., Rueckert, D., & Parisot, S. (2018). Human brain mapping: A systematic comparison of parcellation methods for the human cerebral cortex. *Neuroimage*, 170, 5-30.
- 21) Rolls, E. T., Joliot, M., & Tzourio-Mazoyer, N. (2015). Implementation of a new parcellation of the orbitofrontal cortex in the automated anatomical labeling atlas. *Neuroimage*, 122, 1-5.

- 22) Hagmann, P., Cammoun, L., Gigandet, X., Meuli, R., Honey, C. J., Wedeen, V. J., & Sporns, O. (2008). Mapping the structural core of human cerebral cortex. *PLOS Biology*, 6(7), e159.
- 23) Jellison, B. J., Field, A. S., Medow, J., Lazar, M., Salamat, M. S., & Alexander, A. L. (2004). Diffusion tensor imaging of cerebral white matter: a pictorial review of physics, fiber tract anatomy, and tumor imaging patterns. *American Journal of Neuroradiology*, 25(3), 356-369.
- 24) Basser, P. J., Mattiello, J., & LeBihan, D. (1994). MR diffusion tensor spectroscopy and imaging. *Biophysical Journal*, 66(1), 259-267.
- 25) Shadi, K., Bakhshi, S., Gutman, D. A., Mayberg, H. S., & Dovrolis, C. (2016). A symmetry-based method to infer structural brain networks from tractography data. *Frontiers in Neuroinformatics*, 10, 46.
- 26) Das, T. K., Abeyasinghe, P. M., Crone, J. S., Sosnowski, A., Laureys, S., Owen, A. M., & Soddu, A. (2014). Highlighting the structure-function relationship of the brain with the Ising model and graph theory. *BioMed Research International*, 2014, 237898.
- 27) Friston, K. J., Frith, C. D., Liddle, P. F., & Frackowiak, R. S. J. (1993). Functional connectivity: the principal-component analysis of large (PET) data sets. *Journal of Cerebral Blood Flow & Metabolism*, 13(1), 5-14.
- 28) Crosson, B., Ford, A., McGregor, K. M., Meinzer, M., Cheshkov, S., Li, X., Walker-Batson, D & Briggs, R. W. (2010). Functional imaging and related techniques: an introduction for rehabilitation researchers. *Journal of Rehabilitation Research and Development*, 47, 2.
- 29) Varvatsoulas, G. (2013). The physiological processes underpinning PET and fMRI techniques with an emphasis on the temporal and spatial resolution of these methods. *Psychological Thought*, 6(2), 173-195.
- 30) Mier, W., & Mier, D. (2015). Advantages in functional imaging of the brain. *Frontiers in Human Neuroscience*, 9, 249.
- 31) Ladd, M. E., Bachert, P., Meyerspeer, M., Moser, E., Nagel, A. M., Norris, D. G., Schmitter, S., Speck, O., Straub, S. & Zaiss, M. (2018). Pros and cons of ultra-high-field MRI/MRS for human application. *Progress in Nuclear Magnetic Resonance Spectroscopy*, 109, 1-50.

- 32) Biswal, B., Zerrin Yetkin, F., Haughton, V. M., & Hyde, J. S. (1995). Functional connectivity in the motor cortex of resting human brain using echo-planar MRI. *Magnetic Resonance in Medicine*, 34(4), 537-541.
- 33) Raichle, M. E. (2001). Cognitive neuroscience: Bold insights. *Nature*, 412(6843), 128.
- 34) Barth, M., & Poser, B. A. (2011). Advances in high-field BOLD fMRI. *Materials*, 4(11), 1941-1955.
- 35) Murphy, M. C., Conner, I. P., Teng, C. Y., Lawrence, J. D., Safiullah, Z., Wang, B., Bilonick, R. A., Kim, S. G., Wollstein, G., Schuman, J. S. & Chan, K. C. (2016). Retinal structures and visual cortex activity are impaired prior to clinical vision loss in glaucoma. *Scientific Reports*, 6, 31464.
- 36) Greicius, M. (2008). Resting-state functional connectivity in neuropsychiatric disorders. *Current Opinion in Neurology*, 21(4), 424-430.
- 37) Hyder, F. (2009). Dynamic imaging of brain function. *Methods in Molecular Biology*, 489, 3-21.
- 38) Fox, M. D., & Raichle, M. E. (2007). Spontaneous fluctuations in brain activity observed with functional magnetic resonance imaging. *Nature Reviews Neuroscience*, 8(9), 700.
- 39) De Martino, F., Esposito, F., Van de Moortele, P. F., Harel, N., Formisano, E., Goebel, R., Ugurbil, K. & Yacoub, E. (2011). Whole brain high-resolution functional imaging at ultra high magnetic fields: an application to the analysis of resting state networks. *Neuroimage*, 57(3), 1031-1044.
- 40) Crivello, F., Schormann, T., Tzourio-Mazoyer, N., Roland, P. E., Zilles, K., & Mazoyer, B. M. (2002). Comparison of spatial normalization procedures and their impact on functional maps. *Human Brain Mapping*, 16(4), 228-250.
- 41) Toga, A. W., & Thompson, P. M. (2001). The role of image registration in brain mapping. *Image and Vision Computing*, 19(1-2), 3-24.
- 42) Soddu, A., Vanhauzenhuyse, A., Bahri, M. A., Bruno, M. A., Boly, M., Demertzi, A., Tshibanda, J. F., Philips, C., Stanziano, M., Ovadia-Caro, S., Nir, Y., Maquet, P., Papa, M.,

- Malach, R., Laureys, S., & Noirhomme, Q. (2012). Identifying the default-mode component in spatial IC analyses of patients with disorders of consciousness. *Human Brain Mapping*, 33(4), 778-796.
- 43) Damoiseaux, J. S., Rombouts, S. A. R. B., Barkhof, F., Scheltens, P., Stam, C. J., Smith, S. M., & Beckmann, C. F. (2006). Consistent resting-state networks across healthy subjects. *Proceedings of the National Academy of Sciences*, 103(37), 13848-13853.
- 44) Moussa, M. N., Steen, M. R., Laurienti, P. J., & Hayasaka, S. (2012). Consistency of network modules in resting-state fMRI connectome data. *PLOS One*, 7(8), e44428.
- 45) Ribeiro de Paula, D., Ziegler, E., Abeyasinghe, P. M., Das, T. K., Cavaliere, C., Aiello, M., Heine, L., Perri, C., Demertzi, A., Noirhomme, Q., Charland-Verville, V., Vanhauzenhuysse, A., Stender, J., Gomez, F., Tshibanda, J. L., Laureys, S., Owen, A. & Soddu, A. (2017). A method for independent component graph analysis of resting-state fMRI. *Brain and Behavior*, 7(3), e00626.
- 46) Breakspear, M., Heitmann, S., & Daffertshofer, A. (2010). Generative models of cortical oscillations: neurobiological implications of the Kuramoto model. *Frontiers in Human Neuroscience*, 4, 190.
- 47) Kuramoto, Y. (1986). Chemical oscillations, waves, and turbulence. *Journal of Applied Mathematics and Mechanics*, 66(7), 296.
- 48) Van Vreeswijk, C., Abbott, L. F., & Ermentrout, G. B. (1994). When inhibition not excitation synchronizes neural firing. *Journal of Computational Neuroscience*, 1(4), 313-321.
- 49) Lee, W. H., Bullmore, E., & Frangou, S. (2017). Quantitative evaluation of simulated functional brain networks in graph theoretical analysis. *NeuroImage*, 146, 724-733.
- 50) Pinotsis, D., Robinson, P., & Friston, K. (2014). Neural masses and fields: modeling the dynamics of brain activity. *Frontiers in Computational Neuroscience*, 8, 149.
- 51) Sotero, R. C., Trujillo-Barreto, N. J., Iturria-Medina, Y., Carbonell, F., & Jimenez, J. C. (2007). Realistically coupled neural mass models can generate EEG rhythms. *Neural Computation*, 19(2), 478-512.

- 52) Byrne, A., Avitabile, D. & Coombes, S. (2019). Next-generation neural field model: The evolution of synchrony within patterns and waves. *Physical Review E*, 99, 012313.
- 53) Brush, S. G. (1967). History of the Lenz-Ising model. *Reviews of Modern Physics*, 39(4), 883.
- 54) Fraiman, D., Balenzuela, P., Foss, J., & Chialvo, D. R. (2009). Ising-like dynamics in large-scale functional brain networks. *Physical Review E*, 79(6), 061922.
- 55) Onsager, L. (1944). Crystal statistics. I. A two-dimensional model with an order-disorder transition. *Physical Review*, 65(3-4), 117.
- 56) Khajehabdollahi, S., Abeyasinghe, P., Owen, A., & Soddu, A. (2019). The emergence of integrated information, complexity, and consciousness at criticality. *BioRxiv*, 521567.
- 57) Marinazzo, D., Pellicoro, M., Wu, G., Angelini, L., Cortés, J. M., & Stramaglia, S. (2014). Information transfer and criticality in the Ising model on the human connectome. *PLOS One*, 9(4), e93616.
- 58) Lindquist, M. A., Loh, J. M., Atlas, L. Y., & Wager, T. D. (2009). Modeling the hemodynamic response function in fMRI: efficiency, bias and mis-modeling. *Neuroimage*, 45(1), S187-S198.
- 59) Dotsenko, V. S., Dotsenko, V. S. (2006). Critical behaviour of the phase transition in the 2D Ising Model with impurities, *Advances in Physics*, 32(2), 1983.
- 60) Guldenmund, P., Gantner, I. S., Baquero, K., Das, T., Demertzi, A., Boveroux, P., Bonhomme, V., Vanhaudenhuyse, A., Bruno, M. A., Gosseries, O., Noirhomme, Q., Kirsch, M., Boly, M., Owen, A. M., Laureys, S., Gomez, F. & Soddu, A. (2016). Propofol-induced frontal cortex disconnection: a study of resting-state networks, total brain connectivity, and mean BOLD signal oscillation frequencies. *Brain Connectivity*, 6(3), 225-237.
- 61) Spiegler, A., Knösche, T. R., Schwab, K., Haueisen, J., & Atay, F. M. (2011). Modeling brain resonance phenomena using a neural mass model. *PLOS Computational Biology*, 7(12), e1002298.
- 62) Namazi, H., & Kulish, V. V. (2012). Diffusion Based Modeling of Human Brain Response to External Stimuli. *arXiv preprint arXiv:1204.0576*.

- 63) Namazi, H., & Kulish, V. V. (2015). Fractional diffusion based modelling and prediction of human brain response to external stimuli. *Computational and Mathematical Methods in Medicine*, 2015, 148534.
- 64) Wang, J. H., Zuo, X. N., Gohel, S., Milham, M. P., Biswal, B. B., & He, Y. (2011). Graph theoretical analysis of functional brain networks: test-retest evaluation on short-and long-term resting-state functional MRI data. *PLOS One*, 6(7), e21976.
- 65) Bullmore, E., & Sporns, O. (2009). Complex brain networks: graph theoretical analysis of structural and functional systems. *Nature Reviews Neuroscience*, 10(3), 186.
- 66) Cavaliere, C., Kandeepan, S., Aiello, M., Ribeiro de Paula, D., Marchitelli, R., Fiorenza, S., Orsini, M., Trojano, L., Masotta, O., St. Lawrence, K., Loreto, V., Chronik, B. A., Nicolai, E., Soddu, A. & Estraneo, A. (2018). Multimodal neuroimaging approach to variability of functional connectivity in disorders of consciousness: a PET/MRI pilot study. *Frontiers in Neurology*, 9, 861.
- 67) Kandeepan, S., Maudoux, A., de Paula, D. R., Zheng, J. Y., Cabay, J. E., Gómez, F., Chronik, B. A., Ridder, D., Vanneste, S. & Soddu, A. (2019). Tinnitus distress: a paradoxical attention to the sound? *Journal of Neurology*, 1-11.
- 68) Beckmann, C. F., DeLuca, M., Devlin, J. T., & Smith, S. M. (2005). Investigations into resting-state connectivity using independent component analysis. *Philosophical Transactions of the Royal Society B: Biological Sciences*, 360(1457), 1001-1013.
- 69) McKeown, M. J., & Sejnowski, T. J. (1998). Independent component analysis of fMRI data: examining the assumptions. *Human Brain Mapping*, 6(5-6), 368-372.
- 70) De Luca, M., Beckmann, C. F., De Stefano, N., Matthews, P. M., & Smith, S. M. (2006). fMRI resting state networks define distinct modes of long-distance interactions in the human brain. *Neuroimage*, 29(4), 1359-1367.
- 71) Demertzi, A., Gomez, F., Crone, J. S., Vanhaudenhuyse, A., Tshibanda, L., Noirhomme, Q., Thonnard, M., Charland-Verville, V., Kirsch, M., Laureys, S. & Soddu, A. (2014). Multiple fMRI system-level baseline connectivity is disrupted in patients with consciousness alterations. *Cortex*, 52, 35-46.

- 72) Heine, L., Soddu, A., Gómez, F., Vanhaudenhuyse, A., Tshibanda, L., Thonnard, M., Charland-Verville, V., Kirsch, M., Laureys, S. & Demertzi, A. (2012). Resting state networks and consciousness. *Frontiers in Psychology*, 3, 295.
- 73) Murphy, K., Birn, R. M., & Bandettini, P. A. (2013). Resting-state fMRI confounds and cleanup. *Neuroimage*, 80, 349-359.
- 74) Seidman, M. D., Standring, R. T., & Dornhoffer, J. L. (2010). Tinnitus: current understanding and contemporary management. *Current Opinion in Otolaryngology & Head and Neck Surgery*, 18(5), 363-368.
- 75) De Ridder, D., Elgoyhen, A. B., Romo, R., & Langguth, B. (2011). Phantom percepts: tinnitus and pain as persisting aversive memory networks. *Proceedings of the National Academy of Sciences*, 108(20), 8075-8080.
- 76) Giacino, J. T., Schnakers, C., Rodriguez-Moreno, D., Kalmar, K., Schiff, N., & Hirsch, J. (2009). Behavioral assessment in patients with disorders of consciousness: gold standard or fool's gold?. *Progress in Brain Research*, 177, 33-48.
- 77) Soddu, A., Gómez, F., Heine, L., Di Perri, C., Bahri, M. A., Voss, H. U., Bruno, M. A., Vanhaudenhuyse, A., Philips, C., Demertzi, A., Chatelle, C., Schrouff, J., Thibaut, A., Charland-Verville, V., Noirhomme, Q., Salmon, E., Tshibanda, J. F., Schiff, N. D. & Laureys, S. (2016). Correlation between resting state fMRI total neuronal activity and PET metabolism in healthy controls and patients with disorders of consciousness. *Brain and Behavior*, 6(1), e00424.

Chapter 2

Modeling an Auditory Stimulated Brain Under Altered States of Consciousness using the Generalized Ising Model

2.1 Introduction

The brain is a complex system, characterized by heterogeneous networks of structural connections supporting cognition, and which assist in responding to perceptual information coming from the peripheral nervous system. Modern neuroimaging techniques, such as fMRI and EEG, now permit the comprehensive mapping of these networks in order to understand how information is transmitted within and across them [1]. However, many aspects of the dynamical functioning of the brain under stimulation and in altered states of consciousness induced by anesthetic drugs are still not completely understood [2]. Using engaging stimuli that drive a specific conscious experience (such as, for example, watching a movie) would make it possible to detect whether behaviourally unresponsive patients are having a comparable conscious experience.

Anesthetics generally suppress the body's normal automatic functions, such as breathing, the heartbeat, and blood pressure, as well as the global cerebral metabolic rate [3]. using EEG, it has been shown that low-frequency, high amplitude oscillations increase as the level of anesthesia increases [4]. A number of neuroimaging studies have probed the effects of anesthesia-induced sedation on brain activation when exposed to various types of acoustic inputs. Using propofol, a short-acting medication that results in a decreased level of consciousness that is widely used due to its fast induction and recovery time [5], Naci et al. found that a high cross-subject correlation between sensory-driven auditory cortex in higher-order frontal and parietal regions while listening to a plot-driven audio story while patients were conscious. During deep anesthesia, however, the cross-subject correlation was limited to the auditory cortex, and was almost abolished in fronto-

parietal regions [6]. Davis et al also found that bilateral temporal-lobe responses to complex auditorily-presented sentences were preserved when reduced levels of awareness were induced via propofol [7]. These findings were further confirmed by Dueck et al., who presented musical stimuli to neurosurgical patients after the injection of different concentrations of propofol [8]. Their study showed activation in the superior temporal gyrus (primary and secondary auditory cortex) and in higher-order auditory information processing areas while participants were awake. These activations attenuated with increasing concentrations of propofol but remained partially preserved in the superior temporal gyrus. Additionally, in an auditory word listening fMRI study of functional connectivity, Liu et al. reported that propofol-induced sedation disrupted verbal comprehension and memory by blocking the projection of sensory information to higher-order processing networks and thus preventing information integration [9].

Neuroimaging techniques have allowed us to explore how the brain functions at different levels of consciousness, in both healthy individuals and in patients. However, there are many hypotheses that would be difficult or impossible to directly test using brain imaging. Computational models allow us to simulate the brain in different states and under different conditions, allowing us to test such hypotheses. One such model, the Ising model developed by Ernest Ising, has been adapted from its traditional use in describing the behaviour of magnets to be applied in computational neuroscience [10, 11]. Spin sites capture the dynamics of the BOLD signal with a two-state spin variable, representing activity above and below a baseline. By simulating the Ising model at different temperatures, Fraiman et al. showed that, at the critical temperature T_c (the temperature at which the system exhibits a transition from an ordered phase to a disordered phase), the model can simulate the global behavior of the brain's functional connectivity at rest [11]. They showed that the best fit to the distribution of the functional

correlations of the brain was obtained from the simulations at the critical temperature of the 2D classical Ising model.

The generalized Ising model (GIM), which was introduced by Marinazzo and colleagues [12], is a modification to the 2D classical Ising model, in which spins are no longer restricted to interact with only their neighbours, but may interact with all other spins via differing coupling strengths [12]. The couplings among spin sites are derived from the structural architecture (i.e., the white matter fiber connections) of the brain obtained using diffusion tensor imaging (DTI), and represent a one-to-one relationship between each spin site of the lattice and the corresponding region of the brain. The GIM has been recently employed to simulate resting state fMRI [12 - 15]. Implementing the GIM on two different resolutions of structural connectivity matrices, Marinazzo et al. showed that the total information transfer between the spins, defined by the Shannon entropy, was maximized at criticality [12]. Further, Stramaglia and colleagues compared the correlations between spin sites simulated from the Ising model implemented on the structural connectome against the empirical functional brain correlations—both at the single link level (in which spin sites are flipped one at a time) and at the modular level (in which blocks of correlated spin sites are flipped together). They concluded that when the brain is under anesthesia, similarity between the model and empirical data increases at the modular level [13].

Continuing work to optimize the GIM, Deco et al. studied the Ising model implemented on artificially created structural connectomes with different coupling strengths among the nodes [14]. By examining the entropy of the system at different coupling strengths, they found that the system exhibited rich dynamics when the structural connections of the brain self-organized to form a scale-free network. Such network is characterized by many nodes with high connections (i.e. hubs), following a power-law degree (i.e., the number of connections) distribution. They are called scale-

free, as power laws have same functional form at any scale. Finally, Abeyasinghe et al. [15] calculated the dimensionality of the brain with respect to information transfer during wakefulness, using the GIM, and reported it to be two. In their work, dimensionality was explained in terms of the reactivity of neurons to stimuli, that is, neurons specialized to react to certain stimuli were low dimensional, while neurons that react to mixed stimuli were highly dimensional. In order to calculate dimensionality, they introduced a concept for the distance between two regions in the GIM to be equivalent to the inverse of the normalized fiber connections between the two regions (which is relevant to the information transfer), as there is no direct measure to calculate the distance between the two regions in the GIM.

The goal of the present study was to provide an initial step to see if the GIM can be applied to assess the common neural experience a behaviourally non responsive patient might have. In order to do this, we modelled the brain activity of healthy subjects using the GIM implemented on the structural architecture, in altered states of consciousness, while receiving a naturalistic external stimulus. We predicted that the brain-behaviour response to naturalistic stimuli would be more complex to model compared to stimuli presented in a block design. To our knowledge this is the first study that captures human brain activity in response to real-life external stimuli at different levels of conscious awareness using mathematical modeling. This study might be helpful in future to assess the level of consciousness of patients with disorders of consciousness and help in regaining their consciousness.

2.2 Methodology

The data of healthy subjects were acquired while participants were listening to the audio clip (task condition) as well as while they were rest, at four levels of sedation. Data were then preprocessed and parcellated into 84 regions of interest (ROIs), and the empirical time series of each ROI was extracted. The GIM was then simulated at different temperatures under resting and task conditions, and simulated time series were obtained. Empirical and simulated inter-subject correlations were calculated using the respective time series, and they were then compared to find the temperature that led to the highest degree of similarity. Details of each step are given below.

2.2.1 Task Protocol

fMRI scans were acquired while participants listened to the audio story in four states of consciousness: awake, mild sedation, deep sedation, and recovery. The audio story was played at the start of each session once the wakefulness/sedation level was assessed. The audio story was 5 minutes in duration and was an excerpt from a scene of the movie ‘Taken’ (reported in Naci et al., 2015) that portrays a teenage girl being kidnapped [16].

2.2.2 Administration of Propofol

Before entering the fMRI scanner, a 20G i.v. cannula was inserted into a vein on the dorsum of the non-dominant hand of the participants. The propofol infusion system was connected to the cannula prior to the first scanning session. Intravenous propofol was administered with a Baxter AS 50 (Singapore). An effect-site/plasma steering algorithm was used in combination with the computer-controlled infusion pump to achieve step-wise increments in the sedative effect of propofol. The infusion pump was adjusted to achieve the desired level of sedation, guided by targeted concentrations of propofol, as predicted by the TIVATrainer (the European Society for Intravenous Anesthesia, eurosiva.eu) pharmacokinetic simulation program. The pharmacokinetic

model provided target-controlled infusion by adjusting infusion rates of propofol over time to achieve and maintain the target blood concentrations as specified by the Marsh 3 [17] compartment algorithm for each participant, as incorporated in the TIVA Trainer software.

The four states of consciousness were defined as follows. **1) Awake:** No propofol was administered during the “awake” session. During the awake scan, prior to the administration of propofol, participants were fully awake, alert, and communicating appropriately. **2) Mild sedation:** At the beginning of the mild sedation scan, propofol infusion commenced with a target effect-site concentration of 0.6 µg/ml and oxygen was titrated to maintain SpO₂ above 96%. Once the baseline target effect-site concentration was reached, the participants’ level of sedation was assessed and if deemed to be appropriate for mild sedation (Ramsey 3), the effect-site concentration was maintained. During administration of propofol, participants became calmer and more slowed in their response to verbal communication. Once participants stopped engaging in spontaneous conversation, and speech became sluggish, they were classified as a Ramsey level 3 and were considered mildly sedated. At this level, participants only responded to loud commands. **3) Deep sedation:** Prior to commencing the deep sedation scan, the target effect-site concentration was again increased in increments of 0.3 µg/ml with repeated assessments of responsiveness. Once a Ramsey 5 level of sedation was achieved, no further changes were made, and the participant was maintained at that level. When participants stopped responding to verbal commands and were only rousable to light physical stimulation, they were considered Ramsey level 5 and deeply sedated. Patients were unable to engage in conversation at this level. At Ramsay 5, participants remained capable of spontaneous cardiovascular function and ventilation. **4) Recovery:** Propofol was discontinued following the deep sedation scan and approximately 11 minutes following the

discontinuation of propofol, participants reached Ramsey level 2. This was observed by clear and quick responses to verbal commands.

The mean estimated effect-site propofol concentration was 2.48 (1.82- 3.14) $\mu\text{g/ml}$, and the mean estimated plasma propofol concentration was 2.68 (1.92- 3.44) $\mu\text{g/ml}$. Mean total mass of propofol administered was 486.58 (373.30- 599.86) mg. The variability of these concentrations and doses is typical for studies of the pharmacokinetics and pharmacodynamics of propofol.

2.2.3 Sedation Assessment

Prior to acquiring fMRI data, three independent assessors (two anesthesiologists and one anesthesia nurse) evaluated each participant's Ramsay level by communicating with them in person inside the fMRI scanner room. Participants were also asked to perform a basic verbal recall memory test and a computerized (4 minute) auditory target detection task, which further assessed each individual's wakefulness/sedation level independently of the anesthesia team. Scanning commenced only when the agreement among the three anesthesia assessors on the wakefulness/sedation level was confirmed.

2.2.4 fMRI Data Acquisition

A total of 17 healthy subjects (4 women; mean age 24 years, SD = 5) participated in this study. Noise cancellation headphones (Sensimetrics, S14; www.sens.com) were used for sound delivery at a volume level deemed comfortable by each individual for the duration of the experiment. Functional echo-planar images were acquired (33 slices, voxel size: $3 \times 3 \times 3 \text{ mm}^3$, inter-slice gap of 25%, TR = 2000 ms, TE = 30 ms, matrix size = 64×64 , FA = 75°). The audio story and resting state scans had 155 and 256 volumes, respectively. An anatomical scan was obtained using a T1-weighted 3D MPRAGE (Magnetization Prepared - RApid Gradient Echo)

sequence (32 channel coil, voxel size: 1 x 1 x 1 mm³, TE = 4.25 ms, matrix size = 240 x 256 x 192, FA = 9°).

2.2.5 Preprocessing of fMRI Data

T1 images were preprocessed using the SPM (<http://www.fil.ion.ucl.ac.uk/spm>), FSL (<https://fsl.fmrib.ox.ac.uk/fsl/fslwiki/>), SimpleITK (<http://www.simpleitk.org/>) and Dipy (<http://nipy.org/dipy/>) toolboxes. T1 preprocessing included manual removal of the neck, brain extraction using FSL, correction of low-frequency intensity non-uniformity based on the N4 (non-parametric non-uniform normalization) bias field correction algorithm from SimpleITK, image denoising based on non-local means algorithm from Dipy, and spatial normalization to standard stereotactic Montreal Neurological Institute (MNI) space using the SPM12 normalization algorithm. The initial three volumes of the fMRI data were discarded to avoid T1 saturation effects. Head motion and slice timing corrections were performed on the fMRI data using FSL, followed by artifact correction using RapidArt (<https://www.nitrc.org/projects/rapidart/>). Subsequently, fMRI data were coregistered to a T1 image using SPM12 (<http://www.fil.ion.ucl.ac.uk/spm>) and spatially normalized to MNI space using the SPM12 normalization algorithm. Finally, spatial smoothing of the fMRI data was performed with a Gaussian kernel of 8 mm full-width at half maximum as implemented in SPM12.

2.2.6 fMRI Signal Extraction Based on Parcellation

First, the average time series of each region inside the AAL2 parcellation [18] scheme (<http://www.gin.cnrs.fr/en/tools/aal-aal2/>) was extracted. The extracted time series were then cleaned by removing spurious variance via the regression of nuisance waveforms derived from the average time series obtained from regions of non-interest (white matter and cerebrospinal fluid). This nuisance regressor also included six motion parameters (translation and rotation parameters

in the x, y, and z dimensions) from a rigid body transformation previously estimated using FSL. Finally, the time series were detrended, filtered using a bandpass with a Butterworth filter of cut-off frequencies set at 0.01 Hz and 0.1 Hz, and standardized to have zero mean and unit variance across time.

2.2.7 Extraction of Features from the Audio Clip

The spins of the GIM were coupled with the external field (i.e. the audio clip) via different coupling strengths. The coupling strengths were obtained by performing a general linear model (GLM) between the audio clip and the time series, using the audio clip as the independent variable and the time series of each region as the dependent variables. The coefficients calculated from the GLM, represented the coupling strengths of each spin with the external field. Using the combination of the coupling strengths and the audio clip as the external stimulus, the GIM was simulated. However, the inter-subject correlation (will be discussed in Section 2.2.8) calculated from the simulated data was not able to fit the inter-subject correlation calculated from the empirical data at any temperatures. Therefore, more meaningful time and frequency domain features were extracted from the audio clip to simulate the GIM as follows.

The audio clip was sampled at 44.1 kHz for a duration of 5 minutes. 21 audio features from both the time and frequency domains were extracted from the original audio clip using the software pyAudioAnalysis (<https://github.com/tyiannak/pyAudioAnalysis/>). The three time-domain features were: zero crossing rate (rate of sign changes along a signal), energy (sum of squares of the signal values, normalized by the respective frame length) and entropy of energy (measure of abrupt changes), which were directly extracted from the raw signal samples. The eighteen remaining features were in the frequency domain, obtained from the Fourier transform of the audio signal, and consisted of spectral centroid (center of gravity of the spectrum), spectral spread

(second central moment of the spectrum), spectral entropy (entropy of the normalized spectral energies for a set of sub-frames), spectral flux (the squared difference between the normalized magnitudes of the spectra of the two successive frames), spectral roll off (the frequency below which 90% of the magnitude distribution of the spectrum is concentrated) and thirteen Mel frequency cepstral coefficients (MFCCs). MFCCs are coefficients that collectively make up a Mel frequency spectrum and offer a description of the spectral shape of the sound [19]. Here, the frequency bands are positioned logarithmically (on the Mel scale), which more closely approximates the human auditory system's perceived response or pitch than do the linearly-spaced frequency bands. The audio signal was divided into time frames with lengths of two seconds without overlap, to match the repetition time of the fMRI data, and the above-mentioned audio features were extracted using the average of each frame. Finally, a multicollinearity test was performed on these 21 extracted features after they were normalized between -1 and 1, using a function called “*variation inflation factor*” implemented in RStudio. This function determined that three features had higher collinearity and could therefore be removed, while the remaining 18 features were used in the generalized linear modelling.

2.2.8 Inter-Subject Correlation

Inter-Subject Correlation (ISC) has been used previously to examine highly complex fMRI data acquired during naturalistic stimulation, such as when watching a movie [20, 21]. ISC measures the common neural activity present across subjects by comparing their neural response time series over the course of the naturalistic stimulation. The main advantage of ISC analysis over conventional fMRI analysis is that it does not require *a priori* knowledge of the external stimulus to locate activated brain areas. In ISC analysis, the subject’s brain response to naturalistic stimuli

is used to predict the brain responses within other subjects. Therefore, it is a model-free approach and is useful in measuring the synchronization across brains, induced by the real-life stimulus.

Here, in order to calculate the ISC of the empirical data, the time series from each ROI was initially extracted from the preprocessed fMRI data using the method described in **Sections 2.2.5** and **2.2.6**, and normalized between -1 and 1. Pearson correlations between every pair of subjects were calculated for each ROI using the formulae given in **Eq. 2.1** and then averaged (\bar{r}) over the number of pairs using **Eq. 2.2**.

$$r_{ij} = \frac{\sum_{n=1}^N [(S_i[n] - \bar{S}_i)(S_j[n] - \bar{S}_j)]}{\sqrt{\sum_{n=1}^N (S_i[n] - \bar{S}_i)^2 \sum_{n=1}^N (S_j[n] - \bar{S}_j)^2}} \quad (2.1)$$

$$\bar{r} = \frac{1}{\binom{m^2-m}{2}} \sum_{i=1}^m \sum_{j=2, j>i}^m r_{ij} \quad (2.2)$$

where r_{ij} is the correlation coefficient between the time series of the i^{th} and j^{th} subjects, N is the total number of samples in the time series, S_i and S_j are the time series obtained from i^{th} and j^{th} subjects, respectively, \bar{S}_i and \bar{S}_j denote the means of S_i and S_j and m is the total number of subjects (in our case, $m = 17$). Afterwards, a one-sample t -test using the r_{ij} values of each ROI was performed. Results of the t -tests were Benferroni corrected for multiple comparisons [22], with a significance level of $p < 0.01$ to acquire only the \bar{r} -values of the regions that were significantly different from zero. The ISC of the resting and task data was calculated for all four levels of consciousness, and plotted on a brain map using MATLAB.

2.2.9 Generalized Linear Modelling

Generalized Linear Modelling (GLM) was performed using the 18 audio features ($P(t)$) that survived the multicollinearity test as the independent variables, and the empirical time series as the dependent variable to obtain the coefficients. The coefficients represent the coupling of the external stimulus with the spin sites and we refer to the collective coefficients (84 in our case) of all the ROIs as the β -map. The GLM was repeated on all subjects' empirical data to obtain their β -maps for each audio features. A one-sample t -test was then performed on the audio features using the subjects' β -maps, to obtain the t -maps for each audio features separately. Only those t -values possessing a $p < 0.01$ were used to generate the external stimulus to be used in the GIM. The external stimulus for each condition (awake, mild sedation, deep sedation, recovery) was calculated via **Eq. 2.3**:

$$H_i(t) = \sum_{k=0}^{Np} P^k(t) t_i^k \quad (2.3)$$

where $H_i(t)$ is the external stimulus applied onto i^{th} region, Np is the total number of predictors (=18 in our case), t_i^k is the threshold t -value of the region i for the k^{th} predictor, obtained from the t -test among the β -values, $P^k(t)$ is the time series of the k^{th} predictor and $P^0 = 1$. This $H_i(t)$ was then used as the external stimulus while simulating the GIM.

2.2.10 Generalized Ising Model Simulation

The GIM used an initial 1-D random spin configuration with 84 spins in either the +1 or -1 state, and was in contact with a thermal bath of temperature T . The energy of the spin configuration during spontaneous activity (resting) and non-spontaneous activity (with external stimulus) are given by **Eqs. 2.4** and **2.5**, respectively:

$$E_{rest} = -\sum_{i,j;i \neq j}^N J_{ij} s_i s_j \quad (2.4)$$

$$E_{stim} = -\sum_{i,j;i \neq j}^N J_{ij} s_i s_j - \sum_i^N H_i(t) s_i \quad (2.5)$$

where J_{ij} is the coupling constant between the i^{th} and the j^{th} site (i.e., number of fibers connecting two regions, normalized between 0 and 1), S_i and S_j are the spins of the i^{th} and j^{th} site, and $N (=84)$ is the total number of spin sites. The J_{ij} was obtained from the averaged DTI data of 69 subjects from the Human Connectome Project. The Metropolis Monte Carlo (MMC) algorithm was employed to simulate the system. In order to minimize the energy of the spin configuration using the MMC algorithm, the following steps were performed: 1. A random initial configuration with 84 spins was generated and the initial energy (E_{in}) was calculated. 2. A randomly selected spin was flipped, and the new energy (E_{new}) was calculated. 3. If $E_{new} < E_{in}$, the spin flip was accepted, the new configuration became the new initial configuration with energy $E_{in} = E_{new}$, and the simulation was continued from step 2. 4. If $E_{new} > E_{in}$, the Boltzmann factor $B = \exp^{-\frac{\Delta E}{k_B T}}$ was calculated and a random number r between 0 to 1 was drawn. If $B > r$, the spin was accepted, E_{in} was replaced with E_{new} , and the procedure was repeated from step 2. Alternatively, if $B < r$, the flip was rejected, and the simulation was started over from step 2. These simulations were repeated from step 2 until an equilibrium condition with minimal fluctuations around the equilibrium energy was reached. Once the system was allowed to equilibrate, the equilibrium energy (E), magnetization (M) and susceptibility (χ) were calculated using **Eqs 2.4 – 2.7**:

$$M = \frac{1}{N} |\sum_{i=1}^N S_i| \quad (2.6)$$

$$\chi = \frac{1}{NT} [\langle M^2 \rangle - \langle M \rangle^2] \quad (2.7)$$

Simulation for one time-point in the GIM was considered equivalent after $N \times N \times 10$ (where N is the number of spins) number of flips had been performed. This number of flips confirmed that equilibrium had been reached [17, 21]. One-time point of the GIM was considered to be equivalent to 2 s (one time-point) of the audio clip, as $TR = 2$ s. By repeating these steps to

equal number of time points of fMRI data, each time confirming the equilibrium condition, the simulated time series were obtained.

To first assess the effect of an external stimulus with different coupling strengths, initially, the GIM was tested on the synthesized data. A sinusoidal wave with a frequency of 1/60 Hz and an amplitude of 0.1 was used as the external stimulus, with randomly generated coupling strengths (t -maps) with the range found from the empirical data (-13 to 13). Then, coupling terms were converted to positive values and the simulations were performed using the same parameters to test the effect of the signs of the coupling terms. Afterwards, the GIM was simulated with the real data for the resting ($H(t) \neq 0$) and task conditions ($H(t) \neq 0$) using the external stimulus $H(t)$ described in **Section 2.9**. This procedure was repeated for 250 different temperatures ranging from 0.025 to 6 (unit-less), and at each temperature, the thermodynamic properties such as the energy, magnetization and susceptibility were calculated. The simulations were performed 17 times, using different initial configurations to resemble 17 subjects, for all four levels of consciousness. Next, assuming that the temperature across the subjects was identical, the ISC was calculated on the generated time series for each of the 250 temperatures. The ISC maps calculated from the simulated time series were then plotted at the critical temperature (the temperature that maximized susceptibility), the sub- and super-critical temperatures, and the temperature that minimized the distance between the empirical and simulated ISC (i.e., the temperature that gave the best fit between the empirical and simulated ISC) which was calculated using Kolmogrove-Smirnov test (KS-test) statistic. The KS-test is a method employed to compare two distributions. To calculate the KS-statistic, cumulative functions of both empirical and simulated ISC were plotted in the same graph. Then the distance that minimized the maximum distance between these two plots was given by the KS-statistics. The temperature at which this happens was considered as our best fit

between the empirical and simulated ISC. Since we wanted to compare the pattern of the ISC rather than the actual values, ISC values were normalized such that the maximum was one, and the distance between these normalized ISC values were calculated.

The null distribution for the ISC was generated in two ways; 1) by randomly permuting the J_{ij} and simulating the GIM using the same coupling terms 2) by randomly permuting the coupling terms (beta-values) and simulating the GIM using the un-permuted j_{ij} . Then, to look at the effects in the ISC due to the alterations in both j_{ij} and coupling terms, Pearson correlation coefficients between the empirical ISC and simulated ISC at T^* were obtained.

2.2.11 Construction of Resting State Networks

Even at rest, the brain possesses synchronized regions that oscillate together in time. These regions collectively form the resting state networks (RSN). Although there are several RSNs consistently found in healthy subjects, we focused here on the auditory, default mode network (DMN), executive control network left (ECNL), and executive control network right (ECNR)—each being relevant to the perception of external stimuli [23]. The RSNs of the empirical data were constructed by using the average time series of the regions belonging to each network as the seed and calculating the correlation with all other regions, using their respective time series. These correlation values were then plotted on brain maps. The same procedure was then repeated on the simulated time series. Finally, t -tests were performed between the distributions of the correlation maps between different sedation levels, for each network, to assess the similarity or dissimilarity of the network between these sedation levels.

2.3 Results

First, the results of the synthetic data modeling are presented. Thermodynamic properties such as the energy, magnetization and susceptibility obtained from the average of five GIM simulations on the synthetic data (using sinusoidal external stimulus with random coupling values) are presented in **Fig. 2.1**. As expected, when the spins were positively coupled with the external field, the critical temperature shifted towards a higher value than the critical temperature at zero external field (resting state). Moreover, the critical temperature calculated when the spins were coupled both positively and negatively with the external field shifted to a lower value than that of the zero external field scenario.

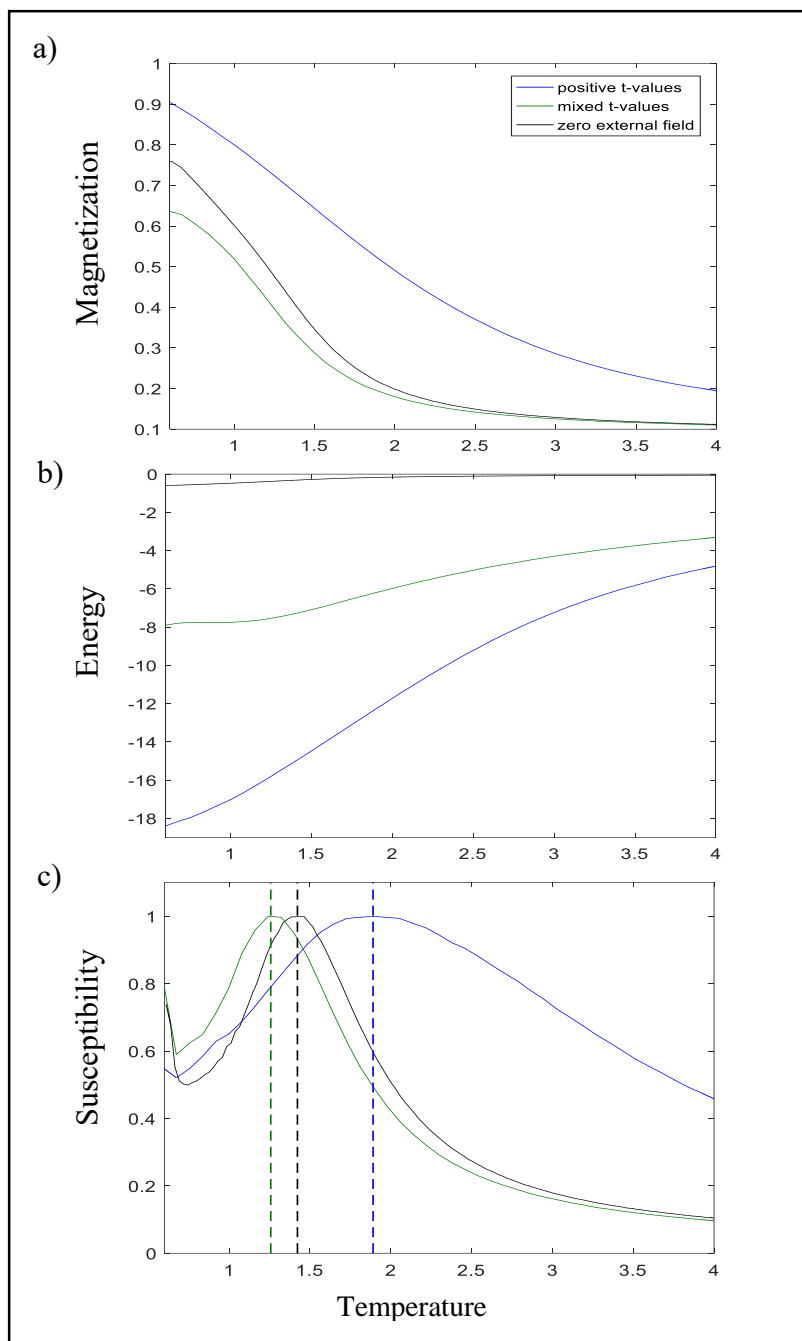


Fig. 2.1 Thermodynamic properties of the synthetic data a) Magnetization b) Energy
c) Normalized susceptibility

Results obtained from simulations using the empirical data are presented in the following sections **Fig. 2.2** displays the variation of the thermodynamic properties during rest and under stimulation for sedated and non-sedated conditions. Plotted values are the mean of 17 simulations along with their standard deviations. The standard deviation at rest is very small and cannot be seen in the plots.

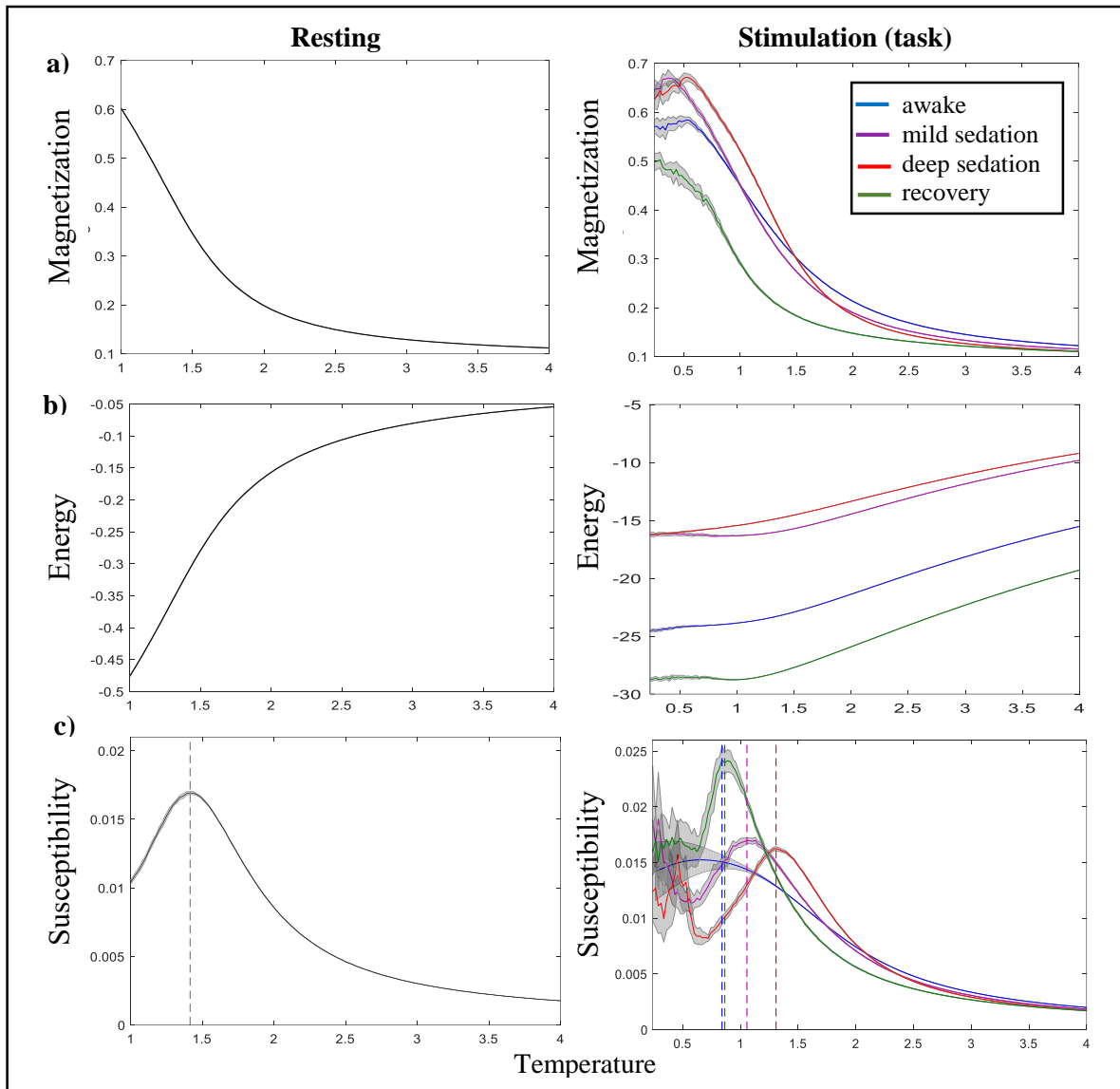


Fig. 2.2 Thermodynamic properties, a) Magnetization b) Energy c) Susceptibility calculated from the GIM during resting and under stimulation at four different levels of consciousness. The dashed lines represent the critical temperatures.

Critical temperatures in each condition were obtained using the maximum of the susceptibility curves shown in **Fig. 2.2** and are plotted in **Fig. 2.3**. Overall, the critical temperature during stimulation shifted towards lower temperature values compared to the resting condition. During stimulation, the critical temperatures increased from awake to mild sedation, and further increased from mild to deep sedation; it then decreased during recovery and reached similar critical value as that of the awake state. However, during all four levels of consciousness, the critical temperature at rest remained the same at a value of 1.41. At rest, T_c did not change, as it depended only upon the input J_{ij} . In contrast, under stimulation—although we still used the same J_{ij} —because we used different t -maps to describe the spins’ interaction with an external field, a change in T_c was observed for different levels of consciousness.

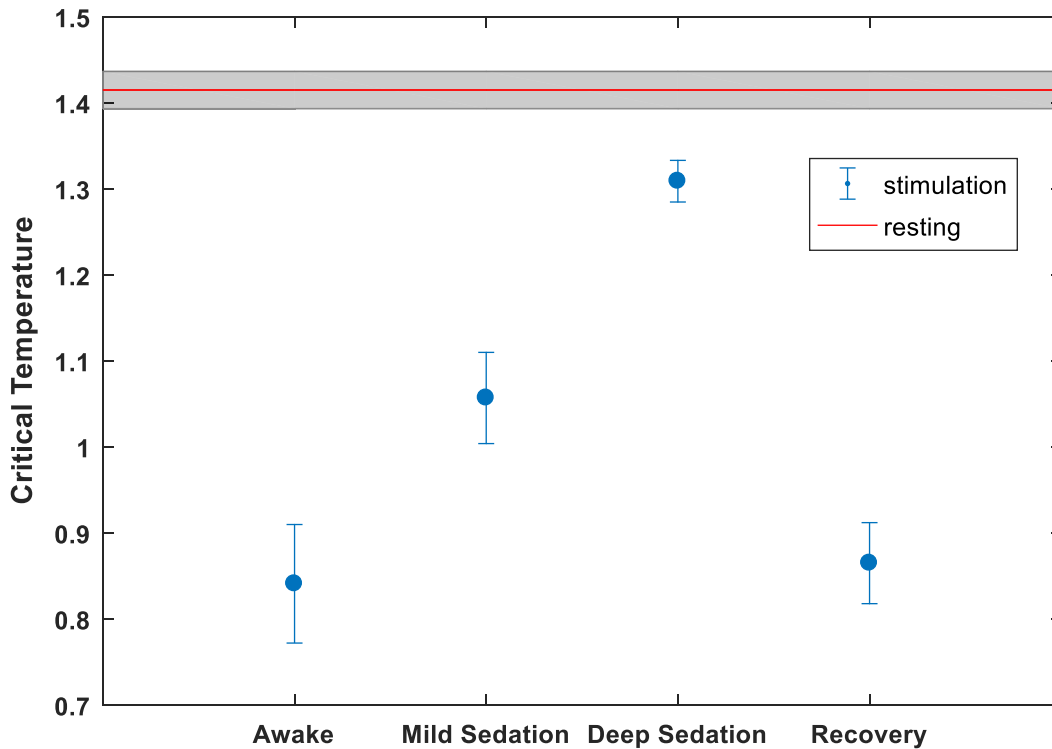


Fig. 2.3 Critical temperature variation during resting and under stimulation at four different levels of consciousness

Fig. 2.4 depicts the distance between the normalized empirical and normalized simulated ISC for the task data, calculated using the KS-test. The sub criticality ($T < T_c$), super criticality ($T > T_c$), and T_{min} (the temperature that minimizes the distance between the correlation matrices of empirical and simulated data) values are defined as published in Abeyasinghe et al. [21]. The criticality (T_c) is far lower than T^* , the value which minimizes the distance between the empirical and simulated ISC. From the results, we can conclude that in order to reach T^* , the system should be in a super critical state.

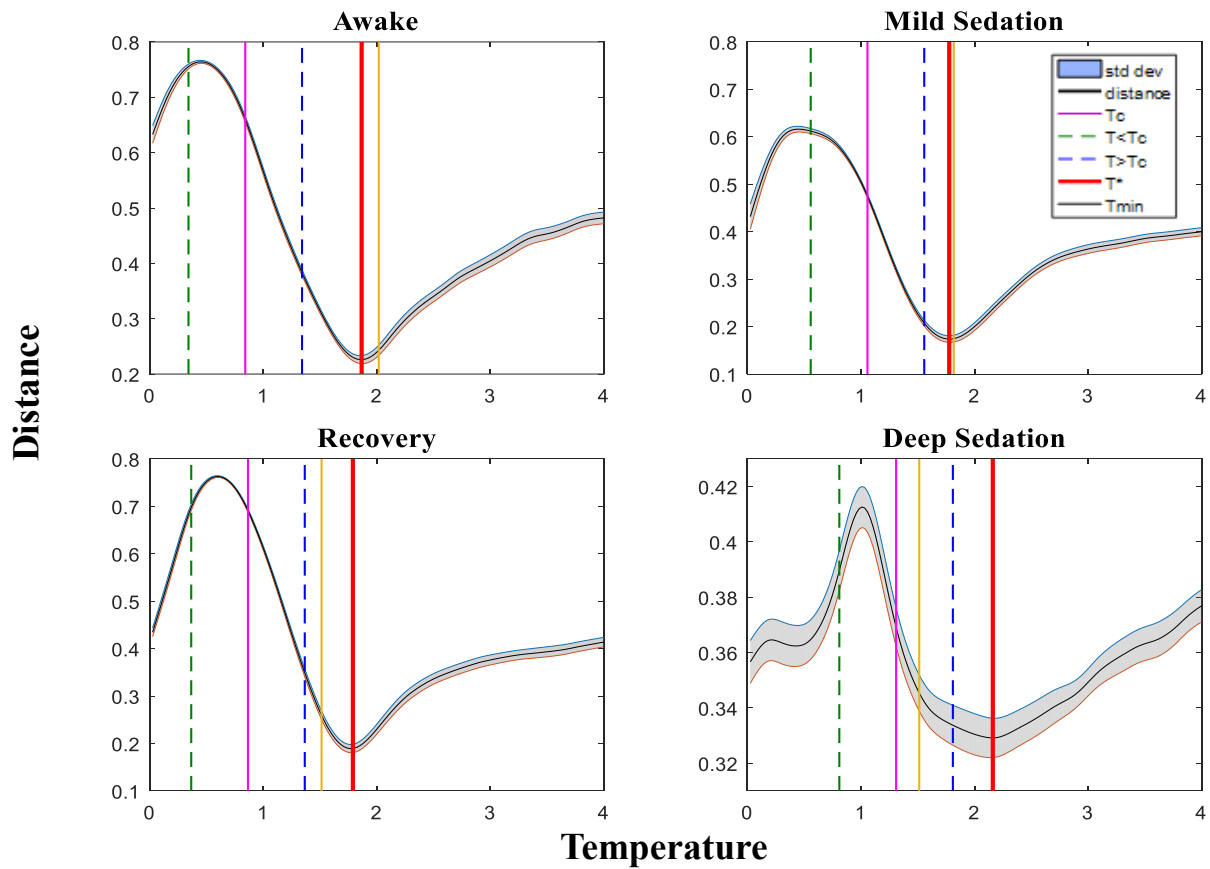


Fig. 2.4 Distance (calculated using the KS-test) between the normalized empirical and simulated ISC under stimulation, at four different levels of consciousness. The red line represents the temperature that minimized distance between normalized empirical and simulated ISC. Magenta, green dashed, and blue dashed lines represent the critical, sub, and super, critical temperatures, respectively, under stimulation. The black line (T_{min}) represents the temperature that minimizes the distance between the empirical and simulated correlation matrices.

To illustrate the correlation between the time series of subjects in a region of primary auditory cortex (ROI 29, left superior temporal gyrus), the empirical and simulated times series obtained from simulations at T^* of two subjects (subjects 1 and 3), in the awake condition are shown in **Fig. 2.5**. The synchronization between the time series of the empirical data during task is evident with a high correlation value ($r = 0.57$) as in **Fig. 2.5a** compared with the correlation in the resting data ($r = -0.18$) in **Fig. 2.5b**. Similar results were obtained in the simulated time series, with correlation values of 0.58 (**Fig. 2.5c**) and 0.10 (**Fig. 2.5d**) in the task and resting conditions respectively.

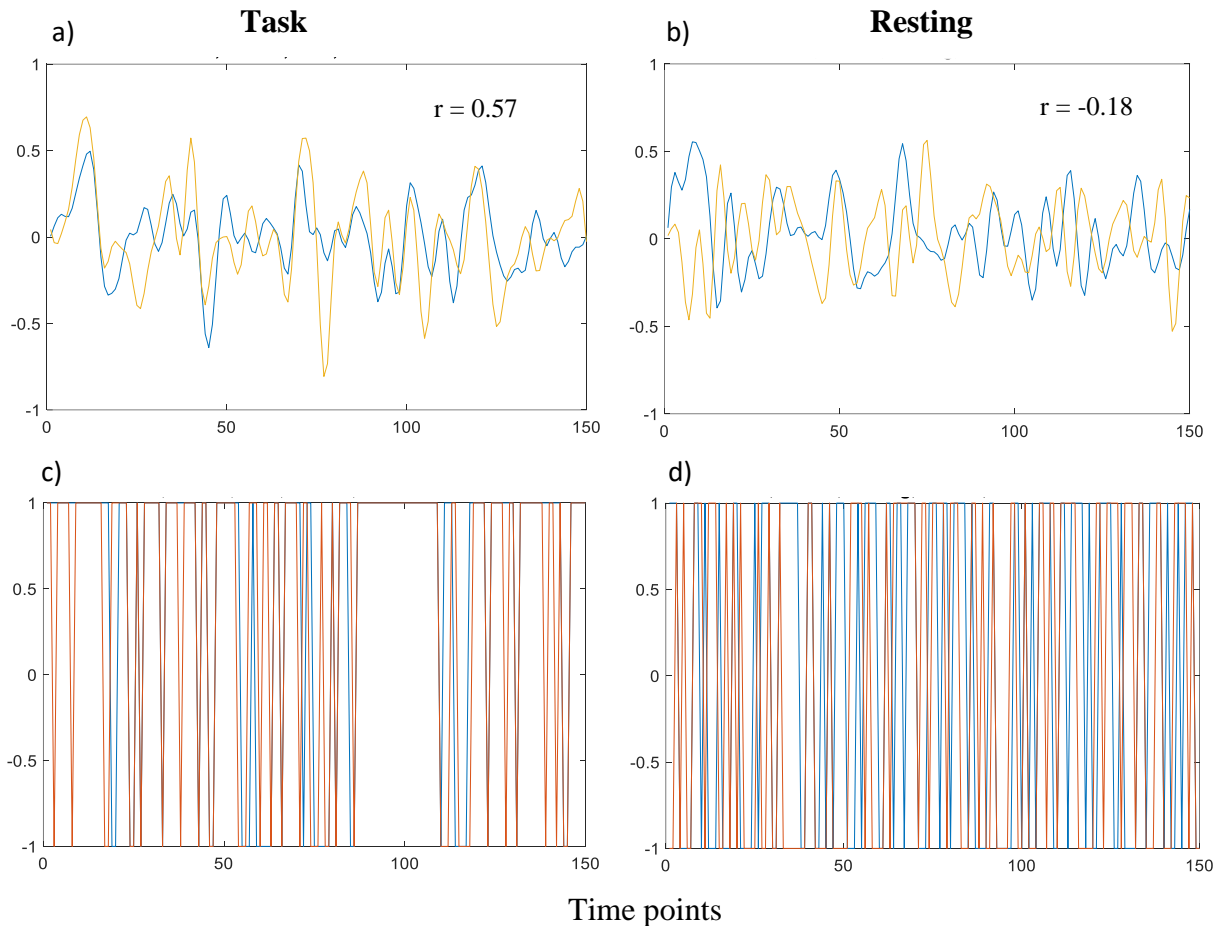


Fig. 2.5 Time series of subjects 1 and 3 for the ROI 29 (left superior temporal) in awake condition for the following data

a) empirical task b) empirical rest c) simulated at T^* for task d) simulated at T^* for rest

Fig. 2.6 shows the ISC obtained from the empirical data for all four levels of consciousness, while the subjects were listening to the audio clip. Overall, a clear pattern of synchronization, which decreased with levels of unconsciousness and increased during the recovery stage was seen, consistent with what has been found previously [24, 25]. In the awake condition, synchronization amongst participants' brain activity in the fronto-parietal, auditory and language areas was observed. Synchronization amongst participants in the frontal-parietal area diminished in the mild and deep sedation conditions, but returned back to its original level during recovery. However, synchronization in the auditory regions remained during unconsciousness, with lower values, similar to results found in prior studies [26]. Moreover, a paradoxical effect of an increase in synchronization was seen in the motor area of the left hemisphere during mild sedation. In contrast, synchronization amongst participants' brain regions was not observed at any levels of consciousness during the resting conditions (i.e., when not listening to the audio clip) and therefore was not reported.

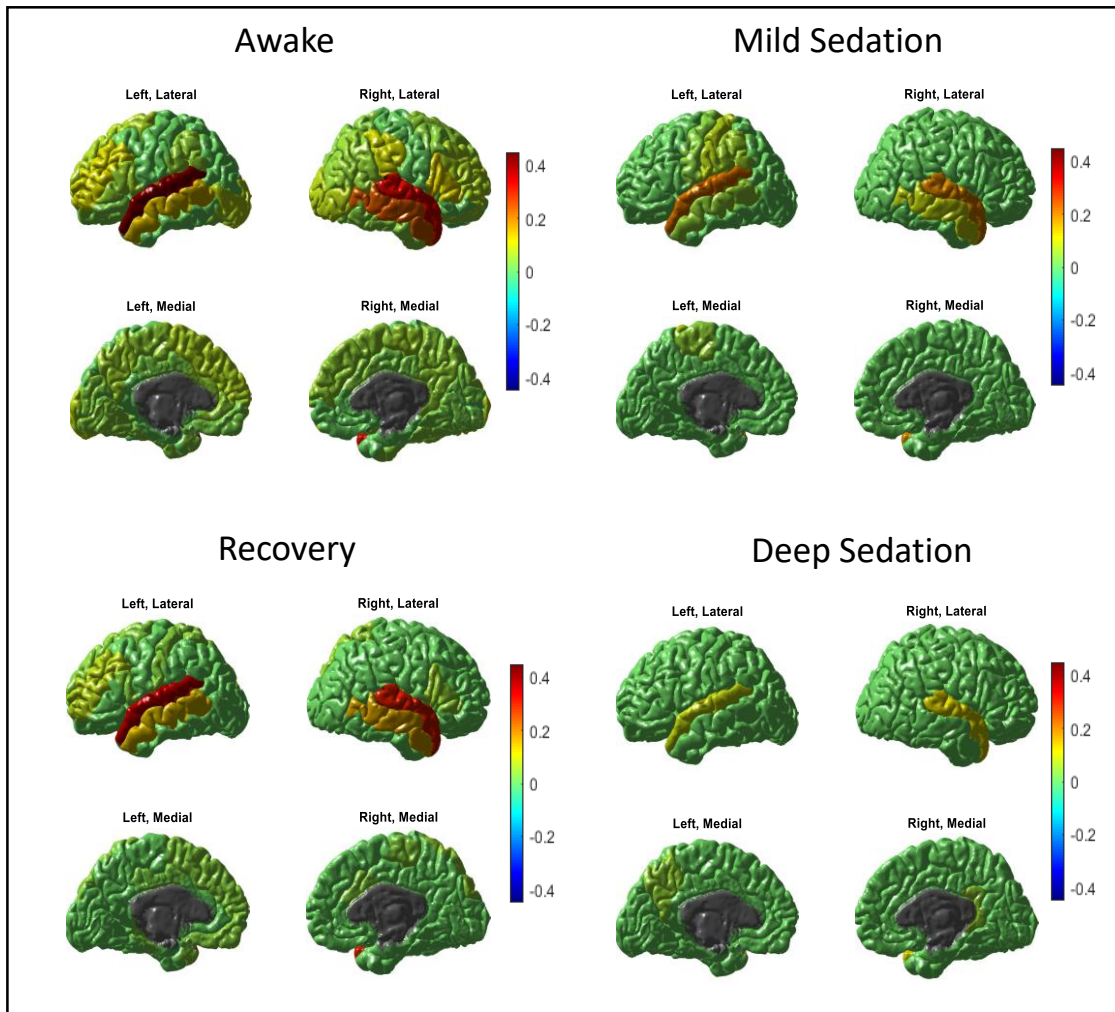


Fig. 2.6 ISC calculated from the empirical task data at four different levels of consciousness.

Fig. 2.7 shows the normalized 18 audio features extracted from the 5-minute audio clip of the movie “Taken” using pyAudio Analysis, along with the intensity of the original audio clip. These audio features were then used in the GLM to calculate the β -values and then finally the t -maps (**A.1**). From the **Fig. A.1**, it can be seen that some of the MFCCs (P8, P9, P11, P13) are properly capturing the auditory perception which was observed in the empirical data (**A.1**).

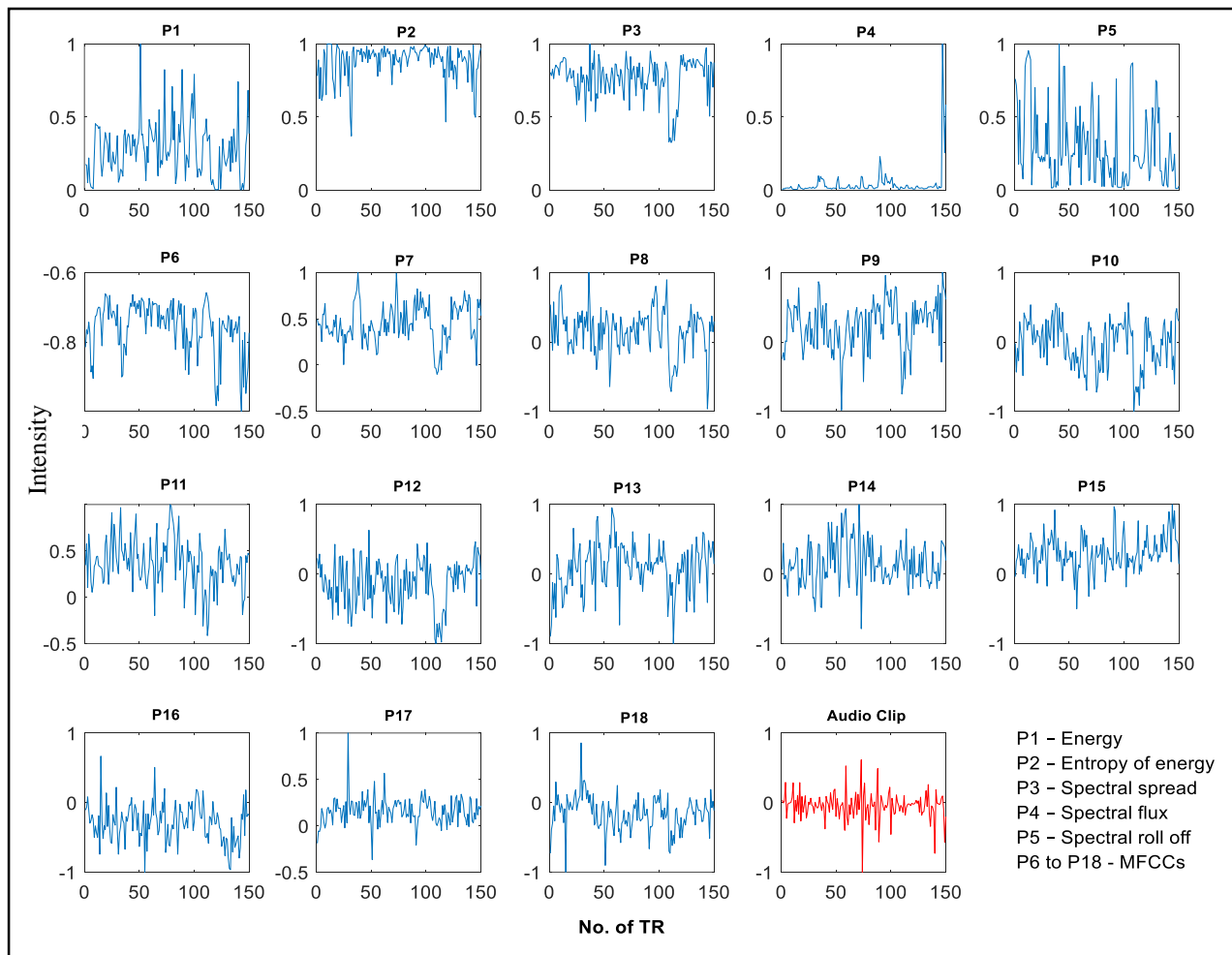


Fig. 2.7 Normalized audio features extracted from the audio clip using pyAudio Analysis and the original audio clip

The ISC calculated from the simulated data under auditory stimulation using the GIM in the awake, mild sedation, deep sedation, and recovery conditions are displayed in **Figs. 2.8 – Fig. 2.11** respectively. At all four levels of consciousness, at the sub-critical level, a full ISC is observed, as activity in most regions is synchronized among the subjects. A visual inspection shows that, at criticality the ISC increases, but then declines at super criticality; further, at a

temperature distant from criticality in the super critical regime (T^*), the pattern of the ISC of the simulated data closely resembled that of the empirical data. In the awake state (**Fig. 2.8**), the frontal-parietal and language regions activated in the empirical data are again synchronized at T^* . Further, in mild sedation (**Fig. 2.9**), at T^* , the paradoxical effect seen in the left hemisphere of the empirical data is also predicted in our model. Moreover, at T^* there were regions that showed synchronization among subjects that was not present in the empirical data. For example, in the simulated data, there was synchronization in the right inferior parietal in deep sedation (**Fig. 2.10**) and in primary somatosensory and motor areas in recovery (**Fig. 2.11**).

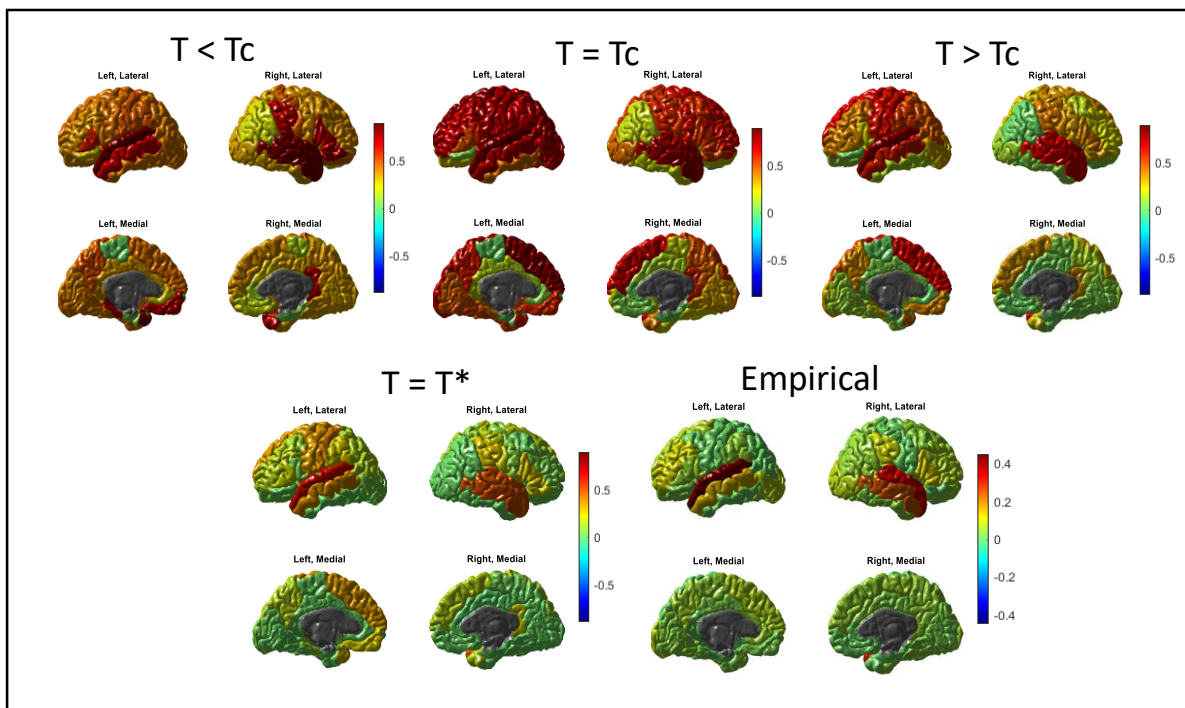


Fig. 2.8 ISC calculated from the simulated task data at the critical (T_c), sub- ($T < T_c$), and super- ($T > T_c$) critical temperatures and at the temperature that minimized the distance between the ISC of the empirical and simulated data (T^*) in the awake condition.

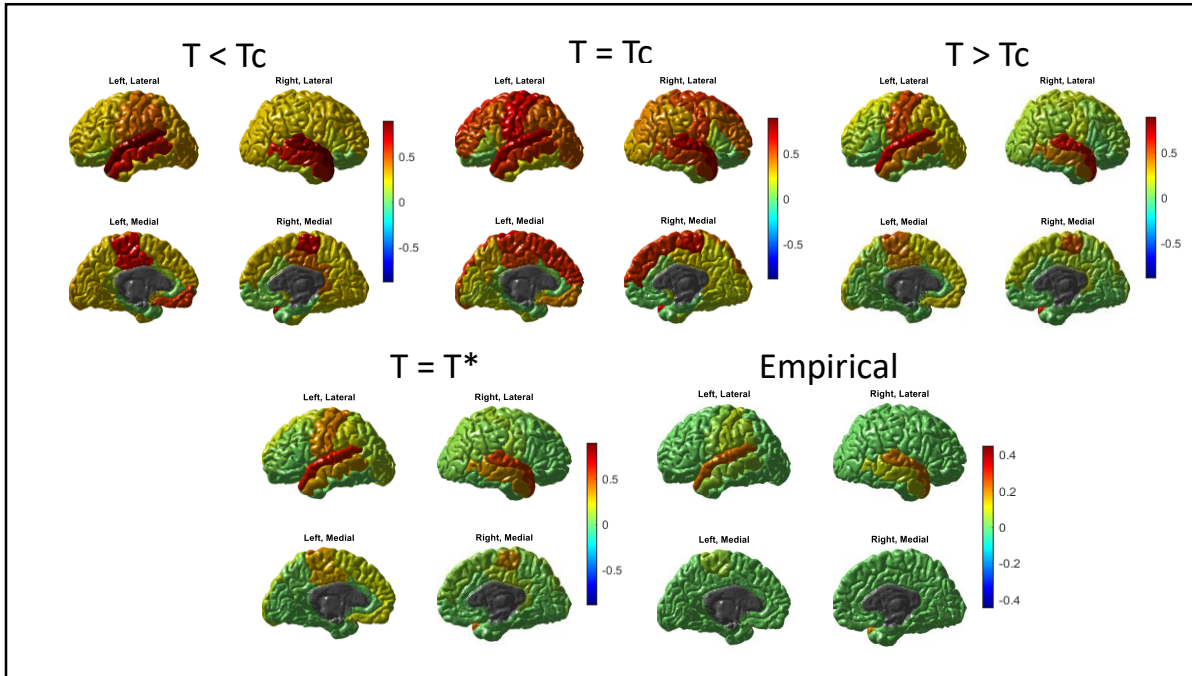


Fig. 2.9 ISC calculated from the simulated task data at the critical (T_c), sub- ($T < T_c$), and super- ($T > T_c$) critical temperatures and at the temperature that minimized the distance between the ISC of the empirical and simulated data (T^*) during mild sedation.

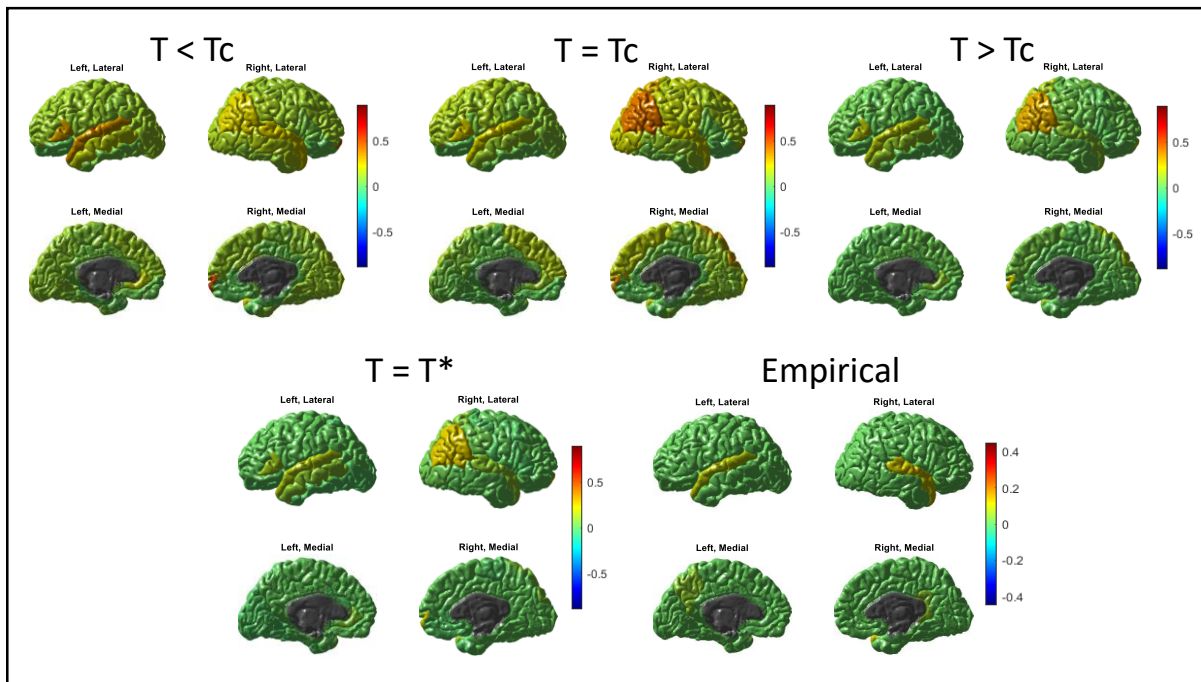


Fig. 2.10 ISC calculated from the simulated task data at the critical (T_c), sub- ($T < T_c$), and super- ($T > T_c$) critical temperatures and at the temperature that minimized the distance between the ISC of the empirical and simulated data (T^*) during deep sedation.

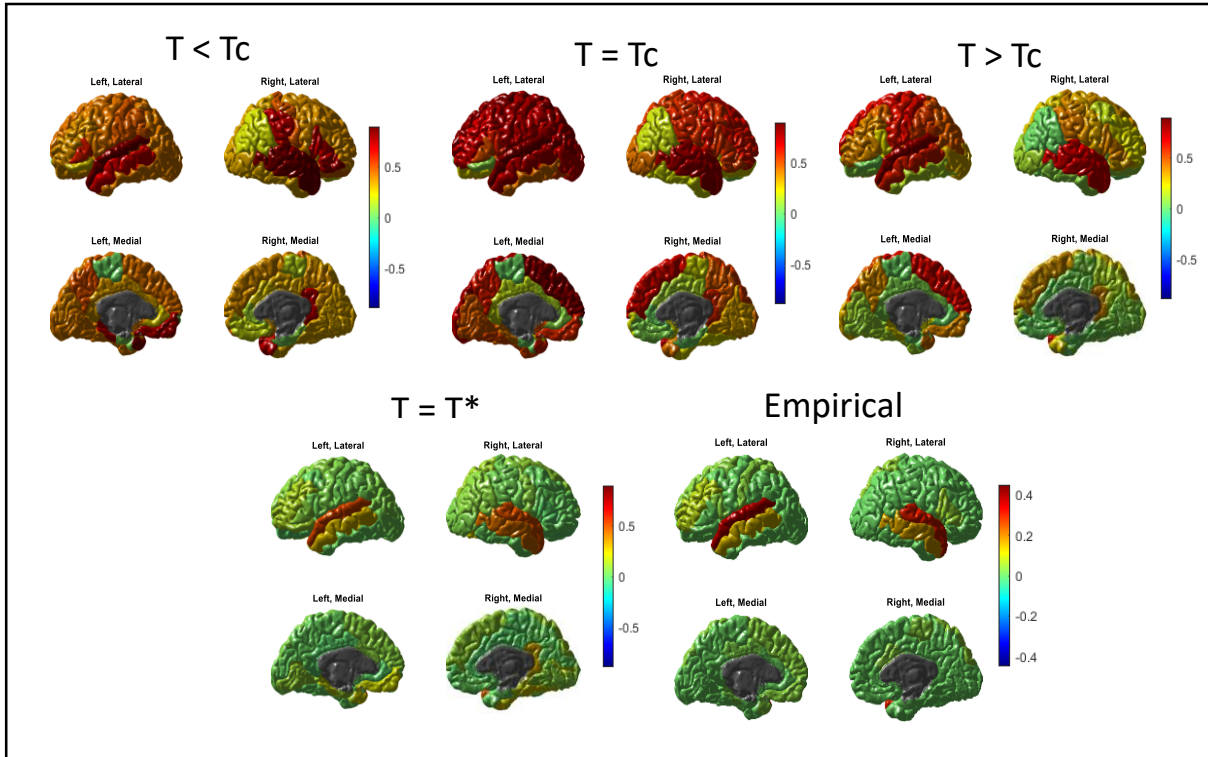


Fig. 2.11 ISC calculated from the simulated task data at the critical (T_c), sub- ($T < T_c$), and super- ($T > T_c$) critical temperatures and at the temperature that minimized the distance between the ISC of the empirical and simulated data (T^*) during recovery.

When the GIM was simulated using the permuted J_{ij} , and permuted coupling strengths obtained from the task condition, the temperature at which the best fit between the empirical and simulated ISC (T^*) varied from the original values, i.e. before permuting the J_{ij} and coupling terms. Correlation values calculated between the empirical ISC and simulated ISC at T^* in different conditions are shown in **Fig. 2.12**. It can be seen that, in all conditions, permuting beta values highly reduced the correlation values, while permuting the J_{ij} did not change much the correlation values. These results indicate that although a contribution from the j_{ij} is seen in the ISC, but the majority of the contribution comes from the coupling terms between the spins and the external field. Ideally having the scrambled data would have permitted to test the null distribution accurately using different coupling strengths obtained from these data.

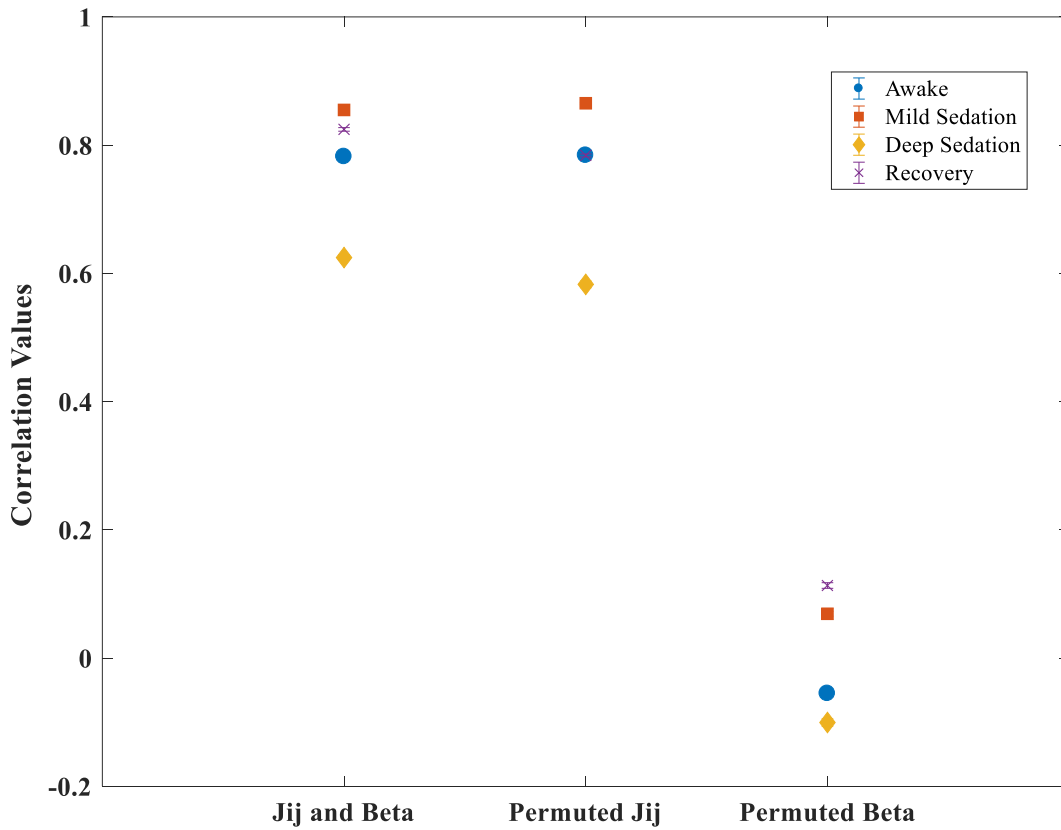
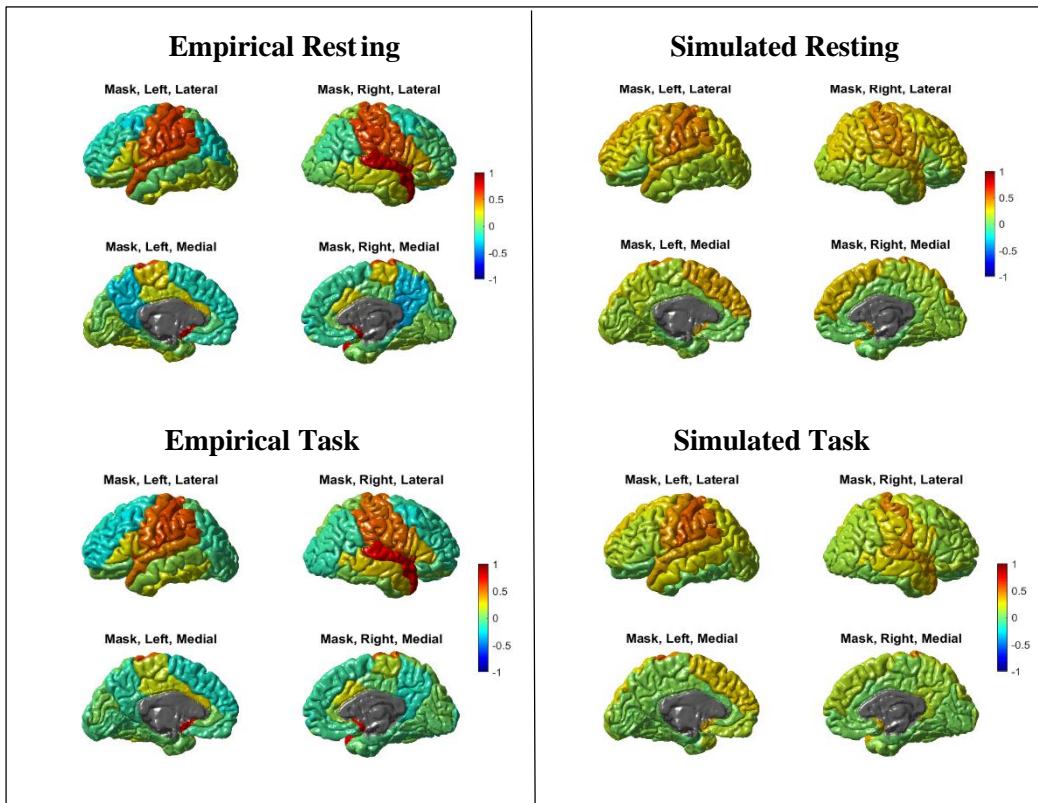


Fig. 2.12 Correlation values calculated between the empirical ISC and simulated ISC at T^* obtained from the GIM simulations performed using J_{ij} and beta values, permuted J_{ij} values and permuted beta values for the awake, mild sedation, deep sedation and recovery.

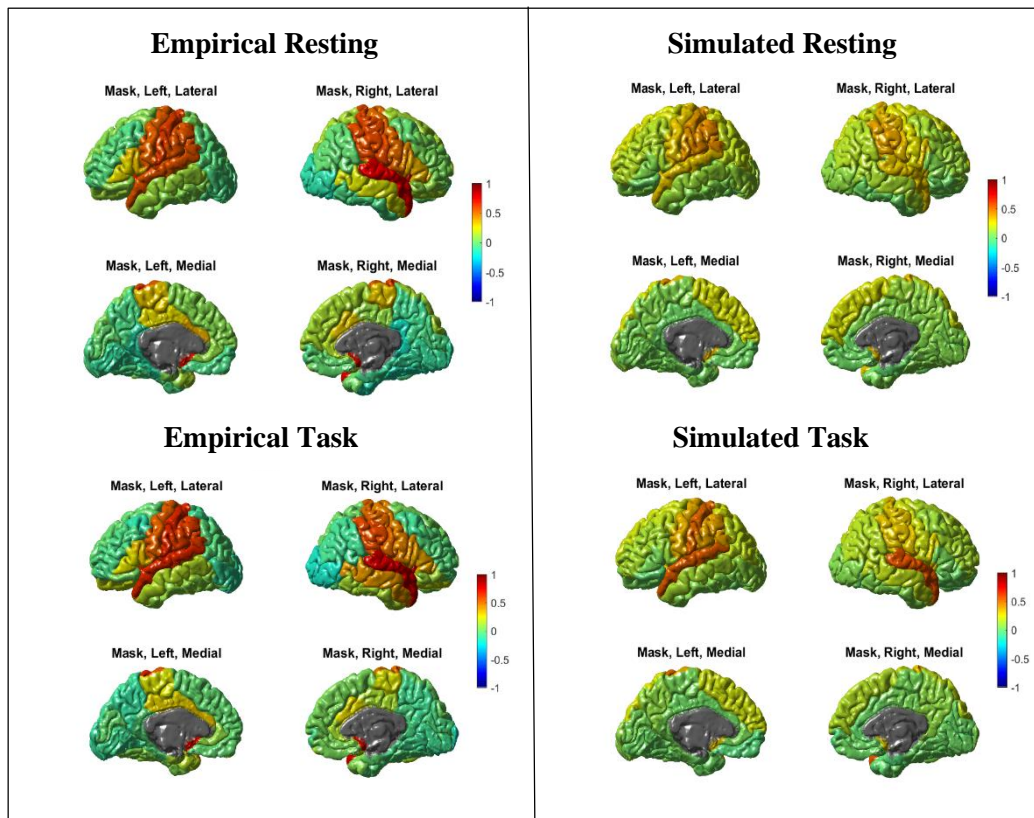
Although we were focusing on how the brain regions synchronize with each other, overall activity of the brain and how they vary between conditions can be observed from the functional connectivity. Functional connectivity describes how activity within different brain regions correlates. These fluctuations underlie ongoing brain activity during rest as well as the ability to perform a task. **Fig. 2.13** shows the auditory network extracted during the awake state, during mild sedation, during deep sedation, and during recovery using the empirical and simulated time series. The DMN, ECNL and ECNR networks are presented in the Appendix (A.2 – A.4). P -stats obtained

from the *t*-tests performed between the distributions of the correlation maps (which was used to build these RSNs), at different sedation levels are presented in **Table. 2.1**. There was no significant difference between the auditory network globally between any conditions (*p*-values are greater than or equal to 0.01), showing that the auditory network is not only globally preserved during rest, but also during stimulation, including when participants were anesthetized. The same scenario was observed for the other networks as well (**A.5 – A.7**).

a) **Awake**



b) **Mild Sedation**



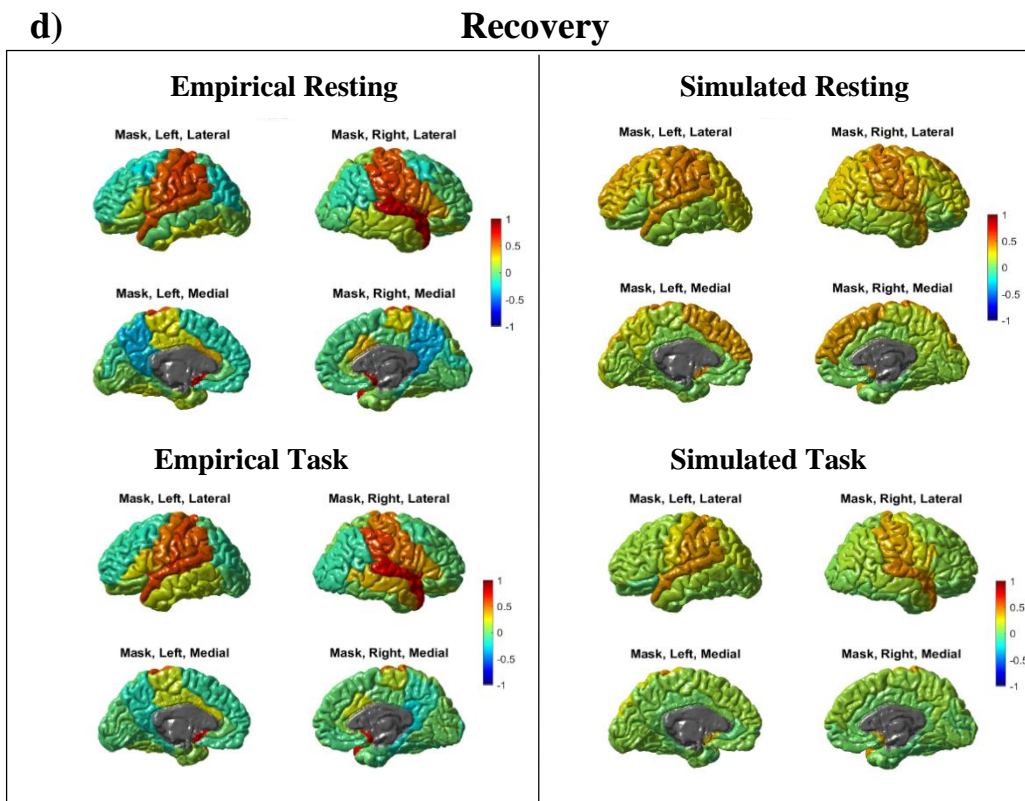
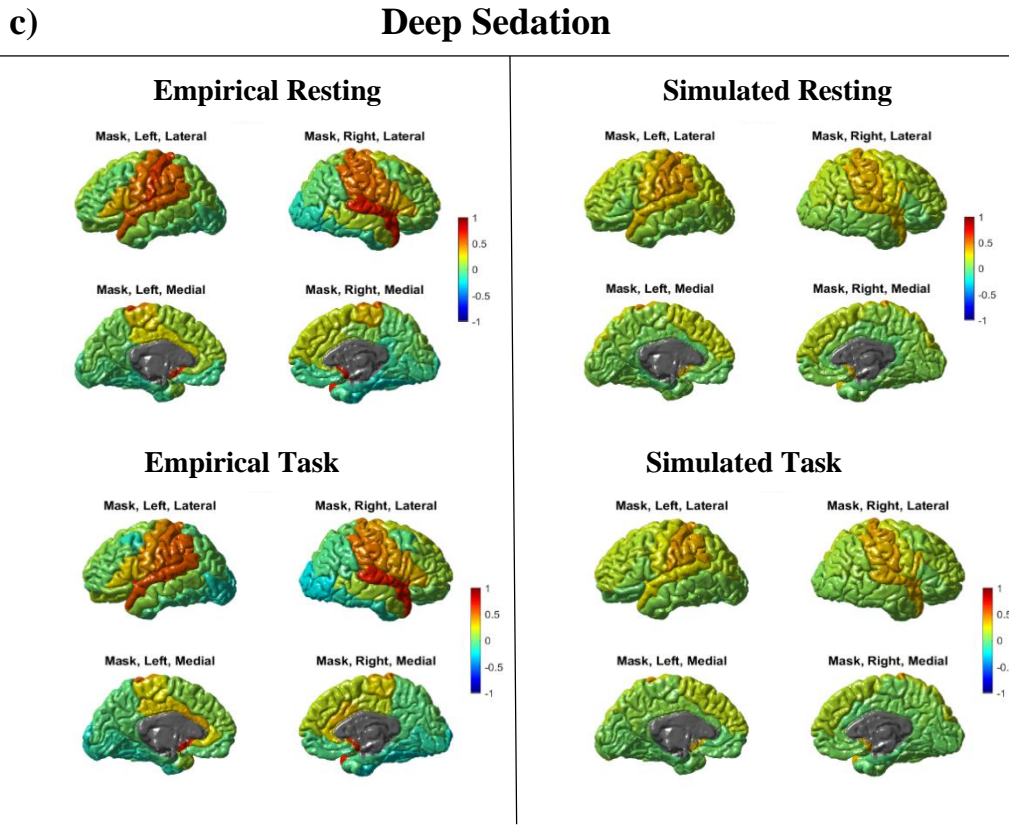


Fig. 2.13 Auditory network of empirical and simulated data at four different levels of consciousness. Networks for the simulated resting and simulated task data were constructed at T_{\min} and T^* respectively

Table 2.1: *P*-stats calculated from the *t*-tests performed between different levels of consciousness for the auditory network

Conditions	Empirical Resting	Empirical Task	Simulated Resting	Simulated Task
Awake vs. Deep Sedation	0.91	0.85	0.01	0.02
Awake vs. Mild Sedation	0.92	0.30	0.66	0.31
Awake vs. Recovery	0.98	0.86	0.77	0.15
Deep Sedation vs. Mild Sedation	0.99	0.38	0.04	0.29
Mild Sedation vs. Recovery	0.94	0.40	0.86	0.73
Deep Sedation vs. Recovery	0.93	0.99	0.02	0.46

2.4 Discussion

fMRI studies indicate that neuronal responses are more ecologically valid under naturalistic conditions than under conventional laboratory conditions using artificial stimuli [27]. Naturalistic paradigms, with the aid of engaging movies or narratives, capture and sustain attention more easily than artificial stimuli or task designs [6]. Therefore, we investigated the capability of the GIM to fit fMRI data obtained during a naturalistic audio listening task at different levels of consciousness as induced by propofol. The GIM was simulated using the Metropolis Monte Carlo algorithm to obtain equilibrium spin configurations when an external stimulus (i.e. an audio clip) was applied, and the ISC at different temperatures was calculated to find the best fit to the empirical ISC.

There are several constraints that can be applied to the coupling of the external field with the spins of the Ising model, which is not exactly what happens in the human brain. When an external field is positively coupled to the spins of the Ising model, all the spins will be coupled with the external field in the same direction (ferromagnetic). With the spins aligned in the same

direction, the system will become more ordered, and the critical temperature (the transition temperature from ordered to disordered) will shift to a higher temperature as shown in **Fig. 2.1**. analogous to previous studies [28, 29]. Conversely, when the spins are both positively and negatively coupled to the external field, the system tends to become disordered, shifting the criticality lower than the spontaneous (without stimulation) critical temperature as predicted in **Fig. 2.1**. Similarly, when the brain is stimulated with the audio signal in the real world, some of the features or predictors extracted from the audio signal tend to negatively couple to certain regions of the brain, while other predictors positively couple with some brain regions. This, in turn, moves the system towards a disordered state, shifting the criticality to a lower value as seen in **Fig. 2.2**. This may allow the brain to engage only on the necessary regions, and to respond to external stimulation in an effective way. In this case, external stimulation does not behave as a source of order—aligning all the spins in the system in one direction—but appears to behave as a source of disorder.

Under stimulation, critical temperatures during unconscious levels (deep sedation) moves close to the spontaneous criticality; and, conversely, during conscious levels, it moves away from spontaneous criticality towards a lower temperature (**Fig. 2.3**). When the external stimulus is presented during deep sedation, the system is less affected, and therefore remains closer to the spontaneous criticality, due to the low coupling strengths of the spins with the external stimulus. This is because the t -values are small and, therefore, the system resembles spontaneous activity, having a critical value significantly closer to that of the spontaneous situation (**Fig. 2.3**). On the other hand, t -values are bigger while in awake or in recovery during stimulation, and therefore push the system further away from spontaneous criticality, as depicted in **Fig. 2.3**. The effect of

the audio clip on the awake and recovery states is stronger than in the deep anesthesia, and the criticality can be considered as a measure of the engagement in the story.

Fraimann et al. [11] had stated that the brain functions at criticality in the awake condition during rest. However, an ongoing debate concerns whether the brain does indeed function at criticality, and some controversial results were reported by Bédard et al. [30], and Dehghani et al. [31], using recordings in animals and humans. They had performed avalanche dynamic (burst of neuronal activity) studies on humans, cats and monkeys using EEG, and had stated the lack of power-law scaling, a characteristic of critical behavior, in both awake and sleep states. Our results indicate that when an external stimulus is applied, dynamics show a departure from criticality towards the super-critical state as observed in **Fig. 2.4**. Temperature was used as a fitting parameter in order to match conditions in the real brain. Here, the T^* does not only depend on the input J_{ij} , but also depends on how the external stimulus couples with the spins. At resting state, T_c is a good approximation and T^* does not move much away from T_c , as there is no ISC. But under stimulation, the ISC constrains the model and T^* moves away from T_c to a higher temperature.

In the Ising model, temperature (T) acts like a thresholding mechanism to maximize the ISC between empirical and simulated data. As T is increased, spins that are mildly coupled with the external field lose their coupling, because the thermal energy provided by the temperature overcomes the interaction between the spins and the external field. This reduces the synchronization among the subjects. However, spins that are strongly coupled with the audio clip, for example spins corresponding to auditory regions, still retain their coupling with the field despite the increase in temperature. At T_c , most of the spins are coupled with the external field, producing a high synchronization on all spins amongst subjects, which is not reflective of

the empirical data. But at T^* , only the necessary spins are coupled to the external field, while the other spins are decoupled with the external field. This leads to synchronization in the necessary regions giving the best match with the empirical data. In all four conditions under stimulation, it became necessary to move away from criticality into the super-critical state to find the best match with the empirical task fMRI data (**Fig. 2.4**).

Changing the overall level of activity due to stimulation changes the sensitivity of neuronal inputs and, therefore, the brain may be dynamically moved into different states to adapt brain functions to momentary demands [32]. Moreover, some studies have proposed that an external time-varying input may give rise to power law avalanche distributions, and the larger networks can be restored when the avalanches within the modules are further pushed into the supercritical regime [33]. When the brain is exposed to a significant level of external input, self-tuning mechanisms of the brain might try to regulate the activity down. This will make the system to depart from criticality, in which the internally generated dynamics was optimized [32].

T -maps obtained from the GLM (**A.1**) show that some of the MFCCs are properly reproducing the auditory perception in varied levels of consciousness. MFCCs are frequency-smoothed log-magnitude spectra derived from a sinusoidal-based expansion of the energy spectrum, and demonstrate good representation of speech signals or of human hearing. These coefficients suppress undesirable spectral variation, particularly at higher frequencies, and therefore may be capturing useful acoustic properties related to auditory perception.

Primary auditory, language, and the fronto-parietal regions belonging to the executive control network appear to have strong ISC among the subjects during the awake and recovery states. These ISC values diminish during sedation (**Fig. 2.8 – Fig. 2.11**) in the empirical and simulated task data. However, in the sedated condition, ISC was present only in primary

auditory regions but with smaller values. This is consistent with these regions' roles in auditory perception and processing external information from the environment, such as listening to a story. Previous studies have shown decreased activity in the fronto-parietal network of anesthetized brains [26, 34]. Loss of information processing in the fronto-parietal regions reveals that complex auditory processing in the higher-order networks—such as the executive control network—is suppressed, but with a reduced amount of processing in the lower-order network—such as the auditory—during unconsciousness.

Moreover, to test whether the ISC is driven by the discernible narrative of the audio clip, it is essential to perform the ISC analysis on scrambled movie data. However, Naci et al. [26] and Dmochowski et al [35] have already reported that a lower ISC was observed for the scrambled version compared to the intact movie and it was limited to the bilateral auditory regions. This shows that the removal of the narrative's meaning leads to disengagement of the fronto-parietal executive network and have caused the reduction in synchrony or the ISC in these areas between the participants.

Spontaneous activity is very robust, and the functional connectivity of the RSNs is globally retained even when the brain is stimulated or anesthetized (**Fig. 2.13, Fig. A.2 – Fig. A.4**). Therefore, spontaneous activity alone cannot describe the effect of consciousness, as RSNs have been measured even in anesthesia. This provides support for the existence of a certain level of functional connectivity in anesthesia [36] and that the RSNs have little functional relevance on the level of consciousness. The brain is susceptible to stimulation without being overloaded, and returns to its original position after the stimulus is removed. Although we did not see a difference in the functional connectivity at different levels of consciousness in the stimulated case, we still see a difference in the ISC between these levels.

2.5 Conclusion

The GIM was able to model the brain activity under naturalistic stimulation, in different levels of consciousness, using a novel ISC technique. At the temperature T^* , which is in a very super critical state, a similar pattern between the empirical and simulated ISC was observed during stimulation. ISC was not observed in the resting condition at any levels of consciousness, due to the lack of the driving force provided by the external auditory stimulation for synchronization. Distinguishing neural signatures of altered consciousness using the simple GIM may aid in the diagnosis of patients with disorders of consciousness and can provide an indication of how their structural connectivity or coupling strengths should be altered in order to regain consciousness.

2.6 Future Work

The GIM with external stimulation is able to capture the brain activity of healthy subjects with different level of consciousness while performing a task. Driving brain activity with an external stimulus from real-world events (for example, listening to a movie) was shown to increase the common neural experiences amongst subjects, and can be used as a benchmark in assisting to the detection of the comparable conscious experiences which behaviourally unresponsive patients might have [16]. Additionally, studies have shown that differences between healthy and diseased individuals have also been linked to differences in the underlying structural connectivity of the brain [37].

In order to assess the awareness of coma and DOC patients, ISC (which is a measure of conscious experience) should be calculated. To attain this goal, the audio clip from the same movie should be played for patients and fMRI data should be acquired. Then GLM should be applied between the fMRI time series and the features of the movie (explained in **Section 2.2.9**) to obtain the coupling strengths (interaction of the external field with the spins). Afterwards, using disrupted

structural connectivities (J_{ij}) of these patients and the coupling strengths, GIM should be simulated to obtain the simulated time series at the temperature T^* which is obtained from the healthy subjects' simulations. Then the ISC map (set of ISC values of each ROI) of the patient can be obtained by calculating the correlation values between the subject's time series with all the 17 healthy subjects' time series and averaging them. These ISC values will give us an idea of how much the patient's time series is correlated with the healthy subjects.

To check the statistical significance of the ISC value of the patient, the null distribution can be created as follows. Time series of each healthy subject should be randomly permuted (shuffling the time points or phase shifting the time series) and the ISC values should be recalculated. This should be repeated 1000 times in order to get a distribution of ISC values for each ROI. The magnitude of the ISC value that fell in the 95th percentile of the null distributions (here termed the ISC_{th}) will represent the threshold for statistical significance of each ROI. Then the location of the ISC value of the patient within the null distribution can be determined. If the ISC falls left of the ISC_{th} , then we can conclude that the patient's ISC is significantly different from the healthy controls, and if not, the patient has an ISC value comparable to the healthy subjects [38]. The GIM will be useful in testing the changes occurring in the ISC values when the modified J_{ij} or altered coupling strengths is used, which cannot be done using only neuroimaging techniques. This might provide some useful information to the clinicians to assist in regaining the patient's consciousness.

Bibliography

- 1) Abreu, R., Leal, A., & Figueiredo, P. (2018). EEG-informed fMRI: a review of data analysis methods. *Frontiers in Human Neuroscience*, 12, 29.
- 2) Hudetz, A. G. (2012). General anesthesia and human brain connectivity. *Brain Connectivity*, 2(6), 291-302.
- 3) Will, U., & Berg, E. (2007). Brain wave synchronization and entrainment to periodic acoustic stimuli. *Neuroscience Letters*, 424(1), 55-60.
- 4) Hagihira, S. (2015). Changes in the electroencephalogram during anaesthesia and their physiological basis. *British Journal of Anaesthesia*, 115(suppl_1), i27-i31.
- 5) Tobias, J. D., & Leder, M. (2011). Procedural sedation: a review of sedative agents, monitoring, and management of complications. *Saudi Journal of Anaesthesia*, 5(4), 395.
- 6) Naci, L., Cusack, R., Anello, M., & Owen, A. M. (2014). A common neural code for similar conscious experiences in different individuals. *Proceedings of the National Academy of Sciences*, 111(39), 14277-14282.
- 7) Davis, M. H., Coleman, M. R., Absalom, A. R., Rodd, J. M., Johnsrude, I. S., Matta, B. F., Owen, A. M. & Menon, D. K. (2007). Dissociating speech perception and comprehension at reduced levels of awareness. *Proceedings of the National Academy of Sciences*, 104(41), 16032-16037.
- 8) Dueck, M. H., Petzke, F., Gerbershagen, H. J., Paul, M., Hesselmann, V., Girnus, R., Krug, B., Goebel, R., Lehrke, R., Sturm, V. & Boerner, U. (2005). Propofol attenuates responses of the auditory cortex to acoustic stimulation in a dose-dependent manner: A fMRI study. *Acta Anaesthesiologica Scandinavica*, 49(6), 784-791.
- 9) Liu, X., Lauer, K. K., Ward, B. D., Rao, S. M., Li, S. J., & Hudetz, A. G. (2012). Propofol disrupts functional interactions between sensory and high-order processing of auditory verbal memory. *Human Brain Mapping*, 33(10), 2487-2498.
- 10) Schaub, M. T., & Schultz, S. R. (2012). The Ising decoder: reading out the activity of large neural ensembles. *Journal of Computational Neuroscience*, 32(1), 101-118.

- 11) Fraiman, D., Balenzuela, P., Foss, J., & Chialvo, D. R. (2009). Ising-like dynamics in large-scale functional brain networks. *Physical Review E*, 79(6), 061922.
- 12) Marinazzo, D., Pellicoro, M., Wu, G., Angelini, L., Cortés, J. M., & Stramaglia, S. (2014). Information transfer and criticality in the Ising model on the human connectome. *PLOS One*, 9(4), e93616.
- 13) Stramaglia, S., Pellicoro, M., Angelini, L., Amico, E., Aerts, H., Cortés, J. M., Laureys, S. & Marinazzo, D. (2017). Ising model with conserved magnetization on the human connectome: Implications on the relation structure-function in wakefulness and anesthesia. *Chaos: An Interdisciplinary Journal of Nonlinear Science*, 27(4), 047407.
- 14) Deco, G., Senden, M., & Jirsa, V. (2012). How anatomy shapes dynamics: a semianalytical study of the brain at rest by a simple spin model. *Frontiers in Computational Neuroscience*, 6, 68.
- 15) Abeyasinghe, P. M., de Paula, D. R., Khajehabdollahi, S., Valluri, S. R., Owen, A. M., & Soddu, A. (2018). Role of dimensionality in predicting the spontaneous behavior of the brain Using the classical Ising model and the Ising model implemented on a structural connectome. *Brain Connectivity*, 8(7), 444-455.
- 16) Naci, L., Sinai, L., & Owen, A. M. (2017). Detecting and interpreting conscious experiences in behaviorally non-responsive patients. *Neuroimage*, 145, 304-313.
- 17) Marsh, B. M. W. M. N., White, M., Morton, N., & Kenny, G. N. C. (1991). Pharmacokinetic model driven infusion of propofol in children. *BJA: British Journal of Anaesthesia*, 67(1), 41-48.
- 18) Hagmann, P., Cammoun, L., Gigandet, X., Meuli, R., Honey, C. J., Wedeen, V. J., & Sporns, O. (2008). Mapping the structural core of human cerebral cortex. *PLOS Biology*, 6(7), e159.
- 19) Giannakopoulos, T. (2015). pyaudioanalysis: An open-source python library for audio signal analysis. *PLOS one*, 10(12), e0144610.
- 20) Hasson, U., Nir, Y., Levy, I., Fuhrmann, G., & Malach, R. (2004). Intersubject synchronization of cortical activity during natural vision. *Science*, 303(5664), 1634-1640.
- 21) Pajula, J., Kauppi, J. P., & Tohka, J. (2012). Inter-subject correlation in fMRI: method validation against stimulus-model based analysis. *PLOS One*, 7(8), e41196.

- 22) McDonald, J. H. (2009). *Handbook of Biological Statistics*, Baltimore, MD: Sparky House Publishing, 2, 6-59.
- 23) Kandeepan, S., Maudoux, A., de Paula, D. R., Zheng, J. Y., Cabay, J. E., Gómez, F., Chronik, B. A., Ridder, D., Vanneste, S. & Soddu, A. (2019). Tinnitus distress: a paradoxical attention to the sound? *Journal of Neurology*, 1-11.
- 24) Boveroux, P., Vanhaudenhuyse, A., Bruno, M. A., Noirhomme, Q., Lauwick, S., Luxen, A., Degueldre, C., Plenevaux, A., Schnakers, C., Philips, C., Brichant, J. F., Bonhomme, V., Maquet, P., Greicius, M. D., Laureys, S. & Boly, M. (2010). Breakdown of within-and between-network resting state fMRI connectivity during propofol-induced loss of consciousness. *Anesthesiology*, 113(5), 1038 – 53.
- 25) Jordan, D., Ilg, R., Riedl, V., Schorer, A., Grimberg, S., Neufang, S., Omerovic, A., Berger, S., Untergehrer, G., Preibisch, C., Schuster, T., Schroter, M., Spoomaker, V., Zimmer, C., Hemmer, B., Wohlschlager, A., Kochs, E. F., Schneider, G. & Schulz, E. (2013). Simultaneous electroencephalographic and functional magnetic resonance imaging indicate impaired cortical top-down processing in association with anesthetic-induced unconsciousness. *The Journal of the American Society of Anesthesiologists*, 119(5), 1031-1042.
- 26) Naci, L., Haugg, A., MacDonald, A., Anello, M., Houldin, E., Naqshbandi, S., Gonzalez-Lara, L. E., Arango, M., Harle, C., Cusack, R. & Owen, A. M. (2018). Functional diversity of brain networks supports consciousness and verbal intelligence. *Scientific Reports*, 8(1), 13259.
- 27) Hasson, U., Malach, R., & Heeger, D. J. (2010). Reliability of cortical activity during natural stimulation. *Trends in Cognitive Sciences*, 14(1), 40-48.
- 28) Arumugam, S., Mydeen, K., Fontes, M., Manivannan, N., Vanji, M. K., RamaTulasi, K. U., Ramos, S. M., Saitovitch, E. B., Prabhakaran, D. & Boothroyd, A. T. (2005). Effect of pressure and magnetic field on bilayer La₁.₂₅Sr₁.₇₅Mn₂O₇ single crystal. *Solid State Communications*, 136(5), 292-296.
- 29) Bałanda, M., Dubiel, S. M., & Pełka, R. (2017). Magnetism of a sigma-phase Fe₆₀V₄₀ alloy: Magnetic susceptibilities and magnetocaloric effect studies. *Journal of Magnetism and Magnetic Materials*, 432, 430-436.

- 30) Dehghani, N., Hatsopoulos, N. G., Haga, Z. D., Parker, R., Greger, B., Halgren, E., Cash, S. S. & Destexhe, A. (2012). Avalanche analysis from multielectrode ensemble recordings in cat, monkey, and human cerebral cortex during wakefulness and sleep. *Frontiers in Physiology*, 3, 302.
- 31) Bedard, C., Kroeger, H., & Destexhe, A. (2006). Does the 1/f frequency scaling of brain signals reflect self-organized critical states?. *Physical Review Letters*, 97(11), 118102.
- 32) Hesse, J., & Gross, T. (2014). Self-organized criticality as a fundamental property of neural systems. *Frontiers in Systems Neuroscience*, 8, 166.
- 33) Dahmen, D., Grün, S., Diesmann, M., & Helias, M. (2019). Second type of criticality in the brain uncovers rich multiple-neuron dynamics. *Proceedings of the National Academy of Sciences*, 116(26), 13051-13060.
- 34) Boly, M., Moran, R., Murphy, M., Boveroux, P., Bruno, M. A., Noirhomme, Q., Ledoux, D., Bnhomme, V., Brichant, J. F., Tononi, G., Laureys, S. & Friston, K. (2012). Connectivity changes underlying spectral EEG changes during propofol-induced loss of consciousness. *Journal of Neuroscience*, 32(20), 7082-7090.
- 35) Dmochowski, J. P., Sajda, P., Dias, J., & Parra, L. C. (2012). Correlated components of ongoing EEG point to emotionally laden attention—a possible marker of engagement?. *Frontiers in Human Neuroscience*, 6, 112.
- 36) Heine, L., Soddu, A., Gómez, F., Vanhaudenhuyse, A., Tshibanda, L., Thonnard, M., Charland-Verville, V., Kirsch, M., Laureys, S. & Demertzi, A. (2012). Resting state networks and consciousness. *Frontiers in Psychology*, 3, 295.
- 37) Johansen-Berg, H., Scholz, J., & Stagg, C. J. (2010). Relevance of structural brain connectivity to learning and recovery from stroke. *Frontiers in Systems Neuroscience*, 4, 146.
- 38) Laforge, G. (2017). Identifying Electrophysiological Components of Covert Awareness in Patients with Disorders of Consciousness. *Electronic Thesis and Dissertation Repository*, 4883.

Chapter 3

Tinnitus Distress: A Paradoxical Attention to the Sound?

3.1 Introduction

Tinnitus is defined as the perception of sound in the absence of any external sound source [1]. About 25% of the adult population has experienced one or more acute tinnitus episodes and about 8% reports having daily or permanent tinnitus [2]. Although some patients benefit from audiological, psychological, pharmacological, or surgical therapies, a large fraction of tinnitus patients are left untreated and waiting for a treatment that would offer permanent relief [3]. Having a good understanding of the underlying neurophysiological mechanism of tinnitus is crucial for the development of specific treatments.

It is known that peripheral lesions in the cochlea or the auditory nerve produce dysfunctional input to central auditory structures and induce changes in the auditory system [4-11]. Associated with plastic changes in central auditory structures, extra-auditory regions have been implicated in the tinnitus pathophysiology [4, 8, 12, 13]. Recently, it has been proposed that the unified percept of tinnitus could be considered an emergent property of multiple, overlapping dynamic brain networks, each encoding a specific tinnitus characteristic [4]. Indeed, more and more researchers suggest that the cortex is organized into parallel, segregated systems of networks that are specialized for processing distinct forms of information [14].

Initially, functional brain imaging methods emphasized task-induced increases in regional brain activity associated with the execution of a wide variety of tasks. More recently, however, a great interest has been developed in the study of the functional organization of the brain at rest [15, 16]. Spontaneous activity in the human brain was detected by Hans Berger in 1924 [17] using

EEG. Indeed, being at rest does not mean that the brain is silent. In fact, during rest, the low frequency fluctuations of the BOLD signal between brain regions, or spontaneous activity, obtained from fMRI indicate ongoing information processing [18]. Associations of regions with synchronous activity are commonly called resting state networks and consist of areas of cortex with a well-defined spatial distribution consistently recognized in healthy awake subjects. Recent comprehensive surveys have shown that resting brain dynamics can be broken down into a relatively small set of consistently found resting-state networks (RSNs) [19,20]. Example of RSNs are: Auditory Network (Aud), Default Mode Network (DMN), Executive Control Network Left (ECNL), Executive Control Network Right (ECNR), Salience Network (Sal), Sensorimotor Network (Sen) and the three visual networks (Lateral, Medial and Occipital).

Regarding tinnitus, preliminary evidence using EEG [21, 22], MEG [10], and PET [23] has indicated that certain clinical characteristics are correlated to certain brain area activations. Specifically, Vanneste et al. [21] in an EEG study found differences in brain connectivity between unilateral and bilateral tinnitus patients in the areas of parahippocampal, angular gyrus, superior premotor cortex and ventrolateral prefrontal cortex. In a second EEG study performed on a group of left-sided narrow-band noise tinnitus patients [22], the same group found that the neural generators of tinnitus changes over time, mostly with increased activity in the auditory cortex, dorsal anterior cingulate cortex, insula and premotor cortex. In an investigation performed using MEG on tinnitus patients [10], it was reported that not only auditory network, but a global tinnitus network which consists of long range cortical connections outside the central auditory system, is responsible for tinnitus. In a PET study on chronic tinnitus patients, it was observed that tinnitus duration and distress were positively correlated with regions involved in attentional and emotional processing [23]. These findings have been further confirmed by an fMRI study, focusing on the

auditory resting-state network demonstrating a positive correlation between the connectivity in the posterior cingulate/precuneus region and a behavioral measurement of tinnitus, the tinnitus handicap inventory (questionnaire to identify, quantify and evaluate the difficulties patients might experience due to tinnitus) [24]. These results have provided some insight into the role of network interaction in the emergence of clinical tinnitus characteristics. To date, the literature lacks a study that specifically addresses the issue of whether tinnitus is an emergent property of dysfunctional interactions within and between networks and whether these dysfunctional network interactions could be related to specific clinical characteristics. If the modification of connectivity leads to the tinnitus percept, a correlation between the strength of the functional inter-regional connectivity and clinical characteristics of tinnitus (e.g. tinnitus distress) should be found. This study addresses this supposition.

The aim of the present study was to investigate the neuronal activation patterns associated with clinical tinnitus characteristics (age, distress, loudness, intensity, duration and hearing loss). We hypothesized that tinnitus clinical characteristics would be associated with specific resting-state activity and functional connectivity patterns and that this could be tested by looking at the spontaneous brain activity of 135 tinnitus patients using resting state fMRI. All tinnitus subjects also received an in depth clinical evaluation.

Additionally, we wanted to see whether the pathology is related solely to the auditory network or to higher order networks responsible for auditory perception. To investigate this, we combined an individual independent component analysis (ICA) with an automated component selection method to select nine components of interest to be used in a second level analysis. We performed stepwise fit analysis to identify the correlation between different tinnitus characteristics and the graph strengths of the functional connectivity pattern of five resting-state networks (Aud,

DMN, ECNL, ECNR and Sal) relevant to tinnitus (out of these nine different networks) [4, 24, 25, 33, 36, 37]. For each resting-state component, the statistical analysis was not restricted to regions that are part of each network of interest but to the full brain.

Stepwise regression is a method of fitting regression models in which the choice of explanatory variables is carried out by an automatic procedure to obtain the set of variables resulting in the best predictive model. In each step, an explanatory variable is considered for addition to or subtraction from the set of explanatory variables based upon statistical criteria. The stepwise procedure either adds the most significant variable (smallest p -value, which should be smaller than the threshold for entrance) such that it will significantly improve the fit or removes the least significant variable (largest p -value, which should be greater than the threshold for exiting) such that the removal gives the most statistically insignificant deterioration of the model fit. P -values are the values that would be achieved if each variable was the single explanatory variable in a simple regression model. Stepwise fit regression allows multicollinearity to a certain extent (variation inflation factor < 5) [26], where the severity of multicollinearity can be tested using a function called “variation inflation factor” (VIF). VIF provides a measure of how much the variance of a regression coefficient is increased due to collinearity.

3.2 Methods

3.2.1 Participants

We assessed 135 tinnitus patients (41 women; mean age 50 years, SD = 15) (**B.1**). Audiological and clinical examinations were performed. Hearing levels were assessed using audiological testing. Pure tones ranging from 250 Hz to 12.5 kHz were presented to each ear until the threshold of detection was reached. They were also asked to identify the best match to the perceived intensity of their tinnitus; the intensity was corrected for the hearing threshold measured

for the according frequency. Self-reported severity of tinnitus impact was measured using the Tinnitus Questionnaire (TQ) [27]. We asked the tinnitus patients to score the tinnitus intensity they experienced on a numeric rating scale, ranging from 0 (none) to 10 (loudest imaginable tinnitus). Exclusion criteria were contraindication for MRI (e.g. presence of ferromagnetic aneurysm (bulge created in the artery due to weakening of an artery wall) clips, pacemakers), hyperacusis (hearing disorder due to increased sensitivity to certain frequencies) or phonophobia (fear to sounds). All patients were free of major neurological, neurosurgical or psychiatric history. The study was approved by the Ethics Committee of the Antwerp University Hospital. Informed consent to participate in the study was obtained from the patients.

3.2.2 fMRI Data Acquisition and Preprocessing

In all patients, functional MRI time series were acquired on a 3T head-only scanner (Siemens Trio, Siemens Medical Solutions, Erlangen, Germany) operated with a standard transmit-receive quadrature head coil. Two hundred multislice T2*-weighted functional images were acquired with a gradient-echo echo-planar imaging sequence using axial slice orientation and covering the whole brain (50 slices; voxel size: $2.5 \times 2.5 \times 2.8 \text{ mm}^3$; matrix size $80 \times 80 \times 50$; repetition time = 3000 ms; echo time = 30 ms; flip angle = 90° ; field of view = $200 \times 200 \text{ mm}^2$). The three initial volumes were discarded to avoid T1 saturation effects. For anatomical reference, a high-resolution T1-weighted image was acquired for each subject (T1-weighted 3D magnetization-prepared rapid gradient echo sequence). Initially, structural and functional data were manually coregistered into standard stereotactic Montreal Neurological Institute (MNI) space. They were then entered into an automatic pipeline in GraphICA (BraiNet - Brain Imaging Solution Inc. - Sarnia, ON, Canada), which included further minute realignment and adjustment for movement-related effects, noise spikes, and spontaneous deep breaths (using ArtRepair toolbox for SPM

(<http://cibsr.stanford.edu/tools/ArtRepair/ArtRepair.htm>) [28]. In GraphICA, fine coregistration, segmentation of the structural data, spatial and functional normalization into standard stereotactic MNI space and spatial smoothing with a Gaussian kernel of 8 mm full-width at half-maximum of the fMRI data are performed as implemented in SPM8.

3.2.3 Extraction and Identification of Resting State Networks

For the RSN identification we used a multiple template matching method which is inbuilt in GraphICA [28]. Initially, the fMRI signal was decomposed into sources of neuronal/physiological origin using ICA, which aims to decompose the signal into a set of statistically independent components (ICs) and their associated time courses [29]. In ICA each spatial map (IC) has an associated time course, which corresponds to the common dynamic exhibited by this component. The component images (spatial maps) were calibrated to the raw data so the intensity values were in units of percent signal change (PSC) from the mean [30]. For the ICA decomposition we used 30 components and the infomax algorithm as implemented in Group-ICA of fMRI toolbox (RRID: SCR-001953; <http://mialab.mrn.org/software/gift/>).

After the ICA decomposition, the nine different RSNs were identified at an individual level. For this, we ran a single subject ICA, and the set of ICs that maximized the goodness-of-fit (absolute value of average voxels falling within the template minus the average voxels outside the template) with a set of predefined binary RSN templates while considering all the RSNs simultaneously was selected [31]. The predefined RSN templates were selected by an expert after visual inspection from a set of spatial maps resulting from a Group ICA decomposition performed on 12 independently assessed controls and were confirmed by another expert for accuracy of structural labeling reported elsewhere [31].

3.2.4 Applying Graph Theory

Once the ICs were identified as the RSNs of interest, a graph theoretical approach was applied on the ICs to visualize and calculate the graph properties of each network [28, 32, 33]. For this analysis, the cortex was parcellated into 1015 regions of interests (ROIs) with anatomical significance, using the Lausanne 2008 Atlas with functions from the Connectome Mapping Toolkit [34]. Each ROI is considered as a node of a graph; the connections between nodes typically carry weights describing the correlation, or the degree of functional connectivity between each pair of nodes. After decomposing the whole brain to components using ICA, the weighted matrices (w_{ij}) for each of the nine RSNs were obtained by calculating the edge weights using **Eq. 3.1**:

$$w_{ij} = |t_i| + |t_j| - |t_i - t_j| \quad (3.1)$$

where w_{ij} represents the connectivity between regions i and j , according to the time course of the corresponding IC (network). t_i and t_j are the t -values which are obtained from the scalar map of the independent component of interest for the nodes i and j respectively [28, 35].

3.2.5 fMRI Second-Level Statistical Analysis

The w_{ij} matrices (“correlation matrices”) of each network for all 135 subjects were obtained using GraphICA. The w_{ij} matrices were thresholded from 0 to 1 in steps of 0.1 and subsequently the mean over the thresholded w_{ij} matrices were obtained to create a threshold independent quantity [35]. Graph strengths (GS) of each 1015 regions (S_i) for all subjects were calculated from the mean thresholded w_{ij} matrix using the formula $S_i = \sum_{j=1}^N w_{ij}$, where N is the number of regions. Then mean GS over the subjects was calculated and the GS values greater than the thresholded GS (values greater than half of the maximum GS value for the network) were plotted (**Fig. 3.1**). It is

important to note that some brain regions may spatially belong to several RSNs (overlapping regions) while other, the isolated regions, only belong to one (**B.2**). This is explained by the fact that some regions have an associated BOLD signal that can fit the dynamic of different ICA components. Therefore, in the plots corresponding to the tinnitus population, regions belonging to the template of the specific network were plotted, while only the isolated regions of other networks were plotted. This arrangement was chosen because overlapping regions will cause concerns to which network they should be assigned in the plots. The assigned RSN of origin of a particular region is based on GraphICA templates created from 12 healthy subjects without tinnitus as discussed in **Section 3.2.3**. and shown in the Appendix (**B.2**) (the axial and sagittal views of the templates for the nine RSNs using the isolated regions (non-overlapping) and the overlapping regions are plotted). We use a circle to represent each region with a GS above threshold and used a different color depending on their RSN of origin. Also for visualization purposes, the distribution of unthresholded mean GS (normalized to 1) on the axial slices of normalized structure for each network is shown in **Fig. 3.2**.

Pearson correlations among the six Behavioural Scores (BS) (i.e., age, tinnitus distress (TQ score), tinnitus duration, tinnitus subjective intensity (numerical rating scale from 0 to 10), tinnitus objective loudness (as measured during the audiological assessment and corrected for the hearing threshold measured for the according frequency), and hearing loss) were calculated (**Table 3.1**). First, to assess how the GS of each network varies with the BS, GS was averaged over the 1015 regions of each network (global GS) for each subject and correlations between the global GS and the BS were calculated (**Table 3.2**) for each of the five networks of interest.

Stepwise fit regression analysis was performed to examine the relationship between BS with GS of each ROI for each network. We used the default values of p -entering = 0.05 and p -

exiting = 0.10 and performed the stepwise fit regression analysis on the GS of each region, network by network using the BS as the predictors. Before stepwise fit regression analysis was performed, we checked the multicollinearity amongst the BSs by calculating VIF and confirming that multicollinearity was not an issue [26]. *T*-statistics and *p*-values for coefficient estimates (between the GS and each BS while keeping the other BSs as covariates) were obtained from the stepwise fit analysis, for each region and for each network separately. We performed multiple comparison correction using the Benjamin Hochberg procedure (using a false discovery rate of 0.25) for the whole brain volume to control the false positives [38] (**Tables 3.3 and 3.4, B.3a, B.3b, B.3c and B.3d**). Although there are other procedures for multiple comparison such as Benferroni, Fisher's least significant difference method, etc., we used the Benjamin Hochberg procedure, as it is less conservative compared to other methods. We visualized the *t*-values of the correlation plots using different colours for each network for the regions that survived the multiple comparison correction (**Fig. 3.3 and B.4**). We were interested in exploring the core networks' behaviour shared by all tinnitus patients, rather than the difference between the groups, irrespective of lateralization. However, given the importance of interhemispheric competition in high-order sensory perception, we compared unilateral (35 patients) and bilateral (100 patients) tinnitus for completeness and have reported the results in Appendix B (**B.5 and B.6**).

3.3 Results

3.3.1 Patients

Patients' demographic characteristics are summarized in **B.1**. Patients ranged in age from 15 to 81 (mean = 50, SD = 15) and had tinnitus for a mean period of 5.8 years ranging from 0.2 to 45.0 years. Tinnitus matched frequencies ranged from 250 Hz to 12.5 kHz (mean = 5000 Hz, SD = 3270 Hz). Corrected tinnitus matched intensities (objective loudness) were 8 dB SL in mean (SD = 9 dB SL). Tinnitus Questionnaire (TQ) score varied across patients from 2 to 75 [27]. According to the TQ score, 56 tinnitus patients (41%) had slight (0-30 TQ score), 40 (30%) moderate (31-46 TQ score), 26 (19%) severe (47-59 TQ score) and 13 (10%) very severe distress (60-84 TQ score). Numeric rating of the tinnitus subjective intensity ranged from 0 to 10 (mean = 5, SD = 3). Hearing loss due to tinnitus had an average value of 32 dB with a standard deviation of 20 dB. According to the World Health Organization grades of hearing impairment [39], 89 (65%) tinnitus patients have a grade 0 impairment (no impairment, 25dB or better - averages of values at 500, 1000, 2000, 4000 Hz - better ear), 30 (22%) have a grade 1 impairment (slight impairment, 26 - 40dB, better ear), 17 (12%) have a grade 2 impairment (moderate impairment, 41-60dB, better ear) and 1 (1%) has a grade 3 impairment (severe impairment, 61 - 80 dB, better ear).

3.3.2 Neural Correlates of Tinnitus Characteristics

It is important to note that when we examined the correlation between clinical characteristics and brain connectivity in the five different resting-state networks of interest, the maps used for the second level analysis were not thresholded. This means that for each network, the statistical analysis was not restricted to regional parts of a thresholded map but rather were performed on a whole-brain image.

The mean GS of the auditory, DMN, ECNL, ECNR and salience networks and the contribution of each network to the mean for the tinnitus patients are displayed in **Figs. 3.1a** and **3.1b** respectively. Although the networks in our tinnitus population are defined to a certain extent by the characteristic region of each network, as shown by the highlighted regions of the colour of that particular network (Aud – 58%, DMN – 69%, ECNL – 52%, ECNR – 58% and Sal – 34%), a few isolated regions belonging to other networks are participating as well (**Fig. 3.1b**). For example, when considering mean GS of the auditory network in our tinnitus population, although the main contribution comes from regions belonging to the auditory RSN template (58%), regions that are found to be part of DMN (15%), ECNL (14%), ECNR (8%) and salience (5%) in the GraphICA control population (**B.2b**) contributed as well. **Fig. 3.2** shows the axial slices implemented on the normalized structure for the mean GS of each network. Mostly the regions belonging to the network have higher mean GS, while regions not belonging to the specific network contributes in the mean GS as well.

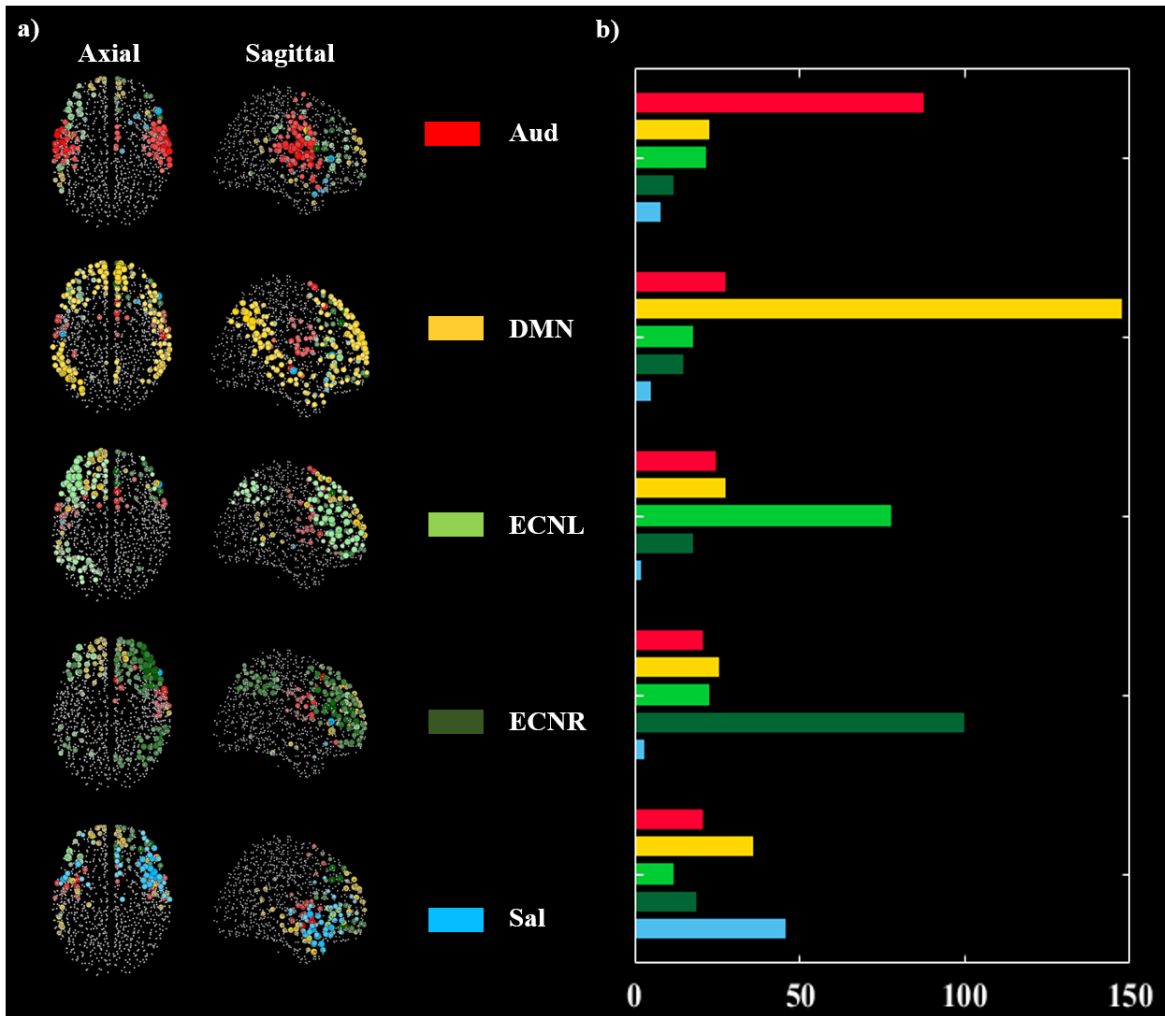


Fig. 3.1 Mean Graph Strength (GS) plots of auditory (Aud), Default Mode Network (DMN), Executive Control Network Left (ECNL), Executive Control Network Right (ECNR) and salience (Sal) separated by different colours for each network for tinnitus patients. Only the GS values greater than 0.5 of the maximum GS value of that network are plotted

- a) Axial and sagittal plots of the networks. Size of the circle represents the value of the GS and the darker the circle, the higher the GS
- b) Contribution of regions of each network in the mean GS plots of the overall network in tinnitus patients

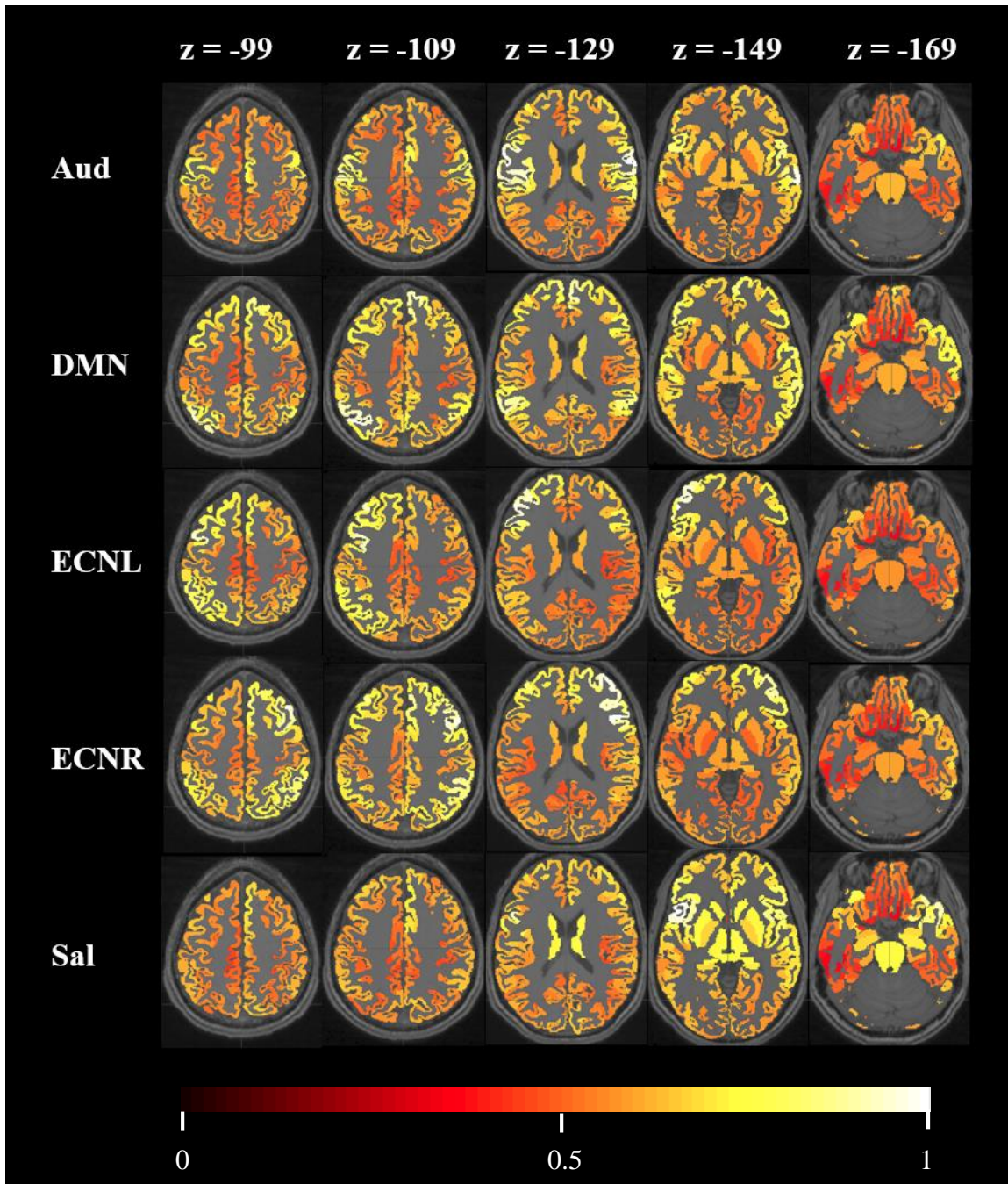


Fig. 3.2 Axial slices of the mean GS (normalized to 1) of tinnitus patients implemented on the normalized structure

Pearson correlations between the BSs are shown in **Table 3.1**. Age and hearing loss showed the strongest significant correlation ($r = 0.67$, $p < 0.01$). Interestingly, distress and tinnitus duration were not correlated, but were both significantly correlated with hearing loss ($r = 0.35$, $p < 0.01$ and

$r = 0.34$, $p < 0.01$, respectively) and subjective tinnitus intensity ($r = 0.44$, $p < 0.01$ and $r = 0.19$, $p = 0.03$, respectively). Hearing loss was significantly correlated with all BSs except tinnitus objective loudness (**Table 3.1**). Age was correlated with duration of the tinnitus ($r = 0.27$, $p < 0.01$) and subjective tinnitus intensity ($r = 0.20$, $p = 0.02$), in agreement with previous studies [39], while the tinnitus objective loudness was not correlated with any BSs.

Table 3.1 Correlation between the BS obtained from 135 patients

BS	Age		Distress		Loudness		Intensity		Duration		Hearing Loss	
	r	p	r	p	r	p	r	p	r	p	r	p
Age			0.17	0.06	0.09	0.30	0.20	0.02*	0.27	< 0.01*	0.67	< 0.01*
Distress					-0.04	0.68	0.43	< 0.01*	0.12	0.18	0.35	< 0.01*
Loudness							-0.06	0.52	-0.01	0.95	0.02	0.80
Intensity									0.19	0.03*	0.34	< 0.01*
Duration											0.34	< 0.01*
Hearing Loss												

* statistically significant p -values

Amongst the correlations between the global GS for each network and BS, the strongest correlations were observed between distress and the ECNR ($r = 0.22$, $p = 0.01$), followed by age and the DMN ($r = 0.18$, $p = 0.03$) (**Table 3.2**). As described above in the methodology section, the variation inflation factors, which quantify the severity of multicollinearity between the BSs (age, distress, loudness, intensity, duration and hearing loss) were 1.9, 1.3, 1.0, 1.3, 1.1 and 2.2 respectively. Since these values are smaller than 5, the multicollinearity among the BSs was not an issue, allowing for stepwise regression analysis to be implemented [26].

Table 3.2 Correlation between the GS averaged over all 1015 regions with BS for tinnitus patients

	Age (years)		Distress (TQ score)		Objective Loudness (dB SL)		Subjective Intensity - VAS (dB)		Duration (years)		Hearing Loss	
	r	p	r	p	r	p	r	p	r	p	r	p
Auditory	0.11	0.19	-0.07	0.42	-0.07	0.43	-0.13	0.14	-0.06	0.52	0.00	0.98
DMN	0.18	0.03*	0.01	0.88	0.02	0.84	0.01	0.90	0.09	0.27	0.15	0.09
ECNL	-0.01	0.95	0.16	0.06	0.04	0.67	0.14	0.10	-0.01	0.90	0.03	0.76
ECNR	0.05	0.57	0.22	0.01*	0.05	0.55	0.13	0.12	0.05	0.59	0.03	0.73
Salience	-0.04	0.64	0.02	0.84	-0.08	0.33	-0.04	0.68	0.02	0.80	0.01	0.88

* statistically significant *p*-values

We then selected the ECNR and the DMN and examined the correlation between distress and age, respectively, and the GS value of all 1015 regions for both networks. Regions with a correlation value which survived the multiple comparison test are depicted in **Fig. 3.3** and further listed in **Tables 3.3** and **3.4**.

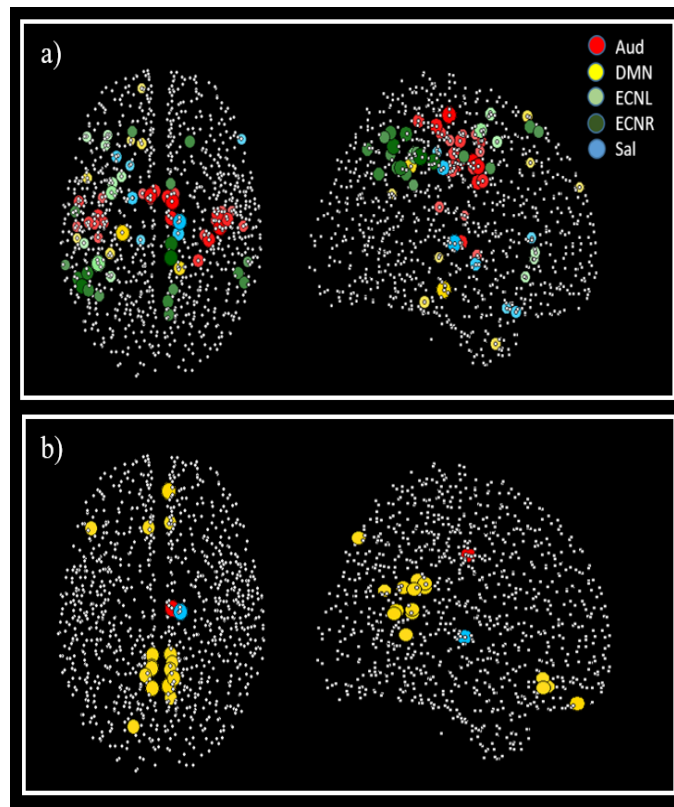


Fig. 3.3 Representation of the correlation between GS and Behavioural Scores (BS) of tinnitus patients for a) ECNR and distress b) DMN and age

Table 3.3 Correlation between the distress and GS on the ECNR network for tinnitus patients

ROI	x	y	z	t-value	p-value	Network
lh.insula	89.81	141.18	-145.73	2.14	0.03	Aud
lh.post central	80.78	127.22	-103.95	2.57	0.01	Aud
lh.posterior cingulate	121.75	141.84	-109.17	3.30	< 0.01	Aud
lh.precentral	87.16	130.93	-98.61	2.74	0.01	Aud
lh.superior frontal	116.40	143.20	-103.17	2.07	0.04	Aud
lh.supramarginal	87.16	118.77	-125.85	2.22	0.03	Aud
rh.insula	165.91	132.01	-140.39	3.04	< 0.01	Aud
rh.post central	160.43	117.36	-92.65	3.19	< 0.01	Aud
rh.posterior cingulate	135.89	139.00	-107.71	3.43	< 0.01	Aud
rh.precentral	167.81	124.58	-88.29	3.47	< 0.01	Aud
rh.superior frontal	137.35	143.51	-99.02	2.64	0.01	Aud
rh.superior parietal	153.45	106.19	-90.38	2.78	0.01	Aud
rh.supramarginal	183.16	125.28	-111.46	2.41	0.02	Aud
Left-Hippocampus	103.15	121.51	-160.17	3.69	< 0.01	DMN
lh.inferior parietal	80.00	90.89	-120.21	2.12	0.04	DMN
lh.middle temporal	79.90	151.88	-182.10	2.45	0.02	DMN
lh.superior frontal	115.90	170.90	-88.55	2.50	0.01	DMN
lh.superior temporal	73.39	118.28	-146.43	1.98	0.05	DMN
rh.precuneus	141.00	102.09	-109.01	3.20	< 0.01	DMN
lh.fusiform	95.13	109.98	-164.81	2.44	0.02	DMN
lh.caudal middle frontal	96.01	143.66	-94.37	3.06	< 0.01	ECNL
lh.lateral orbitofrontal	91.90	170.14	-154.68	2.30	0.02	ECNL
lh.pars triangularis	93.26	175.98	-144.78	2.09	0.04	ECNL
lh.superior parietal	95.69	97.00	-110.41	2.31	0.02	ECNL
lh.supramarginal	87.22	104.50	-104.45	3.50	< 0.01	ECNL
lh.inferior parietal	76.28	91.69	-100.74	3.05	< 0.01	ECNR
lh.superior frontal	109.78	177.55	-94.91	2.15	0.03	ECNR
rh.inferior parietal	179.54	99.42	-112.63	2.40	0.02	ECNR
rh.inferior temporal	186.97	97.09	-166.99	-2.08	0.04	ECNR
rh.precuneus	133.32	83.31	-112.47	2.51	0.01	ECNR
lh.post central	71.87	133.26	-105.16	2.23	0.03	ECNR
lh.supramarginal	79.82	99.20	-96.02	2.79	0.01	ECNR
rh.posterior cingulate	135.66	115.42	-107.26	2.99	< 0.01	ECNR
rh.precuneus	135.04	107.71	-105.41	3.19	< 0.01	ECNR
rh.superior frontal	147.68	172.50	-93.04	2.32	0.02	ECNR
rh.inferior parietal	183.76	93.97	-109.69	2.37	0.02	ECNR
rh.supramarginal	186.11	105.45	-103.50	1.99	0.05	ECNR
Left-Pallidum	109.77	140.49	-149.54	2.58	0.01	Sal
lh.lateral orbitofrontal	99.18	163.96	-168.91	2.37	0.02	Sal
lh.paracentral	114.97	117.77	-103.58	2.01	0.05	Sal
rh.pars triangularis	181.87	173.66	-138.57	2.00	0.05	Sal
rh.posterior cingulate	140.15	121.11	-109.82	2.85	0.01	Sal
Right-Thalamus-Proper	140.83	127.72	-141.05	3.29	< 0.01	Sal

Table 3.4 Correlation between the age and GS on the DMN network for tinnitus patients

ROI	x	y	z	t-value	p-value	Network
rh.posterior cingulate	135.57	129.46	-107.88	2.79	0.01	Aud
Right-Thalamus-Proper	140.83	127.72	-141.05	3.40	< 0.01	Sal
lh.isthmus cingulate	123.18	104.24	-119.26	3.09	< 0.01	DMN
lh.medial orbitofrontal	120.68	173.01	-161.79	2.89	< 0.01	DMN
lh.pars orbitalis	83.60	172.65	-157.86	2.87	< 0.01	DMN
lh.precuneus	123.35	86.49	-131.43	3.10	< 0.01	DMN
lh.superior parietal	110.63	65.89	-100.52	2.96	< 0.01	DMN
rh.isthmus cingulate	134.68	104.58	-120.94	3.02	< 0.01	DMN
rh.medial orbitofrontal	133.18	192.99	-168.08	3.25	< 0.01	DMN
rh.precuneus	133.47	87.85	-130.41	3.23	< 0.01	DMN

In the ECNR, tinnitus-related distress correlated with GS of several regions of the brain. The most significant regions are the part of right precuneus that overlaps with ECNR, left inferior parietal, right posterior cingulate, left and right posterior cingulate regions, right insula, right postcentral, right precentral, left hippocampus, left caudal middle frontal, left supramarginal and the right thalamus ($p < 0.01$). Although the effect of distress mainly affected the ECNR, based on the associated network of each significant region (see color in **Fig. 3.3a**, and associated network listed in **Table 3.3**) it is mostly the interaction between the ECNR and the other resting-state networks that was disturbed. Similar results were obtained within the unilateral and bilateral groups, although the effect of distress on the ECNR in the bilateral group was milder, affecting only a few regions belonging to the auditory network relative to the unilateral group where many regions belonging to all networks were affected (**B.5a**, **B.5b**, **B.6a** and **B.6b**).

In the DMN, a significant correlation between age and GS was primarily seen in the network itself, mostly in the precuneus, cingulate and orbitofrontal regions (see colour in **Fig. 3.3b**, and associated network listed in **Table 3.4**). These results were replicated in the bilateral tinnitus group, where a positive correlation was obtained between age and DMN (bilaterally in the

precuneus, cingulate and inferior parietal regions) as well as with auditory network (**B.5b**, **B.5c**, **B.6b** and **B.6c**).

3.4 Discussion

The present study explored whether clinical characteristics of tinnitus are associated with specific resting-state activity and connectivity patterns. While past fMRI, EEG and MEG studies of tinnitus have analyzed brain activity, they rarely have considered changes in connectivity [7, 9, 22, 31]. As stated in these studies, it appears that abnormal activity localized in specific brain areas are, however, not sufficient to fully explain tinnitus pathophysiology but that tinnitus and tinnitus characteristics are also related to the dysfunctional interaction between separable distributed networks, related to the distress, subjective loudness and duration of tinnitus. Our findings support the hypothesis that the unified percept of tinnitus could be considered an emergent property of multiple overlapping dynamic brain networks [3]. When looking at mean graph strengths of tinnitus patients (**Fig. 3.1**), we see that mean GS of each network has a partial overlap with other networks as well. For example, in our tinnitus population, we observe that some auditory-related brain regions (in red, **Fig. 3.1a**) have resting BOLD activity that is somehow more related to the associated time course of the DMN, ECNR, ECNL and Salience network (see the auditory contribution in each network, **Fig. 3.1b**). In fact, our observation fits the idea that the brain operates via functional interactions between distributed regions, or neural networks, and that the interaction between these networks is rather dynamic and can be reorganized in response to a task, a change in sensory input, a cognitive overload or to learning [41]. This explains why some neural regions can be coupled with a specific network at one time and with a different one if the situation changes (i.e. hearing tinnitus). Of course, if we had the control data, we could have had the equivalent mean

distribution plot in the control data as well. Then this would have permitted us to see whether the distribution we observed in the GS of the tinnitus population is due to the pathology.

As for the association between tinnitus characteristics and brain connectivity, our main finding is the correlation between tinnitus-related distress and the ECNR GS values. The ECN includes portions of the lateral prefrontal cortex and posterior parietal cortex and is thought to be important for externally oriented awareness [42, 43] and cognitive control abilities [41, 44]. This fronto-parietal network is believed to be involved in allocating top-down attentional resources [45]. It is, along with the DMN and the Salience network, considered a “higher-order” network or “control” network, as opposed to auditory, somatosensory or visual networks which are considered as “lower-order” [46, 47]. We discussed previously that the brain can be viewed as a dynamic multi-network interaction. Modification of the functional coupling of these control networks with the sensory cortical regions influence how the information is processed and even if the information is consciously perceived [48]. Functional connectivity analysis of human functional magnetic resonance imaging data revealed that sensory areas that selectively process relevant information are functionally connected with the frontal-parietal network, whereas those that process irrelevant information are simultaneously coupled with the DMN [49]. This shows that the processing of sensory cortical activity is greatly influenced by top-down modulations with the fronto-parietal network associated with top-down enhancement. Our results show that tinnitus, and specifically tinnitus distress, is associated with a modification of functional connectivity not only within the regions of ECNR, but also between regions belonging to different networks. As shown in the correlation plot, higher distress causes higher GS in the regions belonging to the attentive network (ECNR) which might be interpreted as that the burden of tinnitus can be linked to a paradoxical attention to the sound. This can explain the success of cognitive therapies aiming at helping patient

to move their attention away from tinnitus and focussing on other matters [50]. This also stresses the importance of the control of associated factors like the level of alertness, attention or anxiety, as they play a role in the perceived tinnitus distress.

In accordance with previous studies, we showed that age influences the DMN connectivity. Interestingly, the modulation of connectivity takes place mainly between regions of the DMN and not between the DMN and other resting-state networks. We showed an increased GS value with age mostly in the posterior part of the DMN. These results conflict however with previous work showing decreased connectivity between the precuneus and prefrontal cortex with age [51] and should be explored further, while other showed increases or decreases of connectivity with age depending on the observed region of the DMN [52, 53].

Interestingly, there was no significant correlation between the tinnitus objective loudness, the tinnitus subjective intensity (VAS), the tinnitus duration and the mean GS of the five networks of interest. One hypothesis is that these tinnitus characteristics are mainly linked to modification of neuronal activity in specific brain areas and not to the modification of functional interaction between brain regions. When examining the correlation between the different behavioral scores, interestingly, we see that distress does not correlate with duration of tinnitus. This suggests that the long-term duration of the tinnitus percept does not ineluctably result in emotional distress and annoyance and that habituation might not necessarily be a matter of time. This lends support to previous work suggesting that distress and duration should be considered as two independent dimensions for tinnitus [54]. In contrast to previous studies, we do not find a correlation between tinnitus distress and age [55, 56]. However, we corroborate earlier works showing that tinnitus distress is positively correlated with hearing loss. Tinnitus loudness largely depends on the method used for its characterization. It can be assessed using psychophysical matching procedures or can

be subjectively rated using VAS [57]. In agreement with previous work, our study confirmed that VAS intensity ratings correlated with tinnitus-related distress [50], whereas psycho-physically determined tinnitus objective loudness does not [58]. This observation stresses the importance of proper selection of clinical measures when evaluating tinnitus and knowledge of what these measures represent. Certainly, the psycho-physically determined tinnitus objective loudness does not give an accurate representation of the disturbance caused by tinnitus.

3.5 Conclusion

Our findings provide evidence that alterations of functional interactions between key neural circuits of the brain can explain some tinnitus characteristics. Not only auditory regions, but also non-auditory regions are affected by tinnitus pathology. Specifically, the connectivity patterns of the right executive control network which is involved in the perception of external stimuli is mostly being affected by distress of patients with tinnitus. Additionally, tinnitus appears to be a pathological condition that produces hyper-attention towards something that should not be salient to us. Therefore, therapies that aim to modify this abnormal state of alertness towards the tinnitus sound should be able to reduce its perception. Identifying the brain's intrinsic system responsible for the conscious perception of the tinnitus or for the reaction to the noise could help in designing new noise cancellation strategies and open avenues for treatment of tinnitus.

3.6 Future Work

A correlation between tinnitus distress and graph strength was observed from the tinnitus study. Therefore, the next step will be to determine whether we can accurately classify how much distress someone is in based upon their functional connectivities, as extracted from ICA, using our data. The ICA were extracted using GraphICA, which uses rs-fMRI as input, and which does not require the conscious cooperation of the subjects undergoing scanning. If an accurate classification

could be made, could this classifier be used to determine—with an appropriate level of certainty—whether a non-responsive patient is in distress? In order to perform the classification properly, control data from the same scanner in which the tinnitus data was collected is necessary. Data sets from two different scanners might have an inappropriate contribution towards the classification process. Further, in order to keep the analysis simple, we restricted the analysis to only the correlation between GS and BS. We would like to extend this work by performing correlation analysis between other graph properties such as small-worldness and efficiency with BS and explore all the possible alterations in the functional connectivity of the tinnitus pathology. Moreover, we would like to perform correlation analysis on the w_{ij} -values (connectivity measure between the regions i and j) obtained from the scalar maps of each network with the BS. This can provide an indication of how much the interactions between the regions are modified by the pathology.

Bibliography

- 1) Jastreboff, P. J. (1990). Phantom auditory perception (tinnitus): mechanisms of generation and perception. *Neuroscience Research*, 8(4), 221-254.
- 2) Shargorodsky, J., Curhan, G. C., & Farwell WR (2010). Prevalence and characteristics of tinnitus among US adults. *The American Journal of Medicine*, 123(8), 711-718.
- 3) Langguth, B., Kreuzer, P. M., Kleinjung, T., & De Ridder, D. (2013). Tinnitus: causes and clinical management. *Lancet Neurology*, 12(9), 920-930.
- 4) De Ridder, D., Elgoyhen, A. B., Romo, R., & Langguth, B. (2011). Phantom percepts: tinnitus and pain as persisting aversive memory networks. *Proceedings of the National Academic of Sciences*, 108(20), 8075-8080.
- 5) Eggermont, J. J. & Roberts, L. E. (2004). The neuroscience of tinnitus. *Trends in Neurosciences*, 27(11), 676-682.

- 6) Mirz, F., Pedersen, C. B., Ishizu. K., Johannsen, P., Ovesen, T., StÖdkilde-JÖrgensen, H., & Gjedde, A. (1999). Positron emission tomography of cortical centers of tinnitus. *Hearing Research*, 134(1-2), 133-44.
- 7) Schlee, W. (2011). A Global Brain Model of Tinnitus. *Textbook of tinnitus*, ed. Moller (Springer).
- 8) Vanneste, S. & De Ridder, D. (2012). The auditory and non-auditory brain areas involved in tinnitus. An emergent property of multiple parallel overlapping subnetworks. *Frontiers in Systems Neuroscience*, 6, 31.
- 9) Adjamian, P., Sereda, M., & Hall, D. A. (2009). The mechanisms of tinnitus: perspectives from human functional neuroimaging. *Hearing Research*, 253(1-2), 15-31.
- 10) Schlee, W., Weisz, N., Bertrand, O., Hartmann, T., & Elbert, T. (2008) Using auditory steady state responses to outline the functional connectivity in the tinnitus brain. *PLOS One*, 3(11), e3720.
- 11) Schlee, W., Mueller, N., Hartmann, T., Keil, J., Lorenz, I. & Weisz, N. (2009). Mapping cortical hubs in tinnitus. *BMC Biology*, 7, 80.
- 12) Langguth, B., Schecklmann, M., Lehner, A., Landgrebe, M., Poepl, T. B., Kreuzer, P. M., Schlee, W., Weisz, N., Vanneste, S. & De Ridder, D. (2012). Neuroimaging and neuromodulation: complementary approaches for identifying the neuronal correlates of tinnitus. *Frontiers in Systems Neuroscience*, 6, 15.
- 13) Elgoyhen, A. B., Langguth, B., De Ridder, D., & Vanneste, S. (2015). Tinnitus: perspectives from human neuroimaging. *Nature Reviews Neuroscience*, 16(10), 632-642.
- 14) Buckner, R. L., Sepulcre, J., Talukdar, T., Krienen, F. M., Liu, H., Hedden, T., Andrews-Hanna, J. R., Sperling, R. A. & Johnson, K. A. (2009). Cortical hubs revealed by intrinsic functional connectivity: mapping, assessment of stability, and relation to Alzheimer's disease. *Journal of Neuroscience*, 29(6), 1860-1873.
- 15) Bressler, S. L. & Menon, V. (2010). Large-scale brain networks in cognition: emerging methods and principles. *Trends in Cognitive Sciences*, 14, 277–290.

- 16) Fox, M. D. & Raichle, M. E. (2007), Spontaneous fluctuations in brain activity observed with functional magnetic resonance imaging. *Nature Review Neuroscience*, 8, 700-711.
- 17) Haas, L. F. (2003). Hans Berger (1873–1941), Richard Caton (1842–1926), and electroencephalography. *Journal of Neurology, Neurosurgery & Psychiatry*, 74(1), 9-9.17.
- 18) Biswal, B., Yetkin, F. Z., Haughton, V. M. & Hyde, J. S. (1995). Functional connectivity in the motor cortex of resting human brain using echo-planar MRI. *Magnetic Resonance in Medicine*, 34, 537e541.
- 19) Damoiseaux, J.S., Rombouts, S. A., Barkhof, F., Scheltens, P., Stam, C. J., Smith, S. M. & Beckmann, C. F. (2006) Consistent resting-state networks across healthy subjects. *proceedings of the National Academy of Sciences of the United States of America*, 103(37), 13848-53.
- 20) Moussa, M. N., Steen, M. R., Laurienti, P. J. & Hayasaka, S. (2012). Consistency of network modules in resting-state fMRI connectome data. *PLOS One*, 2012;7(8), e44428.
- 21) Vanneste, S., Plazier, M., Van der Loo, E., Van de Heyning, P., & De Ridder, D. (2011). The difference between uni- and bilateral auditory phantom percept. *Clinical Neurophysiology*, 122(3), 578-587.
- 22) Vanneste, S., Van de Heyning, P., & De Ridder, D. (2011). The neural network of phantom sound changes over time: a comparison between recent-onset and chronic tinnitus patients. *European Journal of Neuroscience*, 34(5), 718-731.
- 23) Schecklmann, M, Landgrebe, M., Poepl, T. B., Kreuzer, P., Marienhagen, J., Wack, D. S., Kleinjung, T., Hajak, G. & Langguth, B. (2013). Neural correlates of tinnitus duration and distress: a positron emission tomography study. *Hum Brain Mapping*, 34(1), 233-240.
- 24) Maudoux, A., Lefebvre, P., Demertzi, A., Cabay, J. E., Vanhauzenhuyse, A., Laureys, S. & Soddu, A., (2012). Connectivity graph analysis of the auditory resting state network in tinnitus. *Brain Research*. 1485, 10-21.
- 25) Schmidt, S. A., Akrofi, K., Carpenter-Thompson, J. R. & Husain, F. T. (2013). Default mode, dorsal attention and auditory resting state networks exhibit differential functional connectivity in tinnitus and hearing loss. *PLOS One*, 8(10), e76488.

- 26) Hair, J. F. Jr., Anderson, R. E., Tatham, R. L. & Black W. C. (1995). *Multivariate Data Analysis* (3rd ed). New York: Macmillan.
- 27) Hallam, R. S. (1996). *Manual of the Tinnitus Questionnaire (TQ)*. (London: Psychological Corporation).
- 28) Ribeiro de Paula, D., Ziegler, E., Abeyasinghe, P. M., Das, T. K., Cavaliere, C., Aiello, M., Heine, L., Perri, C., Demertzi, A., Noirhomme, Q., Charland-Verville, V., Vanhauzenhuysse, A., Stender, J., Gomez, F., Tshibanda, J. L., Laureys, S., Owen, A. & Soddu, A. (2017). A method for independent component graph analysis of resting-state fMRI. *Brain and Behavior*, 7(3), e00626.
- 29) Beckmann, C. F., DeLuca, M., Devlin, J. T., Smith, S. M. (2005). Investigations into resting-state connectivity using independent component analysis. *Philosophical Transactions of the Royal Society of London B: Biological Sciences*, 360(1457), 1001-13.
- 30) Holmes, A. & Friston, K. (1998) Generalisability, random effects and population inference. *Neuroimage*, 7, 754.
- 31) Demertzi, A, Gomez, F., Crone, J. S., Vanhauzenhuysse, A., Tshibanda, L., Noirhomme, Q., Thonnard, M., Charland-Verville, V., Kirsch, M., Laureys & S., Soddu, A. (2014). Multiple fMRI system-level baseline connectivity is disrupted in patients with consciousness alterations. *Cortex*, 52, 35-46.
- 32) Soddu, A., Vanhauzenhuysse, A., Bahri, M., Bruno, M. A., Boly, M., Demertzi, A., Tshibanda, J. F., Philips, C., Stanziano, M., Ovadia-Caro, S., Nir, Y., Maquet, P., Papa, M., Malach, R., Laureys, S. & Noirhomme, Q. (2012). Identifying the default mode component in spatial IC analysis of patients with disorders of consciousness. *Human Brain Mapping*, 33(4), 778-96.
- 33) Maudoux, A., Lefebvre, P., Cabay, J., Demertzi, A., Vanhauzenhuysse, A., Laureys, S. & Soddu, A. (2012). Auditory resting-state network connectivity in tinnitus: a functional MRI study. *PLOS One*, 7(5), e36222.
- 34) Gerhard, S., Daducci, A., Lemkaddem, A., Meuli, R., Thiran, J. P. & Hagmann, P. (2011). The connectome viewer toolkit: an open source framework to manage, analyze, and visualize connectomes. *Frontiers in Neuroinformatics*, 5, 3.

- 35) Cavaliere, C., Kandeepan, S., Aiello, M., Ribeiro de Paula, D., Marchitelli, R., Fiorenza, S., Orsini, M., Trojano, L., Masotta, O., St. Lawrence, K., Loreto, V., Chronik, B. A., Nicolai, E., Soddu, A. & Estraneo, A. (2018). Multimodal neuroimaging approach to variability of functional connectivity in disorders of consciousness: a PET/MRI pilot study. *Frontiers in Neurology*, 9, 861.
- 36) Chen, Y., Chen, H., Bo, F., Xu, J., Deng, Y., Lv, H., Cai, Y., Xia, W., Yin, X., Gu, J. & Lu, G. (2018). Tinnitus distress is associated with enhanced resting-state functional connectivity within the default mode network. *Neuropsychiatric Disease and Treatment*, 14, 1919-1927. doi:10.2147/NDT.S164619.
- 37) Trevis, K. J., McLachlan, N. M., Wilson & S. J. (2016). Cognitive Mechanisms in Chronic Tinnitus: Psychological Markers of a Failure to Switch Attention. *Frontiers in Psychology*, 7, 1262. doi:10.3389/fpsyg.2016.01262.
- 38) Benjamini, Y. & Hochberg, Y. (1995). Controlling the false discovery rate: A practical and powerful approach to multiple testing. *Journal of the Royal Statistical Society: Series B (Methodological)*, 289–300.
- 39) WHO (1991). Grades of hearing impairment. *Hearing Network News* 1.
- 40) Bhatt, J. M., Lin, H. W. & Bhattacharyya, N. (2016). Prevalence, severity, exposures and treatment patterns in the United States. *JAMA Otolaryngology-Head & Neck Surgery*, 142(10), 959-965.
- 41) Zanto, T. P. & Gazzaley, A. (2013). Fronto-parietal network: flexible hub of cognitive control. *Trends in Cognitive Science*, 17(12), 602-3.
- 42) Boveroux, P., Vanhaudenhuyse, A., Bruno, M. A., Noirhomme, Q., Lauwick, S., Luxen, A., Degueldre, C., Plenevaux, A., Schnakers, C., Phillips, C., Brichant, J. F., Bonhomme, V., Maquet, P., Greicius, M. D., Laureys, S. & Boly, M. (2010). Breakdown of within- and between-network resting state functional magnetic resonance imaging connectivity during propofol-induced loss of consciousness. *Anesthesiology*, 113, 1038–1053.
- 43) Liu, X., Lauer, K. K., Ward, B. D., Rao, S. M., Li, S. J. & Hudetz, A. G. (2012). Propofol disrupts functional interactions between sensory and high-order processing of auditory verbal memory. *Human Brain Mapping*, 33, 2487–2498.

- 44) Dosenbach, N. U., Fair, D. A., Cohen, A. L., Schlaggar, B. L. & Petersen, S. E. (2008). A dual-networks architecture of top-down control. *Trends in Cognitive Sciences*, 12(3), 99-105.
- 45) Fassbender, C., Simoes-Franklin, C., Murphy, K., Hester, R., Meaney, J., Robertson, I. H. & Garavan, H. (2006). The role of a right fronto-parietal network in cognitive control. *Journal of Psychophysiology*, 20(4), 286-96.
- 46) Power, J. D., Cohen, A. L., Nelson, S. M., Wig, G. S., Barnes, K. A., Church, J.A., Vogel, A. C., Laumann, T. O., Miezin, F. M., Schlaggar, B. L. & Petersen, S. E. (2011). Functional network organization of the human brain. *Neuron*, 72(4), 665-78.
- 47) Guldenmund, P., Gantner, I. S., Baquero, K., Das, T., Demertzi, A., Boveroux, P., Bonhomme, V., Vanhaudenhuyse, A., Bruno, M. A., Gosseries, O. & Noirhomme, Q. (2016). Propofol-induced frontal cortex disconnection: a study of resting-state networks, total brain connectivity, and mean BOLD signal oscillation frequencies. *Brain Connectivity*, 6(3), 225-37.
- 48) Sadaghiani, S., Hesselmann, G., Kleinschmidt, A. (2009). Distributed and antagonistic contributions of ongoing activity fluctuations to auditory stimulus detection. *Journal of Neuroscience*, 29(42), 13410-7.
- 49) Chadick, J. Z. & Gazzaley, A. (2011). Differential coupling of visual cortex with default or frontal-parietal network based on goals. *Nature Neuroscience*, 14(7), 830.
- 50) Wallhausser-Franke, Brade, J., Balkenhol, T., D'Amelio, R., Seegmuller, A. & Delb, W. (2012). Tinnitus: distinguishing between subjectively perceived loudness and tinnitus-related distress. *PLOS One*, 7(4), e34583.
- 51) Vidal-Piñeiro D., Valls-Pedret, C. Fernandez-Cabello, S., Arenaza-Urquijo, E. M., Sala-Llonch, R., Solana, E., Bargallo, N., Junque, C., Ros, E. & Bartres-Faz, D. (2014). Decreased Default Mode Network connectivity correlates with age-associated structural and cognitive changes. *Frontiers in Aging Neuroscience*, 6, 256.
- 52) Washington, S. D. & VanMeter, J. W. (2015). Anterior-posterior connectivity within the default mode network increases during maturation. *International Journal of Medical and Biological Frontiers*, 21(2), 207.

- 53) Ferreira, L. K., Regina, A. C., Kovacevic, N., Martin, M. D., Santos, P. P., Carneiro, C. D., Kerr, D. S., Amaro, Jr. E., McIntosh, A. R. & Busatto, G. F. (2016). Aging effects on whole-brain functional connectivity in adults free of cognitive and psychiatric disorders. *Cerebral Cortex*, 26(9), 3851-65.
- 54) Meyer, M., Luethi, M. S., Neff, P., Langer, N. & Büchi, S. (2014). Disentangling tinnitus distress and tinnitus presence by means of EEG power analysis. *Neural Plasticity*, 2014.
- 55) Schlee, W., Kleinjung, T., Hiller, W., Goebel, G., Kolassa, I. T., Langguth, B. (2011). Does tinnitus distress depend on age of onset? *PLOS One*, 6(11), e27379.
- 56) Brüggemann, P., Szczepek, A. J., Rose, M., McKenna, L., Olze, H. & Mazurek, B. (2016). Impact of multiple factors on the degree of tinnitus distress. *Frontiers in Human Neuroscience*, 10, 341.
- 57) Balkenhol, T., Wallhauser-Franke, E. & Delb, W. (2013). Psychoacoustic tinnitus loudness and tinnitus-related distress show different associations with oscillatory brain activity. *PLOS One*, 8(1), e53180.
- 58) Tyler, R. S. & Conrad-Armes, D. (1983) The determination of tinnitus loudness considering the effects of recruitment. *Journal of Speech, Language, and Hearing Research*, 26(1), 59-72.

Chapter 4

A Multimodal Neuroimaging Approach to Variability of Functional Connectivity in Disorders of Consciousness: A PET/MRI Pilot Study

4.1 Introduction

The improvements of medical interventions in the acute and post-acute phase of severe acquired brain injury have assisted in better treatment for patients with prolonged disorders of consciousness (DOC) [1]. DOC is a medical condition in which consciousness is affected due to severe brain damage or injury. These severe clinical conditions come with serious ethical and social implications, impact health care policies, and can cause severe psychological distress in patients' families [2 – 4]. Distinguishing patients with unresponsive wakefulness syndrome (UWS; i.e. patients showing eyes open, but no behavioral evidence of consciousness [5]) from patients in a minimally conscious state (MCS; i.e., patients showing minimal, inconsistent, but clearly discernible intentional behaviors [6]) is pivotal for decision making throughout the entire care pathway of patients with DOC. Indeed, patients in MCS are more likely to have a better outcome [7, 8], and have a higher probability of clinical response to therapeutic interventions than patients in UWS [9 – 11]. However, in spite of the evolution of neuroscientific and medical understanding of DOC, the clinical identification of volitional behavior still remains a very difficult task [8, 12]. Patients' clinical signs of consciousness are frequently variable across days and even within the same day [13]. These inconsistencies have been often linked to temporal fluctuations of vigilance/awareness. For this reason, at least five repeated behavioral assessments by means of validated assessment tools, such as the Coma Recovery Scale-Revised (CRS-R) [14], are strongly recommended for improving diagnostic accuracy [15]. CRS-R is a collection of items used to

assess awareness and to characterize patients with DOC using their behavioral responses. It is grouped into six sub-scales that assess the responsiveness in auditory, visual, motor, oromotor, communication and arousal skills. The total scores obtained from the above mentioned six categories can range between 0 (worst) to 23 (best). Higher scores signify the presence of behaviors mediated by cognitive input, while low scores signify reflexive activity (involuntary or unconscious reactions).

However, behavioral assessment can be complicated by possible co-existing severe visuo-perceptual, motor or language disabilities that limit clinical expression of consciousness [7, 16]. In this context, a multimodal diagnostic approach, combining clinical and instrumental evaluations, could help in detecting signs of consciousness and making a correct diagnosis [17–19]. Neuroimaging methods, particularly those not requiring the patient’s active response, such as resting-state functional MRI (rs-fMRI) or 18F FDG-PET, can be used to identify residual functional connectivity and neural activity into resting state networks (RSNs), such as the default-mode network (DMN). These networks have been specifically associated with awareness level in such patients, independently from their abilities to produce overt purposeful behaviors [20 – 22]. As reported in Soddu et al. [21], regions belonging to the frontal parietal network and medial prefrontal regions of the DMN are believed to be responsible for consciousness or awareness. Moreover, multimodal imaging integration allows for the collection of a plethora of information data that would be undetectable at the patient’s bedside. However, especially simultaneous acquisition of neuroimaging data within the same temporal framework can assure comparability of the findings, due to the reduce influence of clinical fluctuations typical of patients with DOC. Additionally, the simultaneous acquisition of structural and functional data by hybrid imaging

techniques like PET/MR can improve the patient's compliance, by shortening imaging sessions and reducing logistic issues [23].

The present clinical and neuroimaging pilot study aimed to: (1) investigate possible variability in brain functional connectivity in two distinct fMRI acquisitions within one neuroimaging exam; (2) evaluate the relationship between spontaneous functional brain activity and metabolic activity at different levels of consciousness. For these purposes, we combined simultaneous neuroimaging methods (fMRI and PET) and repeated rs-fMRI acquisition in a sample of three severely brain-injured patients with different level of consciousness in stabilized clinical diagnosis of UWS, MCS, and emergence from MCS (EMCS, i.e., patient who recovered functional communication or/and functional object use [5, 6]). In this respect, in addition to clinical assessments such as CRS-R scores and neurophysiological evaluation, we predict that simultaneous PET/MRI investigation, which provides the possibility to acquire both techniques at the same time-point, may reduce complications related to patients' movements and increase compliance of patients and caregivers. This will be of great importance, especially when it comes to determining metrics of prognostic information.

4.2 Materials and Methods

4.2.1 Participants

For this pilot study, we screened nine severely brain-injured patients consecutively admitted to the neurorehabilitation unit at Maugeri Clinical and Scientific Institutes, in Telese Terme (Italy) from February 2017 to July 2017, fulfilling the following inclusion criteria: (i) clinical diagnosis of UWS, MCS or EMCS according to standard diagnostic criteria [5, 6]; (ii) time from onset longer than 1 month; (iii) traumatic, vascular, or anoxic brain injury (in which the brain is deprived of oxygen). We excluded from the study patients with: (i) severe pathologies

independent from the brain injury (e.g., premorbid history of psychiatric or neurodegenerative diseases); (ii) mixed etiology (e.g., both traumatic and anoxic); (iii) not stabilized and severe general clinical conditions; (iv) contra-indication for MRI (e.g., ferromagnetic aneurysm clips, pacemaker); (v) large brain damage (>50% of total brain volume), as determined by a certified neuroradiologist, and motion parameters > 3 mm in translation and 3° in rotation. Patients were also excluded if their clinical diagnosis had changed in the week before the neuroimaging acquisition.

The study was approved by the local Ethics Committee of IRCCS Pascale (Protocol number: 3/15), and performed according to the ethical standards laid down in the 1964 Helsinki Declaration and its later amendments. Written informed consent was obtained from the legal guardian of the patient.

4.3 Experimental Procedures

4.3.1 Clinical Assessment

One week before and one week after neuroimaging recording, all enrolled patients underwent at least five clinical evaluations, using the Italian version of the CRS-R [24], in order to confirm a stabilized clinical diagnosis of UWS, MCS or EMCS and to gather the best CRS-R total score. Patients' consciousness level (measured by the CRS-R total and sub-scores) was also assessed in the “neuroimaging” day by one trained psychologist (OM) (C.1).

4.3.2 Neurophysiological Evaluation

Standard EEG and event related potentials (ERP) were recorded to complement behavioral assessment and to reduce risk of misdiagnosis. For this purpose, we acquired neurophysiological exams at each patient's bedside across two days in the week preceding the PET/MRI session as well as across two days in the week following the neuroimaging session, and the best organization of EEG background activity and reactivity was considered for classification of neurophysiological patterns, contributing to the patients' clinical diagnosis. In the presence of artifacts in more than 50% of EEG recording time, EEG acquisition was repeated the day after. Two trained clinical neurophysiologists (blinded to patients' etiology, clinical diagnosis and CRS-R score) reviewed the neurophysiological exams.

Standard EEG was recorded from 19 electrodes placed on the scalp, according to international 10 – 20 system (O1, O2, Pz, P3, P4, T5, T6, C3, C4, Cz, T3, T4, Fz, F3, F4, F7, F8, Fp1, and Fp2). Electrodes were placed over the cortex of the brain to detect the electrical activity. The "10" and "20" is a method used to describe the location of the electrodes in the scalp and refer to the fact that the actual distances between adjacent electrodes are either 10% or 20% of the total front–back or right–left distance of the skull. The letters O, P, T, C and F correspond to the occipital, parietal, temporal, central and frontal lobes (central lobe does not exist, but this terminology is used for identification purposes, and is mainly used in sleep studies to determine the sleep stages). Even numbers (2, 4, 6, 8) in the electrodes represent the right hemisphere and odd numbers (1, 3, 5, 7) the left hemisphere, and the smaller the number, the closer the electrode is to the midline. Subscript *z* refers to an electrode placed on the midline and is generally used as a reference. We recorded EEG for a minimum of 35 min, according to standard procedure of eyes-closed waking rest, with filter settings of 0.53 – 70 Hz, and a notch filter on. For the analysis of

predominant activity, forced eye closing was obtained by cotton wool in awake patient (spontaneous eye opening). To analyse EEG reactivity, eye opening and (forced) eye closing were alternated three times during EEG recording. The four basic EEG frequency patterns are beta (14 – 30 Hz), alpha (8 – 13 Hz), Theta (4 - 7 Hz) and delta (1 – 3 Hz) with amplitude ranging between 10 μ V to 100 μ V when measured from the scalp [25]. We classified EEG background activity on the basis of frequency and amplitude of predominant cortical activity present in >50% of recordings, into one of five severity categories, according to criteria recently proposed for patients with prolonged DOC [26] (C.2).

Event related potentials (ERP) were obtained by means of a simple “oddball” paradigm using auditory stimulation and classified as “present” when a P300 cortical response was recorded; in the presence of the N100 (but not the P300) component, the exam ERP was considered “absent,” whereas lack of N100 was considered as a “not reliable” exam [27]. ERPs are used to measure the cognitive, sensory and motor measurements by measuring the EEG activity using the “oddball” paradigm. The oddball paradigm is the presentation of sequences of repetitive stimuli that are infrequently interrupted by a deviant stimulus. The letters N/P stand for the polarity (negative/positive) of the evoked potential of the EEG signal which peaks at 100 and 300 milliseconds after the onset of a stimulus. The P300 and N100 are observed only when the subject is able to distinguish the presence of a deviant stimulus.

4.3.3 PET/MRI Acquisition Protocol

PET/MRI data were simultaneously acquired in the resting state using a Biograph mMR tomograph (Siemens Healthcare, Erlangen, Germany) designed with a multi-ring LSO detector block embedded into a 3 T magnetic resonance scanner. Vacuumed pillows were used to minimize head movements within the scanner. PET/MRI images were acquired in the morning after

customary nursing procedures. Several strategies were used to ensure patients' best vigilance state by: (i) stopping possible sedative drugs (such as benzodiazepine) 15 h before scanning; (ii) administering CRS-R vigilance protocol [14] before PET/MRI acquisition and during neuroimaging exam at the end of first resting state MRI acquisition; and (iii) monitoring eye opening by means of a video camera located into MRI scanner. In case of the appearance of clinical signs of possible drowsiness (i.e., persistence of eye closing), MRI acquisition was stopped and the CRS-R vigilance protocol was administered.

Nominal axial and transverse resolution of the PET system was 4.4 and 4.1 mm FWHM, respectively, at 1 cm from the isocenter. Additional technical details of the scanner are reported elsewhere [28]. A brain PET scan was performed after the intravenous bolus administration of 18F-fluorodeoxyglucose (18F-FDG) tracer. PET and rs-fMRI data acquisition started simultaneously following the intravenous injection of 5 MBq/Kg of 18FDG. No food or sugar were administered to the subjects for at least 6 h prior to FDG injection. Blood glucose was measured at arrival at the PET center in all cases, and FDG was injected only if glycaemia was below 120 mg/dl.

The PET data were acquired in list mode for 60 min; matrix size was 256×256 . PET emission data were reconstructed with an ordered subset-expectation maximization (OSEM) algorithm (21 subsets, 4 iterations) and post-filtered with a three-dimensional isotropic gaussian kernel of 4 mm at FWHM. Attenuation correction was performed using MR-based attenuation maps derived from a dual echo ($TE = 1.23 - 2.46$ ms), Dixon-based sequence (repetition time 3.60 ms), allowing for reconstruction of fat-only, water-only and of fat-water images [29].

During PET acquisition, the following MRI sequences were sequentially run:

- (i) First rs-fMRI acquisition (named “t₁”) by a T2*-weighted single-shot EPI sequence (voxel-size $4 \times 4 \times 4 \text{ mm}^3$, TR/TE = 1000/21.4 ms, flip angle = 82° , 480 time points, FOV (field of view) = 256 mm^2 , multiband factor = 2);
- (ii) Three-dimensional T1-weighted magnetization-prepared rapid acquisition gradient-echo sequence (MPRAGE, 240 sagittal planes, $256 \times 214 \text{ mm}^2$ field of view, voxel size $0.8 \times 0.8 \times 0.8 \text{ mm}^3$, TR/TE/TI 2400/2.25/1000 ms, flip angle 8°);
- (iii) Three-dimensional T2-weighted sequence (240 sagittal planes, field of view = $256 \times 214 \text{ mm}^2$, voxel size $0.8 \times 0.8 \times 0.8 \text{ mm}^3$, TR/TE 3370/563 ms);
- (iv) Three-dimensional fluid attenuation inversion recovery (FLAIR, 160 sagittal planes, field of view = $192 \times 192 \text{ mm}^2$, voxel size $1 \times 1 \times 1 \text{ mm}^3$, TR/TE/TI 5000/334/1800 ms);
- (v) Second rs-fMRI acquisition (named “t₂”) by a T2*-weighted single-shot EPI sequence (voxel-size $4 \times 4 \times 4 \text{ mm}^3$, TR/TE = 1000/21.4 ms, flip angle = 82° , 480 time points, FOV read = 256 mm^2).

In addition, during the same scanning session, axial diffusion weighted images were also acquired for clinical purposes. The two rs-fMRI acquisitions (t₁ and t₂) were separated by a 30 min interval.

4.3.4 fMRI and FDG-PET Processing

Resting state fMRI analysis was performed based on a methodology fully described by Ribeiro and colleagues [30]. Independent component analysis (ICA) [31] followed by template matching to identify RSNs and machine learning classification to automatically recognize a neuronal network or independent component (IC) was used. We extracted the weighted graphs for each of the nine networks of interest as described in the paper [30] and calculated the graph

strength (GS) for each of the 1015 nodes. Finally, for each network we calculated the correlation between GS and the metabolic values.

We focused on the following nine RSNs [30]: auditory, default mode network (DMN), external-control network left (ECNL), external-control network right (ECNR), salience, sensorimotor, visual lateral (VL), visual medial (VM) and visual occipital (VO). The RSNs were assigned as the components with maximum goodness-of-fit (similarity test) when compared to a binary predefined template while considering all the RSNs simultaneously [32]. The templates for each RSN were selected by an expert in RSN pattern recognition, after visual inspection from a set of spatial maps resulting from a Group ICA decomposition performed on 12 independently assessed controls and were confirmed by another expert for accuracy of structural labeling [32]. Subsequently a classifier trained on an 11-dimensional space called a “fingerprint,” that provides both spatial (i.e., degree of clustering, skewness, kurtosis, spatial entropy) and temporal information (i.e., onelag autocorrelation, temporal entropy, power of five frequency bands: 0–008Hz, 0.008–0.02Hz, 0.02–0.05Hz, 0.05–0.1Hz, and 0.1–0.25Hz) of the ICs, was used to select only the neuronal components from the extracted networks [32]. Signals arising from changes in local hemodynamics which result solely from alterations in neuronal activity represented by low-frequency (0.01–0.05Hz) were considered neuronal signals. Non-neuronal signals for fMRI data represent cardiovascular signal dominated by higher frequency and head movement.

Once the neuronal components are identified, a graph theoretical approach was applied on the ICs (GraphICA, BraiNet-Brain Imaging Solution Inc.-Sarnia, ON, Canada) to visualize and calculate the graph strengths of each network [31, 33, 34]. GraphICA performed single-subject ICA with 30 components, ordered using the infomax algorithm as implemented in the Group-ICA of fMRI toolbox (RRID: SCR-001953; <http://mialab.mrn.org/software/gift/>). Instead of working

at the voxel level (around 100,000 voxels) for the analysis, the cortex was parcellated into 1015 regions of interests (ROIs) with anatomical meaning, using the Lausanne 2008 Atlas with functions from the Connectome Mapping Toolkit [35]. Each ROI is considered as a node of a graph; the edges connecting the nodes carry weights describing the correlation, or the degree of connectivity between each pair of nodes. After decomposing the whole brain to components using ICA, the weighted matrices (w_{ij}) for each of the nine components are obtained by calculating the edge weights using the **Eq. 4.1**:

$$w_{ij} = |t_i| + |t_j| - |t_i - t_j| \quad (4.1)$$

where w_{ij} represents the edge weight between nodes i and j according to the time course of the corresponding IC, and t_i, t_j are the t -values which are obtained from the scalar map of the IC of interest for the nodes i and j , respectively.

Furthermore, each patient's two fMRI acquisitions as well as their FDG-PET data were manually co-registered to their structural images. These data, along with the concatenated data (combined t_1 and t_2), underwent an automated pipeline in GraphICA, which includes further minute realignment and adjustment for movement-related effects, fine co-registration, segmentation of the structural and FDG-PET image, and spatial normalization into standard stereotactic Montreal Neurological Institute (MNI) space as performed in SPM8. Considering the relevance of motion for these dataset, as already reported in Soddu et al. [33], motion parameters such as the mean displacement (Δ) and the displacement speed (Σ) during the full acquisition were calculated using the equations explicitly given by **Eq. 4.2** and **Eq. 4.3**,

$$\Delta = \langle \sqrt{\text{Tra}X^2 + \text{Tra}Y^2 + \text{Tra}Z^2 + \text{Rot}X^2 + \text{Rot}Y^2 + \text{Rot}Z^2} \rangle \quad (4.2)$$

$$\Sigma = \langle \sqrt{\Delta_{TR}TraX^2 + \Delta_{TR}TraY^2 + \Delta_{TR}TraZ^2 + \Delta_{TR}RotX^2 + \Delta_{TR}RotY^2 + \Delta_{TR}RotZ^2} \rangle \quad (4.3)$$

Where Δ_{TR} represents the variation of a parameter over a TR (repetition time).

Motion curves were regressed out from the fMRI data when performing preprocessing using Art repair (RRID:SCR-005990; <http://cibsr.stanford.edu/tools/humanbrain-project/artrepair-software.html>), but not the motion parameters. Instead these parameters were calculated to estimate how much the patients have moved in the scanner during each acquisition.

Segmentation of the images in GraphICA was performed at the subject level to create individual segmentations [36]. Following these preprocessing steps, ICA was applied and w_{ij} matrices for each of the nine networks were obtained. Simultaneously the scalar maps of the FDG-PET for the 1015 parcellated regions of the cortex were obtained.

The w_{ij} matrices, which have the dimensions of 1015×1015 , were thresholded from 0 to 1 in steps of 0.01 and subsequently the means of the thresholded w_{ij} matrices were obtained to create a threshold independent quantity. The graph strengths (S_i) for each of the 1015 regions for all three subjects and for the nine networks were calculated from the thresholded w_{ij} , using the **Eq. 4.4**:

$$S_i = \sum_{j=1}^N w_{ij} \quad (4.4)$$

where N is the total number of regions.

Graph strength (GS) was tested at the network level for proportionality with metabolic activity. Specifically, only regions with GS values greater than the thresholded GS (values greater than half of the maximum GS value for the network of interest) were visualized and selected for subsequent calculations.

Networks that were classified as non-neuronal were removed and only the networks classified as neuronal were chosen for the analysis. Using the GS values, the regions belonging to each network (template), regions outside the network, and regions missing in the network for patients in EMCS, MCS and UWS were plotted in different colors for t_1 , t_2 and concatenated data. In the case where the networks from both acquisitions were neuronal, the ratio of fit (ROF) (Eq. 4.5), a measure assessing accuracy of network representation in the analysis, was calculated (Table 4.1).

$$ROF = \frac{(regions\ inside\ the\ mask - regions\ outside\ the\ mask)}{(total\ number\ of\ regions\ which\ should\ belong\ to\ the\ mask)} \quad (4.5)$$

An ROF with a more positive value indicates a high resemblance of the spatial pattern of the network, while a highly negative value means a distorted network. When more regions are inside the network, a higher positive ROF will be obtained and when more regions are outside the network than inside, a negative ROF will be obtained. Because we have another criterion, the FDG-PET, we can determine whether the IC we chose is precise or not by looking at the correlation between the FDG-PET and the graph strengths of that acquisition. For comparison purposes, only the values in which networks were identified as neuronal in both acquisitions are presented. The difference between ROF (ΔROF) values for t_1 and t_2 acquisitions of each RSN was used to assess IC variability. Scalar maps representing GS for each network were presented by choosing the acquisition with the highest ROF value (best finding) between the two acquisitions and was used for further analysis.

As stated above, the DMN includes several cortical regions whose metabolic activity is thought to be related to level of consciousness [20 – 22]. We believe that presenting the GS directly on the normalized structural images, especially for the DMN, has relevance, because it shows the

anatomical pattern of the network and permits us to visualize the level of disruption or completeness. However, it would be redundant to present the GS for all networks in the same modality. To ascertain whether the concatenated data or the data corresponding to the acquisition with the best network between t_1 and t_2 provided the best representation of the network, both the concatenated and the best acquisition data were plotted.

4.3.5 Statistical Analysis

Correlations were performed to measure the similarity between the FDG-PET metabolic maps and the GS activity maps for the whole brain. In order to determine the most representative value of the GS for each region from all the networks, the maximum value out of all the neuronal networks for that region was chosen. We also tested the correlation between the mean value of the GS for each region by considering all the neuronal networks and the FDG-PET, however the relationship was not significant. Z-scores of GS and FDG-PET for each region were calculated and the scatterplots of FDG-PET versus GS were presented for the best and concatenated data for the three patients. The “corrcoef” function was implemented in MATLAB to return the Pearson correlation value (r) between the FDG-PET and GS of the 1015 parcellated ROI. Finally, the distribution of GS for the best and concatenated data and FDG-PET were estimated.

4.4 Results

4.4.1 Clinical Features

From a sample of nine severely brain-injured patients, we were able to consider for PET/fMRI analysis two representative patients with prolonged DOC as well as one patient emerged from MCS (**Fig. 4.1**). Detailed descriptions of patients’ clinical features are provided in **C.3**, and the CRS-R total and subscores in **C.1**. To summarize, one anoxic patient was in UWS (F,

43 year old; time since injury: 8 months; best CRS-R total score: 6; CRS-R total score at neuroimaging study: 6), one traumatic patient in MCS (M, 18 year old; time since injury: 3 months; best CRS-R total score: 11; CRS-R total score at neuroimaging study: 11), and one anoxic patient emerged from MCS 25 days before the neuroimaging study (M, 57 year old; time since injury: 10 months; best CRS-R total score: 22; CRS-R total score at neuroimaging study: 22). The best CRS-R total scores collected for each patient in the weeks before and after the neuroimaging session and in the PET/MRI day are described in **Fig. 4.2**.

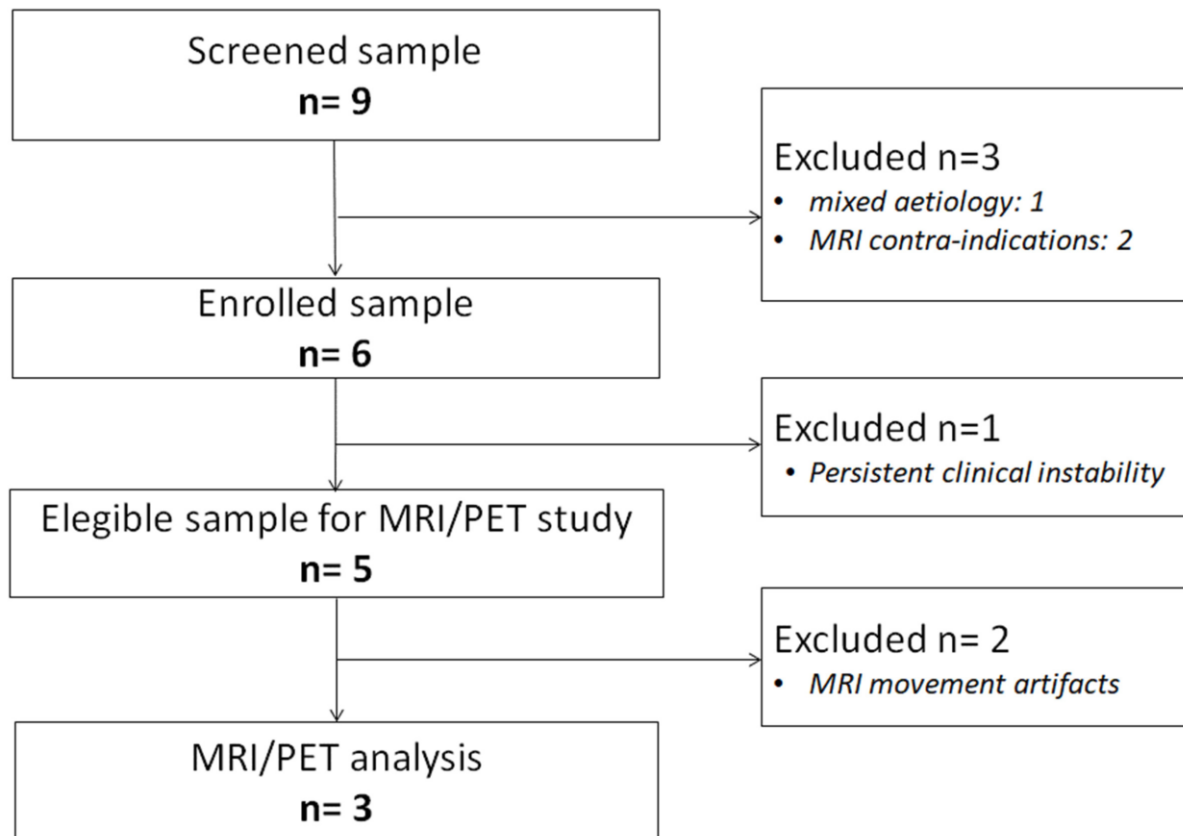


Fig. 4.1 Flow chart of patient selection in each step of the study

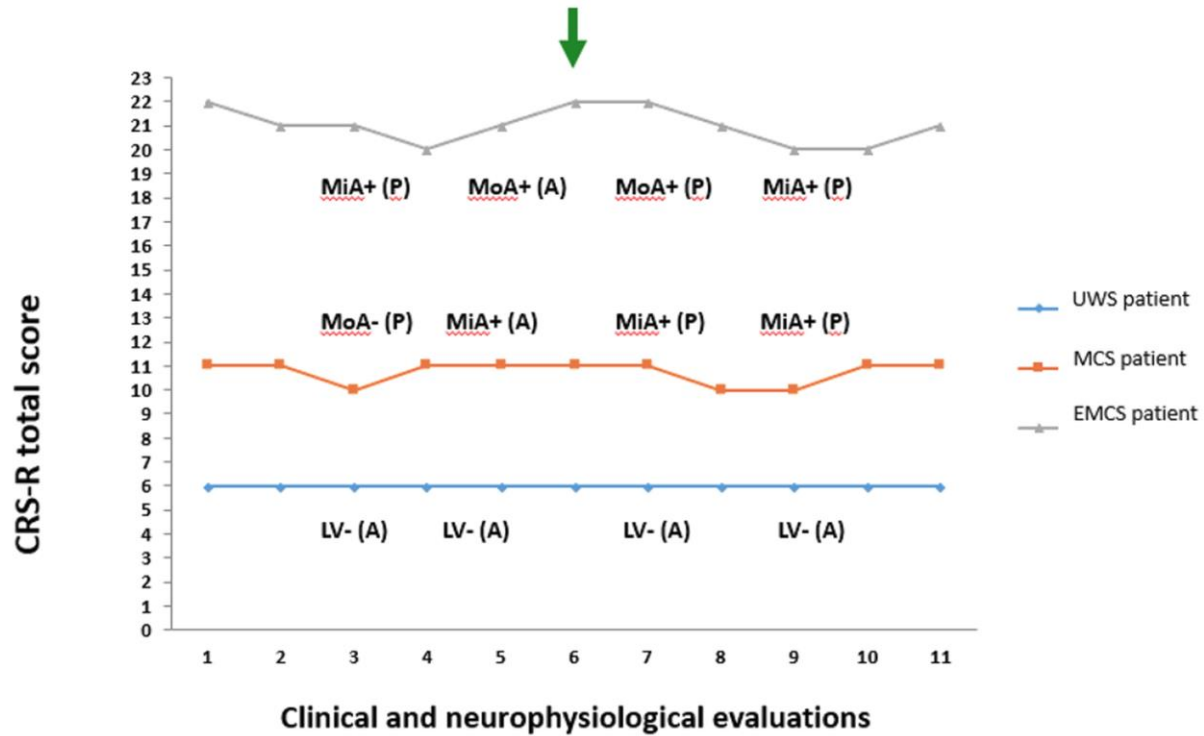


Fig. 4.2 Coma Recovery Scale-Revised total score and neurophysiological (EEG and evoked related potential) evaluations recorded in the 3rd and 5th day before PET/fMRI exam and in the 7th and 9th day after the PET/fMRI exam. The green arrow marks the day of neuroimaging acquisition. The blue diamond and line denote the patient in unresponsive wakefulness syndrome (UWS). The orange square and line denote the patient in minimally conscious state (MCS). The gray triangle and line denote the patient emerged from MCS (EMCS). CRS-R, Coma Recovery Scale-Revised; P, presence of P300 on evoked related potential; A, absence of P300 on evoked related potential; +, presence of EEG reactivity to eye opening and closing; -, absence of EEG reactivity to eye opening and closing; MiA, mildly abnormal EEG background activity; MoA, moderately abnormal EEG background activity; DS, Diffuse slowing EEG background activity; LV, Low voltage EEG background activity.

4.4.2 Neurophysiological Findings

The highest quality neurophysiological findings out of four EEG sessions and four ERP sessions recorded in each patient are summarized in **Fig. 4.2**. In the patient in UWS, we observed a poor organization of cortical activity with predominantly delta activity in the EEG, with an amplitude of less than 20 μV over most brain regions. EEG was not reactive to eye closing (i.e., Low Voltage, LV category) and the patient did not show a P300 in response to the oddball stimulus. In the patient in MCS, we observed predominantly reactive posterior theta EEG activity (amplitude $>20 \mu\text{V}$), with frequent posterior alpha rhythm (i.e., mildly abnormal, MiA category) in three out of four EEG recordings. A P300 cortical response to the oddball stimulus was recorded in three out of four exams. In the patient in EMCS, a predominantly reactive posterior theta EEG activity (amplitude $\geq 20 \mu\text{V}$), with frequent posterior alpha rhythms (i.e., mildly abnormal, MiA EEG category) was recorded in two out of four EEG recordings. In all EEG acquisitions, background activity showed reactivity to eye opening and closing. The “oddball” paradigm evoked a positive cortical component (i.e., P300) in three out of four exams.

4.4.3 Within-Session fMRI Variability

In the patient in EMCS, the DMN appeared spatially preserved during the first (t_1) rs-fMRI acquisition (ROF = 0.19 vs. ROF = 0.01 at t_2), with a main neuronal component (**Fig. 4.3, Table 4.1**). The ECN was well preserved in both acquisitions in the left hemisphere, although in the t_2 rs-fMRI there was some superposition due to other regions, as shown by the negative value of ROF (-0.08 vs. ROF = 0.12 at t_1). The ECN appeared inconsistent in the right hemisphere, and not neuronal in t_1 acquisition. Auditory and salience networks were partially preserved and evident only in the t_2 scan. Moreover, the auditory network appeared more left-lateralized (**Fig. 4.3, Table 4.1**). The sensorimotor network was spatially preserved in t_1 , where it appeared wider for the co-

activation of many nodes outside the network (ROF=-1.71). VL and VO were recognized as not neuronal in both scans, while the spatial pattern of VM appeared to be well preserved in t_1 acquisition, with a higher ROF value (ROF = 0.32 vs. 0.05 at t_2) (**Fig. 4.3, Table 1**).

Table 4.1 ROF values calculated from regions belonging to the GS values, separated into the regions belonging to the network itself and outside the network

Networks	EMCS						MCS						UWS					
	t ₁			t ₂			t ₁			t ₂			t ₁			t ₂		
	In	Out	ROF	In	Out	ROF	ΔROF	In	Out	ROF	In	Out	ROF	ΔROF	In	Out	ROF	ΔROF
Auditory				85	87	-0.01	0.01	41	26	0.06	36	9	0.10	-0.04	108	162	-0.20	0.20
DMN	81	13	0.19	78	76	0.01	0.18	82	8	0.21	107	44	0.18	0.03	53	123	-0.20	-0.20
ECNL	46	27	0.12	57	70	-0.08	0.20	20	142	-0.80	48	88	-0.26	-0.54	29	158	-0.84	-0.84
ECNR				11	0	0.08	-0.08	30	49	-0.15	46	125	-0.60	0.45				
Saliency				30	108	-0.67	0.67	58	303	-2.11	46	228	-1.57	-0.54	16	52	-0.31	1.40
Sensorimotor	39	213	-1.71	2	27	-0.25	-1.46	42	30	0.12	41	13	0.27	-0.15	36	69	-0.32	-0.32
VL								4	79	-0.56	10	75	-0.49	-0.07	42	108	-0.50	0.50
VM	125	37	0.32	37	22	0.05	0.27	93	21	0.26	48	53	-0.02	0.28				
VO								41	54	-0.07	93	57	0.20	-0.27	6	14	-0.04	0.04

*“In” and “Out” represents the total number of regions belonging to an outside of the network. Values of the non-neuronal networks are not presented

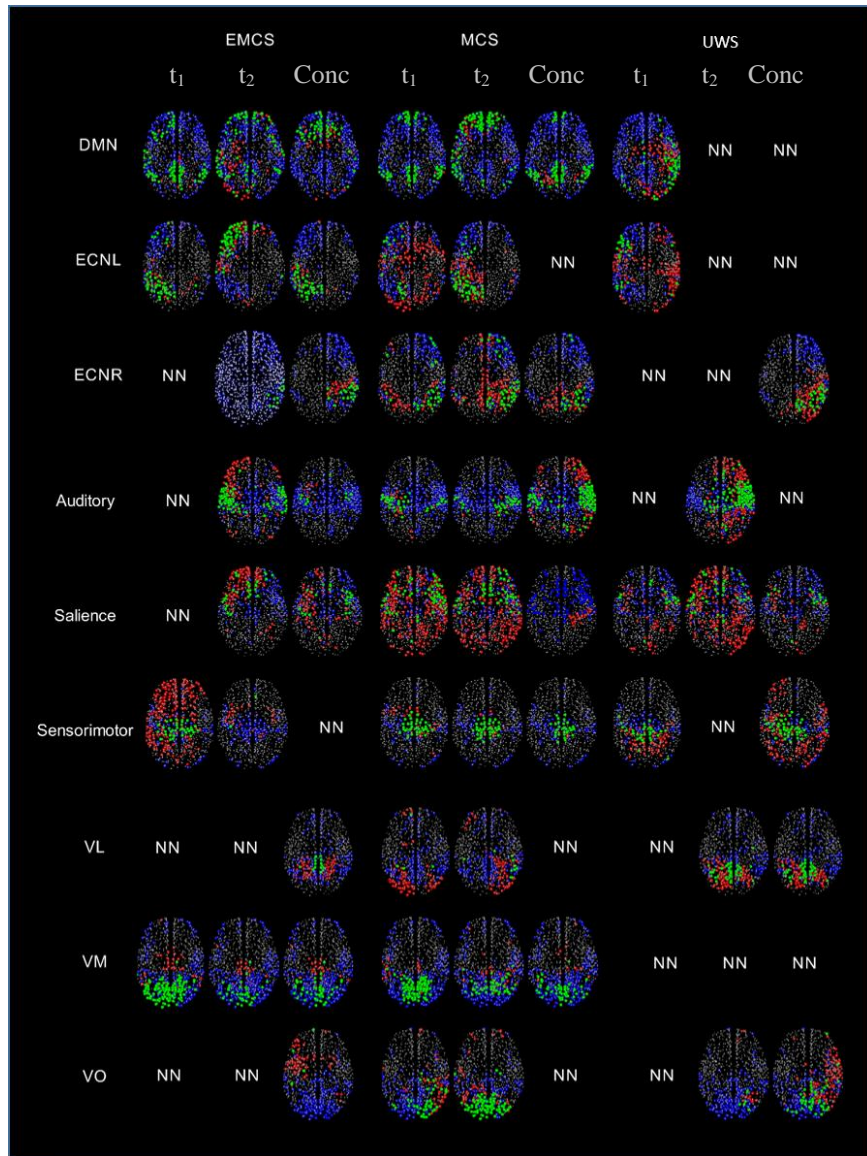


Fig. 4.3 A visual representation of the regions highlighted by the thresholded GS (values greater than half of the maximum GS value for the network), separated by the regions within and outside the network for patients in EMCS, MCS and UWS for nine RSNs. Regions belonging to the network and having GS values greater than the thresholded GS are represented by green, regions which should be in the network but do not have GS values greater than the thresholded GS are represented by blue, regions outside the network but have GS values greater than the thresholded GS are represented by red color. NN represents non-neuronal networks. Here the size of the circle does not represent the value of the GS, all the regions with a GS value are plotted evenly.

In the patient in MCS, the preservation of DMN was clear in both acquisitions (t_1 and t_2), with ROF values of 0.21 and 0.18, respectively. The ECN was partially recognized in both hemispheres in both acquisitions although the number of nodes outside the network was high, as highlighted by the negative values of ROF (**Fig. 4.3, Table 1**). Auditory and sensorimotor networks appeared well preserved in both acquisitions, with a complementary mirrored visualization for the auditory one between t_1 and t_2 . On the other hand, the salience network was evident in both acquisitions, but with a spread of nodes outside the network (ROF = -2.11 and -1.57 at t_1 and t_2 , respectively) (**Fig. 4.3, Table 1**). As for the three visual networks, while the VL was recognized as neuronal in both t_1 and t_2 , but with a poor spatial representation, both VM and VO appeared spatially preserved with a better visualization of VM at t_1 (ROF = 0.26 vs. -0.02 at t_2), and of VO at t_2 (ROF = 0.20 vs. -0.07 at t_1) (**Fig. 4.3, Table 1**).

In the patient in UWS, ECNR was not found in either acquisition, while the DMN and ECNL were partially detected in t_1 , although with high number of regions outside the networks revealed by negative values of ROF (-0.20 and -0.84 respectively) (**Fig. 4.3, Table 1**). In the same manner, salience network was detected in both acquisitions, along with more regions outside the network (ROF = -0.31 and -1.71 respectively). Auditory and sensorimotor networks were identified only in one acquisition, with a higher number of regions belonging outside of the network (ROF = -0.20, -0.32) (**Fig. 4.3, Table 1**). Finally, out of the three visual networks, contrary to the other two patients, VM was not identified in either acquisition. VL and few regions of VO were detected in the second acquisition (**Fig. 4.3, Table 1**). Summarizing, a wider variability was found for ICs representation in the patient in EMCS (mean $|\Delta\text{ROF}| = 0.32$) and in UWS (mean $|\Delta\text{ROF}| = 0.39$) than in MCS case (mean $|\Delta\text{ROF}| = 0.26$).

Comparison between ROF and correlation values for the two acquisitions (obtained between GS and FDG-PET) for the three patients is presented in **Table 4.2**. In 71% of the cases, higher ROF values had higher correlation as well, confirming the appropriateness of the ROF values. Rows demonstrated by red are networks in which the higher ROF did not represent the highest correlation between GS and FDG-PET.

Table 4.2 ROF and Correlation values between GS and FDG-PET) for the two acquisitions of the patients

	EMCS				MCS				UWS/VS			
	ROF		Correlation		ROF		Correlation		ROF		Correlation	
	t ₁	t ₂	t ₁	t ₂	t ₁	t ₂	t ₁	t ₂	t ₁	t ₂	t ₁	t ₂
Auditory					0.06	0.10	0.13	0.19				
DMN	0.19	0.01	0.04	-0.02	0.21	0.18	0.15	0.14				
ECNL	0.12	-0.08	-0.18	-0.12	-0.80	-0.26	-0.08	0.01				
ECNR					-0.15	-0.60	0.09	0.15				
Saliency					-2.11	-1.57	0.11	-0.10	-0.31	-1.71	0.12	0.03
Sensorimotor	-1.71	-0.25	-0.16	0.18	0.12	0.27	0.03	0.05				
VL					-0.56	-0.49	-0.15	0.01				
VM	0.32	0.05	0.33	0.38	0.26	-0.02	0.16	0.08				
VO					-0.07	0.20	-0.01	0.06				

* Only the networks which were recognized as neuronal in both acquisitions are presented.

4.4.4 Mutual fMRI Findings

When considering the best finding between the two rs-fMRI acquisitions (t₁ and t₂) for each network, ICA components classified as neuronal networks were 61, 100, and 44% for patients in EMCS, MCS, and UWS (C.4), respectively. In the patient in EMCS, the DMN and VM networks were fully preserved, and most regions of ECN and sensorimotor were detected as well (C.4). Regions belonging to the network (template) and extra regions were identified in the auditory network, while mainly regions that did not belong to the salience network were detected. Out of the three visual networks, only the VM was identified as neuronal with a good spatial

representation of the network. In the patient in MCS (**C.4**), almost all the networks except the salience network seem to be well preserved, despite the ECNR being spread out to both hemispheres and VL being right-lateralized. In the patient in UWS, the spatial patterns of most of the networks (except the sensorimotor and VM) were not well defined (**C.4**).

The head displacement of the patient in EMCS in the scanner during both t_1 and t_2 acquisitions was 0.09 mm, whereas head displacement for the patient in MCS was 0.03 mm and 0.06 mm, respectively. Overall the lowest displacement was observed for the patient in UWS with the values of 0.02 mm and 0.04 mm respectively (**C.5**). The speed of the patients in the scanner for the t_1 and t_2 acquisitions of patient in EMCS were $2.0 \times 10^{-4} \text{ mms}^{-1}$ and $3.7 \times 10^{-4} \text{ mms}^{-1}$, for patient in MCS: $2.9 \times 10^{-5} \text{ mms}^{-1}$ and $1.9 \times 10^{-4} \text{ mms}^{-1}$, and for patient in UWS: $6.3 \times 10^{-4} \text{ mms}^{-1}$ and $5.6 \times 10^{-5} \text{ mms}^{-1}$ respectively (**C.5**). Low numbers for the speed indicate that rapid movement of the patients in the scanner was very low.

Looking at the spatial distribution of the three most representative axial slices of the GS implemented on the normalized structure of the DMN network, in the best acquisition of both EMCS and MCS, this network was preserved throughout the brain, while in the patient in UWS, the GS seems to be highlighted mostly in the areas outside the network (**Fig. 4.4**). In the concatenated case, the network was present only in the patient in MCS. In the patient in EMCS, only the frontal part was found while in the patient in UWS, the network was not recognized.

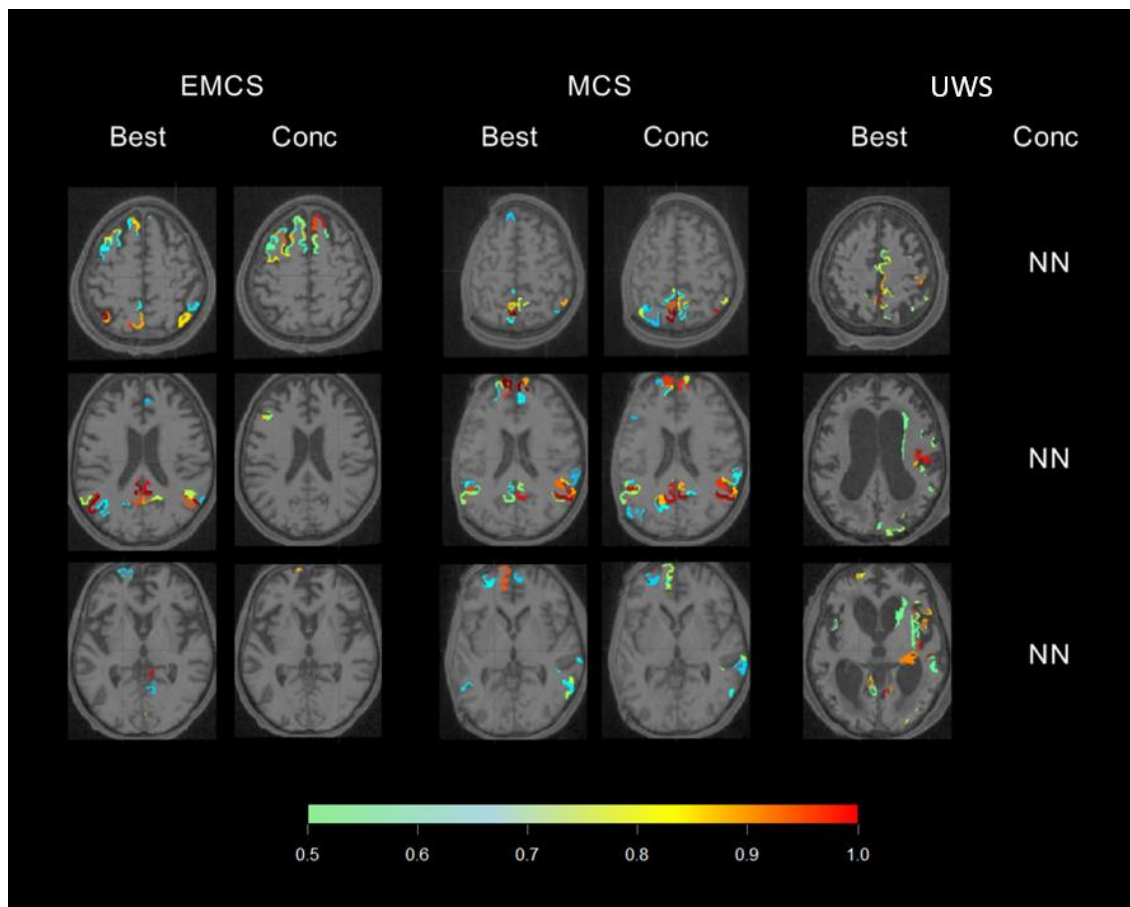


Fig. 4.4 Three most representative axial slices of the GS implemented on the normalized structure of the DMN network are presented for the three patients for the best functional pattern and concatenated data.

4.4.5 Functional-Metabolic Correlation

Considering the functional-metabolic correlation in these patients, a significant positive correlation ($p < 0.05$) existed between the FDG-PET brain activity and GS for all three patients when considering the whole brain (C.6). When considering the best ICs, EMCS had the highest correlation ($r = 0.19$, $p < 0.01$), whereas in the concatenated case, the MCS had the highest correlation ($r = 0.21$, $p < 0.01$). This implies that, when both scans are reasonably good, concatenated data seems to give a better representation. By looking at the three subjects, the patient in UWS had the lowest correlation, with correlation values of 0.08 ($p = 0.02$) and 0.10 ($p < 0.01$) for the best and concatenated data, respectively. Although the correlation values are small, because they are significant, correlation values can be considered valid, considering the low threshold for correlation values with such a large sample size ($N = 1015$) [37]. The positive skewness value of 0.31 for the FDG-PET distribution (Fig. C.7) of the patient in EMCS indicated that there were many regions metabolically more active than the mean PET value. In the patient with UWS, many regions were lower or similar in activity to the mean value, as confirmed by the negative skewness value of -0.01 .

4.5 Discussion

In the present pilot study, we investigated variability within a period of approximately 30 minutes in brain functional connectivity in three severely brain-injured patients (specifically, two patients with DOC and one patient emerged from DOC). Moreover, we employed a methodological approach based on graph theory and ICA, to decompose brain connectivity maps in different networks and to correlate it to glucose metabolic activity simultaneously acquired through a PET/MRI scanner. We demonstrated several differences between the two rs-fMRI

acquisitions that affected in a different way each network and with a different variability in the three patients.

Functional connectivity between the nodes of different resting-state networks is sensitive to normal aging [38] and levels of consciousness [39 – 42], representing a potential biomarker of disease in longitudinal studies [43]. Although being quite variable during pathological conditions, RSNs are thought to be highly reproducible within the same sample [44, 45]. In a recent paper (46), a coactivation patterns approach was used in DOC patients, demonstrating heterogeneous spatial reconfiguration of DMN as well as similar fluctuations of the BOLD signal in patients compared to healthy controls. While these authors referred to BOLD signal oscillations during a single resting-state fMRI session, we scheduled two resting-state acquisitions with a 30-minute interval, to investigate possible variability in functional connectivity within RSNs. Several differences were found between t_1 and t_2 sessions, with higher variability for the EMCS and the UWS case, compared to the patient in MCS. These findings stand in contrast to the substantial stability in the clinical diagnosis determined by repeated behavioral assessments in the present brain-injured patients. However, we speculate that this novel methodological approach is suitable to detect minimal fluctuations in brain connectivity not sufficient to produce relevant behavioral changes (i.e., by changes in clinical diagnosis), but nonetheless are likely related to the variations detected by multiple CRS-R total scores and neurophysiological assessments. However, the nature and clinical significance of the fluctuations of the functional connectivity observed here remain to be established. Furthermore, multimodal investigations, possibly combining neuroimaging and neurophysiological assessment, are necessary to ascertain if variability in brain connectivity is associated to temporal variability of EEG activity characterizing patients with high probability of vigilance fluctuations [47].

On the basis of these considerations, we suggest that this innovative approach for neuroimaging analysis could permit clinicians to better identify the network of best functional brain performance from multiple acquisitions, needed for the diagnostic classification of patients with high likelihood of clinical misdiagnosis. These findings could be extremely interesting, mainly for patients who are clinically diagnosed as UWS, where possible minimal and inconsistent signs of consciousness may not be recognized by behavioral assessments, leading to possible misdiagnosis [12, 48 – 50], and for detecting subtle signs of recovery of consciousness [8, 51, 52]. The same methodology should be applied to larger patient samples, also including a high number of patients without fluctuations of CRS-R total score, to comprehend which variations of functional connectivity might be related to substantial clinical fluctuations or to a basic variability of neuronal network.

The differences in spatial patterns observed in the two acquisitions within the same patient might be due to motion and artifacts. These artifacts affect the nine networks in different manners [33]. However, the present findings suggest that one acquisition is not necessarily capable of detecting spared or impaired networks reliably. Thus, we recommend obtaining more than one acquisition during the scanning interval. Future work should aim to develop a gold standard, that is, the minimum number of acquisitions needed to produce results that will not be significantly different from the results if more acquisitions than this number is being acquired, for choosing the best network out of these acquisitions.

The GS scalar maps of most networks were more similar to the standard template of the networks in the patients in EMCS and MCS than in the patient in UWS. Specifically, all networks of the patient in MCS and seven networks of the patient in EMCS were recognized. This implies that the brain's functional organization was relatively preserved for the patients in EMCS and

MCS. However, the auditory and salience networks had higher GS in regions outside the network, likely in relation to the brain lesions suffered by the patients. In the patient in MCS, although the salience network behaved as neuronal, the spatial pattern was not well-defined, suggesting that this network was distorted and metabolically impaired. Although seven out of the nine networks could be recognized in the patient in UWS, they had hyper-connectivity (confirmed by the negative ROF values), resembling a non-normal condition. This might be related to the severe pathological condition of the patient in UWS, affecting the spatial patterns of most networks [33].

A significant positive correlation was observed between the FDG-PET and GS for all three patients, although the r values were small. Overall, a higher correlation was observed for the patients in EMCS and MCS compared to the UWS case while using the concatenated data. The negative skewness value for the FDG-PET of the patient in UWS (FDG-PET values region by region were normalized by the global signal or mean all over the 1015 regions), is explained by the fact that there are only few regions with metabolic activity above the mean value. In the patient in EMCS, the distribution of the FDG-PET is tailed toward the left with a positive skewness value showing that there are several regions more metabolically active than the average, favoring conscious behavior.

Limitations of the Study

The present study had several limitations. First, we acknowledge that the low number of patients was a major limitation. We selected three patients with different clinical diagnoses (i.e., UWS, MCS and EMCS), to preliminarily investigate possible variability in fMRI connectivity in patients with different levels of consciousness. The small sample size does not allow for generalization, but we hope that our preliminary study could serve as a starting point for devising multicenter studies on larger samples, comparing data of patients with different levels of

consciousness, different etiologies and in different disease phases. Second, we were unable to calculate rigorous associations between patients' behavioral profiles (measured by repeated CRS-R assessments) and their brain connectivity variability, as the two features could not be measured within the same time window.

Subclinical variations in cortical activity that correlate with repeated resting state fMRI may be quantitatively assessed using prolonged EEG monitoring [46]. However, we would like to underline that we enrolled patients that had a stabilized clinical diagnosis (even with slightly fluctuating CRS-R scores), as demonstrated by repeated clinical assessments in the weeks before and after neuroimaging day, and with time from brain injury more than 1 month in order to minimize possible biases related to spontaneous clinical changes in the two different resting MRI acquisitions. Third, a lack of specific alertness level monitoring (such as EEG recording) during scanning acquisition could be a limit for the analysis within and between subjects, as we could not exclude variations in wakefulness as confounders for intrinsic functional connectivity analysis [53]. However, we employed strategies to ensure patients' best vigilance state as described above.

Finally, the lack of a control group was a limitation of the present study, although the choice of the best reference group for patients with DOC is still debated (healthy subjects vs. injured patients that recovered consciousness, such as EMCS). Within-session fMRI variability could have been tested on the controls, if we had the data acquired at two time points in the same scanning session. Nevertheless, rs-fMRI functional connectivity metrics, mainly extracted by ICA, have demonstrated a high test-retest reproducibility [42]. Moreover, other studies have demonstrated the potential of rs-fMRI functional-metabolic correlation assessed by simultaneous PET/MRI in healthy subjects [54], and in other neurological conditions such as Alzheimer disease [55].

4.6 Conclusions

Because repeated fMRI acquisitions within 30 min showed variability in functional connectivity, we suggest performing multiple acquisitions within the same session to pick the best networks (highest ROF) from each acquisition and possibly to compare these findings in longitudinal acquisitions. This procedure, together with the combined simultaneous acquisition of fMRI and PET, could provide useful information for improving characterization of patients with DOC. In a not well-defined number of patients with clinical diagnosis of unresponsive wakefulness syndrome, paraclinical testing (such as fMRI by active task or acquisition in resting state) could reveal cortically mediated cognitive functions (the so-called covert cognition). In this context our approach (i.e., double resting fMRI acquisitions combined with PET scanner) could help clinicians to increase the probability of detecting (spared) functional connectivity, which might provide diagnostic and prognostic information.

4.7 Future Work

This study of patients with disorders of consciousness was a pilot study performed only on three patients. Consequently, we would like to generalize the study to a larger population and see the applicability of GraphICA on distinguishing between different levels of consciousness, such as EMCS, MCS, and UWS/VS using the neuronality test and ROF strategy. Still in most cases, only one acquisition is made to diagnose patients with DOC. Specifically when characterizing VS and MCS patients, a RSN can be easily missed due to some artifacts such as motion of the patient in the scanner. This underlines the importance of acquiring more acquisitions. Even if the network is successfully identified in a single acquisition, but not in others, it still shows that the network is present.

In the future, we will expand upon this pilot study to determine how many acquisitions are necessary to build a gold standard in these patients. The present study on DOC was not performed to understand the mechanism of DOC and to drive any conclusions regarding the pathology; rather, we aimed to develop a necessary strategy to ensure data reliability when acquiring patient data for longitudinal studies. Longitudinal studies require testing the difference between one time-point and another time-point that could be acquired three or six months apart. Therefore, we need to find a strategy to reduce variability within a single scanning session, so that we can justify that the results we see in longitudinal studies are due to the evolution of the patient themselves and not from motion effects or other artifacts. Moreover, steps have been taken in GraphICA to recognize more stable RSNs using the dual regression analysis, which has proven to be a reliable approach [56, 57]. Dual regression allows researchers to investigate individual and group differences in the structure of the networks, as well as to identify subject-specific networks based on networks identified at the group level [57].

Bibliography

- 1) Bernat, J. L. (2006). Chronic disorders of consciousness. *The Lancet*, 367(9517), 1181-1192.
- 2) Sattin, D., De Torres, L., Dolce, G., Arcuri, F., Estraneo, A., Cardinale, V., Piperno, R., Zavatta, E., Formisano, R., D'Ippolito, M., Vassallo, C., Dessi, B., Lamberti, G., Antoniono, E., Lanzilloti, C., Navarro, J., Bramanti, P., Marino, S., Zampolini, M., Scarponi, F., Avesani, R., Salvi, L., Ferro, S., Mazza, L., Fogar, P., Feller, S., De Nigris, F., Martinuzzi, A., Buffoni, M., Pessina, A., Corsico, P. & Leonardi, M. (2017). Analysis of Italian regulations on pathways of care for patients in a vegetative or minimally conscious state. *Functional Neurology*, 32(3), 159.
- 3) Moretta, P., Estraneo, A., De Lucia, L., Cardinale, V., Loreto, V., & Trojano, L. (2014). A study of the psychological distress in family caregivers of patients with prolonged disorders of consciousness during in-hospital rehabilitation. *Clinical Rehabilitation*, 28(7), 717-725.

- 4) Moretta, P., Masotta, O., Crispino, E., Castronovo, G., Ruvolo, S., Montalbano, C., Loreto, V., Trojana, L. & Estraneo, A. (2017). Psychological distress is associated with altered cognitive functioning in family caregivers of patients with disorders of consciousness. *Brain Injury*, 31(8), 1088-1093.
- 5) American Academy of Neurology. (1994). Multi-Society Task Force on PVS. Medical aspects of the persistent vegetative state—First of two parts. *The New England Journal of Medicine*, 330, 1499-1508.
- 6) Giacino, J. T., Ashwal, S., Childs, N., Cranford, R., Jennett, B., Katz, D. I., Kelly, J. P., Rosenberg, J. H., Whyte, J., Zafonte, R. D. & Zasler, N. D. (2002). The minimally conscious state: definition and diagnostic criteria. *Neurology*, 58(3), 349-353.
- 7) Estraneo, A., Moretta, P., Loreto, V., Santoro, L., & Trojano, L. (2014). Clinical and neuropsychological long-term outcomes after late recovery of responsiveness: a case series. *Archives of Physical Medicine and Rehabilitation*, 95(4), 711-716.
- 8) Estraneo, A., & Trojano, L. (2018). Prognosis in disorders of consciousness. In *Coma and disorders of consciousness*, Springer, Cham, 17-36.
- 9) Schnakers, C., & Monti, M. M. (2017). Disorders of consciousness after severe brain injury: therapeutic options. *Current Opinion in Neurology*, 30(6), 573-579.
- 10) Estraneo, A., Pascarella, A., Moretta, P., Masotta, O., Fiorenza, S., Chirico, G., Crispino, E., Loreto, V. & Trojano, L. (2017). Repeated transcranial direct current stimulation in prolonged disorders of consciousness: a double-blind cross-over study. *Journal of the Neurological Sciences*, 375, 464-470.
- 11) Cavaliere, C., Aiello, M., Di Perri, C., Amico, E., Martial, C., Thibaut, A., Laureys, S. & Soddu, A. (2016). Functional connectivity substrates for tDCS response in minimally conscious state patients. *Frontiers in Cellular Neuroscience*, 10, 257.
- 12) Schnakers, C., Vanhaudenhuyse, A., Giacino, J., Ventura, M., Boly, M., Majerus, S., Moonen, G. & Laureys, S. (2009). Diagnostic accuracy of the vegetative and minimally conscious state: clinical consensus versus standardized neurobehavioral assessment. *BMC Neurology*, 9(1), 35.

- 13) Cortese, M. D., Riganello, F., Arcuri, F., Pugliese, M. E., Lucca, L. F., Dolce, G., & Sannita, W. G. (2015). Coma recovery scale-r: variability in the disorder of consciousness. *BMC Neurology*, 15(1), 186.
- 14) Giacino, J. T., Kalmar, K., & Whyte, J. (2004). The JFK Coma Recovery Scale-Revised: measurement characteristics and diagnostic utility. *Archives of Physical Medicine and Rehabilitation*, 85(12), 2020-2029.
- 15) Wannez, S., Heine, L., Thonnard, M., Gosseries, O., Laureys, S., & Coma Science Group Collaborators. (2017). The repetition of behavioral assessments in diagnosis of disorders of consciousness. *Annals of Neurology*, 81(6), 883-889.
- 16) Majerus, S., Gill-Thwaites, H., Andrews, K., & Laureys, S. (2005). Behavioral evaluation of consciousness in severe brain damage. *Progress in Brain Research*, 150, 397-413.
- 17) Cavaliere, C., Aiello, M., Di Perri, C., Fernandez-Espejo, D., Owen, A. M., & Soddu, A. (2015). Diffusion tensor imaging and white matter abnormalities in patients with disorders of consciousness. *Frontiers in Human Neuroscience*, 8, 1028.
- 18) Schiff, N. D. (2006). Multimodal neuroimaging approaches to disorders of consciousness. *The Journal of Head Trauma Rehabilitation*, 21(5), 388-397.
- 19) Bruno, M. A., Majerus, S., Boly, M., Vanhaudenhuyse, A., Schnakers, C., Gosseries, O., Bouveroux, P., Kirsch, M., Demertzi, A., Bernard, C., Hustinx, R., Moonen, G., & Laureys, S. (2012). Functional neuroanatomy underlying the clinical subcategorization of minimally conscious state patients. *Journal of Neurology*, 259(6), 1087-1098.
- 20) Coleman, M. R., Davis, M. H., Rodd, J. M., Robson, T., Ali, A., Owen, A. M., & Pickard, J. D. (2009). Towards the routine use of brain imaging to aid the clinical diagnosis of disorders of consciousness. *Brain*, 132(9), 2541-2552.
- 21) Soddu, A., Gómez, F., Heine, L., Di Perri, C., Bahri, M. A., Voss, H. U., Bruno, M. A., Vanhaudenhuyse, A., Philips, C., Demertzi, A., Chatelle, C., Schrouff, C., Thibaut, A., Charland-Verville, V., Noihomme, Q., Salmon, E., Tshibanda, J. F., Schiff, N. D. and Laureys, S. (2016).

Correlation between resting state fMRI total neuronal activity and PET metabolism in healthy controls and patients with disorders of consciousness. *Brain and Behavior*, 6(1), e00424.

22) Stender, J., Gosseries, O., Bruno, M. A., Charland-Verville, V., Vanhaudenhuyse, A., Demertzi, A., Chatelle, C., Thonnard, M., Thibaut, A., Heine, L. Soddu, A., Boly, M., Schaners, C., Giedde, A. & Laureys, S. (2014). Diagnostic precision of PET imaging and functional MRI in disorders of consciousness: a clinical validation study. *The Lancet*, 384(9942), 514-522.

23) Aiello, M., Cavaliere, C., & Salvatore, M. (2016). Hybrid PET/MR imaging and brain connectivity. *Frontiers in Neuroscience*, 10, 64.

24) Estraneo, A., Moretta, P., De, A. T., Gatta, G., Giacino, J. T., & Trojano, L. (2015). An Italian multicentre validation study of the coma recovery scale-revised. *European Journal of Physical and Rehabilitation Medicine*, 51(5), 627-634.

25) Burgess, A. P. (2019). How conventional visual representations of time-frequency analyses bias our perception of EEG/MEG signals and what to do about it. *Frontiers in Human Neuroscience*, 13, 212.

26) Estraneo, A., Loreto, V., Guarino, I., Boemia, V., Paone, G., Moretta, P., & Trojano, L. (2016). Standard EEG in diagnostic process of prolonged disorders of consciousness. *Clinical Neurophysiology*, 127(6), 2379-2385.

27) Duncan, C. C., Barry, R. J., Connolly, J. F., Fischer, C., Michie, P. T., Näätänen, R., Polich, J., Reinvang, I. & Van Petten, C. (2009). Event-related potentials in clinical research: guidelines for eliciting, recording, and quantifying mismatch negativity, P300, and N400. *Clinical Neurophysiology*, 120(11), 1883-1908.

28) Delso, G., Fürst, S., Jakoby, B., Ladebeck, R., Ganter, C., Nekolla, S. G., Schwaiger, M. & Ziegler, S. I. (2011). Performance measurements of the Siemens mMR integrated whole-body PET/MR scanner. *Journal of Nuclear Medicine*, 52(12), 1914-1922.

29) Berker, Y., Franke, J., Salomon, A., Palmowski, M., Donker, H. C., Temur, Y., Mottaghy, F. M., Kuhl, C., Izquierdo-Garcia, D., Fayad, Z. A., Kiessling, F. & Schulz, V. (2012). MRI-based attenuation correction for hybrid PET/MRI systems: a 4-class tissue segmentation technique using

a combined ultrashort-echo-time/Dixon MRI sequence. *Journal of Nuclear Medicine*, 53(5), 796-804.

30) Ribeiro de Paula, D., Ziegler, E., Abeyasinghe, P. M., Das, T. K., Cavaliere, C., Aiello, M., Heine, L., Perri, C., Demertzi, A., Noirhomme, Q., Charland-Verville, V., Vanhaudenhuyse, A., Stender, J., Gomez, F., Tshibanda, J. L., Laureys, S., Owen, A. & Soddu, A. (2017). A method for independent component graph analysis of resting-state fMRI. *Brain and Behavior*, 7(3), e00626.

31) Beckmann, C. F., DeLuca, M., Devlin, J. T., & Smith, S. M. (2005). Investigations into resting-state connectivity using independent component analysis. *Philosophical Transactions of the Royal Society B: Biological Sciences*, 360(1457), 1001-1013.

32) Demertzi, A., Gomez, F., Crone, J. S., Vanhaudenhuyse, A., Tshibanda, L., Noirhomme, Q., Thonnard, M., Charland-Verville, V., Kirsch, M., Laureys, S. & Soddu, A. (2014). Multiple fMRI system-level baseline connectivity is disrupted in patients with consciousness alterations. *Cortex*, 52, 35-46.

33) Soddu, A., Vanhaudenhuyse, A., Bahri, M. A., Bruno, M. A., Boly, M., Demertzi, A., Tshibanda, J. F., Philips, C., Stanziano, M., Ovadia-Caro, S., Nir, Y., Maquet, P., Papa, M., Malach, R., Laureys, S. & Noirhomme, Q. (2012). Identifying the default-mode component in spatial IC analyses of patients with disorders of consciousness. *Human Brain Mapping*, 33(4), 778-796.

34) Maudoux, A., Lefebvre, P., Cabay, J. E., Demertzi, A., Vanhaudenhuyse, A., Laureys, S., & Soddu, A. (2012). Connectivity graph analysis of the auditory resting state network in tinnitus. *Brain Research*, 1485, 10-21.

35) Gerhard, S., Daducci, A., Lemkaddem, A., Meuli, R., Thiran, J. P., & Hagmann, P. (2011). The connectome viewer toolkit: an open source framework to manage, analyze, and visualize connectomes. *Frontiers in Neuroinformatics*, 5, 3.

36) Fischl, B., Salat, D. H., Busa, E., Albert, M., Dieterich, M., Haselgrove, C., Van der Kouwe, A., Killiany, R., Kennedy, D., Klaveness, S., Montillo, A., Makris, N., Rosen, B. & Dale, A. M.

(2002). Whole brain segmentation: automated labeling of neuroanatomical structures in the human brain. *Neuron*, 33(3), 341-355.

37) Newbold, P., Carlson, W. L., & Thorne, B. (2007). *Statistics for business and economics*. 6.

38) Greicius, M. D., Krasnow, B., Reiss, A. L., & Menon, V. (2003). Functional connectivity in the resting brain: a network analysis of the default mode hypothesis. *Proceedings of the National Academy of Sciences*, 100(1), 253-258.

39) Bonhomme, V., Vanhaudenhuyse, A., Demertzi, A., Bruno, M. A., Jaquet, O., Bahri, M. A., Plenevaux, A., Boly, M., Boveroux, P., Soddu, A., Brichant, J. F., Maquet, P. & Laureys, S. (2016). Resting-state network-specific breakdown of functional connectivity during ketamine alteration of consciousness in volunteers. *Anesthesiology: The Journal of the American Society of Anesthesiologists*, 125(5), 873-888.

40) Guldenmund, P., Gantner, I. S., Baquero, K., Das, T., Demertzi, A., Boveroux, P., Bonhomme, V., Vanhaudenhuyse, A., Bruno, M. A., Gosseries, O., Noirhomme, Q., Kirsch, M., Boly, M., Owen A. M., Laureys, S., Gomez, F. & Soddu, A. (2016). Propofol-induced frontal cortex disconnection: a study of resting-state networks, total brain connectivity, and mean BOLD signal oscillation frequencies. *Brain connectivity*, 6(3), 225-237.

41) Demertzi, A., Antonopoulos, G., Heine, L., Voss, H. U., Crone, J. S., de Los Angeles, C., Bahri, M. A., Di Perri, C., Vanhaudenhuyse, A., Charland-Verville, V., Kronbichler, M., Trinka, E., Philips, C., Gomez, F., Tshibanda, L., Soddu, A., Schiff, N. D., Whitfield-Gabrieli, S. & Laureys, S. (2015). Intrinsic functional connectivity differentiates minimally conscious from unresponsive patients. *Brain*, 138(9), 2619-2631.

42) Vanhaudenhuyse, A., Noirhomme, Q., Tshibanda, L. J. F., Bruno, M. A., Boveroux, P., Schnakers, C., Soddu, A., Perlberg, V., Ledoux, D., Brichant, J. F., Moonen, G., Maquet, P., Greicius, M. D., Laureys, S. & Boly, M. (2009). Default network connectivity reflects the level of consciousness in non-communicative brain-damaged patients. *Brain*, 133(1), 161-171.

43) Persson, J., Pudas, S., Nilsson, L. G., & Nyberg, L. (2014). Longitudinal assessment of default-mode brain function in aging. *Neurobiology of Aging*, 35(9), 2107-2117.

- 44) Jovicich, J., Minati, L., Marizzoni, M., Marchitelli, R., Sala-Llonch, R., Bartrés-Faz, D., Arnold, J., Benninghoff, J., Fiedler, U., Roccatagliata, L., Picco, A., Nobili, F., Blin, O., Bombois, S., Lopes, R., Bordet, R., Sein, J., Ranjeva, J. P., Didic, M., Gros-Dagnac, H., Payoux, P., Zoccatelli, G., Alessandrini, F., Beltramello, A., Bargallo, N., Ferretti, A., Caulo, M., Aiello, M., Cavaliere, C., Soricelli, A., Parnetti, L., Tarducci, R., Floridi, P., Tsolaki, M., Constantinidis, M., Drevelegas, A., Rossini, P. M., Marra, C., Schonknecht, P., Hensch, T., Hoffmann, K. T., Kuijter, J. P., Visser, P. J., Barkhof, F., Frisoni, G. B. & Consortium. P. (2016). Longitudinal reproducibility of default-mode network connectivity in healthy elderly participants: a multicentric resting-state fMRI study. *Neuroimage*, 124, 442-454.
- 45) Termenon, M., Jaillard, A., Delon-Martin, C., & Achard, S. (2016). Reliability of graph analysis of resting state fMRI using test-retest dataset from the Human Connectome Project. *Neuroimage*, 142, 172-187.
- 46) Di Perri, C., Amico, E., Heine, L., Annen, J., Martial, C., Larroque, S. K., Soddu, A., Marinazzo, D. & Laureys, S. (2018). Multifaceted brain networks reconfiguration in disorders of consciousness uncovered by co-activation patterns. *Human Brain Mapping*, 39(1), 89-103.
- 47) Piarulli, A., Bergamasco, M., Thibaut, A., Cologan, V., Gosseries, O., & Laureys, S. (2016). EEG ultradian rhythmicity differences in disorders of consciousness during wakefulness. *Journal of Neurology*, 263(9), 1746-1760.
- 48) Owen, A. M., Coleman, M. R., Boly, M., Davis, M. H., Laureys, S., & Pickard, J. D. (2006). Detecting awareness in the vegetative state. *Science*, 313(5792), 1402-1402.
- 49) Owen, A. M., & Coleman, M. R. (2008). Functional neuroimaging of the vegetative state. *Nature Reviews Neuroscience*, 9(3), 235.
- 50) Owen, A. M., & Coleman, M. R. (2008). Detecting awareness in the vegetative state. *Annals of the New York Academy of Sciences*, 1129(1), 130-138.
- 51) Estraneo, A., Moretta, P., Loreto, V., Lanzillo, B., Santoro, L., & Trojano, L. (2010). Late recovery after traumatic, anoxic, or hemorrhagic long-lasting vegetative state. *Neurology*, 75(3), 239-245.

- 52) Steppacher, I., Kaps, M., & Kissler, J. (2014). Will time heal? A long-term follow-up of severe disorders of consciousness. *Annals of Clinical and Translational Neurology*, 1(6), 401-408.
- 53) Tagliazucchi, E., & Laufs, H. (2014). Decoding wakefulness levels from typical fMRI resting-state data reveals reliable drifts between wakefulness and sleep. *Neuron*, 82(3), 695-708.
- 54) Aiello, M., Salvatore, E., Cachia, A., Pappatà, S., Cavaliere, C., Prinster, A., Nicolai, E., Salvatore, M., Baron, J. C. & Quarantelli, M. (2015). Relationship between simultaneously acquired resting-state regional cerebral glucose metabolism and functional MRI: a PET/MR hybrid scanner study. *Neuroimage*, 113, 111-121.
- 55) Marchitelli, R., Aiello, M., Cachia, A., Quarantelli, M., Cavaliere, C., Postiglione, A., Tedeschi, G., Montella, P., Milan, G., Salvatore, M., Salvatore, E., Baron, J. C. & Pappata, S. (2018). Simultaneous resting-state FDG-PET/fMRI in Alzheimer Disease: Relationship between glucose metabolism and intrinsic activity. *Neuroimage*, 176, 246-258.
- 56) Nickerson, L. D., Smith, S. M., Öngür, D., & Beckmann, C. F. (2017). Using dual regression to investigate network shape and amplitude in functional connectivity analyses. *Frontiers in Neuroscience*, 11, 115.
- 57) Beckmann, C. F., Mackay, C. E., Filippini, N., & Smith, S. M. (2009). Group comparison of resting-state FMRI data using multi-subject ICA and dual regression. *Neuroimage*, 47(Suppl 1), S148.

Chapter 5

Discussion and Future Work

5.1 Discussion

This thesis has focused on novel techniques and tools that can be used to study functional connectivity changes of the brain. We have applied these tools to three different populations representing healthy and diseased brains. We investigated the functional brain connectivity in altered states of consciousness as induced by propofol under a naturalistic paradigm, and in pathological conditions—tinnitus and severe brain injury—using the generalized Ising model (GIM) and independent component graph analysis (GraphICA) [1], respectively. Our results indicate that both Ising model and GraphICA are promising approaches for studying healthy and diseased brain dynamics [2, 3].

5.1.1 The Generalized Ising Model

Propofol is a short-acting medication that results in decreased levels of consciousness and is used for general anesthesia [4]. Although it is the most commonly used anesthetic in the world, much remains unknown about the mechanisms by which it induces a loss of consciousness. Characterizing anesthesia-induced alterations to brain network activity provides a powerful framework for understanding the neural mechanisms of unconsciousness. Therefore, we used the GIM to study changes in functional connectivity with propofol-induced sedation in healthy subjects while they listened to an audio clip from a movie. The external stimulus (audio clip) is believed to be at least partially driving a synchronization process of the brain activity and provides a similar conscious experience in different subjects. In order to observe the common

synchronization among the subjects, a novel technique called the inter subject correlation (ISC) was implemented [5].

The GIM has proven successful in explaining the brain's behaviour at the critical temperature (i.e., temperature at which the transition from ordered to disordered state occurs) (T_c) in the awake condition without any stimulus [6, 7, 8]. To our knowledge, no studies have thus far successfully modelled brain activity during a real-life complex stimulus at various stages of wakefulness. We showed that the GIM—modified to incorporate the naturalistic external field—was able to fit the empirical task fMRI data (data obtained while listening to the audio clip) in the awake state, in mild sedation, in deep sedation, and in recovery, at a temperature T^* which is well above the critical temperature. T^* is the temperature that minimizes the distance between the normalized empirical and simulated inter-subject correlation (ISC), for which a similar pattern to that of the empirical ISC was observed. Moreover, the critical temperatures in the stimulated scenario were lower than the critical temperature in the resting condition. The system tends to become more disordered due to the mixed signs of coupling strengths between the features of the audio clip and the spins, shifting the critical temperature to lower values. This shifting was more prominent in non-sedation than in sedation, due to high engagement of the subjects with the movie in the non-sedative case.

The ISC was witnessed only in the task condition (with stimulation), but not in the resting state condition, confirming the necessity of a driving force to synchronize the brain regions among subjects. Moreover, in agreement with previous studies, synchronization was more evident during the awake and recovery conditions compared to sedation, suggesting an absence of awareness of the stimulus during sedation [9]. Primary auditory, language, and the fronto-parietal regions belonging to the executive control network appear to have strong ISC during the awake state;

they are disrupted during mild and deep sedations; and they are re-established in recovery, as reported in previous studies [10].

We modified the existing generalized Ising model and demonstrated for the first time that it can be used to model the brain activity of awake as well as sedated subjects when the subjects were exposed to a naturalistic stimulus. This is challenging, since the variation of the naturalistic stimulus is not repetitive, but is random and complicated. This project showed that the simple generalized Ising model can be extended to model the functional connectivity in situations where a time varying stimulation is applied.

The GIM with an external field combined with the novel ISC technique could provide an alternative way to calculate a measure of awareness a non-responsive patient might have. The main advantage of using the GIM is that, it can be simulated using structural connectivity and coupling strengths of these patients which can be hypothetically altered, until a similar ISC (conscious experience) of the healthy subject is obtained. Coupling strengths can be assumed to be related with the metabolic activity. Astrocytes, are cells in the neuronal system which provide structural and functional support to the neurons and also assist in controlling the metabolic activity, by regulating the blood flow to regions of the brain. Inflammation in these astrocytes tend to inhibit the blood flow, resulting in reduction of metabolic activity. Treating these inflamed astrocytes, might help to re-gain the metabolic activity and finally increase the coupling strengths. In this regard, the simulations might provide some hints to the clinicians on which structural connectivity or brain regions of these patients should be mainly targeted to re-establish similar conscious experience of a healthy person.

5.1.2 Tinnitus

Tinnitus, the perception of noise or ringing in the ears in the absence of an external stimulus, is often a disturbing symptom for which the underlying functional neuroanatomy is not fully understood [11]. GraphICA was implemented in order to extract the networks and to evaluate the functional connectivity patterns in patients suffering from tinnitus. Stepwise-fit analysis was performed to investigate whether a correlation exists between tinnitus behavioural scores and functional brain connectivity of five resting state networks comprising the auditory, the default mode, the external control left and right, and the salience network. Results indicated that alterations of functional interactions between key neural circuits of the brain are not limited to one single network. In particular, tinnitus distress showed a strong positive correlation with the connectivity pattern within and between the right executive control network and the other four resting state networks, indicating that tinnitus distress is probably the consequence of a hyperactive attentive condition [2].

Lack of a control group from the same scanner was a limitation in the tinnitus study. Control data were not collected due to ethical issues with scanning controls in the hospital, where only scans of pathological conditions are performed. With respect to **Fig. 3.1**, it would be extremely important to have controls because this would enable us to see the distribution of each network with respect to other networks in the healthy brain. It would then allow us to determine whether the distribution of the tinnitus population is significantly different from the healthy controls, in order to conclude whether it is a sign of pathology. In future studies, controls for the study of tinnitus should be a population with hearing impairment without a tinnitus experience, because tinnitus often creates hearing impairment. Despite this limitation, it is important to stress that we found correlations within the tinnitus group itself, suggesting that the findings are related

to tinnitus perception. Further, when examining the correlation of BSs with GSs in tinnitus patients, we believe that the inclusion of control data will bias the results due to the lower variability in the BSs. For example, controls might not have any level of distress and therefore it would not be appropriate to consider the correlation between distress and GS. On the other hand, having the control data would have permitted us to perform additional analyses comparing controls and tinnitus patients. Calculating the GSs of the patients and controls using GraphICA would have allowed us to see the regions showing differences in the GSs between the two populations. This would have given us further information on which regions are involved in tinnitus.

Despite these limitations, we were able to show that GraphICA was a valuable tool in investigating this patient population, especially when differences leading to the pathology might be quite subtle.

5.1.3 Disorders of Consciousness (DOC)

Clinical history and behavioural assessments are often not sufficient to give an accurate diagnosis and prognosis of individuals with disorders of consciousness. Multimodal neuroimaging markers combining clinical and neuroimaging techniques have been developed to support clinical assessments of these patients [12]. We assessed the functional connectivity of three severely brain injured patients in the exit minimally conscious state (EMCS), in the minimally conscious state (MCS), and in the unresponsive wakefulness syndrome/vegetative state (UWS/VS), using data obtained from hybrid FDG-PET/MRI. ICA was implemented on the rs-fMRI data (which were acquired with a temporal gap of 30 minutes) to extract the resting-state networks, and graph theory was applied to visualize these networks. Functional connectivity analysis calculated using the graph strengths of each region showed several differences between the two rs-fMRI acquisitions. Each network was affected in a different way with different variability for the three patients, which

might be attributed to motion and artifacts [3]. Moreover, a higher functional/metabolic correlation was demonstrated for EMCS and MCS compared to UWS/VS when using the best graph strength maps, which were characterized by the highest ratio of fit (the ratio between regions outside the network subtracted from regions belonging to the network, over the actual total number of regions belonging to the network). These findings suggest that multiple acquisitions in the same scanning session should be acquired and compared with longitudinal acquisitions, in order to reduce the mis-diagnosis of patients.

Again, in this study the lack of a control group from the same scanner was a constraint. The choice of an adequate control group itself is a challenging issue, considering that similar brain lesions can lead to different consciousness statuses in different patients. Certainly, a challenge in inter-subject correlation analysis is to define the required sample size in the way that the results are reliable [13]. As widely reported in literature, each Disorders of Consciousness (DOC) patient represents a unique case with specific brain lesions and clinical/imaging patterns that often affect the translatability of results from group-level to single-subject. In this context, we decided to limit our study to only three cases. In order to show for the first time inter-subject variations of functional connectivity patterns in a DOC patient, analyzed by a recently published graph-based ICA method (GraphICA), we decided to describe the potentiality of this pivotal PET/MR study with two repeated resting fMRI acquisitions in the simplest experimental design. For this reason, we selected three patients with different clinical diagnosis (i.e. VS/UWS, MCS and EMCS), to preliminarily investigate possible variability in fMRI connectivity in patients with different level of consciousness. We acknowledge that the small sample size does not allow any generalization and a study using a larger number of patients with this tool would provide the opportunity to explore many aspects of DOC. However, we believe that our innovative methodological approach,

coupling double acquisition of resting state fMRI with PET, along with the neuronality test and ratio of fitness, could provide clinicians with information useful to characterize the best patients' functional brain organization. Regardless of the huge structural changes in the brain due to severe brain injury, GraphICA was still able to preprocess and parcellate the data and successfully provide information on the functional connectivity of these patients.

We were able to show, that this novel combination of graph theory and ICA can be used not only to infer information about patients with subtle brain damage, but can be extended to brains which are severely damaged after serious brain injuries. To our knowledge, GraphICA is the first tool that applies graph theory to brain networks derived from ICA to evaluate graph properties of the brain network. Most of the available tools use correlation matrices to assess functional connectivity or compare directly scalar maps extracted from ICA. GraphICA approach could be further used to calculate any other graph properties such as the degree, small-worldness, efficiency, beyond the graph strength calculated for the described. These properties will enable to obtain more information about the organization of the brain at the network level and provide more insights on the functionality of the brain.

5.2 Future Work

The novel tools we have used in this thesis can be used to study brain functionality in many important contexts. GIM can be applied onto patients with altered perception of consciousness to assess the similar conscious experience they have compared to a healthy person. GraphICA could be applied to any population with abnormal brains to describe their functional connectivity and can be widely adopted to answer many questions in neuroscience.

The three studies in this thesis focus on techniques and models which can be used to investigate the changes in brain activity in populations with altered states of consciousness. The

GIM incorporated with external field was able to model the brain activity of unconscious state in addition to awake state. The details of the effects of anesthetics, once introduced into the body, can be seen in three stages; induction period, maintenance period and emergence period. As reported in Brown et al. [14], during the induction period (mild sedation), a paradoxical excitation (purposeless movements) is observed, where the EEG pattern resembles a minimal conscious state. In the maintenance period (unconscious), the overall EEG pattern looks like a vegetative state. Finally, the EEG pattern of emergence from anesthesia looks similar to the awake state.

Some patients with DOC may not be able to communicate while continuing to possess adequate levels of cognition and the ability to understand events happening in their environment [10]. The simulations on these patients will depend mainly on the interaction of the patients with the external stimulus while a minor contribution arises from the structural connectivity as well. Since the structural connectivity of the UWS patient might be more disrupted compared to healthy subjects and the patient might have less interaction with the external stimulation, we expect the results to be closely related to that of the unconsciousness state discussed in Chapter 2. For the MCS patient, due to moderate amount of disruption in the structural connectivity and moderate interaction with the external stimulation, it might closely resemble the mild sedative state as discussed in Chapter 2. The EMCS patient closely resembles a healthy subject, and might have results similar to the awake state as discussed in Chapter 2.

In this context, the GIM can be applied onto DOC patients (EMCS, MCS and UWS), using their disrupted connectivity, although the effect of pharmacologically induced unconsciousness might sometimes vary with respect to pathologically induced unconsciousness. We might also be able to obtain a measure of the distress level that a non-responsive patient is experiencing, by using the classification process as mentioned in the future work in Chapter 3. This might shed light onto

patients with DOC to assist in relieving their distress levels and enable at least to some extent to regain their consciousness. In conclusion, the tools developed in this thesis can be applied to a wide variety of patient populations and which might allow to solve further problems in neuroscience, specifically benefiting patients to move forward in their lives.

Bibliography

- 1) Ribeiro de Paula, D., Ziegler, E., Abeyasinghe, P. M., Das, T. K., Cavaliere, C., Aiello, M., Heine, L., Perri, C., Demertzi, A., Noirhomme, Q., Charland-Verville, V., Vanhaudenhuyse, A., Stender, J., Gomez, F., Tshibanda, J. L., Laureys, S., Owen, A. & Soddu, A. (2017). A method for independent component graph analysis of resting-state fMRI. *Brain and Behavior*, 7(3), e00626.
- 2) Kandeepan, S., Maudoux, A., de Paula, D. R., Zheng, J. Y., Cabay, J. E., Gómez, F., Chronik, B. A., De Ridder, D., Vanneste, S. & Soddu, A. (2019). Tinnitus distress: a paradoxical attention to the sound? *Journal of Neurology*, 1-11.
- 3) Cavaliere, C., Kandeepan, S., Aiello, M., Ribeiro de Paula, D., Marchitelli, R., Fiorenza, S., Orsini, M., Trojano, L., Masotta, O., St. Lawrence, K., Loreto, V., Chronik, B. A., Nicolai, E., Soddu, A. & Estraneo, A. (2018). Multimodal neuroimaging approach to variability of functional connectivity in disorders of consciousness: a PET/MRI pilot study. *Frontiers in Neurology*, 9, 861.
- 4) Tobias, J. D., & Leder, M. (2011). Procedural sedation: a review of sedative agents, monitoring, and management of complications. *Saudi Journal of Anaesthesia*, 5(4), 395.
- 5) Pajula, J., Kauppi, J. P., & Tohka, J. (2012). Inter-subject correlation in fMRI: method validation against stimulus-model based analysis. *PLOS One*, 7(8), e41196.
- 6) Fraiman, D., Balenzuela, P., Foss, J., & Chialvo, D. R. (2009). Ising-like dynamics in large-scale functional brain networks. *Physical Review E*, 79(6), 061922.
- 7) Abeyasinghe, P. M., de Paula, D. R., Khajehabdollahi, S., Valluri, S. R., Owen, A. M., & Soddu, A. (2018). Role of dimensionality in predicting the spontaneous behavior of the brain using the

classical Ising model and the Ising model implemented on a structural connectome. *Brain Connectivity*, 8(7), 444-455.

8) Marinazzo, D., Pellicoro, M., Wu, G., Angelini, L., Cortés, J. M., & Stramaglia, S. (2014). Information transfer and criticality in the Ising model on the human connectome. *PLOS One*, 9(4), e93616.

9) Boly, M., Moran, R., Murphy, M., Boveroux, P., Bruno, M. A., Noirhomme, Q., Ledoux, D., Bonhomme, V., Brichant, J. F., Tononi, G., Laureys, S. & Friston, K. (2012). Connectivity changes underlying spectral EEG changes during propofol-induced loss of consciousness. *Journal of Neuroscience*, 32(20), 7082-7090.

10) Naci, L., Cusack, R., Anello, M., & Owen, A. M. (2014). A common neural code for similar conscious experiences in different individuals. *Proceedings of the National Academy of Sciences*, 111(39), 14277-14282.

11) Jastreboff, P. J. (1990). Phantom auditory perception (tinnitus): mechanisms of generation and perception. *Neuroscience Research*, 8(4):221-254.

12) Aiello, M., Salvatore, E., Cachia, A., Pappatà, S., Cavaliere, C., Prinster, A., Nicolai, E., Salvatore, M., Baron, J. C. & Quarantelli, M. (2015). Relationship between simultaneously acquired resting-state regional cerebral glucose metabolism and functional MRI: a PET/MR hybrid scanner study. *Neuroimage*, 113, 111-121.

13) Pajula, J., & Tohka, J. (2016). How many is enough? Effect of sample size in inter-subject correlation analysis of fMRI. *Computational Intelligence and Neuroscience*, 2016, 2.

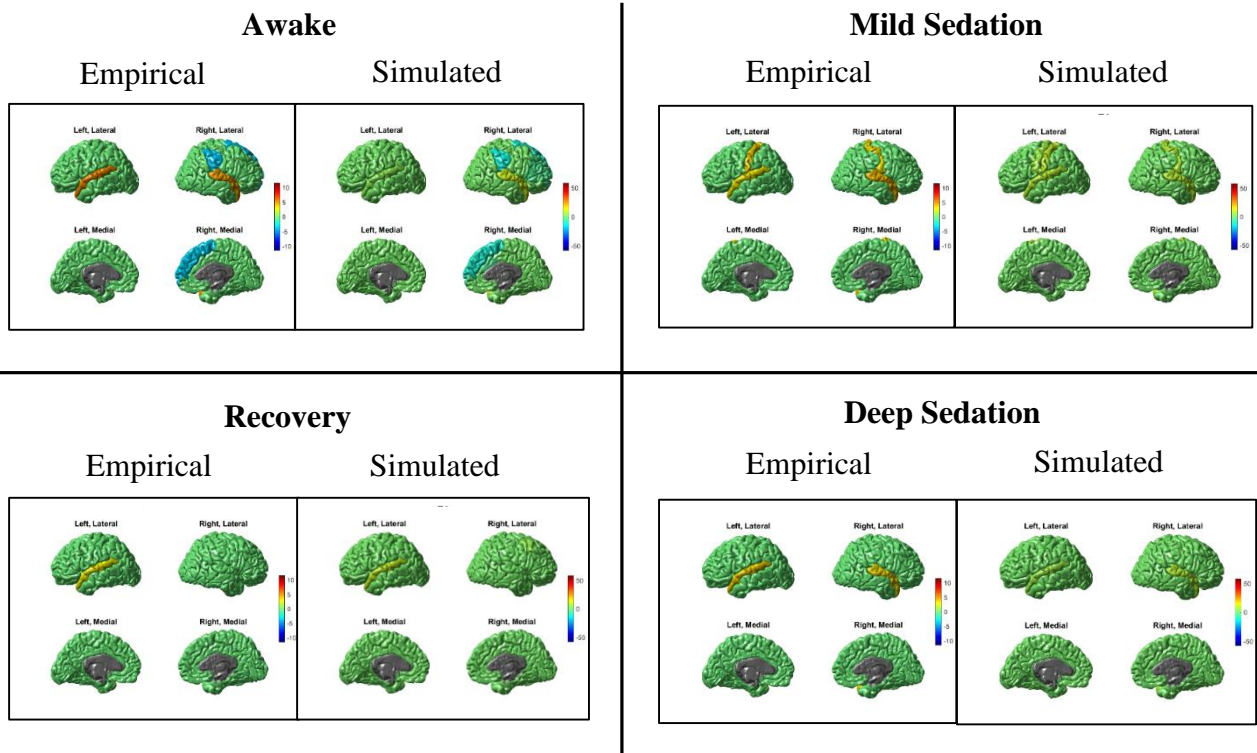
14) Brown, E. N., Lydic, R., & Schiff, N. D. (2010). General anesthesia, sleep, and coma. *New England Journal of Medicine*, 363(27), 2638-2650.

Appendix A

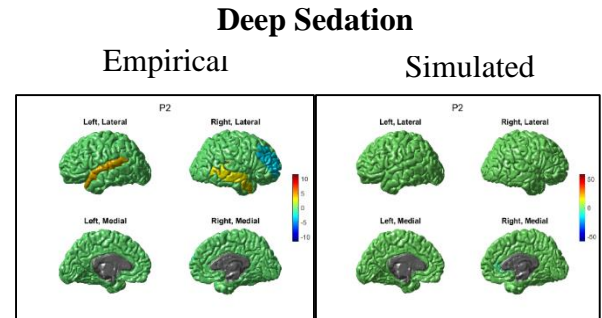
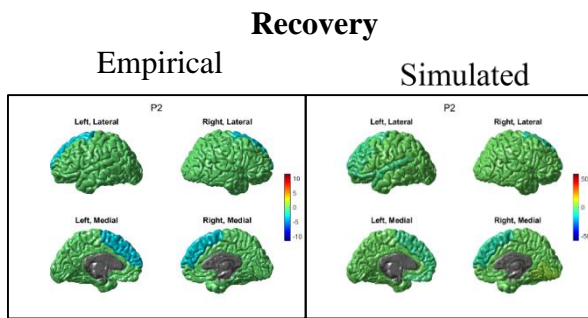
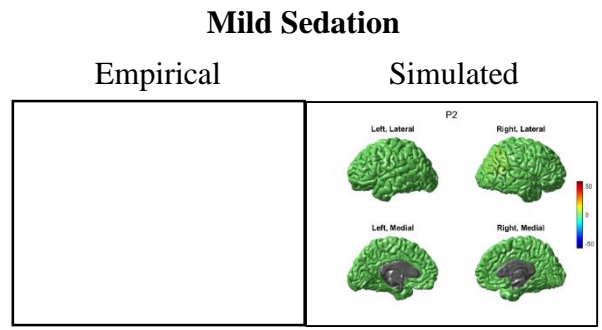
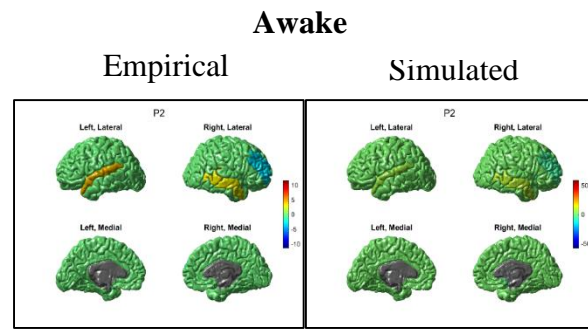
Appendices: Chapter 2

A.1 t -maps of the empirical and simulated data at T^* obtained from the β -values (coefficients) calculated using GLM between the subjects' time series and the 18 audio features (P1 – P18) are presented. Only t -values for which the p -values were less than 0.01 are presented. The audio features are as follows: P1 – energy, P2 – entropy of energy, P3 – spectral spread, P4 – spectral flux, P5 – spectral roll-off and P6 - P18 are the thirteen Mel frequencies.

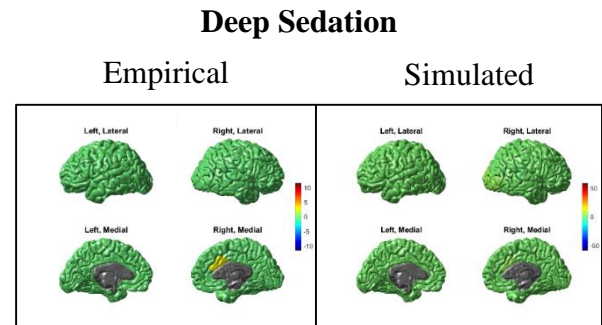
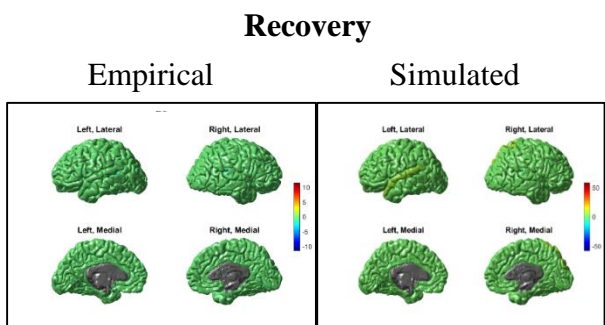
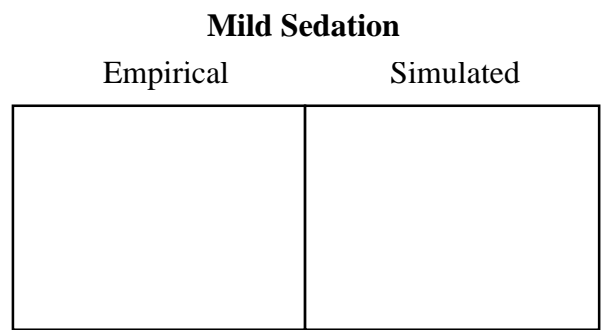
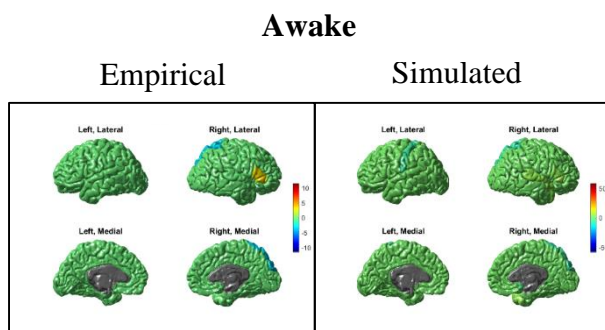
P1



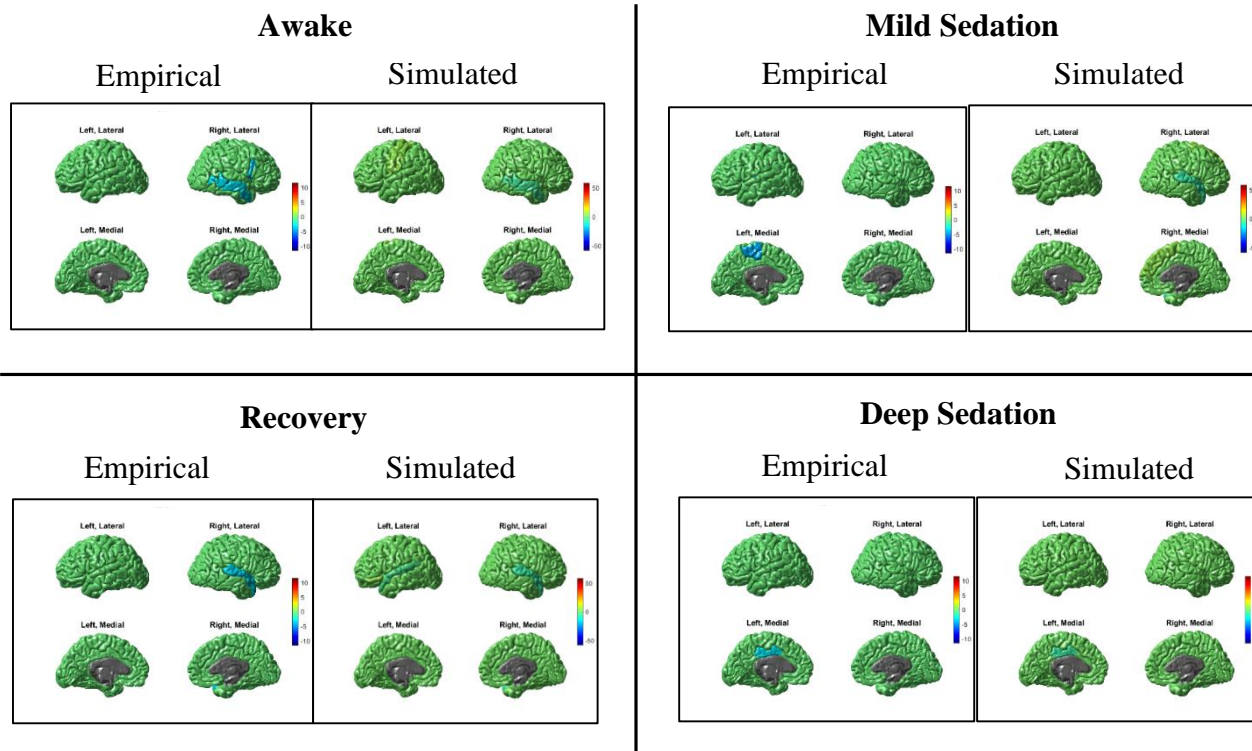
P2



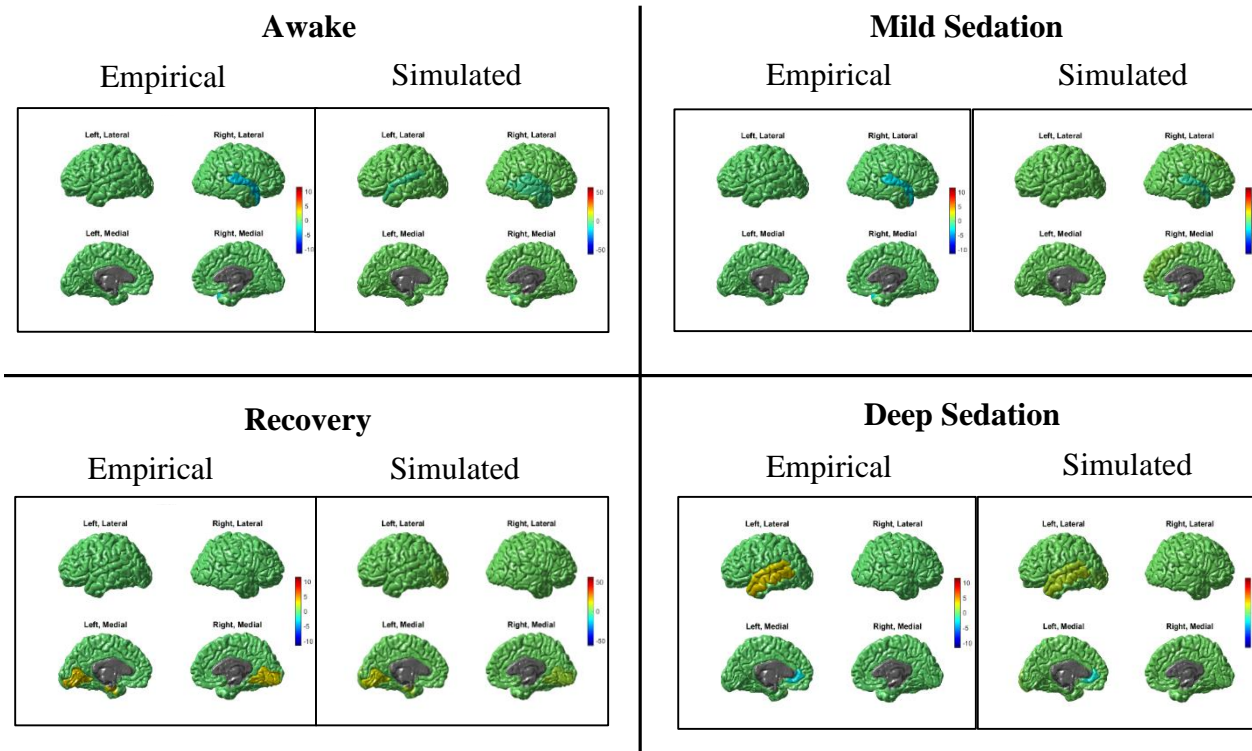
P3



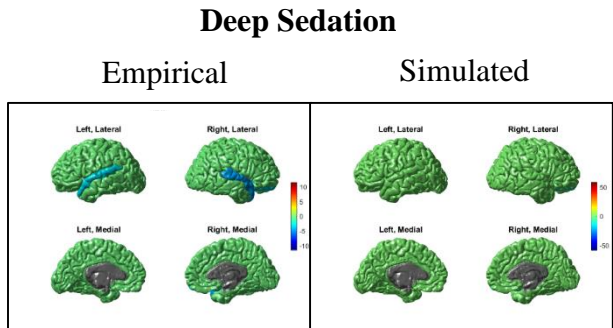
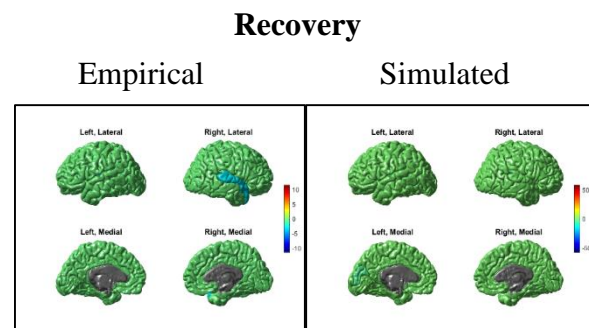
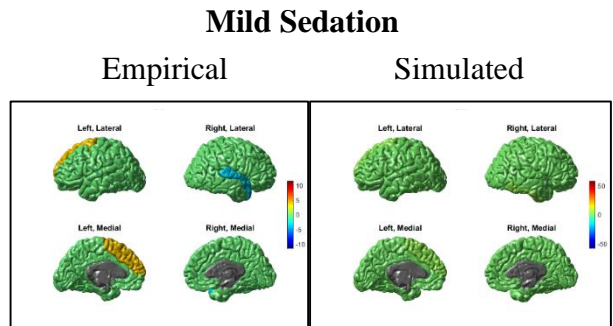
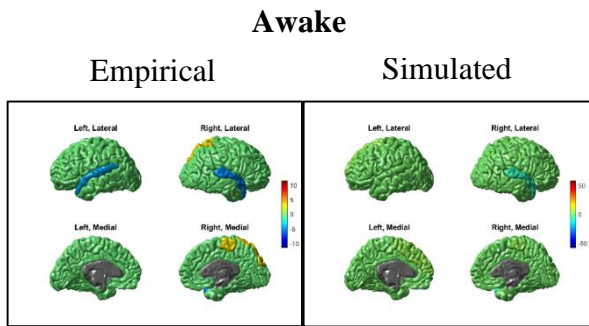
P4



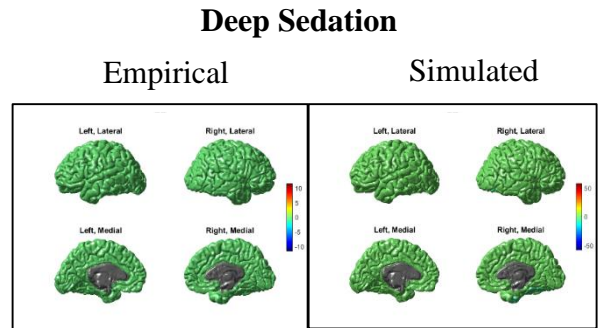
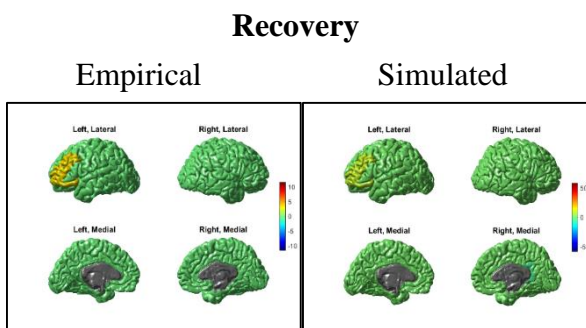
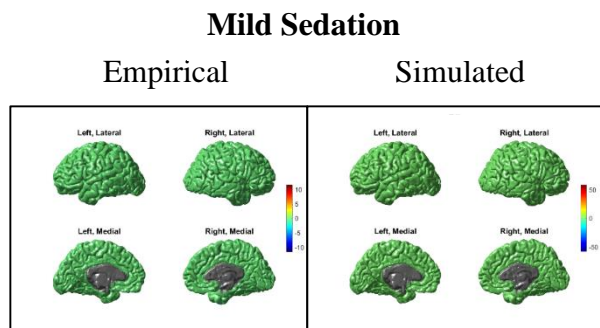
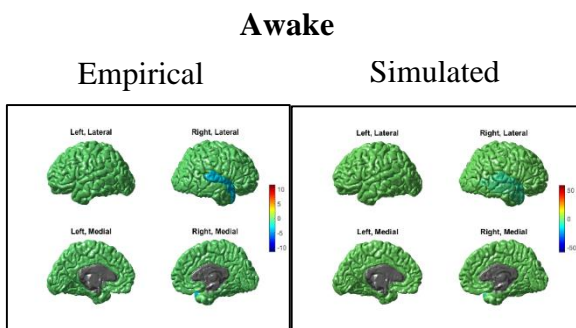
P5



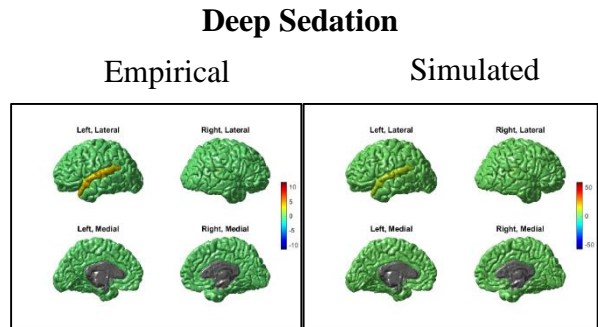
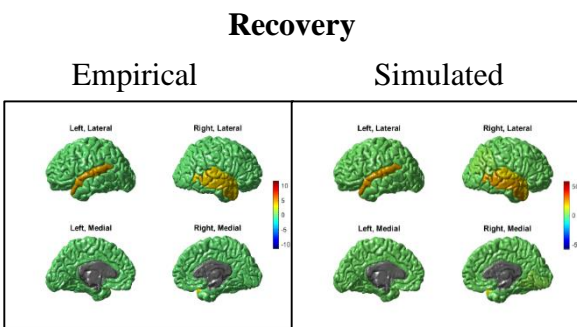
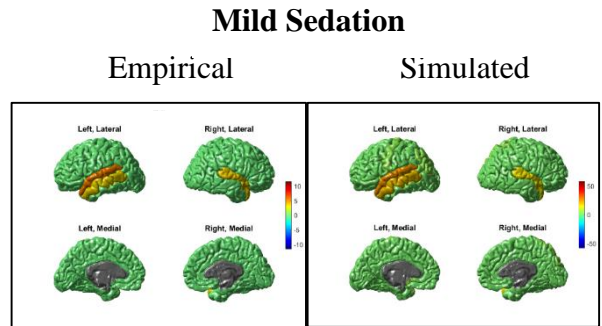
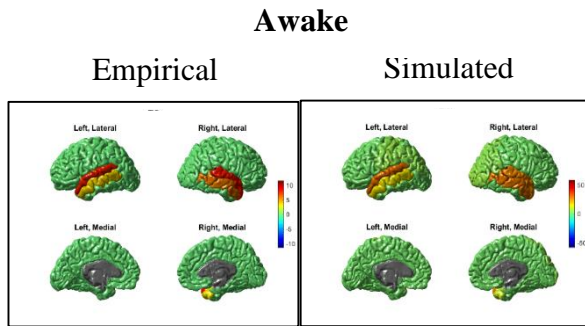
P6



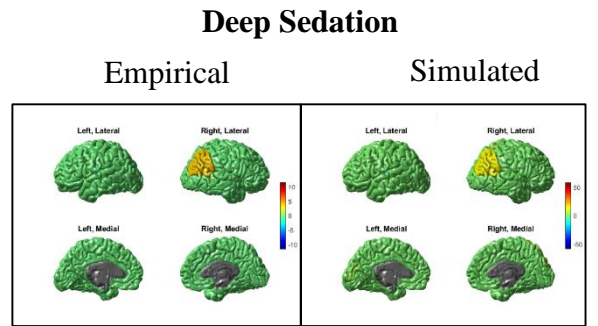
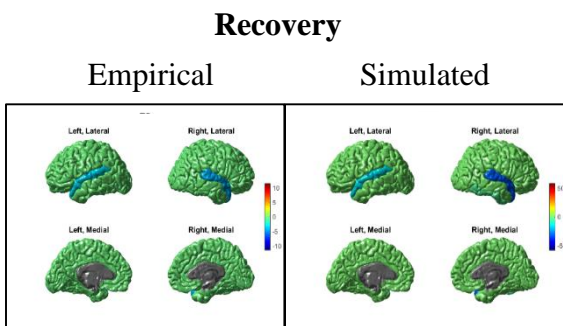
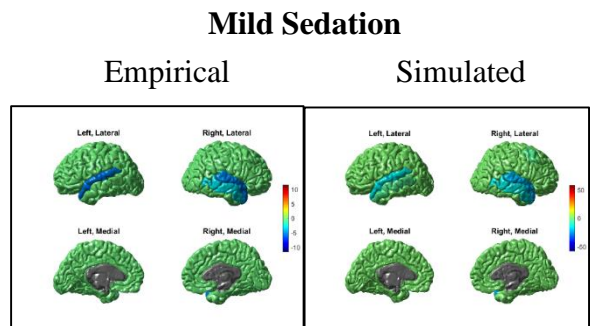
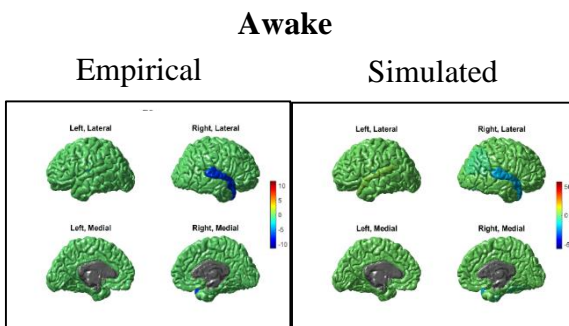
P7



P8



P9

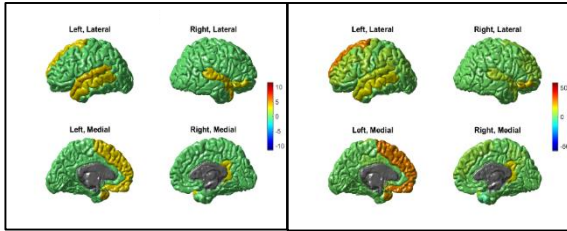


P10

Awake

Empirical

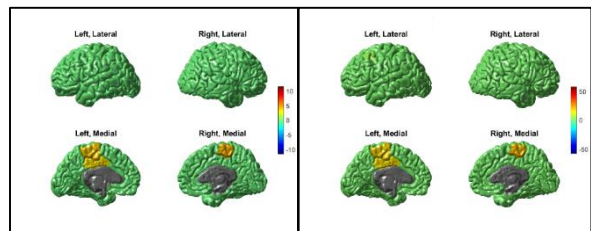
Simulated



Mild Sedation

Empirical

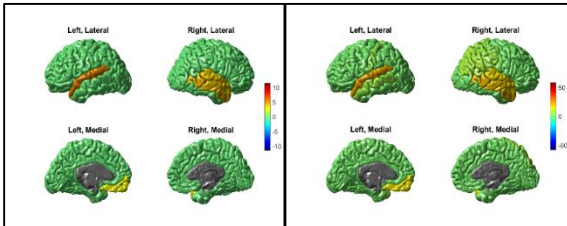
Simulated



Recovery

Empirical

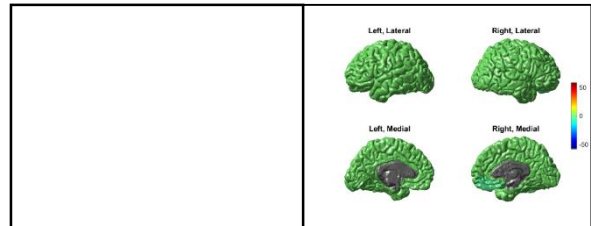
Simulated



Deep Sedation

Empirical

Simulated

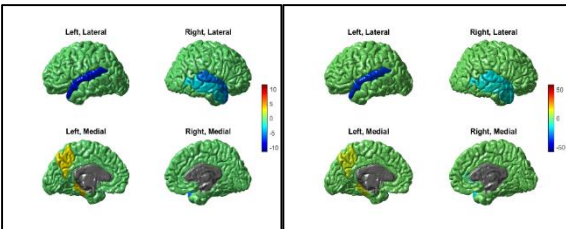


P11

Awake

Empirical

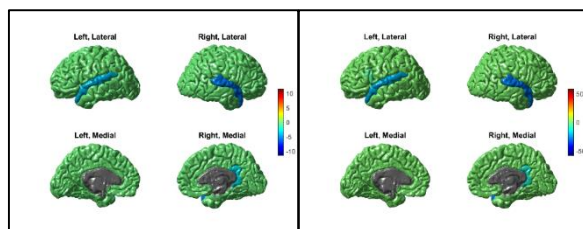
Simulated



Mild Sedation

Empirical

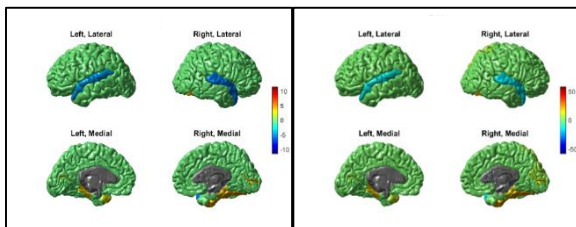
Simulated



Recovery

Empirical

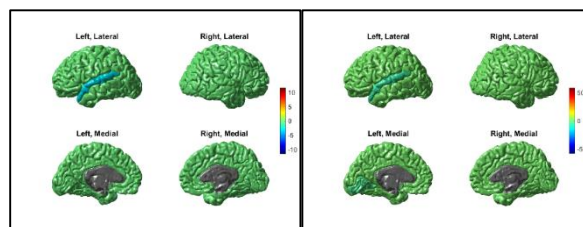
Simulated



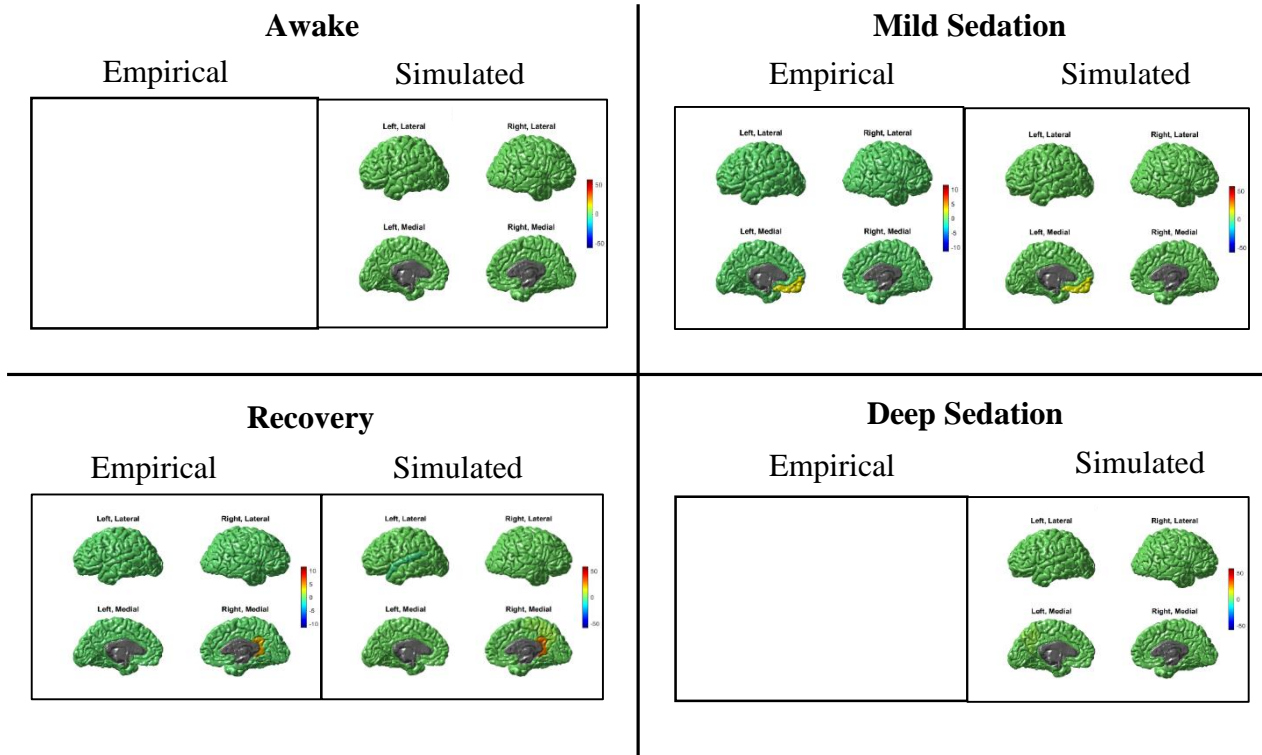
Deep Sedation

Empirical

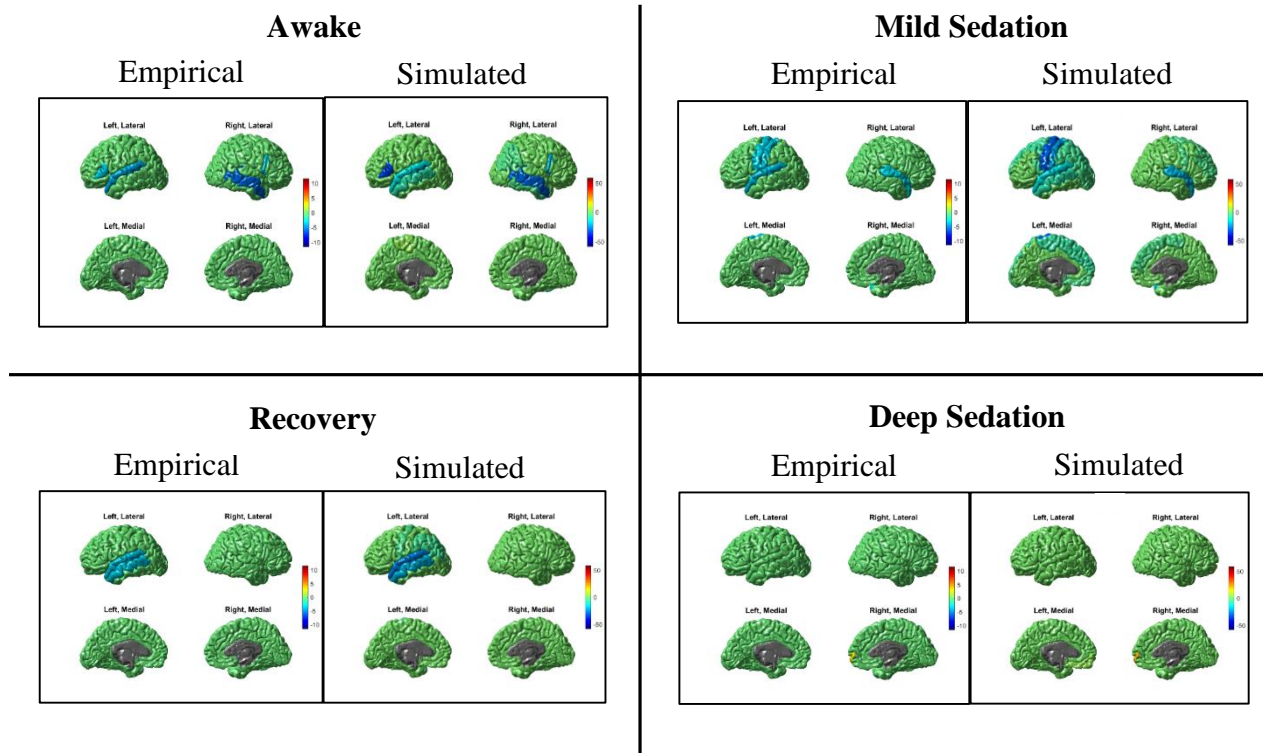
Simulated



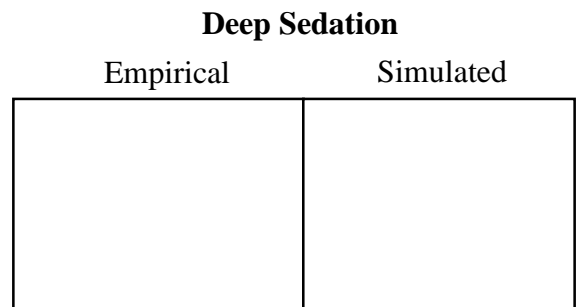
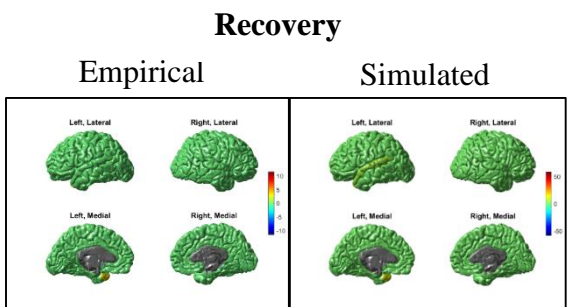
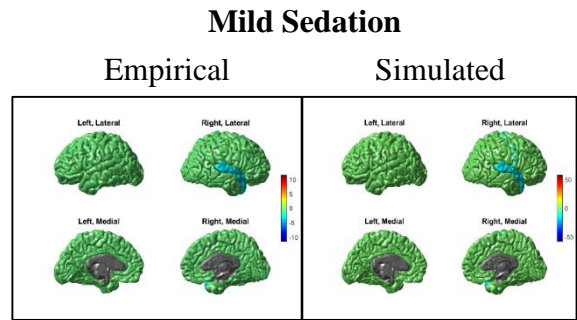
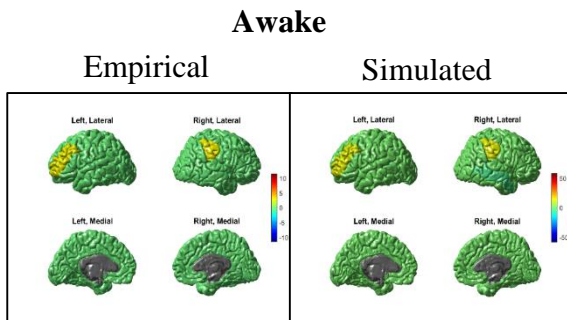
P12



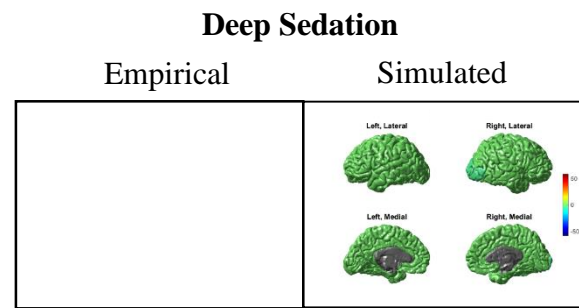
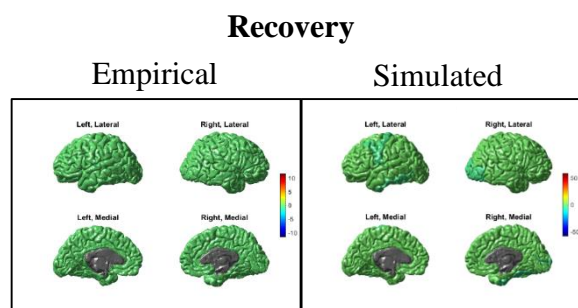
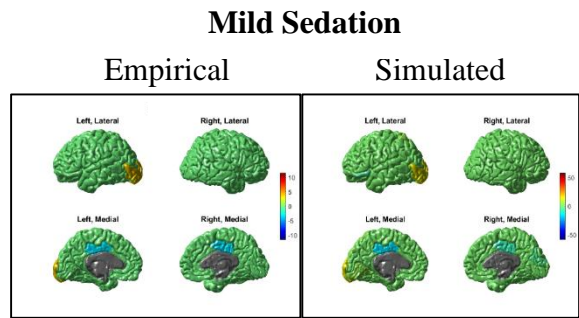
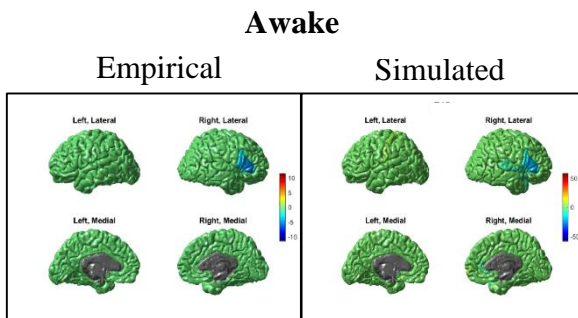
P13



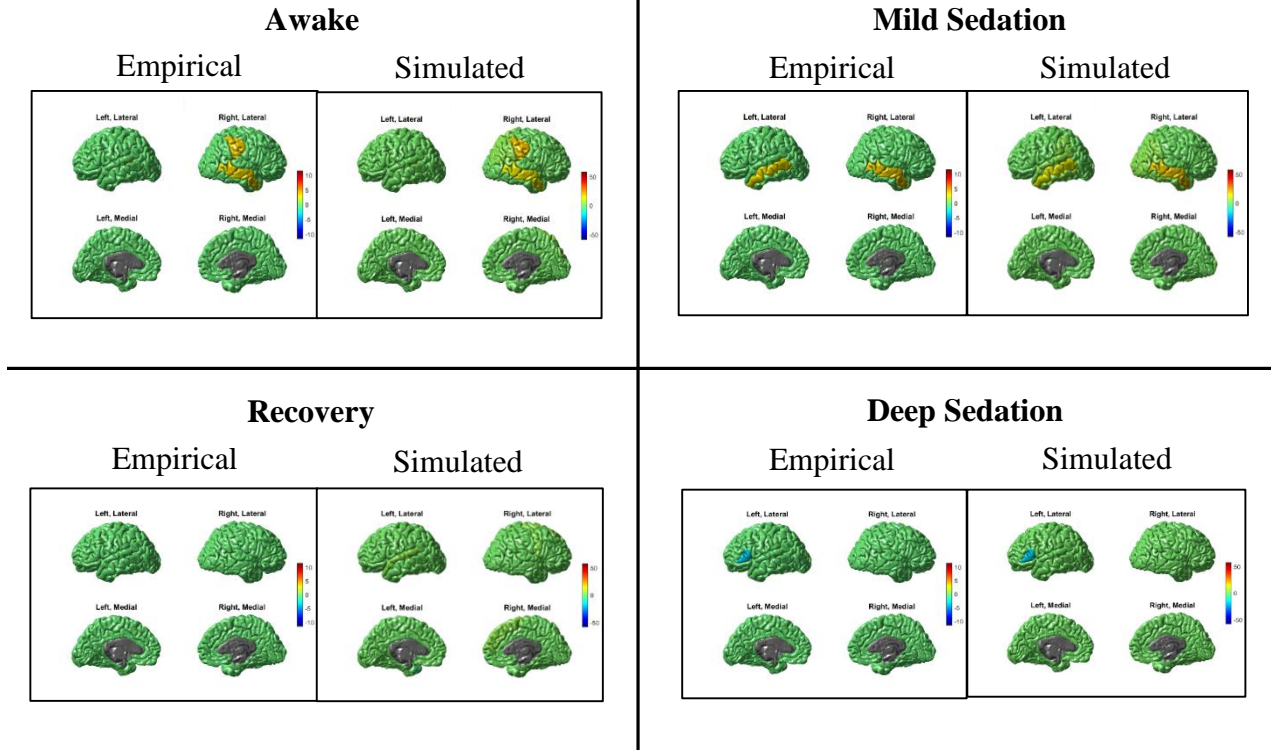
P14



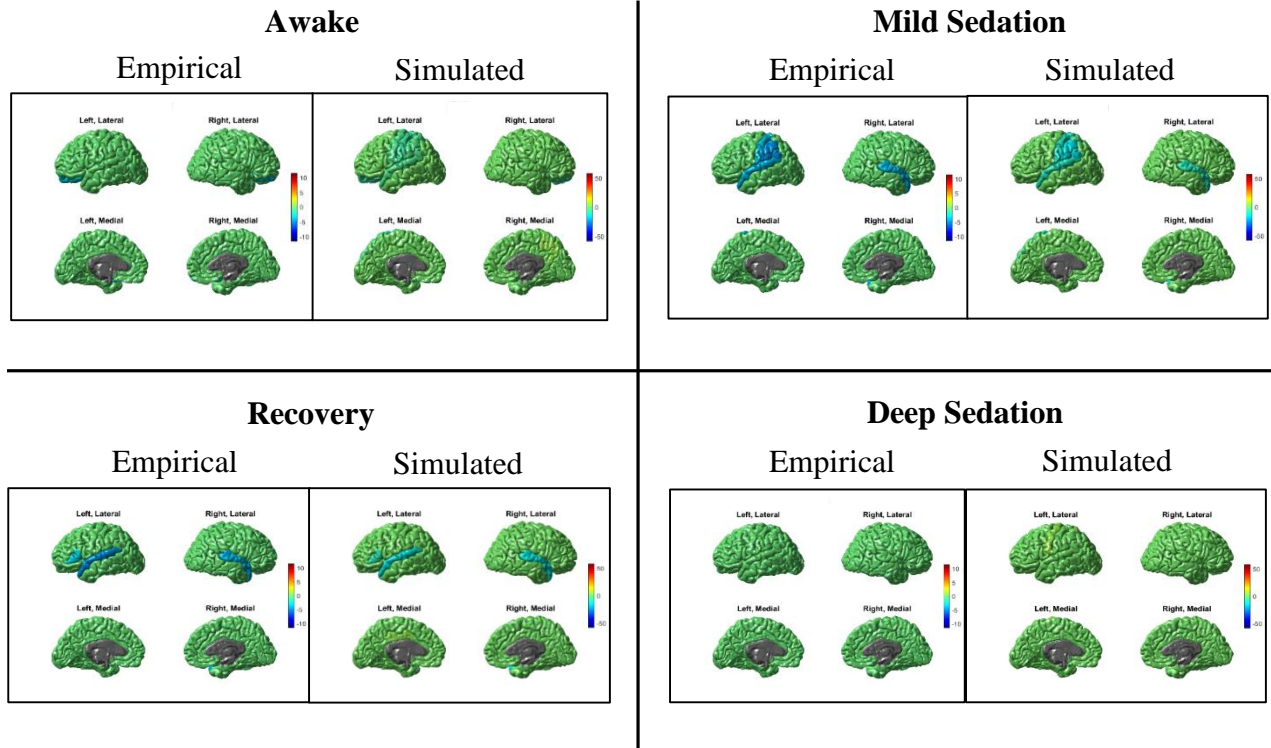
P15



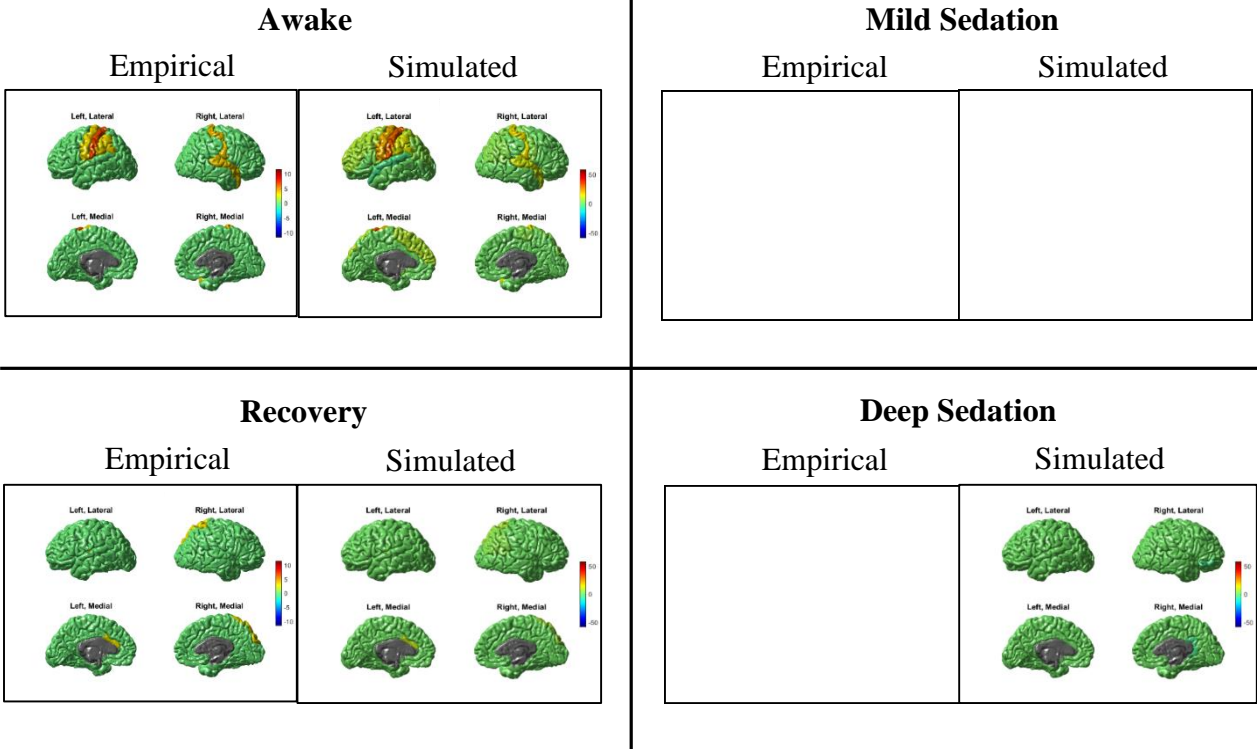
P16



P17

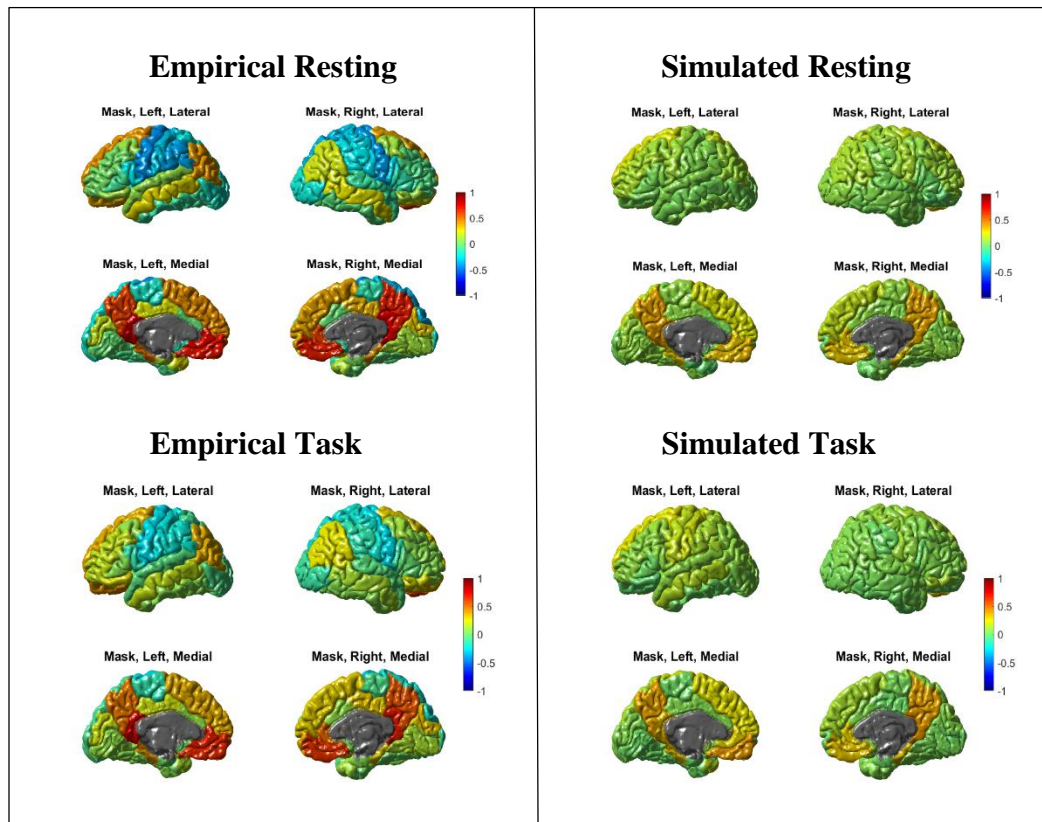


P18

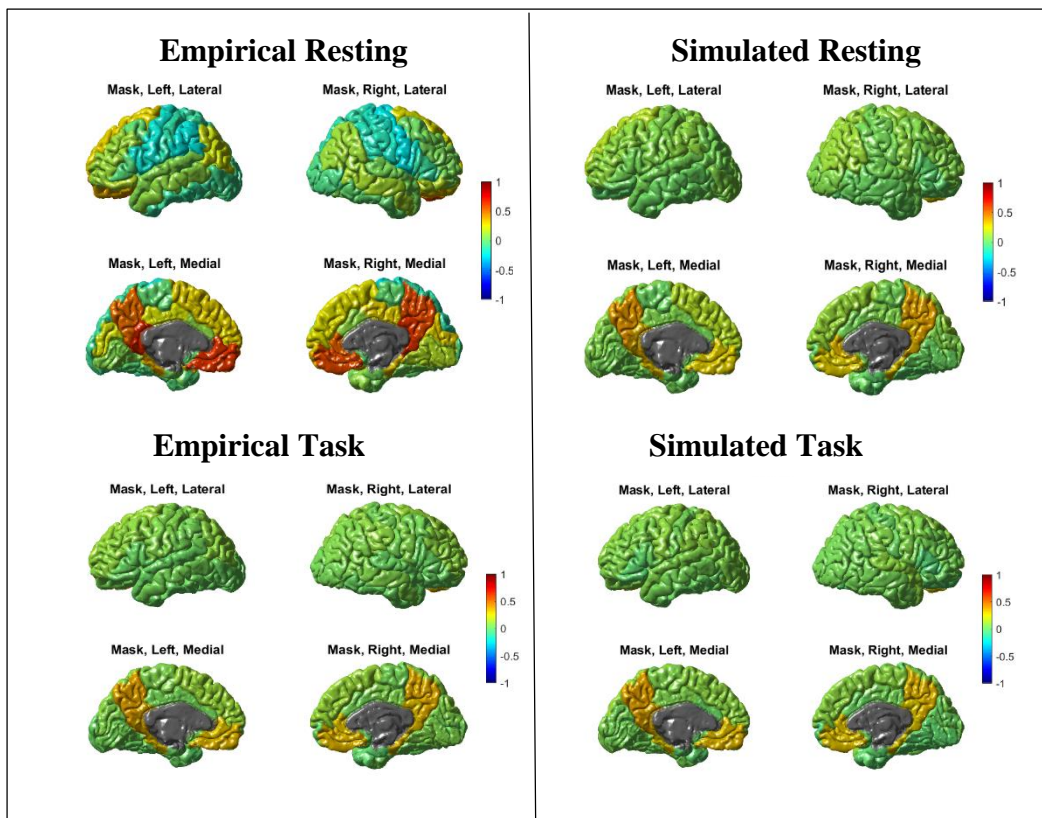


A.2 DMN of empirical and simulated data under all levels of consciousness. Networks for the simulated resting and task data were constructed at T_{\min} and T^* respectively

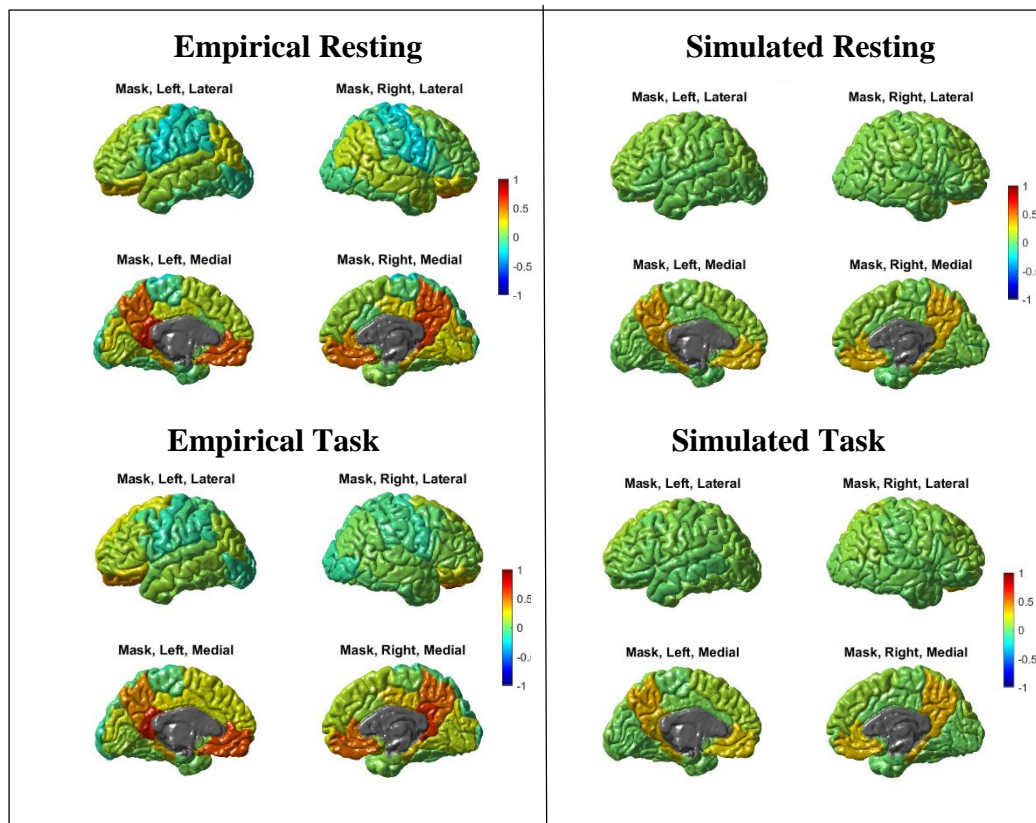
Awake



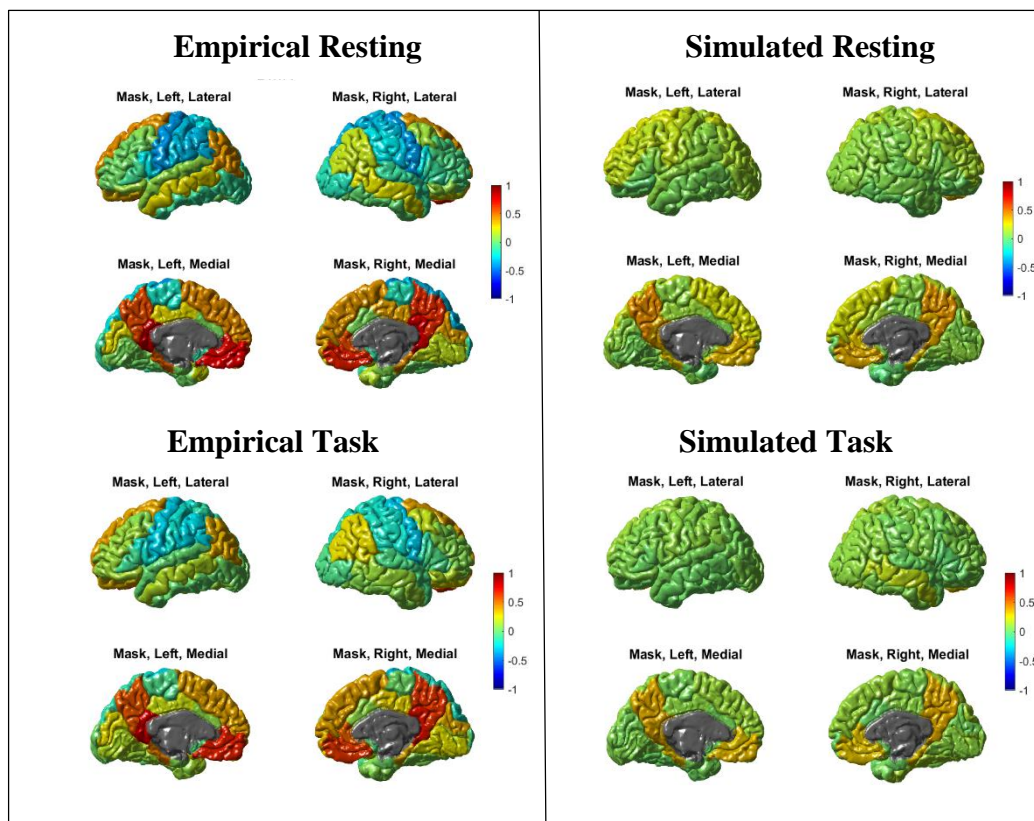
Mild Sedation



Deep Sedation

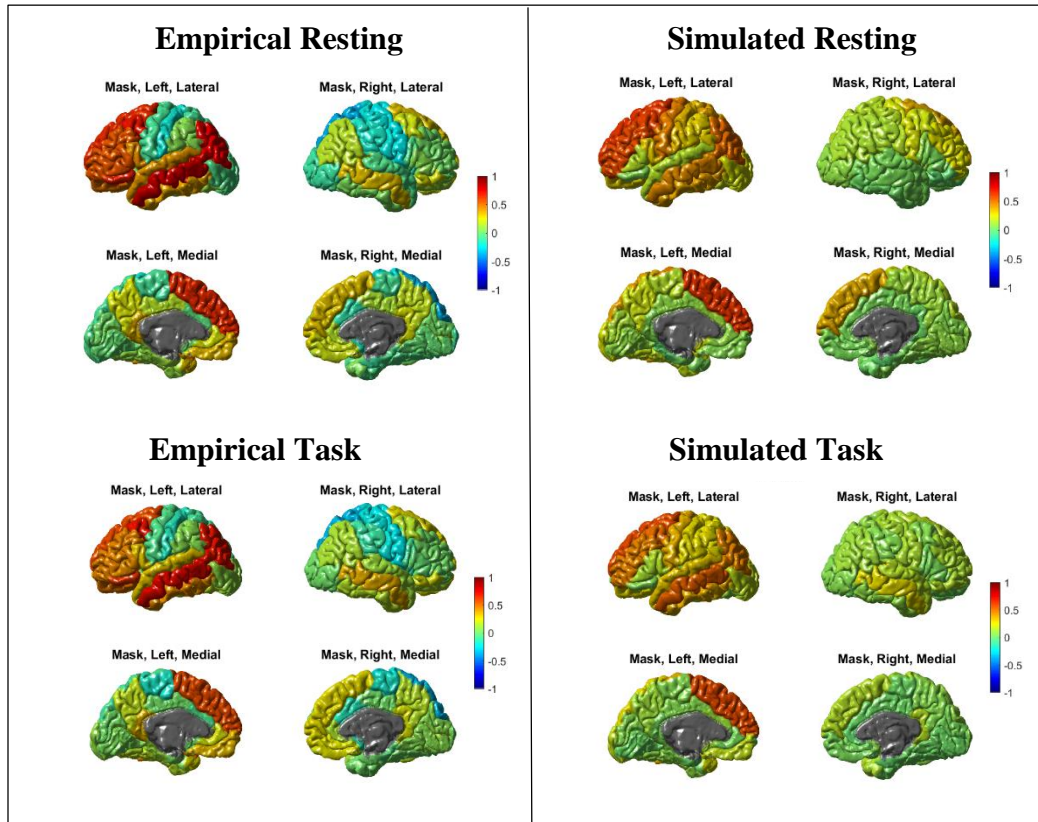


Recovery

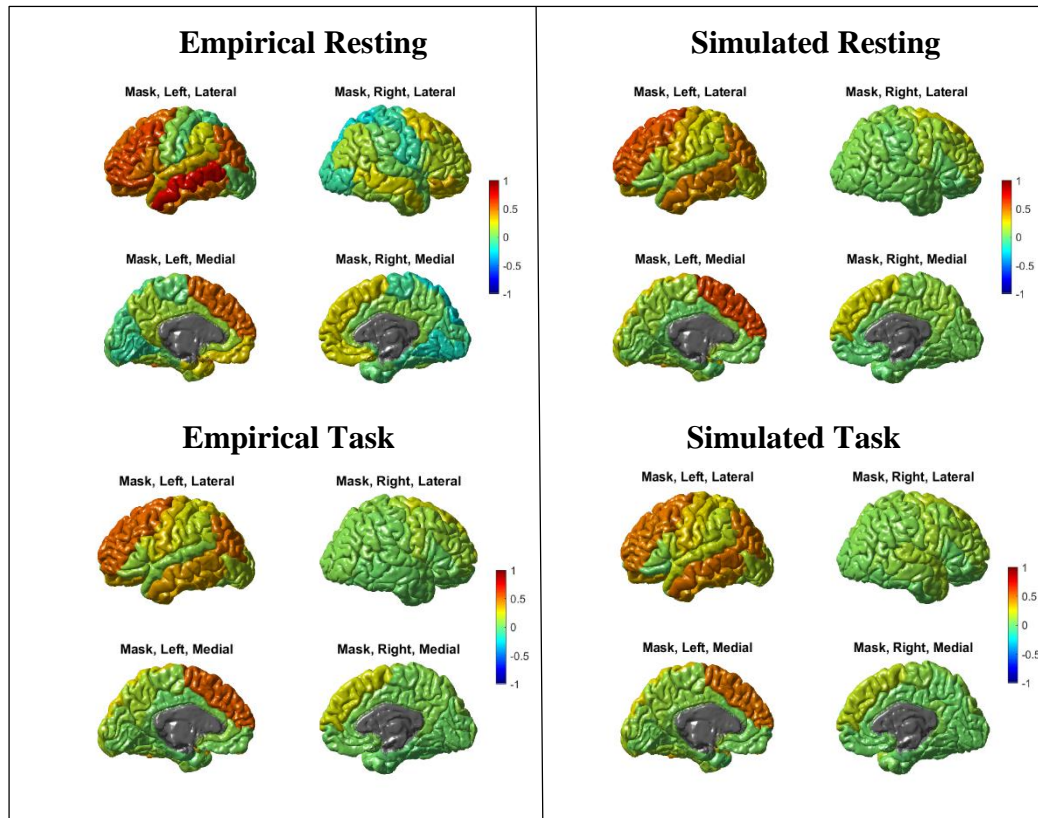


A.3 ECNL of empirical and simulated data under all levels of consciousness. Networks for the simulated resting and task data were constructed at T_{\min} and T^* respectively

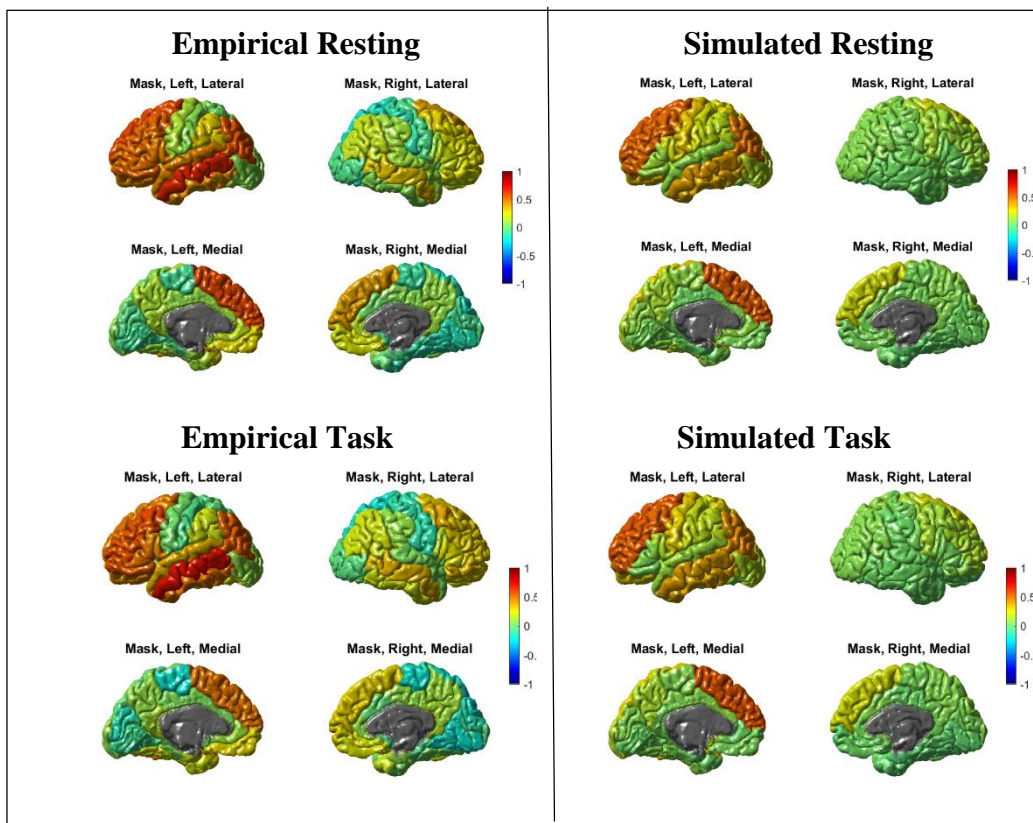
Awake



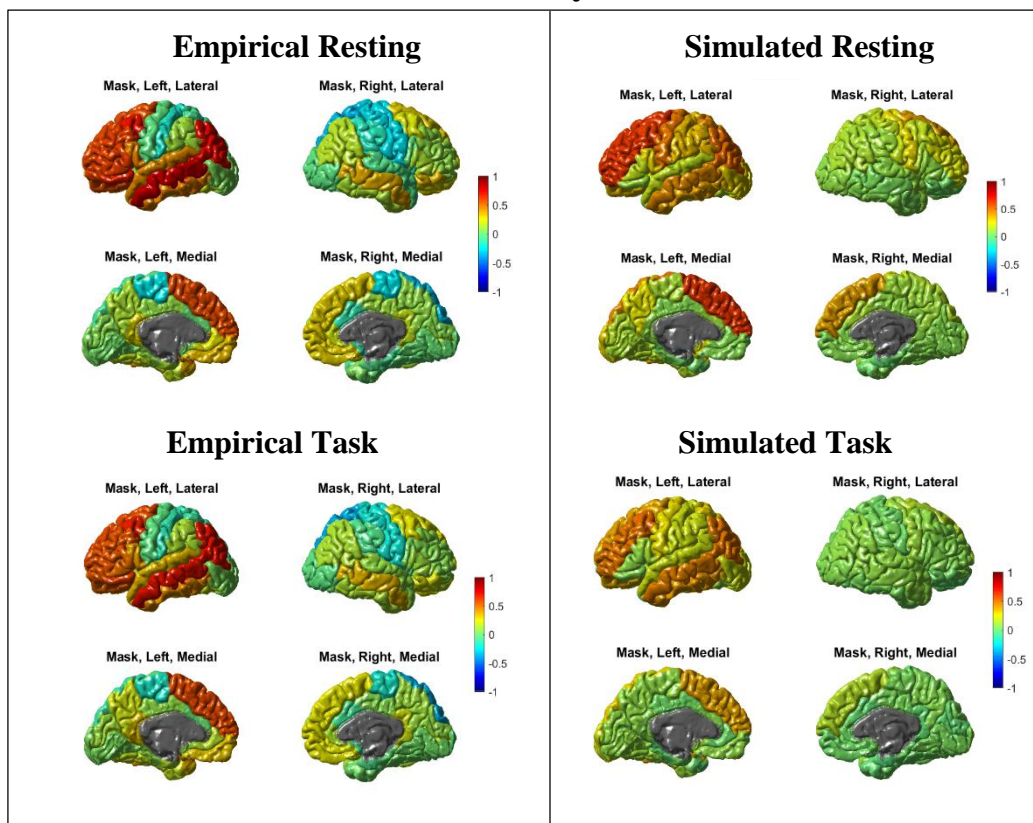
Mild Sedation



Deep Sedation

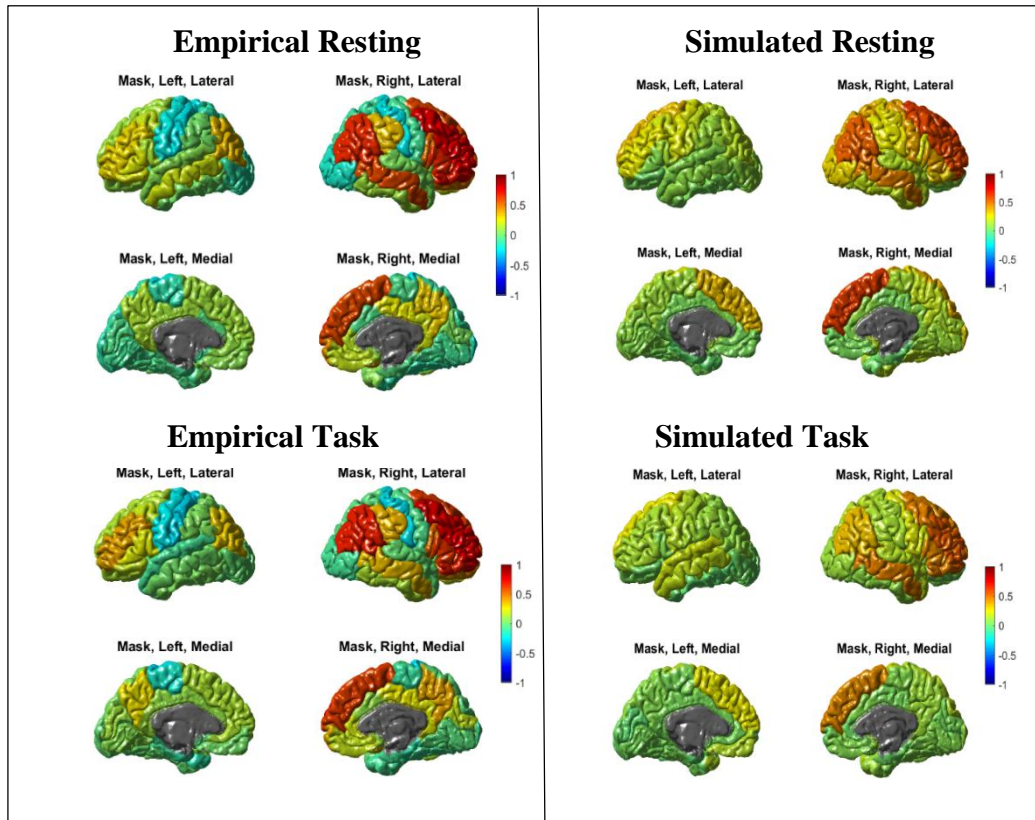


Recovery

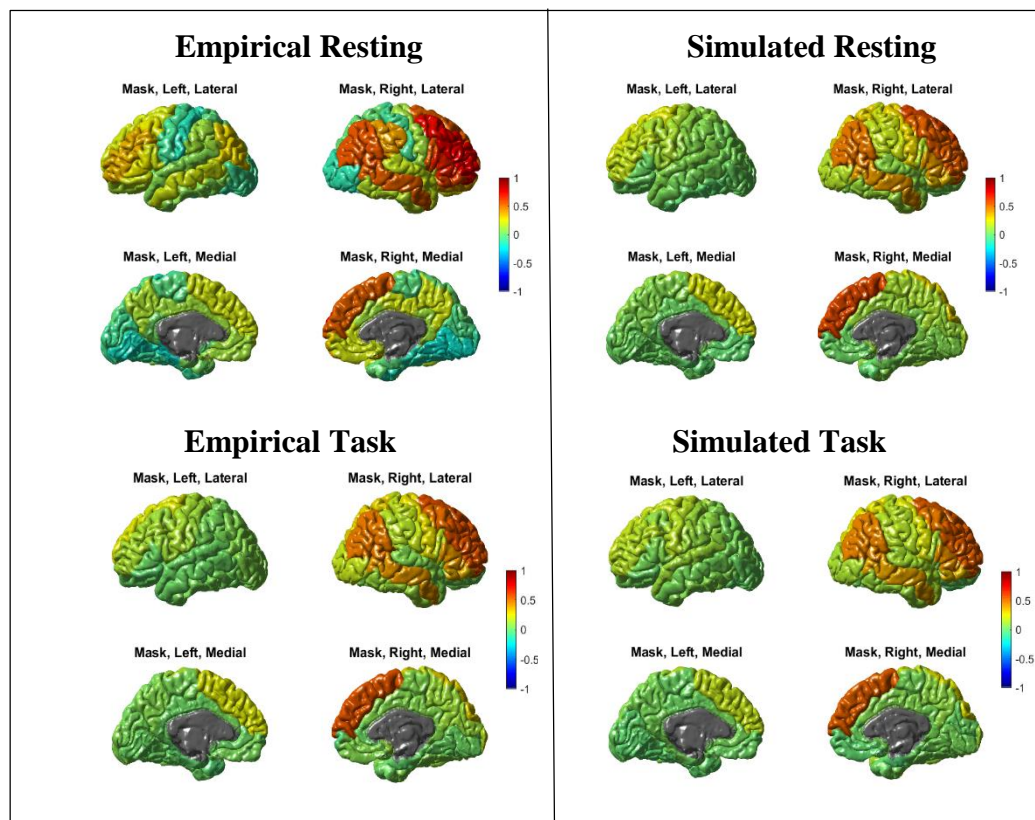


A.4 ECNR of empirical and simulated data under all levels of consciousness. Networks for the simulated resting and task data were constructed at T_{\min} and T^* respectively

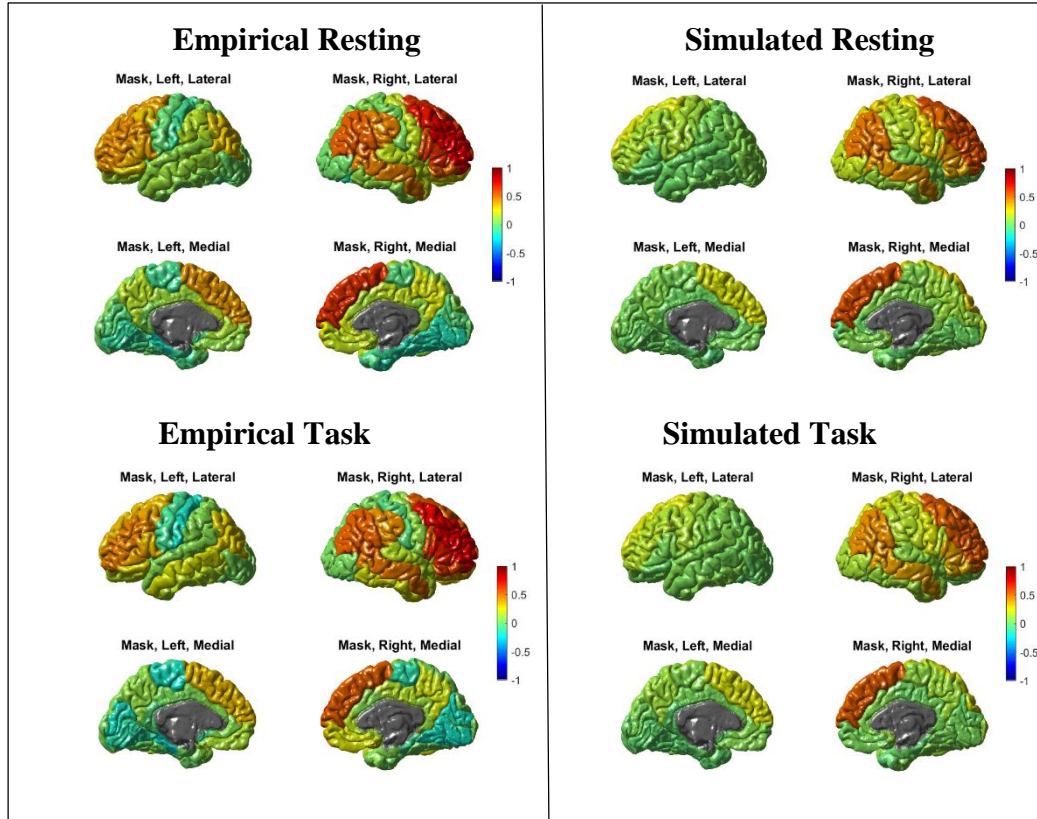
Awake



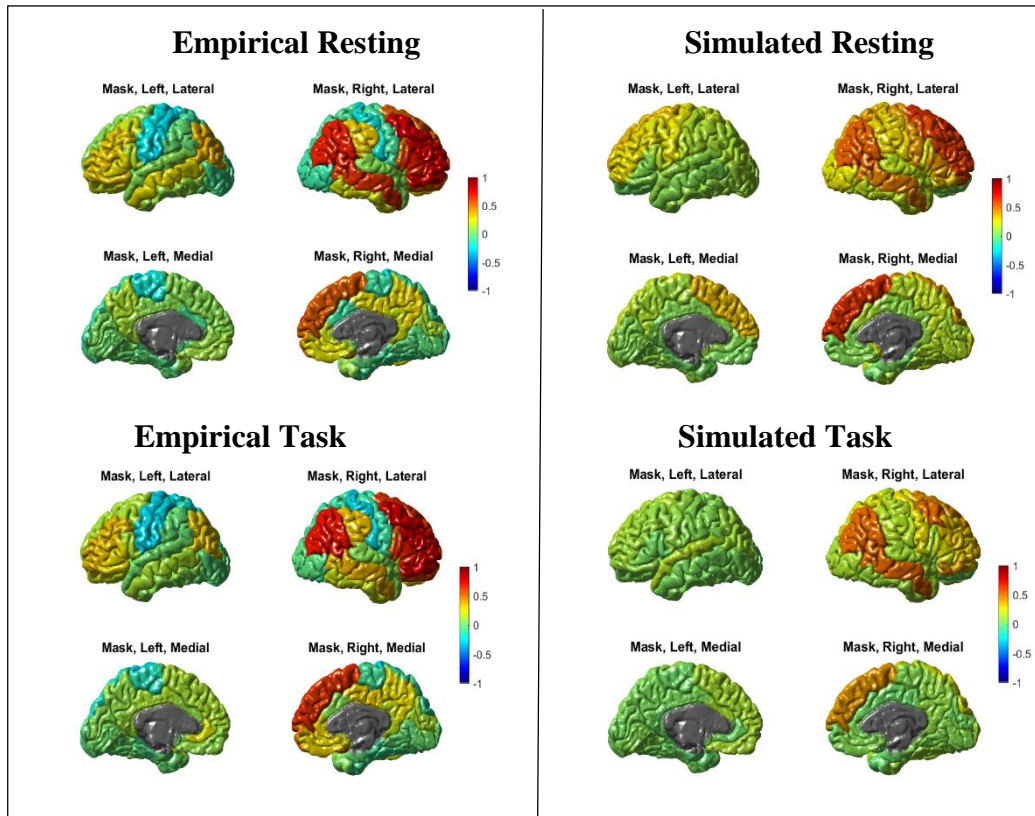
Mild Sedation



Deep Sedation



Recovery



A.5: *P*-stats obtained from the DMN network at different levels of consciousness

	Empirical Resting	Empirical Task	Simulated Resting	Simulated Task
Awake vs. Deep Sedation	0.76	0.82	0.04	0.06
Awake vs. Mild Sedation	0.94	0.66	0.38	0.06
Awake vs. Recovery	0.80	0.99	0.96	0.25
Deep Sedation vs. Mild Sedation	0.79	0.46	0.24	0.97
Mild Sedation vs. Recovery	0.83	0.66	0.36	0.46
Deep Sedation vs. Recovery	0.99	0.84	0.04	0.48

A.6: *P*-stats obtained from the ECNL network at different levels of consciousness

	Empirical Resting	Empirical Task	Simulated Resting	Simulated Task
Awake vs. Deep Sedation	0.90	0.99	0.02	0.02
Awake vs. Mild Sedation	0.89	0.71	0.67	0.11
Awake vs. Recovery	0.64	0.51	0.24	0.07
Deep Sedation vs. Mild Sedation	0.98	0.69	0.05	0.45
Mild Sedation vs. Recovery	0.71	0.75	0.46	0.82
Deep Sedation vs. Recovery	0.69	0.49	0.21	0.60

A.7: *P*-stats obtained from the ECNR network at different levels of consciousness

	Empirical Resting	Empirical Task	Simulated Resting	Simulated Task
Awake vs. Deep Sedation	0.59	0.61	0.01	0.14
Awake vs. Mild Sedation	0.74	0.63	0.55	0.20
Awake vs. Recovery	0.53	0.35	0.78	0.12
Deep Sedation vs. Mild Sedation	0.82	0.98	0.05	0.82
Mild Sedation vs. Recovery	0.75	0.65	0.39	0.77
Deep Sedation vs. Recovery	0.91	0.67	0.01	0.94

Appendix B

Appendices: Chapter 3

B.1 Patients' demographic characteristics

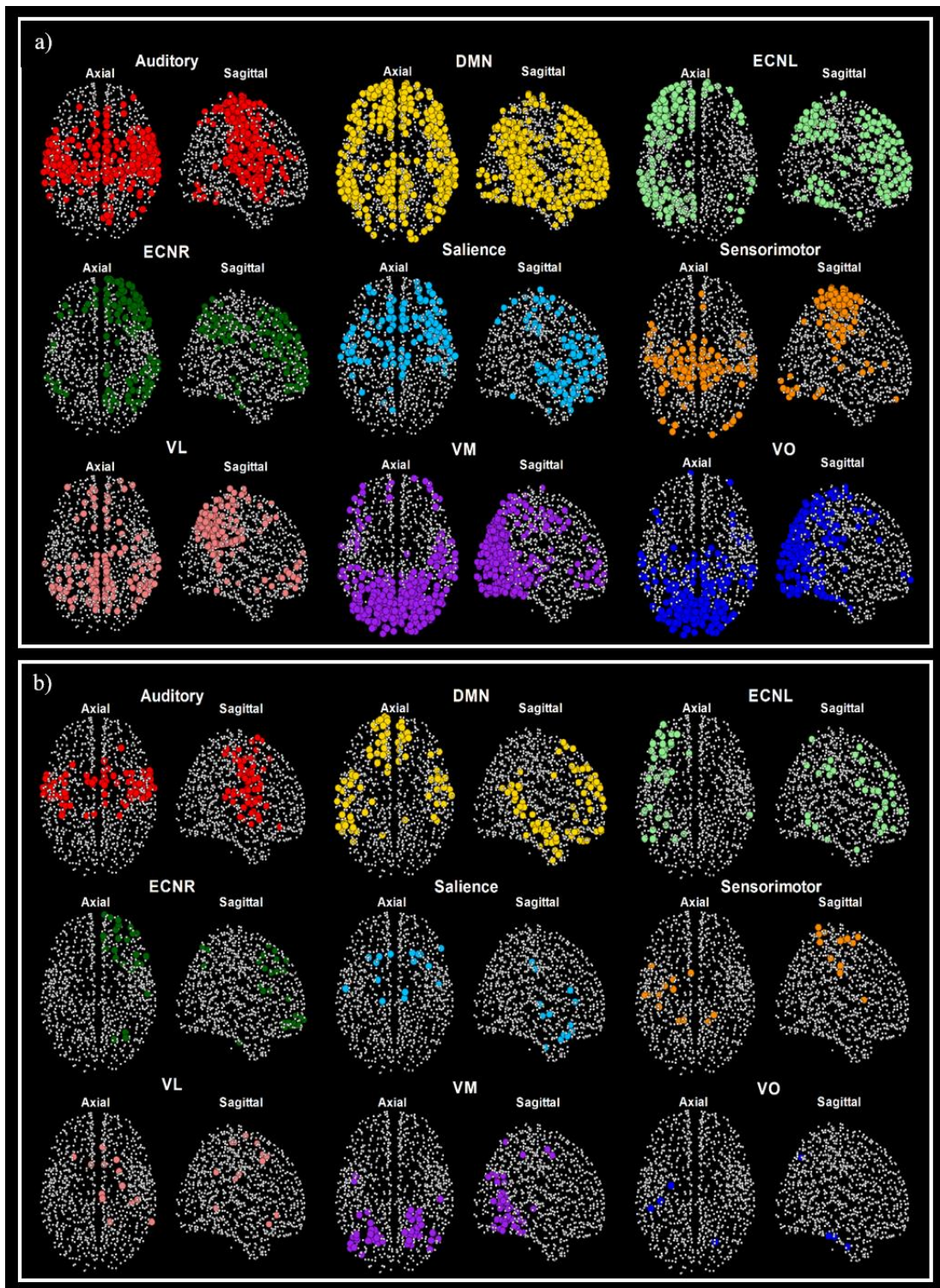
Patient	Age (years)	Sex	Distress (TQ score)	Objective Loudness (dB SL)	Subjective Intensity - VAS (dB)	Duration (years)	Hearing Loss
1	26	M	20	7	3	10.00	8.13
2	44	M	23	25	8	3.00	8.13
3	44	M	52	10	6	5.00	6.88
4	45	F	68	5	10	1.00	12.50
5	61	M	11	10	3	3.00	41.88
6	44	M	57	17	0	3.00	48.13
7	49	M	21	0	2	2.00	11.25
8	18	F	46	0	4.5	0.67	7.50
9	58	M	52	0	7	1.00	33.13
10	27	M	19	0	3	12.00	16.88
11	76	M	25	5	7	10.00	73.13
12	60	F	21	5	6	5.00	67.50
13	40	M	29	0	7	4.00	26.25
14	59	M	27	0	3	10.00	26.25
15	43	F	21	10	5	0.67	10.00
16	57	M	20	5	2	10.00	31.25
17	28	M	20	10	3	6.00	10.00
18	50	F	39	4	8	20.00	17.50
19	65	M	37	5	5	45.00	64.38
20	72	F	2	15	7	6.00	38.13
21	29	M	25	20	1	1.00	3.75
22	37	M	17	25	5	1.00	16.25
23	64	M	27	25	2	5.00	39.38
24	64	M	31	5	6	6.00	28.13
25	21	M	12	15	0	0.75	5.00
26	31	F	30	0	5	1.00	11.88
27	57	F	45	15	6.5	8.00	30.00
28	48	F	33	5	7	2.00	25.63
29	58	M	69	15	5	1.00	30.00
30	50	F	70	0	2	0.17	10.63
31	52	M	31	25	3	2.00	32.50
32	50	M	40	5	5	5.00	26.25
33	28	M	21	0	2	4.00	5.00
34	29	M	23	0	3	1.00	7.50
35	51	M	35	5	10	20.00	47.50
36	41	M	48	3	2	0.50	21.88
37	47	F	40	5	8	2.00	30.00
38	41	M	20	5	4	3.00	10.63
39	18	M	19	0	3	0.67	9.38
40	52	M	25	5	7	0.33	32.50

41	50	M	41	3	2	1.00	70.00
42	44	M	49	5	7	10.00	46.25
43	56	F	34	15	6	5.00	40.00
44	65	M	32	28	7	2.00	27.50
45	54	M	30	-5	4	1.00	23.13
46	45	F	59	0	9	3.00	30.00
47	63	F	39	20	5	3.00	21.25
48	65	M	30	0	1	10.00	57.50
49	58	M	64	4	8	10.00	58.13
50	60	M	47	10	6	4.00	30.00
51	54	M	36	-10	6	1.50	48.13
52	54	M	25	0	2	1.00	30.00
53	48	M	16	5	10	10.00	33.13
54	37	F	59	0	8	7.00	33.75
55	45	M	46	0	7	10.00	18.75
56	52	M	48	0	8	5.00	46.88
57	74	M	33	5	7	3.00	46.88
58	61	M	59	0	7	5.00	52.50
59	52	F	47	5	7	5.00	53.75
60	41	M	35	10	2	0.25	19.38
61	42	M	31	0	6	1.00	50.63
62	55	M	45	30	3	1.00	22.50
63	25	M	28	0	2	7.00	17.50
64	40	F	48	10	6	1.00	10.00
65	37	F	18	5	3	0.92	20.00
66	58	M	42	7	7.5	3.00	56.88
67	67	M	21	5	5	20.00	61.88
68	15	M	26	10	3	0.67	2.50
69	42	M	34	0	3	1.00	12.50
70	53	F	8	5	3	2.00	29.38
71	29	M	50	2	5	2.00	12.50
72	58	M	21	5	1	7.00	41.25
73	65	F	66	0	7	8.00	52.50
74	21	M	54	0	8	4.00	2.50
75	81	F	36	15	5	2.00	59.38
76	50	M	21	2	6	1.00	21.88
77	67	M	50	40	4	9.00	41.88
78	40	M	61	25	9	25.00	65.00
79	29	M	11	10	3	2.00	17.50
80	56	M	33	0	7	20.00	40.63
81	27	M	18	12	4	1.00	8.13
82	60	F	61	0	8	15.00	45.63
83	65	M	51	25	8.5	16.00	53.75
84	53	M	7	1	2	1.00	11.88
85	49	M	63	0	7	8.00	31.88
86	62	F	21	0	3	2.00	16.25
87	58	F	59	15	8	10.00	66.25
88	60	F	59	9	7	2.00	45.63
89	50	M	45	10	4	25.00	40.63
90	40	M	40	16	9	10.00	26.88

91	29	M	29	9	5	1.00	21.88
92	40	F	54	0	7	2.00	51.25
93	44	M	22	5	4	7.00	27.50
94	61	F	29	5	7	3.00	60.63
95	49	M	35	25	3	1.00	15.63
96	60	F	44	0	3	0.33	32.50
97	57	M	47	0	5	6.00	26.25
98	57	F	14	0	8	1.00	15.00
99	51	M	29	20	2	4.00	24.38
100	35	M	27	5	2	2.00	5.63
101	66	F	70	0	0	12.00	46.88
102	81	F	44	10	6	4.00	54.38
103	37	F	31	5	5	15.00	3.13
104	72	M	23	5	5	4.00	43.13
105	46	F	52	9	2	0.50	24.38
106	36	M	16	4	5	7.00	16.88
107	60	F	12	20	0	1.00	20.00
108	32	F	6	20	3	2.00	1.25
109	63	M	40	5	7	1.50	36.25
110	61	M	42	0	8	5.00	80.63
111	47	M	49	8	7	5.00	25.00
112	71	M	49	10	5	1.00	88.75
113	38	M	64	5	8	0.33	16.88
114	77	M	45	5	4	40.00	49.38
115	46	M	34	0	7	3.00	36.88
116	56	M	52	5	7	10.00	36.25
117	41	M	24	25	7	10.00	24.38
118	63	M	19	10	2	1.00	15.63
119	65	M	57	1	5	12.00	59.38
120	29	M	37	0	5	1.00	11.25
121	69	M	6	0	1	1.00	40.00
122	26	M	38	5	3	2.00	6.25
123	67	F	61	35	8	6.00	59.38
124	45	M	15	5	4	4.50	50.63
125	73	M	43	5	6	2.00	46.25
126	59	F	20	10	5	15.00	13.13
127	57	M	72	25	9	1.50	82.50
128	55	F	33	15	7	7.00	38.75
129	71	M	39	5	7	30.00	62.50
130	26	M	48	10	6	0.13	8.75
131	54	F	27	1	8	2.00	23.75
132	27	F	20	25	0	1.00	21.88
133	59	F	44	10	8	1.00	31.25
134	61	M	14	25	4	10.00	40.63
135	62	M	75	0	10	5.00	73.75

M – Male, F – Female, Intensity (objective loudness) - best match to the perceived intensity of their tinnitus; the intensity was corrected for the hearing threshold measured for the according frequency, subjective intensity – evaluation of the tinnitus loudness on a scale of 0 to 10, Hearing loss - mean of the hearing threshold of 500-1000-2000-4000Hz for both ears.

B.2 Masks of resting state networks



Axial and sagittal views of the masks of nine Resting State Network (RSN)s a) using all the regions (overlapping) belonging to the network b) using isolated regions (non-overlapping) only

B.3 Correlation between behavioural scores (BS) and graph strength (GS) for tinnitus patients

a) *T*-stats obtained from the correlation between the age and GS on the auditory network

ROI	x	y	z	t-value	p-value	Network
lh.superior frontal	135.55	148.00	-88.64	3.02	< 0.01	Aud
rh.fusiform	173.83	93.19	-160.55	3.26	< 0.01	Aud
rh.postcentral	163.14	114.04	-79.64	4.59	< 0.01	Aud
rh.precentral	158.67	122.28	-79.69	2.90	< 0.01	Aud
rh.superior temporal	188.17	146.65	-151.05	2.62	0.01	Aud
rh.supramarginal	182.53	117.86	-100.83	3.38	< 0.01	Aud
lh.bankssts	78.72	105.78	-147.64	2.80	0.01	DMN
rh.middle temporal	186.60	146.51	-170.54	2.91	< 0.01	DMN
lh.inferior temporal	81.37	92.32	-157.04	2.66	0.01	ECNL
rh.pars orbitalis	165.87	197.05	-158.26	4.70	< 0.01	ECNR
rh.rostral middle frontal	152.23	199.76	-151.43	3.39	< 0.01	ECNR
rh.inferior temporal	179.04	135.72	-178.77	2.70	0.01	Sal
rh.lateral orbitofrontal	150.46	160.41	-167.89	2.80	0.01	Sal

b) *T*-stats obtained from the correlation between the duration and GS on the DMN network

ROI	x	y	z	t-value	p-value	Network
rh.posterior cingulate	135.89	139.00	-107.71	4.61	< 0.01	Aud
lh.rostral middle frontal	103.01	197.58	-144.95	3.09	< 0.01	DMN
rh.medial orbitofrontal	134.30	175.92	-161.38	2.87	< 0.01	DMN

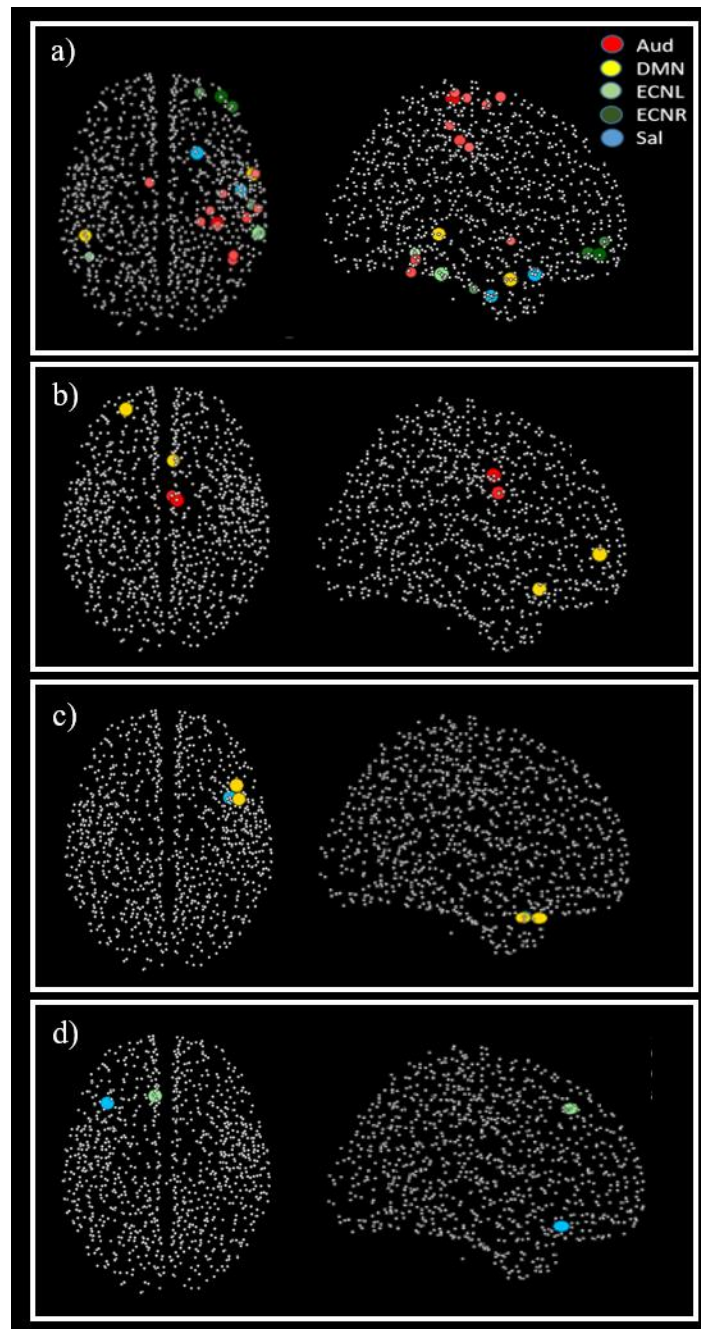
c) *T*-stats obtained from the correlation between the hearing loss and GS on the DMN network

ROI	x	y	z	t-value	p-value	Network
rh.superior temporal	168.00	154.80	-172.11	4.06	< 0.01	Sal
rh.superior temporal	172.39	162.61	-172.64	3.65	< 0.01	DMN

d) *T*-stats obtained from the correlation between the subjective intensity (VAS) and GS on the salience network

ROI	x	y	z	t-value	p-value	Network
lh.superior frontal	109.55	162.20	-86.65	-3.72	< 0.01	ECNL
lh.lateral orbitofrontal	91.10	167.51	-163.35	-3.82	< 0.01	Sal

B.4 Representation of the correlation between BS and GS of tinnitus patients



a) Aud and age

b) DMN and duration

c) DMN and hearing loss

d) Sal and subjective intensity

NB: The correlation between BS and all the networks are positive except between the Sal and subjective intensity

B.5 *T*-stats obtained from the correlation between BS and GS for tinnitus patients with different types of lateralization

a) *T*-stats obtained from correlation between the distress and GS on the ECNR for bilateral tinnitus patients

ROI	x	y	z	t-value	p-value	Network
lh. posterior cingulate	121.75	141.84	-109.17	3.02	< 0.01	Aud
rh. postcentral	178.05	132.42	-109.89	3.00	< 0.01	Aud
rh. posterior cingulate	135.89	139.00	-107.71	2.98	< 0.01	Aud

b) *T*-stats obtained from correlation between the age and GS on the auditory network for bilateral tinnitus patients

ROI	x	y	z	t-value	p-value	Network
lh. precentral	117.34	124.64	-71.19	2.60	0.01	Aud
lh. superior frontal	119.81	140.77	-78.88	3.09	< 0.01	Aud
rh. fusiform	173.83	93.19	-160.54	3.22	0.01	Aud
rh. postcentral	163.14	114.04	-79.63	3.78	< 0.01	Aud
rh. precentral	158.67	122.28	-79.69	2.66	0.01	Aud
rh. superior temporal	188.17	146.65	-151.05	3.46	< 0.01	Aud
rh. supramarginal	182.53	117.86	-100.83	3.58	< 0.01	Aud
lh. bankssts	78.72	105.78	-147.64	2.87	< 0.01	DMN
rh. middle temporal	177.91	147.39	-178.11	3.35	< 0.01	DMN
lh. inferior temporal	72.08	82.99	-152.66	3.04	< 0.01	ECNL
lh. pars triangularis	79.58	174.86	-147.36	3.19	< 0.01	ECNL
rh. inferior temporal	189.80	107.92	-167.97	3.94	< 0.01	ECNL
rh. inferior temporal	185.19	125.92	-175.31	2.46	0.02	ECNR
rh. pars orbitalis	165.87	197.05	-158.26	4.40	< 0.01	ECNR
rh. rostral middle frontal	152.23	199.76	-151.43	3.05	< 0.01	ECNR
rh. superior parietal	160.01	84.12	-92.21	2.69	0.01	ECNR
rh. inferior temporal	179.04	135.72	-178.77	2.55	0.01	Sal

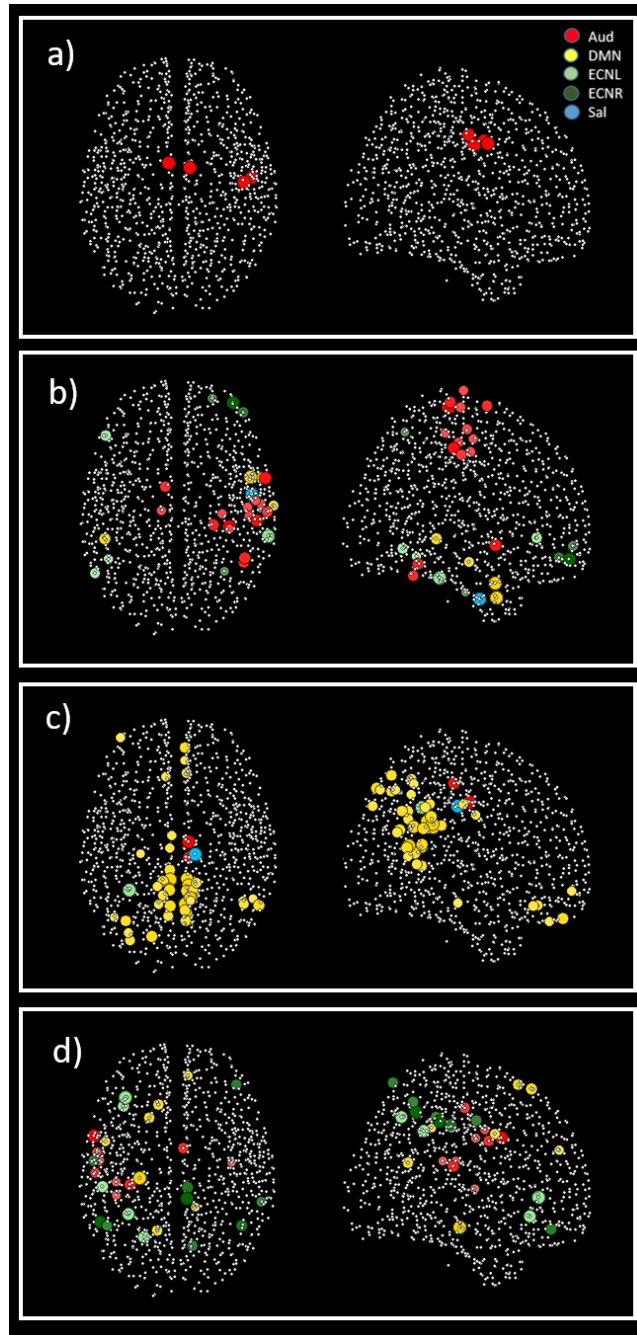
c) *T*-stats obtained from correlation between the age and GS on the DMN for bilateral tinnitus patients

ROI	x	y	z	t-value	p-value	Network
rh. paracentral	136.19	119.07	-98.18	2.57	0.01	Aud
rh. posterior cingulate	135.57	129.463	-107.88	2.73	0.01	Aud
Left-Hippocampus	103.15	121.511	-160.17	2.44	0.02	DMN
lh. inferior parietal	93.08	76.21	-94.24	3.08	< 0.01	DMN
lh. isthmus cingulate	123.18	104.24	-119.26	3.83	< 0.01	DMN
lh. medial orbitofrontal	120.68	173.01	-161.79	2.73	0.01	DMN
lh. posterior cingulate	123.22	125.24	-108.73	2.74	< 0.01	DMN
lh. precuneus	123.35	86.49	-131.43	3.40	< 0.01	DMN
lh. rostral middlefrontal	99.06	204.65	-155.24	2.51	0.01	DMN
lh. superior parietal	110.63	65.89	-100.52	3.31	< 0.01	DMN
rh. inferior parietal	183.24	87.04	-112.55	3.27	< 0.01	DMN
rh. isthmus cingulate	135.80	100.36	-117.63	3.82	< 0.01	DMN
rh. medial orbitofrontal	133.18	192.99	-168.08	3.26	< 0.01	DMN
rh. precuneus	134.51	81.42	-122.21	3.86	< 0.01	DMN
lh. superior parietal	95.69	97.00	-110.41	2.64	0.01	ECNL
rh. posterior cingulate	140.15	121.11	-109.82	3.39	< 0.01	Sal

d) *T*-stats obtained from correlation between the distress and GS on the ECNR for unilateral tinnitus patients

ROI	x	y	z	t-value	p-value	Network
lh. insula	96.31	117.24	-128.63	3.84	< 0.01	Aud
lh. postcentral	72.84	124.99	-98.50	3.42	< 0.01	Aud
lh. precentral	71.76	150.15	-114.12	4.40	< 0.01	Aud
lh. supramarginal	87.16	118.78	-125.85	2.74	0.01	Aud
rh. insula	165.91	132.01	-140.39	2.47	0.02	Aud
rh. posterior cingulate	132.97	141.77	-115.73	3.60	< 0.01	Aud
Left-Hippocampus	103.15	121.51	-160.17	3.77	< 0.01	DMN
lh. precentral	79.99	146.07	-111.82	2.62	0.01	DMN
lh. precuneus	115.06	85.98	-127.01	3.02	< 0.01	DMN
lh. superior frontal	115.90	170.90	-88.55	3.16	< 0.01	DMN
rh. precuneus	141.00	102.09	-109.01	2.36	0.02	DMN
rh. superior frontal	136.11	190.44	-120.46	2.44	0.02	DMN
lh. lateral orbitofrontal	91.90	170.14	-154.68	3.12	< 0.01	ECNL
lh. pars triangularis	92.51	158.70	-135.72	3.50	< 0.01	ECNL
lh. superior parietal	95.69	97.00	-110.41	3.31	< 0.01	ECNL
lh. supramarginal	77.59	115.71	-108.07	2.97	< 0.01	ECNL
lh. inferior parietal	76.28	91.69	-100.74	3.05	< 0.01	ECNR
lh. post central	71.87	133.26	-105.16	2.45	0.02	ECNR
rh. inferior parietal	172.77	89.48	-95.70	2.76	0.01	ECNR
rh. pars orbitalis	169.26	184.33	-161.46	2.59	0.01	ECNR
rh. posterior cingulate	135.66	115.42	-107.26	2.71	0.01	ECNR
rh. precuneus	135.04	107.71	-105.41	3.12	< 0.01	ECNR
rh. superior parietal	139.33	75.89	-85.37	2.49	0.02	ECNR
rh. supramarginal	186.11	105.45	-103.50	2.39	0.02	ECNR

B.6 Representation of the correlation between BS and GS for tinnitus patients with different types of lateralization



a) ECNR and distress for bilateral

b) Aud and age for bilateral

c) DMN and age for bilateral

d) ECNR and distress for unilateral

Appendix C

Appendices: Chapter 4

C.1. Coma recovery scale-revised total and sub-scores of the EMCS, MCS and UWS patients. They were collected in the day of neuroimaging and five days in one week before and after.

Assessment	Case 1 UWS	Case 2 MCS	Case 3 EMCS
1	6 (2-0-1-2-0-1)	11 (3-3-2-1-0-2)	22 (3-5-6-3-2-3)
2	6 (2-0-1-2-0-1)	11 (3-3-2-1-0-2)	21 (3-5-5-3-2-3)
3	6 (2-0-1-2-0-1)	10 (3-3-2-0-0-2)	21 (3-5-5-3-2-3)
4	6 (1-0-2-2-0-1)	11 (3-3-2-1-0-2)	20 (3-5-5-2-2-3)
5	6 (1-0-2-1-0-2)	11 (3-3-2-1-0-2)	21 (3-5-5-3-2-3)
*6	6 (1-0-2-1-0-2)	11 (3-3-2-1-0-2)	22 (4-5-5-3-2-3)
7	6 (1-0-2-1-0-2)	11 (3-3-2-1-0-2)	22 (4-5-5-3-2-3)
8	6 (2-0-1-1-0-2)	10 (3-3-2-0-0-2)	21 (3-5-5-3-2-3)
9	6 (2-0-1-1-0-2)	10 (3-3-2-1-0-1)	20 (3-5-5-2-2-3)
10	6 (2-0-1-1-0-2)	11 (3-3-2-1-0-2)	20 (3-5-5-2-2-3)
11	6 (2-0-1-1-0-2)	11 (3-3-2-1-0-2)	21 (4-5-5-2-2-3)

Note. CRS-R=coma recovery scale-revised; UWS= unresponsive wakefulness syndrome; MCS=minimally conscious state; EMCS=emergence from MCS.

* indicates neuroimaging day. The changes in CRS-R total or subscores are marked in bold

C.2 Classification criteria for visual analysis of EEG background activity

EEG background activity category	EEG features
Normal	Presence of predominant posterior alpha rhythm and of the APG, without focal or hemispheric slowing or epileptiform abnormalities
Mildly abnormal	Presence of predominant posterior theta activity ($\geq 20 \mu\text{V}$), symmetric or not, with frequent (10-49% of recording) posterior alpha rhythms
Moderately abnormal	Presence of predominant posterior theta activity ($\geq 20 \mu\text{V}$), symmetric or not, poorly organized APG, even with rare ($< 1\%$ of recording) or occasional (1-9% of recording) posterior alpha rhythms
Diffuse slowing	Presence of predominant diffuse theta or theta/delta rhythms at amplitude $\geq 20 \mu\text{V}$, without APG
Low voltage	Presence of predominant EEG activity (theta or delta) $< 20 \mu\text{V}$ over most brain regions

C.3 Clinical sketches of patients

Case 1 (patient in UWS). A 43-year-old woman was admitted to the intensive care unit because of cardio-respiratory arrest following septic shock with rhabdomyolysis in October 2016. After the severe anoxic brain injury, she remained in a comatose state for 20 days and then recovered arousal with cyclic eye opening. When she was admitted to the neurorehabilitation unit, 50 days after injury, the patient was classified to be in UWS by repeated behavioural assessments using Coma Recovery Scale-Revised (CRS-R). The diagnosis was confirmed by serial assessments during the following 6 months, on the day of MR/PET session and in the weeks before and after MR/PET session. Across repeated evaluations, CRS-R evidenced presence of sound localization (auditory scale= 2), abnormal posture in response to nociceptive stimulus (motor scale= 1), reflexive chewing movements following introduction of tongue blade (oro-motor scale= 1) and eye opening upon stimulation (arousal scale= 1), whereas no behavioural responses were elicited by visual stimuli or communication was present (visual and communication scales= 0). Some inconsistent behavioural changes were only observed on auditory and motor scales: on some evaluations, the patients showed a clear startle response to auditory stimuli but no localization to sound, whereas her right upper limb sometimes moved away from the point of nociceptive stimulation. Nonetheless, her CRS-R total score did not change in the weeks before and after MR/PET session.

Case 2 (patient in MCS). A 18-year-old boy was hospitalized in a comatose state because of a severe closed brain injury due to a car accident in September 2017. He underwent a left temporo-parietal decompressive craniectomy and emptying of a wide left epidural hematoma. Twenty days later he was admitted to our neurorehabilitation unit and diagnosed to be in

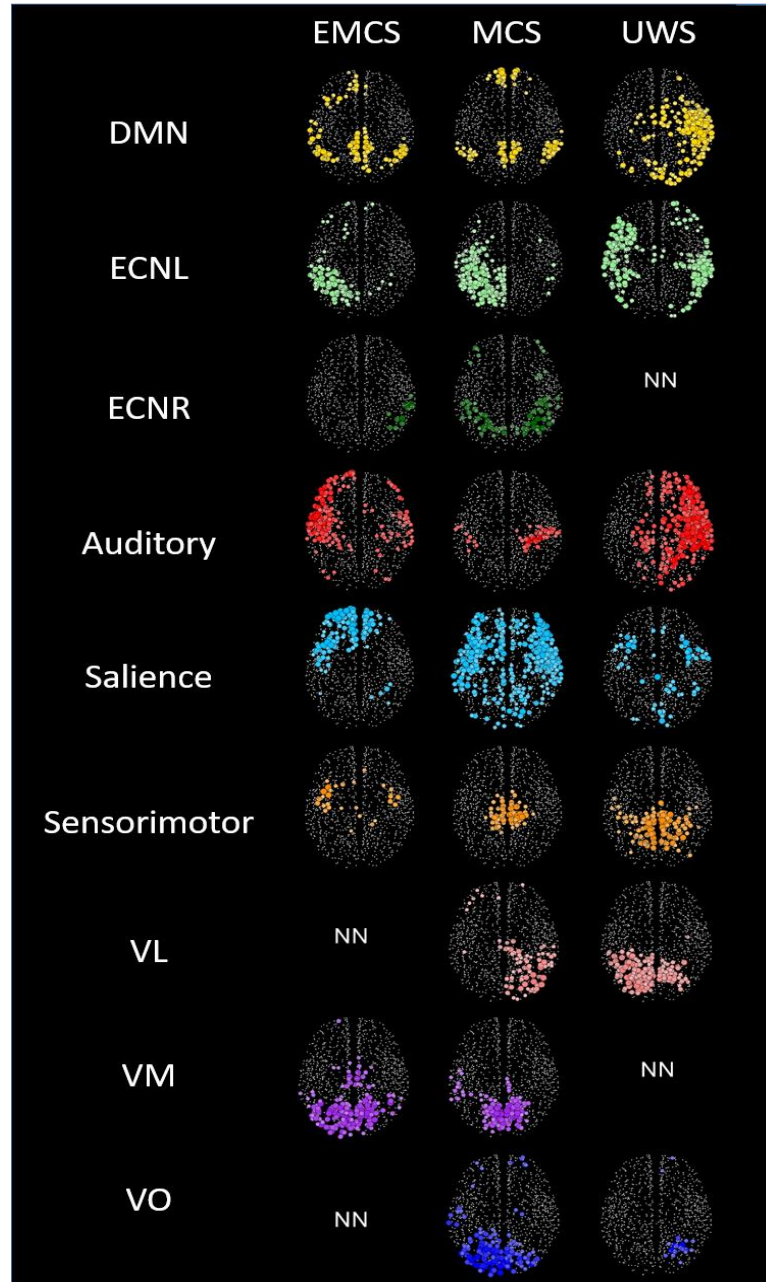
UWS/V.S. In one month he recovered visual tracking and reproducible movements to command such as eyes closure, head and left arm movements (CRS-R total score=11). He was enrolled in the study 3 months after brain injury, when he was in stabilized medical conditions. At that time his diagnosis was MCS and the patients showed reproducible eye, head and arm movements to verbal command (auditory scale= 3), visual pursuit (visual scale=3), arm flexion withdrawal to nociceptive stimulus (motor scale= 2), reflexive chewing movements following introduction of tongue blade (oro-motor scale= 1) and eye opening without stimulation (arousal scale= 2), whereas communication was not present (communication scales= 0). Repeated clinical assessments allowed to notice inconsistent oral reflexive movements in the days before (3rd day) and after the RM/PET session (8th and 9th day), thus CRS-R total score ranged 10-11 without change in clinical diagnosis.

Case 3 (patient in EMCS). A 57-year-old man acutely developed a severe anoxic brain injury following a cardiac arrest after his first heroin dose in March 2017. Fifteen days later, he was admitted to our neurorehabilitation unit in clinical condition of UWS. About 2 months after brain injury, he recovered ability to follow verbal commands such as “open your mouth and close your eyes” (auditory scale= 3) and automatic motor responses (motor scale=5) and then, 2 months later, the ability to pursuit a moving object or person (visual scale=3), to recognize two distinct objects (visual scale= 5) and to follow object-related verbal commands, such as “look at the glasses” (CRS-R auditory scale=3). At 5 months post injury, he further recovered functional and appropriate verbal communication, thus emerging from MCS (CRS-R total score= 21). During the subsequent 25 days, his serial CRS-R total scores ranged 20-22, since the patient did not show consistent movement to command or automatic motor responses in all CRS-R assessments. Because of agitation, low-dosage quetiapine was administered; we stopped

quetiapine 15 hours before PET/MRI scanning, as foreseen by our study protocol. On the day of neuroimaging acquisition, his CRS-R total score was 22.

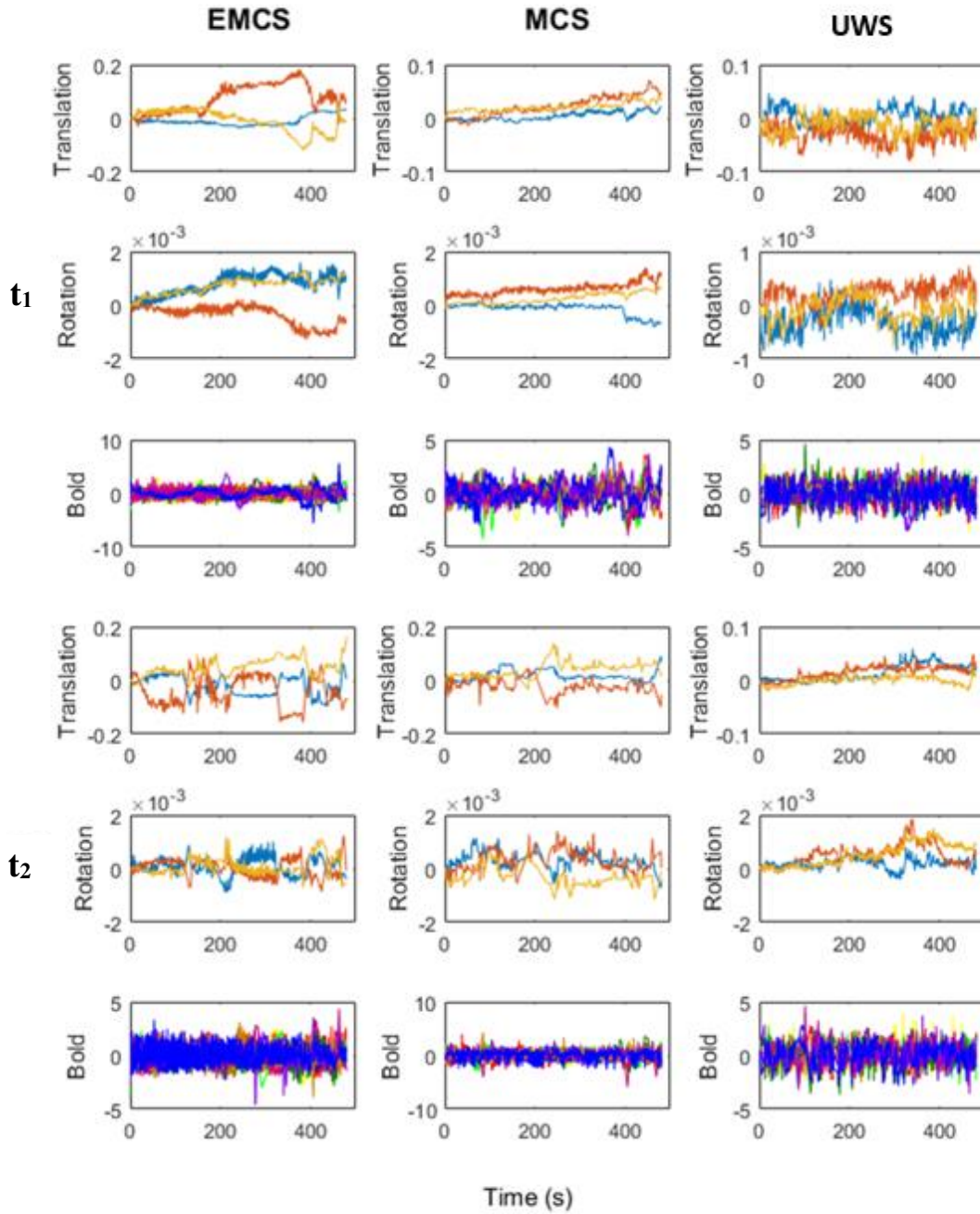
C.4 GS scalar maps of the nine RSNs of patients in EMCS, MCS, and UWS patients

From the two acquisitions, only the networks classified as neuronal are shown. When both acquisitions had neuronal components, the highest ROF value was used to choose the best spatial pattern of the network.

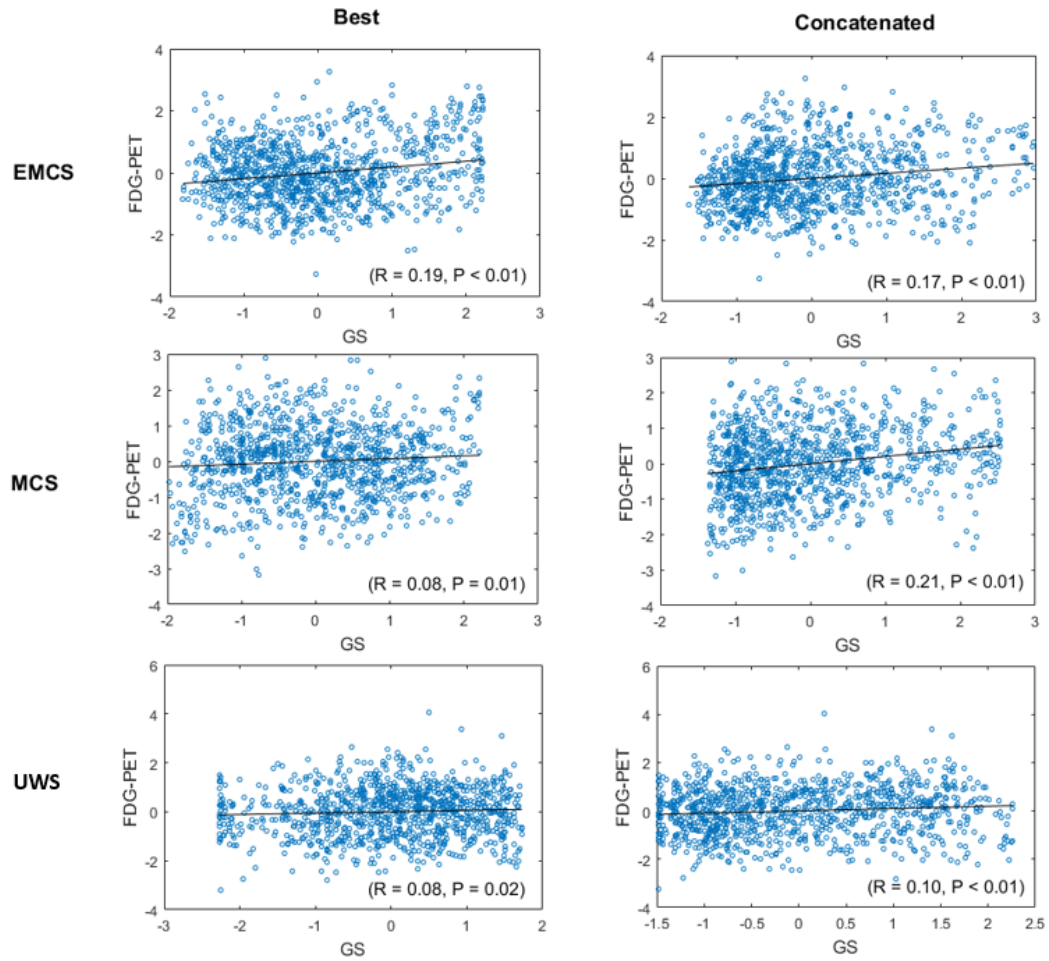


The size of the circle represents the strength of the GS. The darker the circle, the higher the GS. Only the GS values greater than 0.5 of the maximum GS value of that network are plotted.

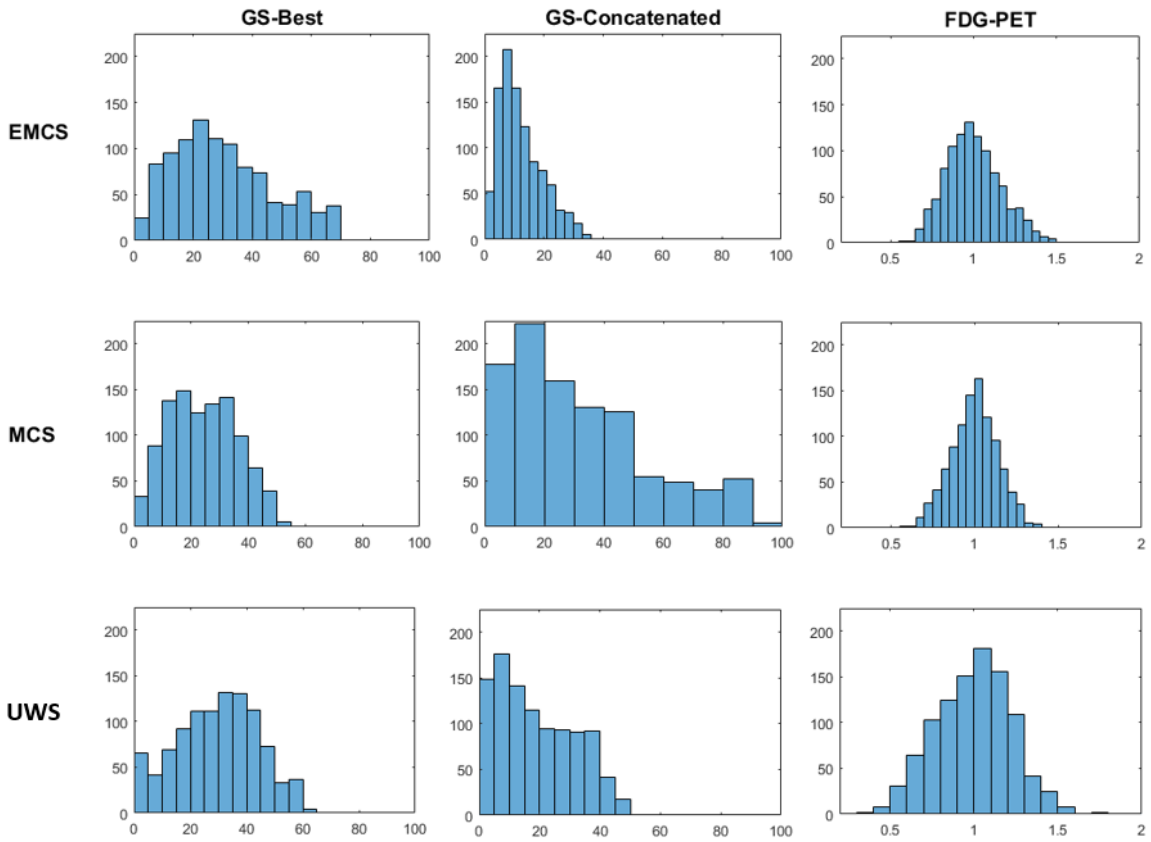
C.5 Motion curves of EMCS, MCS and UWS patients. Motion curve illustrate translation (in mm) for x (blue), y (red), and z (orange) and rotation (in °) for pitch (blue), roll (red), and yaw (orange) parameters, and the time courses of each the nine RSNs (auditory, DMN, ECNL, ECNR, salience, sensorimotor, VL, VM, and VO) over 480 s.



C.6 Scatter plots for the EMCS, MCS and patients in UWS showing the correlation between the FDG-PET and GS of the 1015 parcellated ROI. Solid line indicates the best linear fit to the data and on the southeast corner of each scatter plot the linear correlation value is reported along with its statistical p-value



C.7 Distribution plots of GS for the best acquisition, concatenated data and FDG-PET for patients in EMCS, MCS and UWS



Curriculum Vitae

Name: Sivayini Kandeepan

**Post-secondary Education
and Degrees:**

University of Western Ontario,
London, Ontario, Canada
2016 - 2020

M.Sc. in Physics
The University of Western Ontario
London, Ontario, Canada
2013 - 2016

M.Sc. in Nanoscience and Nanotechnology
Postgraduate Institute in Science,
University of Peradeniya, Sri Lanka
2010 - 2013

B.Sc. Honours Degree in Physics
University of Peradeniya, Sri Lanka
2004 - 2008

Honors and Awards: Lillian Margaret & Walter David Jackson Scholarship in Physics,
2014

Western Graduate Research Scholarship (WGRS)
2013 – Present

University Prize for Academic Excellence 2007/2008,
University of Peradeniya

Related Work Experience: Graduate Teaching and Research Assistant
The University of Western Ontario,
London, Ontario, Canada
2013 – 2019

Lecturer, November 2010 - August 2013
University of Sri Jayewardenepura, Sri Lanka

Lecturer, September 2009 - September 2010
University of Peradeniya, Sri Lanka

Publications:

Kandeepan, S., Maudoux, A., de Paula, D. R., Zheng, J. Y., Cabay, J. E., Gómez, F., Chronik, B. A., Ridder, D., Vanneste, S. & Soddu, A. (2019). Tinnitus distress: a paradoxical attention to the sound?. *Journal of neurology*, 266(9), 2197 – 2207

Cavaliere, C., Kandeepan, S., Aiello, M., Ribeiro de Paula, D., Marchitelli, R., Fiorenza, S., Orsini, M., Trojano, L., Masotta, O., St. Lawrence K., Loreto, V., Chronik, B.A., Nicolai, E., Soddu, A. & Estraneo, A. (2018). Multimodal neuroimaging approach to variability of functional connectivity in disorders of consciousness: a PET/MRI pilot study. *Frontiers in neurology*, 9, 861

Kandeepan, S., Paquette, J. A., Gilroy, J. B., & Mittler, S. (2015). OMCVD Gold Nanoparticles Covalently Attached to Polystyrene for Biosensing Applications. *Chemical Vapor Deposition*, 21(10-11-12), 275-280

M. Dhananjaya, S. Kandeepan (nee Sivayoganathan), U.D.R. Malkanthi, P.M. Jayaweera, Photocatalytic degradation of methylene blue on FeTiO₃/TiO₂/PbS heterojunctions, Sri Lanka Association for the Advancement of Science, **2012**, 70 (extended abstract)

Oral Presentations:

“Modeling an Auditory Stimulated Brain Under Altered States of Consciousness”, Coffee talk organized by Brain and Mind Institute, University of Western Ontario, January 2020

“Assessing Variability of Functional Connectivity in Patients with Disorders of Consciousness using a Multimodal Neuroimaging Approach: A PET/MRI Pilot Study”, 13th World Congress on Brain Injury, organized by International Brain Injury Association (IBIA), March 2019, Sheraton Centre Hotel, Toronto

3MT (3 minute) competition, Faculty Heats 2016 conducted by the Graduate and Postdoctoral studies, University of Western Ontario

Poster Presentations:

“Multimodal neuroimaging approach to disorders of consciousness: a PET/MRI study”, Fallona family interdisciplinary showcase, April 2018, University of Western Ontario

“Dysfunctional Interactions between Networks in Tinnitus”, Western Research Forum, March 2018, University of Western Ontario

“OMCVD Gold Nanoparticles Covalently Attached to Polystyrene for Bio-Sensing Application”, 6th Annual Nano Ontario Conference, November 5 – 6, 2015, University of Ottawa, Canada

“Immobilized AuNPs fabricated on –OH Functionalized Polystyrene using Organo Metallic Chemical Vapor Deposition (OMCVD)”, 5th Annual Nano Ontario Conference, November 6 - 7, 2014, University of Windsor, Canada

Workshops:

Completed the “teaching assistant training program (TATP)”, an interdisciplinary course for graduate teaching assistants on the strategies and practice of university teaching, August 2017, University of Western Ontario

“Some possibilities for Research in Sri Lanka”, Workshop on Nanoscience and nanotechnology, Postgraduate Institute in Science, University of Peradeniya, Sri Lanka, December 2009